STUDIA UNIVERSITATIS
BABEŞ-BOLYAI

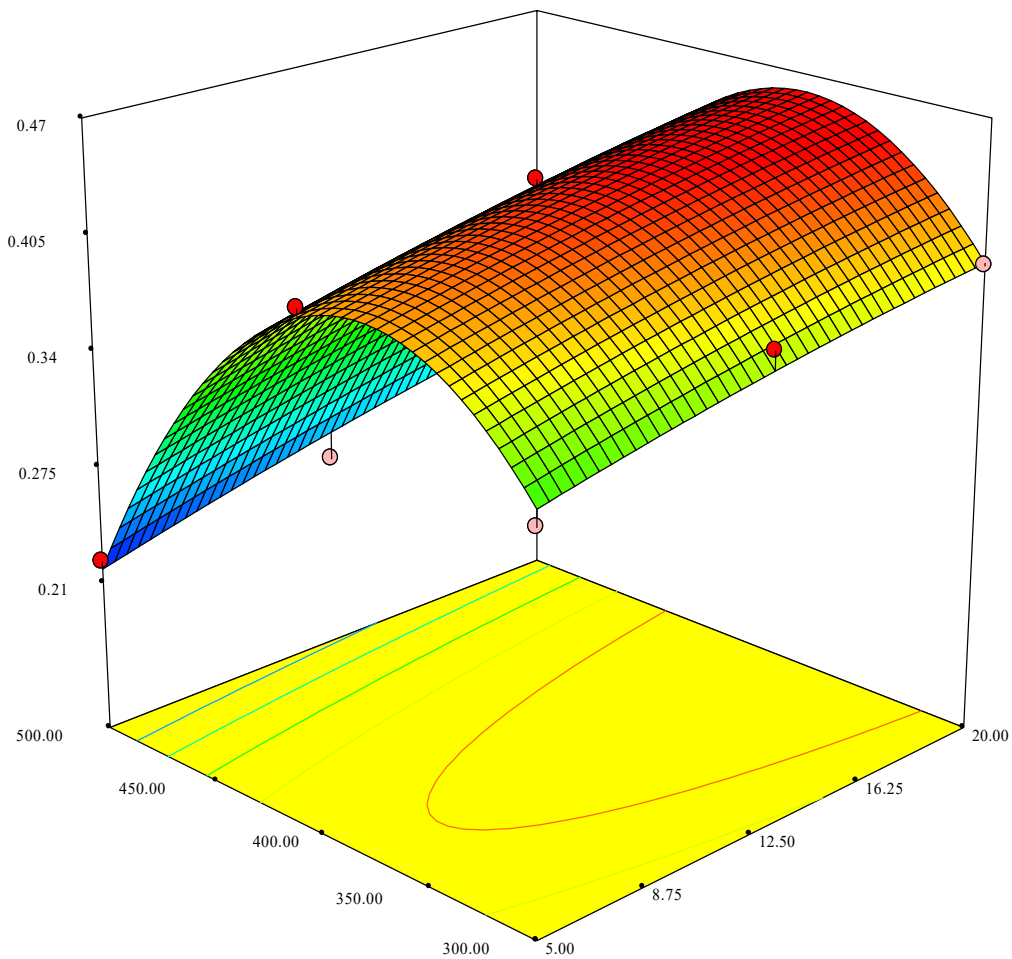

CHEMIA

1/2021

STUDIA UNIVERSITATIS BABEȘ-BOLYAI CHEMIA

1/2021

http://chem.ubbcluj.ro/~studiachemia/;
studiachemia@chem.ubbcluj.ro
http://www.studia.ubbcluj.ro/serii/chemia/index_en.html

YEAR **Volume 66 (LXVI) 2021**
MONTH **MARCH**
ISSUE **1**

S T U D I A
UNIVERSITATIS BABEŞ–BOLYAI
CHEMIA

1

ISSUE DOI:10.24193/subbchem.2021.1

STUDIA UBB EDITORIAL OFFICE: B.P. Hasdeu no. 51, 400371 Cluj-Napoca, Romania, Phone + 40 264 405300 *6452

CUPRINS – CONTENT – SOMMAIRE – INHALT

Studia Universitatis Babes-Bolyai Chemia has been selected for coverage in Thomson Reuters products and custom information services. Beginning with V. 53 (1) 2008, this publication is indexed and abstracted in the following:

- Science Citation Index Expanded (also known as SciSearch®)
- Chemistry Citation Index®
- Journal Citation Reports/Science Edition

STUDIA UBB CHEMIA, LXVI, 1, 2021 (p. 7-8)
(RECOMMENDED CITATION)

E D I T O R I A L

Prof. Dr. Luminita Silaghi-Dumitrescu at her 70th anniversary
Editor in chief *Studia UBB Chemia*
The 9th of March 2021

On the occasion of Prof. Dr. Luminita Silaghi-Dumitrescu's 70th birthday anniversary, the editorial board of *Studia Universitatis Babes-Bolyai* journal, at which she is serving as Editor in Chief for *Chemia* series since the year 2000, wish to honor her as an outstanding member of Babes-Bolyai University's academic community (dean of the Faculty of Chemistry and Chemical Engineering in 2000-2007, vice-rector of Babes-Bolyai University in 2008-2011) with a lifetime of academic and scientific experience characterized by great

devotion, integrity and morality. It has been our privilege to be the colleagues of Prof. Dr. Luminita Silaghi-Dumitrescu and we express the best wishes to her for a good health and every success in her future endeavors.

On behalf of the Editorial Board of *Studia UBB Chemia*
Castelia Cristea
Executive Editor

STUDIA UBB CHEMIA, LXVI, 1, 2021 (p. 9-21)
(RECOMMENDED CITATION)
DOI:10.24193/subbchem.2021.1.01

DEVELOPMENT OF ELECTROCHEMICAL METHODS FOR PRODUCTION OF PURE THALLIUM

YENLIK ZH. USSIPBEKOVA[a], GULZIYA A. SEILKHANOVA[a]*, ANDREY V. BEREZOVSKIY[a], ANDREY P. KURBATOV[a], MICHAEL K. NAURYZBAEV[a]

ABSTRACT. In this work, the electrochemical studies were carried out to improve the purity of rough thallium. The results were obtained by the rough thallium refining through the anodic deposition of thallium oxide (Tl2O3), followed by its reduction to Tl+ by hydroxylamine and repeated electrolysis. At the same time, platinum anode material was replaced with glassy carbon material to reduce economic costs in production. It was found that the addition of ammonium thiocyanate after the dissolution of thallium oxide(III) in nitric acid promotes the inhibition of re-formation of thallium oxide at the anode, as well as more complete oxidation of trivalent thallium to a monovalent state. The thallium obtained in this way is characterized by a purity of 99.96%. Based on the obtained experimental data the principal schemes for obtaining pure thallium are proposed.

Keywords: *thallium, glassy carbon, discharge ionization, refining, thallium oxide, reduction, polarity reversal, electrolysis.*

INTRODUCTION

Currently, the successful development of many branches of chemical, metallurgical, instrument-making, space fields is directly related to the use of new materials based on rare elements with specific application characteristics. Due to its physical and chemical characteristics, in particular, thallium, as well as its compounds of high purity, are widely used in many areas of science and technology. It is known that alloys containing thallium have high wear resistance, inertness with respect to acids, fusibility [1-5]. Thallium

[a] Al-Farabi Kazakh National University, Faculty of Chemstry and Chemical Technology, 71 Al-Farabi av., 050040 Almaty, Kazakhstan
**Corresponding author: g_seilkhanova@mail.ru*

compounds are widely used in optical and radiation engineering [6-8]. Thallium and its compounds are very toxic [9, 10]. However, the toxicity of thallium is not a fundamental reason to refuse to use it. Nevertheless, pyrometallurgical methods, where high temperatures and pressures are applied, fade into the background in the age of development of hydrometallurgy. There are various methods for refining thallium. These include amalgam methods, vacuum distillation, zone recrystallization, electrolysis [2]. The amalgam method makes it possible to obtain high-purity thallium from dilute solutions after decomposition of thallium concentrates. The disadvantage of this method is the use of a toxic metal - mercury. The methods of vacuum distillation and zone recrystallization are characterized by a complex technological implementation of the process of obtaining a pure metal. Studies have shown that thallium is successfully purified by zone recrystallization and by drawing out from the melt of the impurities of copper, aluminum, zinc, cadmium, mercury, cobalt and magnesium [11]. However, there is no effect of purification of thallium by crystallization methods from lead impurities. In this regard, electrolysis as a method of refining is one of the best methods for producing high-purity metals [12]. It is characterized by the simplicity of instrumentation, the ability to effectively conduct processes at normal temperatures and pressures, and high performance. In [13-17] the authors demonstrated the fundamental possibility of electrochemical thallium refining through the stage of production of thallium oxide (III).

In this regard, research in the field of electrochemical methods for producing high purity thallium has particular relevance.

This paper presents the results of the development of methods for producing pure thallium, which can be used to optimize the technology of refining rough thallium. The object of the study was the model solution of the following composition: 95% - Tl, 2.5% - Pb, 0.75% - Cu, 1.5% - Cd, 0.25% - Fe. This composition corresponds to 95% rough thallium.

RESULTS AND DISCUSSION

In order to obtain pure thallium, the polarization curves of thallium sulfate (Tl_2SO_4) were recorded, and the thallium recovery potential was found. Previously, it was investigated that the maximum conditional current efficiency of thallium is typical for sulfate solution than nitrate and acetate, due to the lower contribution of adverse reactions. Sulfate electrolyte was chosen for this purpose [18].

As can be seen from Figure 1, a wave at a potential of –0.85 V is observed in the sulfate electrolyte on the polarization curve in the cathode region, which corresponds to the process of thallium reduction ($Tl^{+}+1e^{-}\rightarrow Tl^{0}$), and then hydrogen is released. On the reverse course of the polarization curve, an anode peak is observed at a potential of -0.7 V, which corresponds to the dissolution of the precipitated thallium ($Tl^{0}\rightarrow Tl^{+}+1e^{-}$).

Table 1. The conditional current efficiency at different sweep rates

Electrode	v [mV/s]	Output current, %
Glass carbon	50	60.0±3.3
	20	83.0±3.7
	10	59.0±2.9
	5	58.0±2.6

The conditional current efficiency at different sweep rates was also calculated during the study. The results showed that 20 mV/s is an optimal rate (Table 1). At a sweep rate of 50 mV/s thallium ions cannot settle on the cathode due to the high speed, hence, the dissolution at the anode is less. At low sweep rates other side reactions can occur along with thallium deposition, therefore the current is not completely consumed for thallium reduction. Based on the results obtained, a sweep rate of 20 mV/s was chosen for further research.

In order to optimize the process of purification of rough thallium, studies were carried out in a bulk electrolysis cell at a potential of -0.85 V, in which a glassy carbon plate was used as the cathode, platinum served as the anode, the reference electrode was silver chloride electrode. It has been established that in addition to deposition on the cathode of thallium ($Tl^{+}+1e^{-}\rightarrow Tl^{0}$), at the anode at pH>2, the platinum plate is covered with a dark brown precipitate, which is the trivalent thallium oxide (Tl_2O_3) according to the literature [19,20]. In this case, the following reaction takes place at the anode:

$$2Tl^{+}+ 3H_2O = Tl_2O_3 + 6H^{+} + 4e^{-} \qquad [1]$$

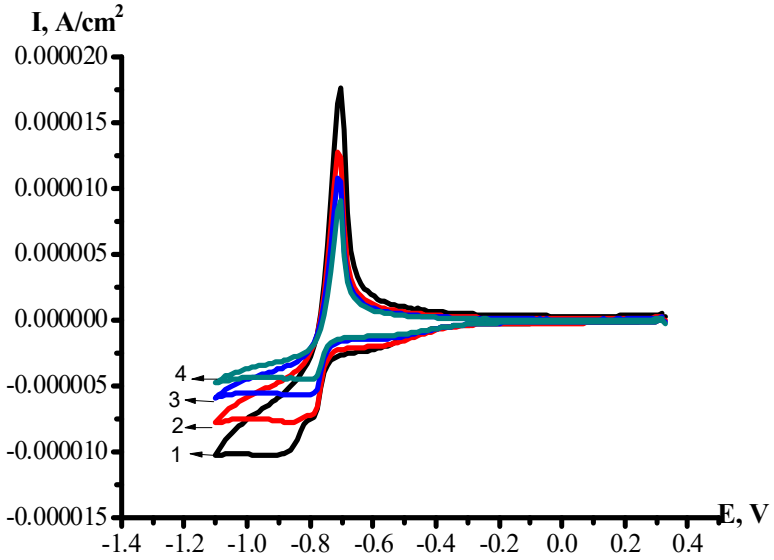

Figure 1. Polarization curves of Tl_2SO_4 on glassy carbon electrode at different scan rates, Experimental conditions: electrolyte, 10^{-3} mol L^{-1} Tl_2SO_4; scan rates, 1-50, 2- 20, 3- 10, 4- 5mV/s; starting potential 0.3 V, pH=2

The fact of the anodic formation of Tl_2O_3 in the work was used for the selective deposition of thallium from the model solution of the following composition: 95% - Tl, 2.5% - Pb, 0.75% - Cu, 1.5% - Cd, 0.25% - Fe (this composition corresponds to 95% rough thallium). The results of qualitative and quantitative analysis of impurities of cathode and anode sediments obtained by atomic emission spectroscopy are presented in table 1. As can be seen from this table, almost complete deposition of lead ions in the form of $PbSO_4$ occurs after contact with sulfuric acid with a model solution. At the same time, high content of other impurities (copper, cadmium, iron) is observed in the cathode precipitate, due to close or more positive electrode potentials.

Influence of pH. The most pure, *i.e.* with a smaller amount of these impurities is the anodic precipitate - Tl_2O_3. It should be noted that its most dangerous impurity is an admixture of iron, which co-precipitates with thallium oxide, due to the close pH values of hydrate formation [21]. After electrolysis, Tl_2O_3 is formed at the anode (at pH=5, the degree of purity of the oxide is 99.60%), then this oxide was dissolved in concentrated nitric acid. Then, thallium (III) was reduced by hydroxylamine to the monovalent state:

$$2Tl^{3+} + 2NH_2OH = 2Tl^{+} + N_2O + H_2O + 4H^{+} \quad [2]$$

Further, repeated electrolytic cathode emission of thallium on glassy carbon at pH = 2 was carried out. As can be seen from table 2, the degree of purity of thallium was 99.73%.

Also, an attempt was made to obtain pure thallium by replacing the polarity. In this case, the platinum plate on which the thallium oxide is deposited becomes the cathode and repeated electrolysis was carried out at pH = 11. At the second stage of electrolysis, pure platinum was used as the anode. The electrolysis was carried out at a potential of -0.85 V for 30 minutes. During repeated electrolysis, thallium reduction directly from Tl_2O_3 was observed. At lower pH values, reduction to metallic thallium is complicated by the side reaction of hydrogen evolution, since the overvoltage of hydrogen on platinum is low. As can be seen from table 1, in this case, the purity of the precipitated thallium is 99.81%. This method has the potential for implementation in production, since it is less time-consuming, however it is necessary to develop optimal conditions for increasing the purity of thallium.

Table 2. The content of impurities in the anode and cathode sediments.

Electrode, pH	Content of Tl, %	Content of Cd, %	Content of Cu, %	Content of Fe, %	Content of Pb, %
before electrolysis	95.00±0.07	1.50±0.05	0.75±0.02	0.25±0.01	2.50±0.08
Cathode (GC), pH=2	97.40±0.09	0.93 ±0.01	1.50±0.05	0.17 ±0.01	0
Cathode, pH=5	98.70±0.08	0.72 ±0.06	0.45±0.02	0.13±0.01	
Anode, pH=5 (degree of purityTl_2O_3)	99.60±0.09	0.03 ±0.01	0.07±0.01	0.30±0.02	0
Cathode (GC), pH=1 after reduction with hydroxylamine (from Tl_2O_3)	99.73±0.01	0.02±0.002	0	0.26±0.01	0
Cathode (GC), after replacing polarity	99.81±0.003	0.03±0.001	0.006±0.001	0.10±0.02	0

Based on the analysis of experimental data, the following schemes for obtaining pure thallium are proposed, which are presented in Figures 2-3. In the proposed schemes, the production of pure thallium is carried out by repeated electrolysis of the solution obtained by dissolving the anode precipitate Tl_2O_3.

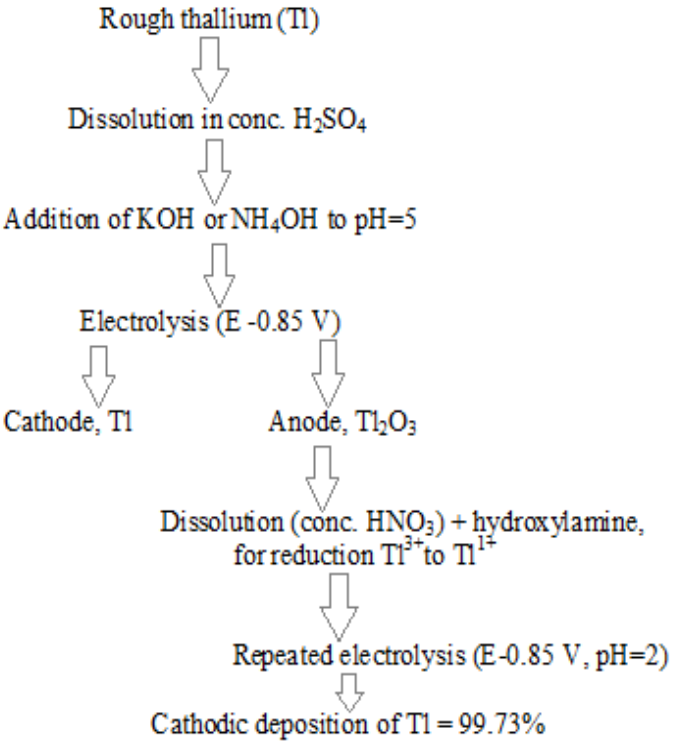

Figure 2. The scheme for obtaining pure thallium using hydroxylamine

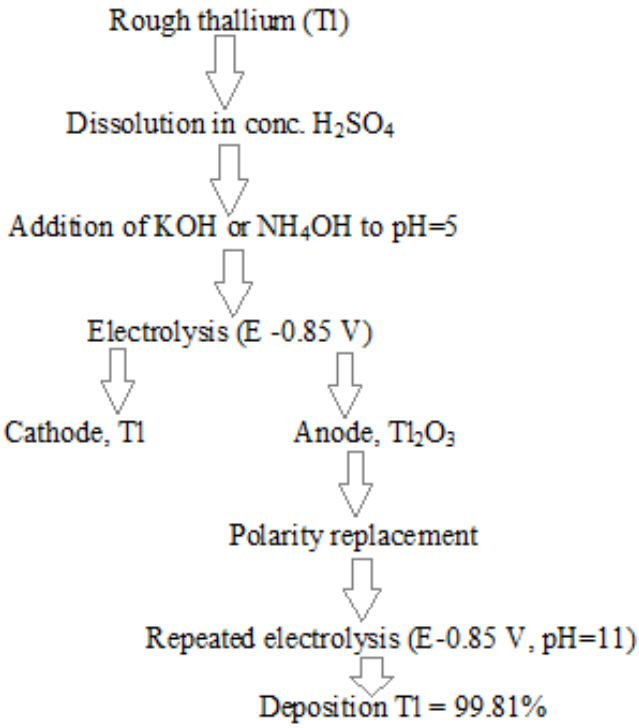

Figure 3. The scheme for obtaining pure thallium by replacing the polarity

The influence of reducing agent. Based on the results of quantitative analysis, it was established that the main impurity, which is found in thallium oxide (III), is an iron impurity. 10 ml of 10^{-2} mol L^{-1} solution of ammonium thiocyanate (NH_4SCN) was added to bind iron ions to the electrolyte formed by dissolution of thallium oxide (III) in nitric acid. It is known that this results in the formation of the iron thiocyanate complex [22]:

$$Fe^{3+} + 3SCN^{-} = Fe(SCN)_3 \quad [3]$$

It was found that the addition of thiocyanate also contributes to the inhibition of the process of re-formation of thallium oxide. It should be noted that after the dissolution of thallium oxide (III) in nitric acid, repeated electrolysis to produce metallic thallium should be carried out at pH=1-2.

Since at higher pH values Tl_2O_3 is precipitated, the formation of which is undesirable at this stage. And at low pH values, the formation of metallic thallium at the cathode is complicated by the parallel hydrogen release. Therefore, for electrolysis at higher pH values, it is necessary to introduce an additive into the electrolyte, which will inhibit the re-formation of Tl_2O_3 at the anode. For this purpose, as well as a complexing agent, a low molecular weight ligand of ammonium thiocyanate was added to the electrolyte. As a result of the addition of ammonium thiocyanate, in addition to iron thiocyanate, thallium (I) thiocyanate is formed, which is soluble in water [21]:

$$3Tl^{3+}+4SCN^{-}+4H_2O= 3Tl^{+}\ SCN^{-}+HCN+7H^{+}+SO_4^{2-} \qquad [4]$$

This allows thallium to be converted from oxidation state (+3) to thallium (+1), which also eliminates the possibility of re-formation of Tl_2O_3.

Figures 4 (a and b) show the cyclic voltamogramms of thallium without the addition of ammonium thiocyanate (a), with the addition of thiocyanate (b). In Figure 4a, in the anode part, two peaks are clearly visible: the peak at -0.6 V ($Tl^0 \rightarrow Tl^+ + 1e^-$) corresponds to the dissolution of metallic thallium, and the peak at -0.48 V ($Tl^+ \rightarrow Tl^{3+} + 2e^-$) - to the oxidation of monovalent thallium to trivalent. Figure 4b shows one peak at -0.6 V ($Tl^0 \rightarrow Tl^+ + 1e^-$) corresponding to the dissolution of metallic thallium. The obtained experimental data prove that, with the addition of ammonium thiocyanate, trivalent thallium is absent in the solution, i.e. it is completely reduced to its oxidation state (+1).

When metal thallium is obtained, dendrites are formed at the cathode, which reduces in this place the distance between the cathode and the anode. The decrease of the interelectrode distance leads to a decrease in electrical resistance, and, consequently, to a local increase in current density [23]. The latter causes the accelerated deposition of thallium on the dendrite and its accelerated growth. Dendrite growth can eventually lead to a short circuit between the cathode and the anode. In the presence of dendrites, a highly developed cathode surface holds a large amount of electrolyte and is poorly washed, that worsens the quality of the target product, and also reduces the purity of thallium.

To improve the cathode surface, various surface-active additives are introduced into the electrolytes: glue (wood), gelatin, etc. [24]. One explanation of the mechanism of surfactants is that they are adsorbed on the most active parts of the surface, and at the same time induce a local increase in electrical resistance, which prevents the growth of dendrite, as a result, the surface becomes smoother, and the cathodic precipitate more dense. After the cathode surface is aligned, the colloidal particle is desorbed into the electrolyte.

Solutions of additives are introduced into the circulating electrolyte. Usually glue and gelatin are introduced together. It is known from the literature that 20 g of glue and 40 g of gelatin are usually injected per ton of produced metal [25].

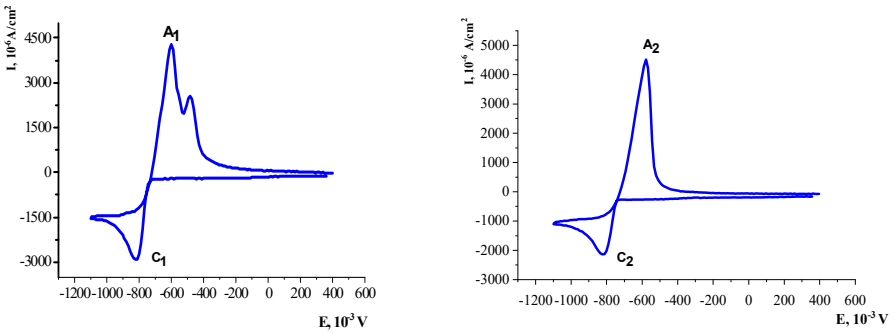

a) b)

Figure 4. Polarization curves of 10^{-2} mol L^{-1} Tl_2SO_4 on glassy carbon electrode without (a) and with the addition of 10^{-2} mol L^{-1} ammonium thiocyanate (b). Experimental conditions: scan rate, 20 mV*s-1; starting potential 0.3 V, pH=2

In this work, 10 ml of a solution containing 0.0001 g of wood glue and 0.0002 g of gelatin were added to the electrolyte to obtain pure thallium. In this case, a homogeneous cathodic precipitate of thallium was obtained, the purity of which is not deteriorated in comparison with thallium obtained without these additives. In the case of thallium without surfactant additives, it is a spongy mass poorly kept on the cathode. As it is known, continuous mixing of the solution is required to intensify the adsorption of surfactants on the electrode [26]. For these purposes, a magnetic stirrer was used, and the effect of the stirring rate of the solution on electrochemical processes was studied, the cyclic voltamogramms are shown in Figure 5.

As can be seen from the obtained polarization curves, there is an increase in the currents of reduction and oxidation of thallium with an increase in stirring rate of the electrolyte. In this case, there is a linear dependence of the current density in the anode and cathode processes on the square root of the stirring rate, which indicates the diffusion mode of the cathodic and anodic processes with the participation of thallium.

After repeated electrolysis using this method, cathode thallium was obtained with a purity of 99.96% (Tl, %=99.96, Cd, %=0.03, Cu,%=0.01).

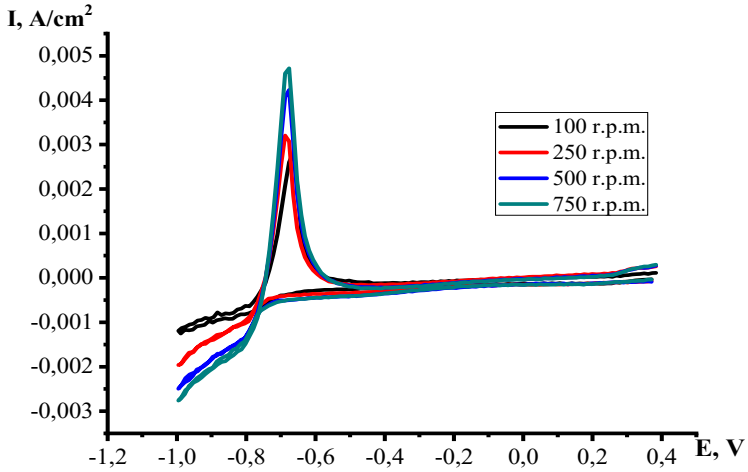

Figure 5. Polarization curves of 10^{-2} M Tl_2SO_4 on glassy carbon electrode at different stirring rates. Experimental conditions: scan rates,20mV*s-1; starting potential 0.3 V, pH=2.

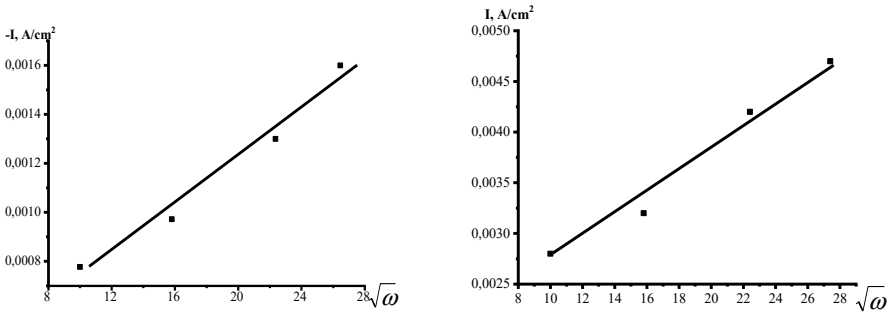

a) b)

Figure 6. The dependence of the catodic (a) and anodic (B) peak current densities on $\sqrt{\omega}$, where ω is the stirring rate of solution. Experimental conditions: see Fig 5.

Based on the obtained experimental data, the following scheme for obtaining pure thallium is proposed:

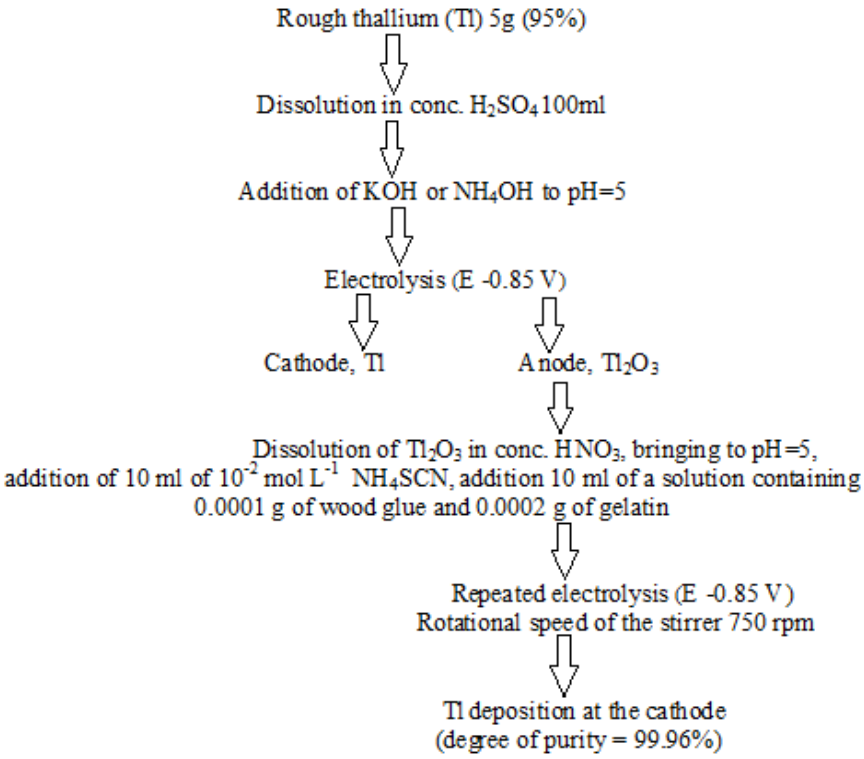

Figure 7. The scheme for obtaining pure thallium with the addition of ammonium thiocyanate, wood glue and gelatin; electrolysis pH=2.

Thus, it was found that the addition of hydroxylamine to restore to monovalent state of thallium, after the dissolution of thallium oxide in nitric acid, and the purity of thallium is significantly increased. For this purpose, platinum anode material was also replaced with glassy carbon material to reduce the economic costs of production.

CONCLUSIONS

Thus, the best results showed that the addition of thiocyanate, after the dissolution of thallium oxide in nitric acid contributes to the inhibition of the re-formation of thallium oxide at the anode, oxidation of trivalent thallium to monovalent and production of thallium with a purity of 99.96 %, due to the disposal of iron impurities.

EXPERIMENTAL

In this paper, the measurements were carried out with a computer interfaced AUTOLAB-30 potentiostat-galvanostat. Glassy carbon electrode was used as a working electrode (GC, surface area 1 cm^2). The auxiliary electrode was a platinum electrode (surface area 1 cm^2), a silver chloride electrode (Ag/AgCl, KCl 3M) served as reference electrode (E= -0.222 V). In addition, hydroxylamine solution, 10^{-2} mol L^{-1} was used as a reducing agent, ammonium thiocyanate solution, 10^{-2} mol L^{-1} – as a complexing agent, wood glue (synthetic wood glue - a condensation product of urea with formaldehyde in an alkaline and acidic environment (urea-formaldehyde resin MP-RHK)) and gelatin (food grade) were used to improve the quality of the cathode precipitate. In order to dissolve the obtained thallium (III) oxide and to precipitate lead ions, 63% HNO_3 and 93.6% H_2SO_4 (CP grade) were used, respectively. Sulfate electrolyte (Tl_2SO_4, CP grade) and aqueous solution salts of lead, copper, cadmium and iron ($PbSO_4$, $CuSO_4$, $CdSO_4$, $FeSO_4$, CP grade) were used as the test electrolyte.

Qualitative and quantitative analysis of impurities of cathode and anode sediments was carried out by atomic emission spectroscopy (Perkin Elmer, 5ICP OES 8000, Germany).

REFERENCES

1. S.S. Korovina *Rare and Scattered elements. Chemistry and technology. V. 1. M: MISiS*, **1996**, pp 375.
2. A.N. Zelikman, B.G. Korshunov *Metallurgy of rare metals:* textbook for high school. – 2nd edition, **1991**, pp 432.
3. S.V. Kharitonov, V.I. Zarembo, *J. Anal. Chem*., **2005**, *60(11),* 1187-1192.
4. C. Somayye, M.A. Taher, H. Fazelirad, *Microchim Acta*, **2013**, *11-12*, 1157–1163.
5. A. De Leenheer, H. Nelis, W. Lambert, *Encyclopedia of Analytical Science*. A. Townshend (ed.). **1995**, *9*, pp 560.
6. T.A. Kuketaev, Khabarshy, *Herald*, **2008**, 69.
7. B.S. Sheiman, *Emergency medicine*. **2014**, 4, 52-57.
8. S. Moeschlin, *Clin. Toxicol*. **1980**, *17,* 133–146.
9. F. Kemper, H. Bertram, *Thallium. Metall of Their Compound*, Germany, Muenster, **1991**, pp 1271-1241.
10. J.O. Nriagu (Ed.) *Thallium in the Environment*, Advances in Environmental Science and Technology, NY: Wiley and Sons, **1998**, 29, pp 284.

11. http://metal-archive.ru/metallurgiya-chistyh-metallov/2251-poluchenie-chistogo-talliya.html
12. B.B. Damaskin, O.A. Petry, G.A. Zirlina, *Electrochemistry*, 2 ed., edited and added, M.: Chemistry, Kolos, **2006**, pp 672.
13. A.P. Kurbatov, G.A. Seilkhanova, M.K. Nauryzbaev, Ye. Zh. Ussipbekova, A. V. Berezovskiy, Innovative patent for invention № 29953 Electrolytic method for producing pure thallium, published 15.06. Bulletin №6. **2015**.
14. G.A. Seilkhanova, A.P. Kurbatov, M.K. Nauryzbaev, A.V. Berezovskiy, A.A. Utesheva, Utility patent model № 1514 Electrochemical methods of obtaining pure thallium, published 30.06. Bulletin - № 6b. **2016**;
15. G.A. Seilkhanova, Ye. Zh. Ussipbekova, A.P. Kurbatov, M.K. Nauryzbaev, A.V. Berezovskiy, A.A. Utesheva KZ. Utility patent model № 2286 Electrolytic method for producing rough thallium, published 31.07. Bulletin - № 14**. 2017**;
16. G.A. Seilkhanova, Ch. Jeyabhrathi, F. Scholz, A.P. Kurbatov, M.K. Nauryzbaev, A. Berezovskiy, *I. J. Anal. Chem*. **2015**, Article ID 357514, doi:10.1155/2015/357514.
17. G.A. Seilkhanova, A.P. Kurbatov, A.V. Berezovskiy, M.K, Nayryzbaev, *Studia UBB Chemia*, **2017**, *62 4(II)*, 421-432.
18. G.A. Seilkhanova, Ye. Zh. Ussipbekova, A.P. Kurbatov, A.V. Berezovskiy, *Bulletin of Al-Farabi Kazakh National University. Chemical series*, **2014**, 2 (74), 47-52.
19. S.Y. Vasiliev, Anode electrocrystallization in thallium-oxide system // Abstract. diss. Moscow, **1996**, 25-32.
20. Ye. Zh. Ussipbekova, G.A. Seilkhanova, F. Scholz, A.P. Kurbatov, A.V. Berezovskiy, B.S. Bakirova, M.K. Nauryzbaev, *News NAN RK. Chemical series*, **2014**, 5(408), 53-58.
21. V.V. Eremin, S.I. Kargov, I.A. Uspenskaya, N.E. Kuzmenko, V.V. Lunin, *The basis of physical chemistry, Theory and problems*, M.: Exam, **2005**, pp 480
22. N. L. Glinka *General Chemistry*. 30 ed., **2003**, pp 728.
23. L.F. Kozin, *Kiev Sciences*, **1983**, 37.
24. https://ohranatruda.ru/ot_biblio/norma/386456/ (Russian language)
25. http://www.textreferat.com/referat-1569.html (Russian language)
26. G.A. Tsirlina, *Electrochemistry*, **1995**, *31*, 219-221.

STUDIA UBB CHEMIA, LXVI, 1, 2021 (p. 23-34)
(RECOMMENDED CITATION)
DOI:10.24193/subbchem.2021.1.02

ZERO-VALENT IRON NICKEL MODIFIED NATURAL ZEOLITE MATERIAL: CHARACTERIZATION AND ENVIRONMENTAL ASPECT OF APPLICATION – FIRST RESULTS

NENAD S. KRSTIĆ[a,*], VLADIMIR D. DIMITRIJEVIĆ[a], MAJA N. STANKOVIĆ[a], DEJAN T. DULANOVIĆ[a], MILOŠ G. ĐORĐEVIĆ[a,b], MILOŠ MARINKOVIĆ[a], DRAGAN M. ĐORĐEVIĆ[a]

ABSTRACT. The aim of this study was preparation of one low cost and environmentally friendly material for wastewater treatment toward both inorganic and organic pollutants, based on natural zeolite from one of the largest zeolite deposits in Serbia (Zlatokop, Vranjska Banja). The idea was to integrate zero-valent bimetallic FeNi particles onto zeolite, based on liquid-phase reduction method. Obtained material zvFeNi@zVB showed good sorption properties with high removal efficiency under the investigated conditions toward inorganic (M(II) heavy metal ions Cu, Cd, Pb, Zn) and organic (dyes Reactive Blue 19 and Methylene Blue) pollutants. Compared with pure FeNi material, modified zeolite (zvFeNi@zVB) showed better sorption properties and "faster clean" water from evaluated pollutants.

Keywords: *low cost-, environmentally friendly- material, bimetallic zero-valent FeNi particles, zeolite, wastewater treatment.*

INTRODUCTION

Water pollution by inorganic and organic hazardous materials presents serious environmental problem throughout the world. Different ways of water contamination can be produced by numerous sources (industry, agriculture, human activities). The main goal of many studies from different parts of the world was to find high efficiency material for water

[a] *University of Niš, Faculty of Science and Mathematics, Department of Chemistry, Višegradska 33, 18000 Niš, Serbia*
[b] *PUC for water supply and sewerage "Naissus", Kneginje Ljubice 1/1, 18000 Niš, Serbia*
[*] *Corresponding author, e-mail: nenad.krstic84@yahoo.com*

treatment. That material must be cheap and easy to prepare, but at the same time made from some natural and widely available material or an industrial nus-product; and of course, to be environmentally friendly [1-3].

Different materials and methods for water treatments can be found in the literature, like untreated and/or the chemically modified biomasses, such as papaya wood [4], Coriandrum sativum [5], peanut hull pellets [6], sago waste [7], rice husk ash and neem bark [8], grape stalk wastes [9], Lagenaria vulgarias shell [1,2] etc. Natural and chemically modified zeolites are widely used as low-cost material for water treatment due to their three-dimensional aluminosilicate framework high surface area and good ion-exchangeable capacity. Zeolite was chemically modified by acids, bases, or salts treatment and/or hydrothermally [10-14]. Recently, researchers have modified natural zeolites with inorganic salts (like iron, manganese) to enhance their affinity towards pollutants by making the surface area larger and number of active sites increased [15-17].

Materials based on zero-valent metal (for example iron, iron-nickel) particles, such as clay modification materials, have been investigated in recent years as a potential sorbent [18-22].

The goal of our study was to prepare a new low cost and environmentally friendly material based on chemically modified natural zeolite. That was done by treating natural zeolite with zero-valent, bimetallic iron-nickel particles. The natural zeolite was collected from one of the largest Serbian deposits (Zlatokop deposit near Vranjska Banja). We have chosen this zeolite because there were no data of its application in the literature (in the context of this type of the modification). Due to comparison and evaluation of its potential, beside zero-valent iron nickel zeolite (zvFeNi@zVB) material, bimetallic zero-valent iron nickel (zvFeNi) referent material was synthetized as well. After the preparation of these materials preliminary environmental application on wastewater treatment was conducted as sorption experiments of removing inorganic (M(II) heavy metal ions Cu, Cd, Pb, Zn) and organic (anthraquinone reactive dye C.I. Reactive Blue 19 (RB 19) and Methylene Blue - MB) pollutants. Also, FTIR, SEM-EDX, XRD, and BET characterizations of new prepared materials were done.

RESULTS AND DISCUSSION

Fourier Transform Infrared (FTIR) Spectrometry

The FTIR spectra of natural zeolite (zVB), zero-valent iron-nickel (zvFeNi) material and zero-valent iron-nickel chemically modified zeolite (zvFeNi@zVB) material recorded in the wavelength region between 400 and

4000 cm^{-1} are shown in Figure 1. The FTIR spectrum of natural zeolite from Zlatokop locality (Vranjska Banja, Serbia) which is shown on Figure 1a is characterized by bands typical for alumo-silicate materials. Detailed FTIR analysis of zVB is given in our previous study [14]. The low peak (Fig. 1b) at around 3400 cm^{-1} belongs to stretching vibrations of -OH group from small trace of iron-oxide hydroxide, while adsorption peaks around 460 and 530 cm^{-1} correspond to Fe-O stretching vibrations. This peaks in FTIR spectrum of zvFeNi material can be explained by air corrosion of iron [22,23].

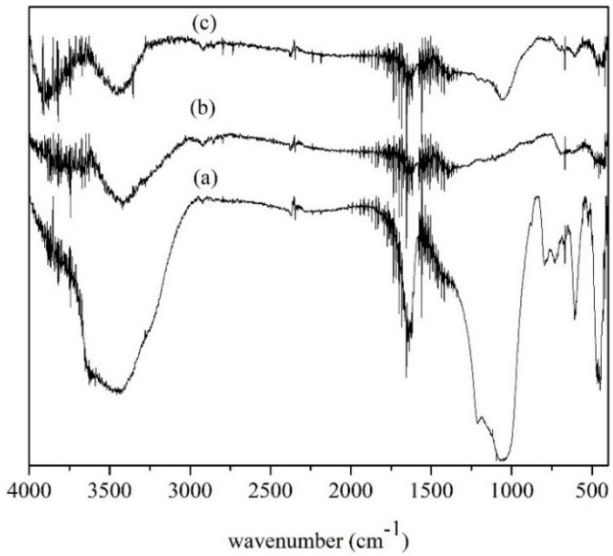

Figure 1. FTIR spectra of: (a) zVB, (b) zvFeNi and (c) zvFeNi@zVB material.

Changes in FTIR spectrum obtained from zvFeNi@zVB compared to spectra of natural zeolite (Figure 1a) are presented in Figure 1c. Intensity decrease of the adsorption peaks at around 690 and 790 cm^{-1} is a result of partly destruction of Si-O and Al-O bands by treatment with $NaBH_4$ during preparation of zero-valent iron nickel particles. Good integration (loading) of FeNi particles onto natural zeolite is observed in Figure 1, where the adsorption peaks of FeNi spectrum (Figure 1b) are also appeared in zvFeNi@zVB spectrum (Figure 1c) [24].

X-ray diffraction analysis

XRD diffractograms of zvFeNi and zvFeNi@zVB samples are shown in Figure 2. As reported in our previous research, zeolite that was used in the study is good quality with clinoptilolite as dominant mineral, more than 90%

(an intense peak at the 2θ angle of 22°). Also, investigated natural zeolite contained other minerals like quartz, mordenite, albite and calcite in minority [14]. According to the data from XRD diffractograms high intense peak of 2θ angle of c.a. 45° indicates the presence of zero valent metals Fe^0 and Ni^0 in zvFeNi and zvFeNi@zVB material. Low intense peaks at about 2θ angle of 35° and 65° indicates a present of small amount of iron oxide hydroxide which is in accordance with FTIR data [21,25].

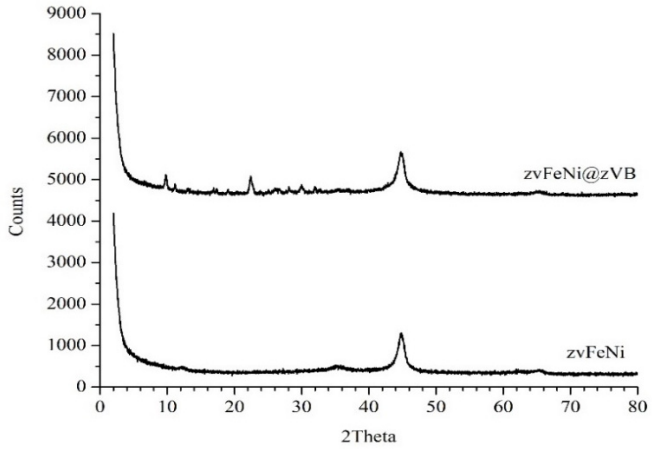

Figure 2. XRD diffractograms of: zvFeNi and zvFeNi@zVB material.

Scanning electron microscopy with energy dispersive X-ray spectroscopy

The morphology of obtained materials zFeNi (Figure 3a) and zvFeNi@zVB (Figure 3b) was observed by scanning electron microscopy. These micrographs show porous structure with a low agglomeration [19].

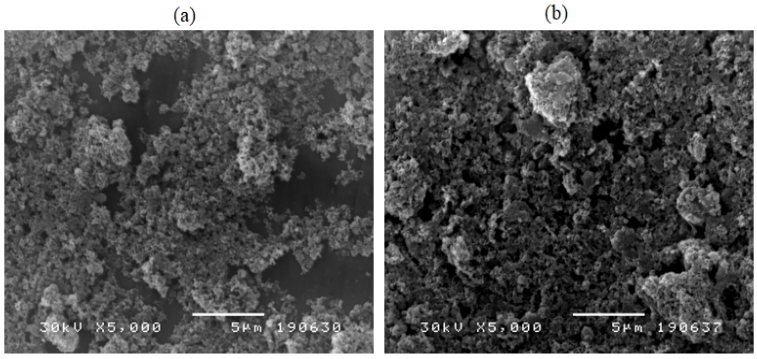

Figure 3. SEM micrographs of: (a) zvFeNi and (b) zvFeNi@zVB materials.

The elemental composition of investigated materials was evaluated by electron dispersive X-ray analysis (Figure 4). In EDX spectrum of zvFeNi material (Figure 4a) intensive characteristic peaks for iron and nickel were identified, which confirmed bimetallic nature of obtained material. The presence of oxygen peak was a result of small iron oxidation during manipulation with material, which was in accordance with data obtained by FTIR and XRD analyses. Data from Figure 4b indicate good integration of bimetallic zero-valent iron nickel particles into aluminosilicate structure of zeolite. The appearance of the peak for copper in EDX spectrum on Figure 4c indicate sorption ability (affinity) of zvFeNi@zVB toward copper(II) ion from waste waters.

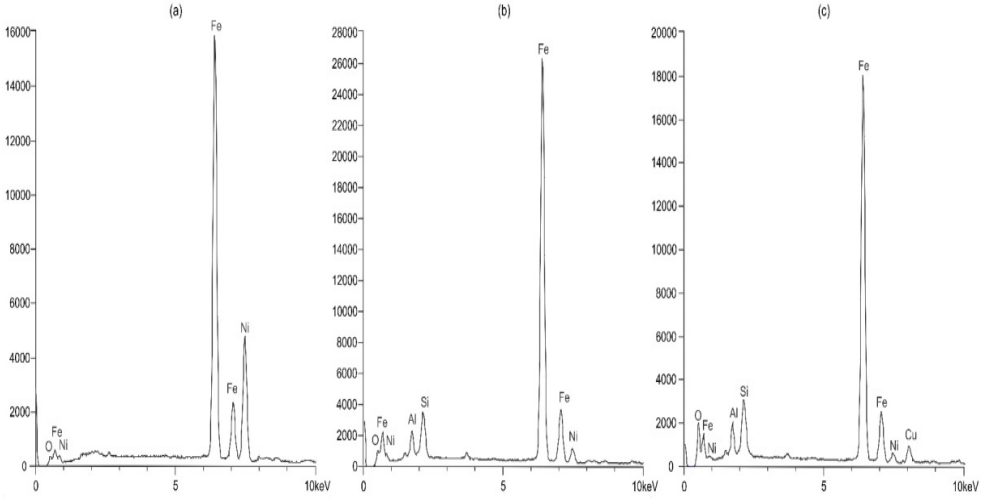

Figure 4. EDX spectra of: (a) zvFeNi, (b) zvFeNi@zVB material and (c) zvFeNi@zVB material after treatment of Cu contaminated water

Environmental aspect of obtained materials - preliminary sorption results

The effect of contact time on the residual concentration of analyzed inorganic and organic pollutants, in aqueous solution with zvFeNi and zvFeNi@zVB material is shown in Fig. 5. Experiments were performed with model wastewater system at an initial concentration of 50.0 mg dm^{-3}, a sorbent dose of 4.0 g dm^{-3}, at 20±0.5°C and pH 5.0.

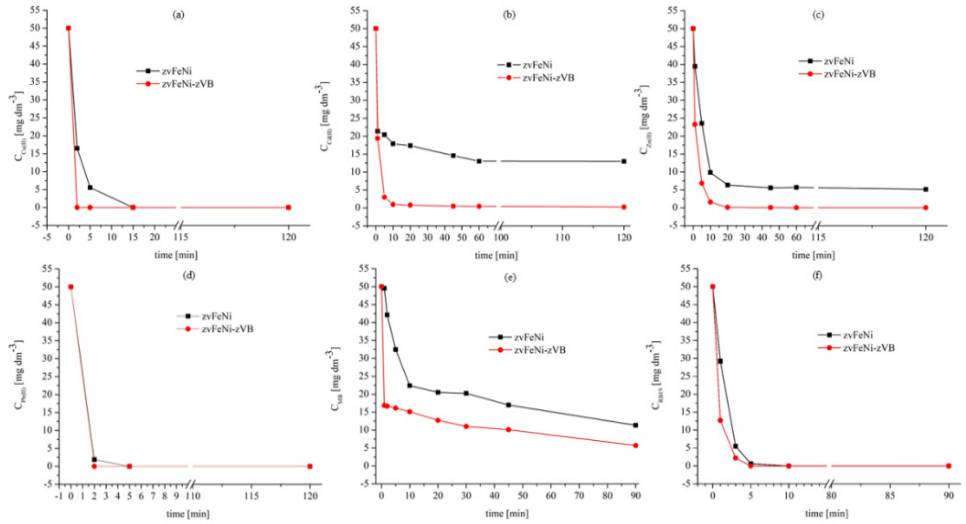

Figure 5. Effect of contact time on removal: (a) Cu(II) ion, (b) Cd(II) ion, (c) Zn(II) ion, (d) Pb(II) ion, (e) MB and (f) RB19 by zvFeNi (■) and zvFeNi@zVB (●) material.

The adsorption capacity, q_e [mg g^{-1}], and removal efficiency, *RE [%]*, of the investigated materials calculated according to equation (1) and (2) are shown in Figure 6.

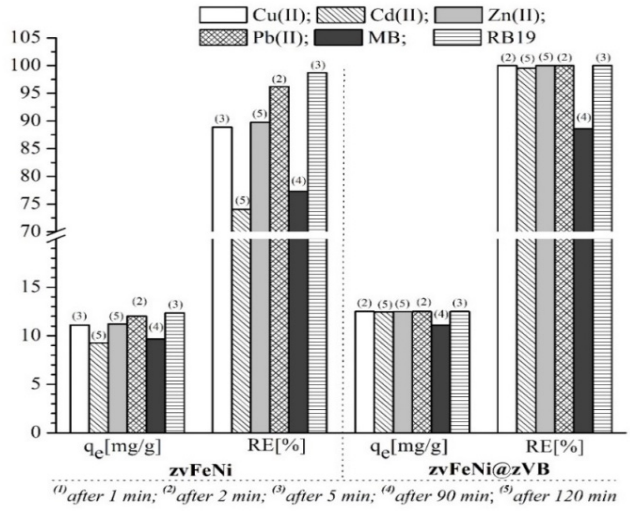

Figure 6. The adsorption capacity and removal efficiency of zvFeNi and zvFeNi@zVB material toward investigated pollutants in aqueous solution

These preliminary results, based on data from Figures 5 and 6, indicate that zero-valent iron-nickel (zvFeNi) and zero-valent iron-nickel modified natural zeolite (zvFeNi@zVB) materials showed good sorption properties toward investigated pollutants. Both materials were very efficient toward copper(II) and lead(II) ions. After five minutes zvFeNi removal efficiency toward Cu(II) was 88.90% (q_e = 11.11 mg g^{-1}) and it totally removed this ion after fifteen minutes (RE = 100%), while zvFeNi@zVB material showed better sorption characteristics (faster remove this heavy metal ion) and after two minutes completely removed Cu(II) ion from aqueous solution, RE = 100% and q_e = 12.50 mg g^{-1}. In the case of Pb(II) ion zvFeNi@zVB showed the same properties like in the situation of removing Cu(II) ion (RE = 100% and q_e = 12.50 mg g^{-1}), while the zvFeNi material showed better removal properties toward Pb(II) than Cu(II) ion, and totally removed it after five minutes. Material zvFeNi is potentially good sorbent to „clean" water from cadmium(II) and zink(II) ions $RE_{Cd(II)}$= 74.05% and $RE_{Zn(II)}$= 89.76% ($q_{e(Cd(II))}$ = 9.26 mg g^{-1} and $q_{e(Cd(II))}$ = 11.22 mg g^{-1}), but zeolite modified with zero-valent iron-nickel particles showed better cleaning properties toward these heavy metal ion $RE_{Cd(II)}$= 99.54% and $RE_{Zn(II)}$= 99.97% ($q_{e(Cd(II))}$ = 12.44 mg g^{-1} and $q_{e(Cd(II))}$ = 12.497 mg g^{-1}). Investigated materials showed good removal efficiency toward methylene blue 77.31% (q_{eMB}= 9.66 mg g^{-1}) zvFeNi and 88.60% (q_{eMB}= 11.07 mg g^{-1}) zvFeNi@zVB. In the case of reactive blue 19 zvFeNi@zVB removed 95.6% after three minutes, and 100% after five minutes, while zvFeNi removed 98.70% after five minutes and totally removed RB19 after 10 minutes. Material obtained as modification of zeolite with zero-valent metals showed better sorption properties than material which contained only zero-valent iron-nickel particles. Also, zvFeNi@zVB material faster removed some pollutants from water than zvFeNi material (Figures 5 and 6), probably due to high surface area and porous and rigid structure of zeolite [26, 27].

Since these were preliminary sorption tests, zvFeNi@zVB material will be further examined under different experimental conditions (contact time, pH of solution, pollutant concentration, particle size of zeolite, temperature, dose of sorbent etc).

Surface Area Analysis Using the Brunauer-Emmett-Teller Method

The textural properties of the zvFeNi and zvFeNi@zVB material (BET surface area, BJH cumulative desorption pore volume and average pore diameter) are shown in Table 1. These textural properties could be important characteristics for the sorption properties of investigated materials, because they can affect the sorption efficiency of selected pollutants.

Table 1. Textural properties of the zvFeNi and zvFeNi@zVB material

Material	BET surface area S_{BET} (m^2g^{-1})	Average pore diameter (nm)	BJH cumulative desorption pore volume (cm^3g^{-1})
zvFeNi	85.74	9.87	0.30
zvFeNi@zVB	56.34	11.33	0.22

The determined textural properties of the analyzed samples, indicates that zvFeNi sample has a slightly larger BET specific surface area (85.74 m^2g^{-1}) and BJH cumulative desorption pore volume (0.30 cm^3g^{-1}) compared to the zvFeNi@zVB sample BET (56.34 m^2g^{-1}) and BJH (0.22 cm^3g^{-1}), also zvFeNi sample has a slightly smaller average pore diameter (9.87 nm) compared to the zvFeNi@zVB sample (11.33 nm). These differences in BET surface area between obtained materials are probably due to size of powdered zeolite particles compared to obtained clear zvFeNi particles. Despite a little difference in textural properties both material are very efficient toward sorption of the investigated pollutants. Additionally, we also suggest that improvements of the adsorption activity of the mentioned zvFeNi@zVB sample were obtained. Improvements were done in a way to synergism physico-chemical properties such as greater pore diameter, more favorable composition of crystal phases, and potentially greater number of active sites as well as the absence of internal and/or external diffusion restrictions under the selected process parameters.

The N_2 adsorption/desorption isotherms of the analyzed samples showed a typical s-shape behavior of IV-type with a type-H3 of hysteresis loop that indicated the existence of mesopores (Figure 7). The characteristic presence of this type of hysteresis loop, can be attributed to multilayer adsorption followed by capillary condensation, and, where additionaly, aggregates particles forming slit-like pores [14,27].

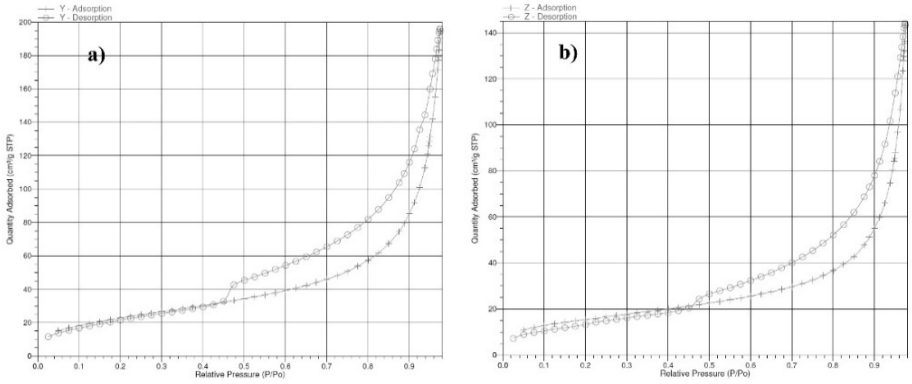

Figure 7. N_2 adsorption/desorption isotherm of: a) zvFeNi and b) zvFeNi@zVB material

The pore system of samples was in the meso-pores range, with pores characterized with maxima in pore size between 30-35 nm for sample zvFeNi, and maxima in pore size between 30–40 nm for sample zvFeNi@zVB (Figure 8). According to the BJH desorption isotherms (Figure 8) average pore diameter for zvFeNi and zvFeNi@zVB samples were around 10 nm in size and 11 nm in size respectively.

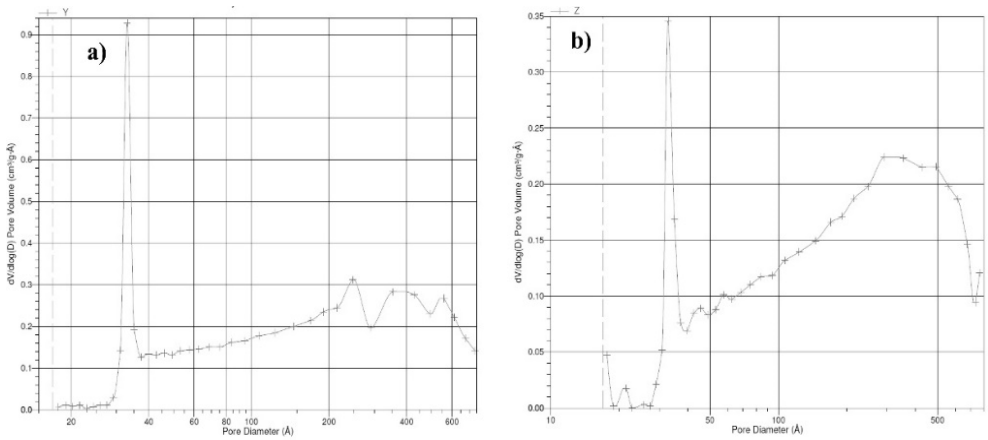

Figure 8. Pore size distribution of: a) zvFeNi and b) zvFeNi@zVB material

CONCLUSIONS

According to the data obtained with FTIR, XRD, SEM-EDX and BET good integration of bimetallic zero-valent iron nickel particles onto alumo-silicate structure of natural zeolite was achieved. Obtained material (zvFeNi@zVB) showed porous structure with the pore system in a mesopore range. zvFeNi@zVB material showed good sorption affinities for both inorganic and organic investigated water pollutants. Compared to FeNi material, zvFeNi@zVB remove investigated pollutants faster and with very high removal efficiency. Based on BET data both materials showed s-shape behavior of IV-type with type-H3 of hysteresis loop, which can be attributed to multilayer adsorption. Since these preliminary sorption tests showed good results and obtained material zvFeNi@zVB is low cost and environmental friendly, it will be further examined under different experimental conditions (contact time, pH of solution, pollutant concentration, particle size of zeolite, temperature, dose of sorbent etc.) toward inorganic and organic water pollutants.

EXPERIMENTAL SECTION

Materials and chemicals

Natural zeolite (zVB) was sampled from Zlatokop deposit (located in south-eastern Serbia, near the place Vranjska Banja) [14]. The raw zeolite was grounded in ball mill until it became powder, and then washed with deionized water on shaker and dried in oven overnight at 105 °C.

Used chemicals were p.a. grade, $FeCl_3 \times 6H_2O$, $NiSO_4 \times 6H_2O$, $NaBH_4$ and obtained from Merck K.G.A (Darmstadt, DE), while ethanol was obtained from Zorka Pharma (Serbia). All solutions were prepared with deionized water (18 MΩ).

Synthesis of zero-valent iron-nickel (zeolite) materials

The zvFeNi@zVB and zvFeNi materials were prepared based on liquid-phase reduction method by Shi et al. [20] and Weng et al. [21]. Iron and nickel solution 7.1×10^{-1} M and 7.1×10^{-1} M respectively, were prepared by dissolving exact mass of their salts in 30 mL H_2O:EtOH (1:4 v/v) solution. Solution was then shaking for half hour under the nitrogen atmosphere. After that, 2 g of powdered and prepared natural zeolite (washed with deionized water) was added to iron-nickel solution and shook for 15 minutes. Freshly prepared 1.1 M $NaBH_4$ solution was added drop by drop until complete reduction in system was done. All the time during the reduction process solution was shaking under the nitrogen atmosphere.

Characterization of zero-valent iron-nickel (zeolite) materials

Fourier Transform Infrared (FTIR) Spectrometry

The FTIR spectra of samples were obtained by using KBr pellets with Fourier transform infrared spectrometer Bomem Hartmann & Braun MB-100 spectrometer, in the wavelength range 4000 – 400 cm^{-1}.

X-ray diffraction (XRD) analysis

Zeolite samples were finely ground using a mortar and pestle and placed into standard sample holders. Data was collected with a Bruker D8 Advance X-ray Diffractometer (Bruker, Germany) in theta-theta geometry in reflection mode with Cu Kα radiation. Data collection was between 5-70° 2θ, step size of 0.02° and a counting time of 1 second per step. Scanning electron microscopy with energy dispersive X-ray spectroscopy (SEM-EDX)

The morphology and elemental information of investigated samples were analyzed by scanning electron microscope (SEM JEOL-JSM 5300) equipped with energy dispersive X-ray analysis spectrometer (EDS -QX 2000S system).

Surface Area Analysis Using the Brunauer-Emmett-Teller (BET) Method

The specific surface area was measured by a nitrogen adsorption using the Micromeritics Gemini 5 Surface Area Analyzer, USA.

Environmental aspect of application

Environmental aspect of application, preliminary sorption abilities of zero-valent iron-nickel (zvFeNi) material and zero-valent iron-nickel chemically modified zeolite (zvFeNi@zVB) material were investigated in waste water model system with M(II) heavy metal ions (Cu, Pb, Cd, Zn) as described in our previous investigations. The dropping concentrations of Cu(II), Pb(II), Cd(II) and Zn(II) ion in the solution during time were determined by using an atomic absorption spectrophotometer (AASAnalyst 300, Perkin–Elmer, USA), after filtration through a 0.45 μm membrane filter (Agilent Technologies, Germany) [1-3].

Content of organic industrial colours RB19 and MB in the samples was determined at 592 nm and 660 nm, respectively, using the UV–Vis technique by the spectrophotometer Shimadzu UV–vis 1650 PC (Shimadzu, Japan), after filtration through a 0.45 μm membrane filter (Agilent Technologies, Germany) [29,30].

The adsorption capacity of the investigated materials, qe [mg g-1], at equilibrium was calculated as:

$$q_e = \frac{(C_0 - C_e) \times V}{m} \qquad \text{Eq. (1)}$$

where qe is the amount of pollutant (M(II)-ion or organic colour) adsorbed per unit weight of the adsorbent, V is the volume of solution, C0 is the initial concentration of pollutant [mg dm^{-3}], Ce is the equilibrium pollutant concentration [mg dm-3], and m is the mass of the adsorbent [g].

The metal removal efficiency, RE [%], of the investigated materials was estimated according to the following equation:

$$RE = \frac{C_0 - C_e}{C_0} \times 100 \qquad \text{Eq. (2)}$$

where C0 and Ce are the initial and equilibrium concentrations [mg dm-3] of pollutant in solution, respectively.

ACKNOWLEDGEMENTS.

This work was supported by the Ministry of Education, Science and Technological Development of the Republic of Serbia, Contract No. 451-03-9/2021-14/200124.Experimental work was completed at Faculty of Sciences and Mathematics, University of Niš, Serbia.

REFERENCES

1. M.N. Stanković; N.S. Krstić; I.J. Slipper; J.Z. Mitrović; M.D. Radović; D.V. Bojić; A.L. Bojić*; Aust. J. Chem.*, **2013**, *66*, 227-236.
2. M.N. Stanković; N.S. Krstić; J.Z. Mitrović; S.M. Najdanović; M.M. Petrović; D.V. Bojić; V.D. Dimitrijević; A.L. Bojić; *New J. Chem.*, **2016**, *40*, 2126-2134.
3. V.D. Dimitrijević; M.N. Stanković; D.M. Djordjević; I.M. Krstić; M.G. Nikolić; A. Lj. Bojić; N.S. Krstić; *Stud. U. Babes-Bol. Che.*, **2019**, *64*(1), 19-39.
4. A. Saeed; M.W. Akhter; M. Iqbal; *Sep. Purif. Technol.*, **2005**, *45*, 25-31.
5. D. Karunasagar; M. V. Krishna; S. V. Rao; J. Arunachalam; *J. Hazard. Mater.*, **2005**, *118*, 133-139.
6. P.D. Johnson; M.A. Watson; J. Brown; I.A. Jefcoat; *Waste Manage*, **2002**, *22*, 471-480.
7. S.Y. Quek; D.A.J. Wase; C.F. Forster; *Water SA*, **1998**, *24*, 251-256.
8. A.K. Bhattacharya; S.N. Mandal; S.K. Das; *Chem. Eng. J.*, **2006**, *123*, 43-51.
9. I. Villaescusa; N. Fiol; M. Martínez; N. Miralles; J. Poch; J. Serarols; *Water Res.*, **2004**, *38*, 992-1002.
10. G. Yuan; H. Seyama; M. Soma; B.K.G. Theng; A: Tanaka; *J. Environ. Sci. Heal. A*, **1999**, *34*, 625-648.
11. H. Cui; L.Y. Li; J.R. Grace; *Water Res.*, **2006**, *40*, 3359-3366.
12. S. Wang; Y. Peng; *Chem. Eng. J.*, **2010**, *156*, 11-24.
13. I. Elaiopoulos; T. Perraki; E. Grigoropoulou; *Micropor. Mesopor. Mat.*, **2010**, *134*, 29-43.
14. N.S. Krstić; M.N. Stanković; D.M. Đorđević; V.D. Dimitrijević; M.M. Marinković; M.G. Đorđević; A.L. Bojić; *Bulg. Chem. Commun.*, **2019**, *51*, 394-399.
15. M.K. Doula; *Water Res.*, **2006**, *40*, 3167-3176.
16. M.J. Jimenez-Cedillo; M.T. Olguín; C. Fall; *J. Hazard. Mater.*, **2009**, *163*, 939-945.
17. Z. Li; J. Jean; W. Jiang; P.H. Chang; C.J. Chen; L. Liao; *J. Hazard. Mater.*, **2011**, *187*, 318-323.
18. A. Ghauch; A. Tuqan; H.A. Assi; *Environ. Pollut.*, **2009**, *157*, 1626-1635.
19. H. Kang; Z. Xiu; J. Chen; W. Cao; Y. Guo; T. Li; Z. Jin; *Environ. Technol.*, **2012**, *33*, 2185-2192.
20. I.N. Shi; X. Zhang; Z.L. Chen; *Water Res.*, **2011**, *45*, 886-892.
21. X. Weng; S. Lin; Y. Zhong; C. Zuliang; *Chem. Eng. J.*, **2013**, *229*, 27-34.
22. X. Weng; Zh. Chen; Zu. Chen; M. Megharajc; R. Naiduc; *Colloids Surf. A Physicochem. Eng. Asp.*, **2014**, *443*, 404-409.
23. P.K. Raul; R.R. Devi; I.M. Umlong; S. Banerjee; L. Singh; M. Purkait; *J. Nanosci. Nanotechno.*, **2012**, *12*, 3922-3930.
24. D.M. Djordjević; M.N. Stanković; M.G. Djordjević; N.S. Krstić; M.A. Pavlović; A.R. Radivojević; I.M. Filipović; *Stud. U. Babes-Bol. Che.*, **2019**, *57*(4), 39-54.
25. Z. Fang; X. Qiu; J. Chen; X. Qui; *J. Hazard. Mater.*, **2011**, *185*, 958-969.
26. E. Alvarez-Ayuso; A. Garcia-Sanchez; X. Querol; *Water Res.*, **2003**, *37*, 4855-4862.
27. X. Li; C. Lin; Y. Wang; M. Zhao; Y. Hou; *Procedia Environ. Sci.*, **2010**, *2*, 1598-1612.
28. E. Kouvelos; K. Kesore; T.A. Steriotis; H.P. Grigoropoulou; D. Bouloubasi; N. Theopilou; S. Tzintzos; N. Kanelopoulos; *Microp. Mesopor. Mat.*, **2007**, *99*, 106-111.
29. I.Z. Momčilović; M.M. Purenović; M.N. Miljković; A.L. Bojić; M. Randjelović; *Hem. Ind.*, **2011**, *65*, 123-129.
30. I.D. Radović; J.Z. Mitrović; D.V. Bojić; M.D. Antonijević; M.M. Kostić; R.M. Baošić; A.L. Bojić; *Water SA*, **2014**, *40*, 1-18.

STUDIA UBB CHEMIA, LXVI, 1, 2021 (p. 35-48)
(RECOMMENDED CITATION)
DOI:10.24193/subbchem.2021.1.03

POROUS SILICAS FROM MIXTURES OF $Na_2Si_3O_7$ AQUEOUS SOLUTION AND TEOS. INFLUENCE OF SODIUM SILICATE AMOUNT

ELENA-MIRELA PICIORUS[a], PAULA SVERA (IANASI)[b*], CATALIN IANASI[a*]

ABSTRACT. Silicon-based mesoporous materials have become increasingly used in various fields as industry, medicine, environment, etc. We developed five samples in mild conditions, at room temperature, of mesoporous silica by substituting tetra-ethyl-orthosilicate (TEOS) with different amount of sodium silicate ($Na_2Si_3O_7$) precursor by maintaining the total ratio for SiO_2 at 1.8g. Acetic acid (CH_3COOH)/hydrochloric acid (HCl) aqueous solution was used as catalyst keeping the pH at 5. The samples were examined by FT-IR, Raman Spectroscopy, Scanning Laser Confocal Microscopy and Nitrogen Adsorption-Desorption Isotherms. The results indicate enhancements when $Na_2Si_3O_7$ was added. Sample with TEOS and lowest amount of $Na_2Si_3O_7$ displayed the best surface area value (750 m^2/g) and total pore volume (0.63 cm^3/g). Highest amount of $Na_2Si_3O_7$ in the sample (P5) has considerably influenced the roughness of the material.

Keywords: *$Na_2Si_3O_7$, TEOS, mesoporous materials, roughness, porosity*

INTRODUCTION

Silica nanoparticles have received, in the last few years, an increased attention and interest of scientific community due to their wide applications such as photovoltaic cells [1], semiconductor electronic devices, catalysts and ceramics [2, 3]. In addition, amorphous SiO_2 nanoparticles are widely used for the fabrication of electronic substrates, thin film substrates, electrical and thermal insulators, humidity sensors and other applications. The silica particles

[a] *"Coriolan Drăgulescu" Institute of Chemistry, 24th Mihai Viteazul Bvd., 300223, Timişoara, România*
[b] *National Institute for Research and Development in Electrochemistry and Condensed Matter, 144th Dr.A.P. Podeanu Street, 300569, Timişoara, România*
**Corresponding authors, e-mails: cianasic@yahoo.com and paulasvera@gmail.com*

play an important role for each of these products. In some cases, the quality of these products is highly dependent on the size and size distribution of the silica particles [4-6]. The optical properties of silica nanoparticles can be attained with respect to the surface defects correlated with large surface/volume ratio. The synthesis of the SiO_2 nanoparticles can be achieved by several methods: combustion, plasma, hydrothermal and sol-gel processing [7-9]. Among these methods, the sol-gel method has an important advantage such as low temperature synthesis, control of reaction kinetics by varying the composition of chemicals, low cost and ease in controlling the properties of SiO_2, purity and homogeneity or other modifications of the material composition. In the past reports, the silica particles were synthesized from an expensive raw *material such as TEOS.* For many years, researchers have studied the sol-gel process starting from TEOS precursor. Bogush and Zukoski [10] obtained monodispersed silica particles with their sizes ranging from 40 nm to several micrometers using-controlled hydrolysis of tetraethylortho-silicate (TEOS) in ethanol, followed by condensation (polymerization) of the dispersed phase material. Simpler approach was conducted by Arenas et al. [11] that synthesized silica xerogels using only TEOS as precursor, acetic acid and acetone. They observed that the simultaneous addition of acetic acid, hydrochloric acids used as catalysts and acetone as solvent at room temperature (20 ^oC) conduct to the formation of amorphous silica materials with surface area up to 850 m^2/g and a pore volume of 0.24 cm^3/g. Dubey et al. [12] have synthesized silica nanoparticles for industrial applications using TEOS, ETOH, acetic acid and PVP as surfactant via sol-gel method. They obtained amorphous, mono-dispersed silica nanoparticles with 25 nm in diameter. Colloidal silica nanoparticles were synthesized by Lazareva et al. [13] starting from TEOS and by varying the catalyst type (HCl, NH_3), temperature of the thermal treatment (50-70 °C) and ratio of molar reactants, resulting in particles with sizes between 12 and 150 nm. Guo et al. [14] synthesized SiO_2 nanoparticles by sol-gel method using PEG 1000 as surfactant, TEOS as silica source and ammonia as catalyst. By varying the amount of PEG-1000 between 0.025 g and 0.1 g they obtained an average size of the particles between 9 and 35 nm.

However, using inexpensive source materials (Na_2SiO_3 or $Na_2Si_3O_7$) is required for the mass production of the SiO_2 particles. The molar ratio between silica and sodium oxide plays an important role in the chemical behavior of sodium silicate [15]. Chenge Liu [16] investigated the relationship between the rate of particle growth and factors as pH value, particle size, and the molar ratio of SiO_2:Na_2O. Many studies are using for their synthesized materials only sodium silicate as silica precursor without any other source of silica or template agent in order to obtain more ordered framework structures.

One example in this direction are synthesized silica nanoparticles via facile and economic sol-gel processing, using sodium silicate (Na_2SiO_3) as precursor [17]. They have obtained amorphous particles with almost well-defined and regular spherical structures, including a diameter of 25 nm. Ui et al. [18] synthesized mesoporous nanosilica powders from sodium silicate (Na_2SiO_3) in acid medium (pH 1-6), using anionic surfactant, sodium dodecyl sulfate (SDS). They demonstrated the pH influence over the surface area of the aforementioned synthesised materials, indicating a value of 1370 m^2/g in case of pH=3, which decreased to 984 m^2/g at pH=4. More studies regarding the pH influence were conducted by Hayrapetyan et al. [19], considering the effect of pH on the growth process of the colloidal silica sol particles.

However, few studies were made by substituting only the TEOS component with sodium silicate. Following this direction, Liu et al. [20] have synthesized mesoporous silica from mixtures of sodium silicate and TEOS in acetic acid/sodium acetate buffer (pH 4.4) using PEO-PPO-PEO as template. They obtained a surface area of 624 m^2/g for the sample where the content of sodium silicate was higher comparatively with the introduced amount of TEOS. Chun et al. [21] synthesized silica mesoporous from $Na_2Si_3O_7$ with TEOS and Pluronic F127 using supercritical method. Their observation regarding the synthesized TEOS based silicas under the supercritical CO_2 atmosphere include the increase of surface area by 3.8 times. Therefore, the formation of mesopores in $Na_2Si_3O_7$ and TEOS based silicas are resulted from collapsing micropores in supercritical CO_2 atmosphere. Fantini et al. [22] produced cage-like mesoporous silica using TEOS and sodium silicate in the presence of triblock copolymer template. Similar values for surface areas were obtained with both silica precursors. Mesoporous organosilicas [20] were prepared by using different silica precursor (organotrialkoxysilane with methyl, vinyl, 3-mercaptopropyl functionalities) and sodium silicate. The results show that the materials prepared from sodium silicate- organotrialkoxysilane have more ordered framework structure and narrower pore diameter distribution compared with the materials prepared from TEOS-organotrialkoxysilane. The organic-inorganic hybrid materials have higher surface area (between 890-1040 m^2/g) and pore volume (between 0.7-1.09 cm^3/g).

Herein, in our work, we used sol-gel route for the synthesis of mesoporous silica from mixtures of $Na_2Si_3O_7$ aqueous solution and tetraethylorthosilicate, both used as silica precursors (source of SiO_2), in CH_3COOH/HCl aqueous solutions (pH 5) without using any template. We have gradually replaced the TEOS with sodium silicate aqueous solution, because the $Na_2Si_3O_7$ is an economic raw material, environmentally benign and thermally stable. We selected to use acetic acid due to its ease dissolution in a wide variety of precursors, enabling a multitude of multi-cation solutions [23].

RESULTS AND DISCUSSION(S)

Infrared characteristics of sodium silicate xerogels

In order to confirm the presence of development of SiO_2, the samples were characterized using FT-IR analysis. The spectra of the samples dried at temperature of 100 °C are shown in **Figure 1**.

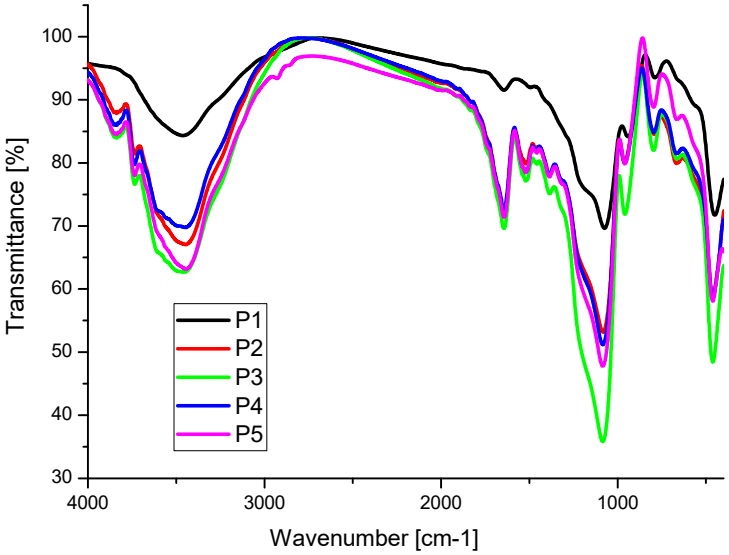

Figure 1. FT-IR spectra of the TEOS xerogels replaced with sodium silicate under acidic conditions

Silicate xerogels show the peaks of amorphous silica at 3463-3448 cm^{-1} and could be assigned to the stretching vibration of the H_2O molecules [24]. Same vibrations can be attributed to the -OH stretching on the silica surface which can also indicate the remaining water from the synthesis, indicating incomplete TEOS condensation [25]. The band appeared at 1646-1641 cm^{-1} is due to bending vibration of the H_2O molecules [26]. The broad band in the range of 1092-1060 cm^{-1} originates from the Si-O-Si asymmetric stretching vibration [27]. Absence of the 1168 and 812 cm^{-1} is an indicator for the low level of hydrolysis process [28] which may have been replaced by the condensation indicated in the literature [29]. The band at 959-942 cm^{-1} is due to the silanols groups and the Si-O stretching vibrations [30]. The changes in the intensity of the same band is an indicator for the level of the

hydrolysis and condensation level that occurs, whereas smaller peak indicates lower hydrolysis and therefore increased condensation [25]. It should be noted the fact that the Si-OH and Si-O- bonds have both specific bands closely located (960-920 cm^{-1}) which in present case is harder to evidence due to the band overlap [7]. The band at 794-781 cm^{-1} is responsible for the Si-O-Si symmetric stretching vibrations [31-34]. The bands at 474-455 cm^{-1} could be assigned to the Si-O asymmetric bending vibration of Si-O-Si [33]. In the literature the ≈960 cm^{-1} peak is also referred as an indicator for the C-H rocking vibrations specific for the methyl group present in TEOS [28]. Other carbon related groups interfering with the ones specific for the Si are presented by the O-C-C deformations located at ≈473 cm^{-1} [28]. In case of $Na_2Si_3O_7$ apart from the already aforementioned Si-O specific bonds, there are no expectations for other bands [35]. The pH during the synthesis influences greatly the results and therefore the peak intensities [35].

Raman Spectroscopy

In **Figure 2**(a), (b), the Raman spectra are shown for samples obtained by substituting tetra-ethyl-orthosilicate (TEOS) with different percent of sodium silicate ($Na_2Si_3O_7$) in two section of domain.

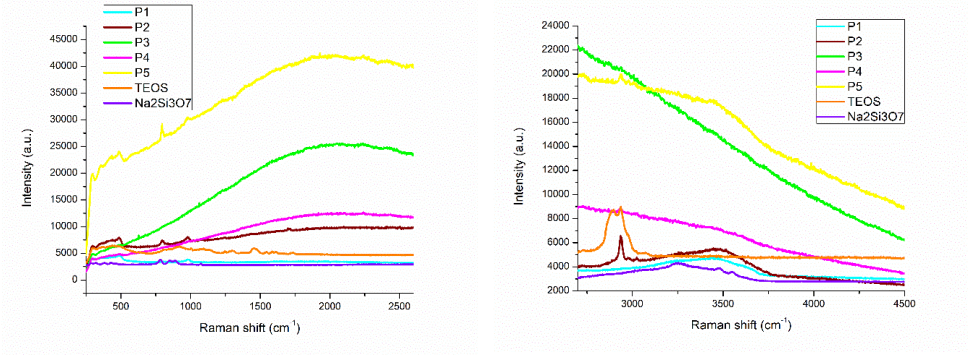

Figure 2(a), (b)**.** Raman spectra of the samples with different percent of sodium silicate ($Na_2Si_3O_7$)

For the TEOS sample, specific bands (200-400, 430-490, 500-651, 812-815, 865-890, 912-1008, 1048, 1096, 1110-1135, 1195-1292, 1454-1481, 1500-1700 cm^{-1}) were confirmed accordingly to the literature [36,37]. The most prominent bands are located at 438, 914, 1008, 1096 and 1135 cm^{-1}.

Si-O peaks which are expected for both TEOS and $Na_2Si_3O_7$ materials are generally observed in the 540-440 cm^{-1} region, with a specific broad band, accompanied by the presence of another specific peak around 950-1100 cm^{-1} [38,39]. In addition, siloxane rings which were also detected in the 1000-1300 cm^{-1} area, correspond to the asymmetrical Si-O stretching specific for dissolved silicates and solid glasses [36]. Other indicator for the amorphous glass type materials is the intensity of the 531-480 cm^{-1} Si-Si bond stretching, whereas the higher value indicates presence of metallic silicon compounds while lower value indicates the presence of amorphous silicon materials [40]. More Si bonds were detected, such as Si-O symmetric stretching vibrations in the 700-1000 cm^{-1} range [36], Si-O-Si stretching vibrations at 809 cm^{-1} [41] or 1049 cm^{-1} [37], symmetric stretching of Si-OH at 960 cm^{-1} [41] and asymmetric stretching of Si-O-C at 1906 cm^{-1} [41]. Wide band in the 430-490 cm^{-1} region is visible due to the silane bond bending [37]. Raman peaks in the region of 600-650 cm^{-1} are resulted from the connections between alkoxy groups and silicon atoms, which are also an indicator for the hydrolysis efficiency [37]. According to the literature the peak around 651 cm^{-1} is representative for the TEOS molecules consisting of four ($-OC_2H_5$) groups connected to the silicon atom [37]. This peak also is the main indicator for the hydrolysed TEOS [37], which is gradually replaced by the condensation reaction that takes place instead [29]. The hydrolysis-condensation processes are a consequence of the pH, solvent and H_2O amount used in the synthesis and as a result acid or base-catalysed displacement reactions that take place [29]. The displacement reactions are represented by the protonation of OH or OR substituents bounded to the Si (in acidic conditions) or by the direct attack of the hydroxyl or silanolate anions to the Si (in the basic conditions) [29]. In the material it is observed the presence of the silica-methyl group's connectivity indicated by the 460 cm^{-1} band [41] which may be overlapped by the 400-450 cm^{-1} SiO_2 stretching bonds [37]. In addition, rocking C-H (760 cm^{-1}) [41], C-H asymmetric bending (1412 cm^{-1}) [41], C-H symmetric stretching (2907 cm^{-1}) [41, 42] and C-H asymmetric stretching (2974 cm^{-1}) vibrations are also present [41]. According to other studies the 880 cm^{-1} is assigned to C-C-O stretching [37] as a consequence of low hydrolysis that takes place. Si-C bonds were also registered in the Raman spectra, being confirmed by the presence of the 1250 cm^{-1} peak [42]. The existence of silanols and silicon oxide bands on the surface is evidenced by the 977 cm^{-1}, respectively the 1096 cm^{-1} peak [42].

Regarding the $Na_2Si_3O_7$ sample, vibrational energies of Na-O were expected and found below 300 cm^{-1} area [36]. It should be mentioned that this Na-O bonds have less influence on the Si-O bonding, expecting less modifications in the 1000-1300 cm^{-1} area. In the same work [36] it is mentioned

that materials prepared in basic conditions, have achieved higher intensity values in comparison to the acid media prepared materials. Using alcohol in the synthesis may also affect the structure orientation of the silica materials [36]. The 780 cm^{-1} peak which is only present in case of $Na_2Si_3O_7$ also indicates the presence of Si monomers, whereas the 485 cm^{-1} peak is an indicator of siloxane rings [36]. Symmetric deformation (δ_s) at 423 cm^{-1} was assigned to the (X) O-Si-O(X) where x is presented as Na, H, or negative ionic charge [38, 43]. The higher intensity of 1050 cm^{-1} peak in comparison to the one located at 980 cm^{-1} is suggesting (in both TEOS and $Na_2Si_3O_7$) that the doubled siloxane rings are not suffering any breakage [36]. The two peaks located around 450 and 650 cm^{-1} are showing the siloxane rings, in this case, the TEOS having less since the 450 peak is lower in intensity [36]. Peaks below 300 cm^{-1} may show the breakage of large siloxane rings that contain more than 6 members.

When comparing the P1, P2, P3, P4, P5 and the precursors (TEOS and $Na_2Si_3O_7$), overall signal intensity is different, suggesting fluorescence interference. The higher energy excitation source (514 nm visible laser) can strongly influence the appearance of the spectra [44], still the main peaks for the Si based compounds are observed as expected around 971 cm^{-1}, together with ≈801 cm^{-1} and ≈501 cm^{-1} followed by the less prominent peaks under 501 cm^{-1}.

Scanning Laser Confocal Microscopy

A series of images were captured, at 10x and presented in **Figure 3**. The samples show tempered glass chips like appearance of the crystals, with various size and shapes. The obtained images show differences with the increasing Na content and decreasing TEOS content, revealing unlike presence of triangle and pyramidal shaped like crystals, which are visible in case of sample P4 and less in P5. With the maximum 2.5 g Na, the P5 crystals shrink to smaller dimensions.

Calculated roughness values from the 50x images (see **Figure 4**) (Average roughness (Sa), Mean Square Root Roughness (Sq), Maximum peak height (Sp), Maximum valley depth (Sv), Maximum peak-to valley height (Sz), Surface kurtosis (Sku), Surface skewness (Ssk)) for P1, P2, P3, P4 and P5 samples are shown below in **Table 1**.

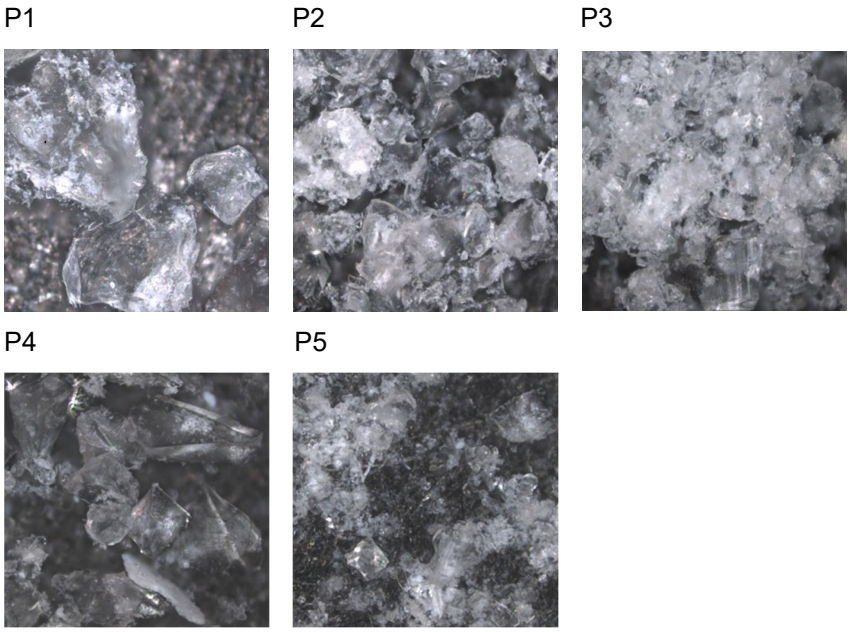

Figure 3. Images of samples obtained at 10x

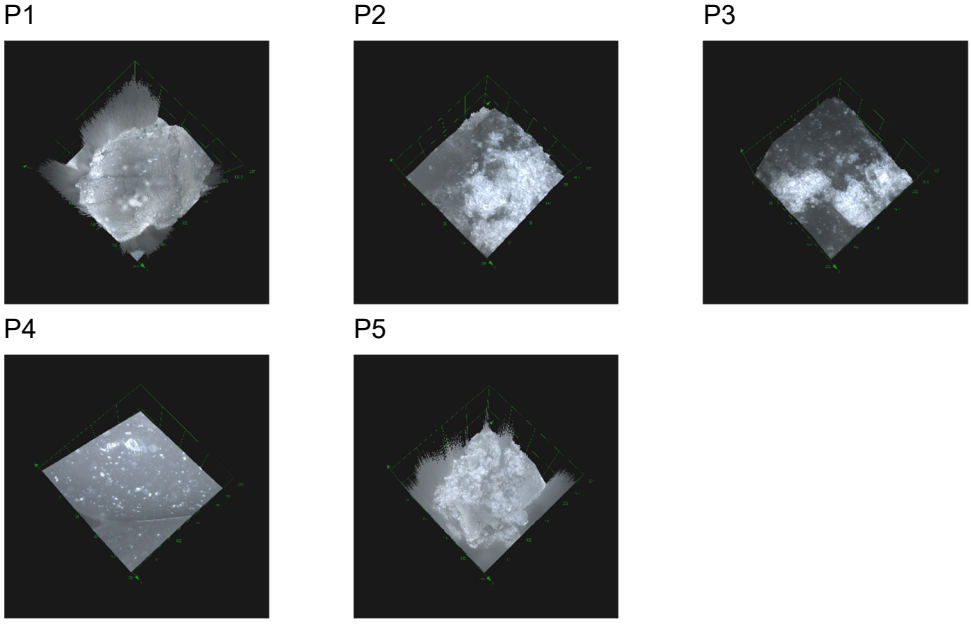

Figure 4. Images obtained for silica nanoparticles

Table 1. Data parameters for silica nanoparticles

Whole area (258 µm x 258 µm)	Average roughness (Sa)	Mean Square Root Roughness (Sq)	Maximum peak height (Sp)	Maximum valley depth (Sv)	Maximum peak-to valley height (Sz)	Surface kurtosis (Sku)	Surface skewness (Ssk)
P1	12.984	20.540	140.365	67.171	207.536	8.77	1.056
P2	4.046	5.570	93.368	50.002	143.370	5.100	-0.149
P3	2.988	4.416	76.284	69.074	145.358	7.174	-0.062
P4	1.506	5.270	154.246	31.426	185.672	4.133	-1.592
P5	9.202	13.276	79.037	29.641	108.677	7.145	-1.467

Roughness parameters are used for characterizing the roughness of a material, whereas the most important parameters are Sa and Sq. Both Sa and Sq parameters indicate the average roughness of the material using different calculation formula. For the analysed materials, highest average roughness is attributed to the P1, followed by the P5, P2, P4 and P3 sample. High rugosity in case of the P5 resulted due to the presence of very small crystals and therefore inability to analyse the surface of one single crystal as it was in the case of the rest of the samples.

Ssk (skewness) is sensitive to the peak/valley overall tendency on the surface of the material, whereas positive skewness (Ssk > 0) is more present in case when high spikes protrude above a flatter average distribution, and negative skewness (Ssk < 0), on the other hand, indicate deep valleys in a smoother area, which is more specific for porous materials. In our case only one sample has positive skewness, which is also visible from the 2d image of the sample (P1) presenting large crystals.

All samples show the presence of inordinately high peaks and low valleys based on the kurtosis (Sku) sharpness parameter of the profile (Sku > 3) which is probably due to the “tempered glass chips” nature of the sample, with occasional geometric morphologies that also imply the presence of more edges.

Textural Characteristics

The N_2 adsorption–desorption isotherms are given in **Figure 5**.

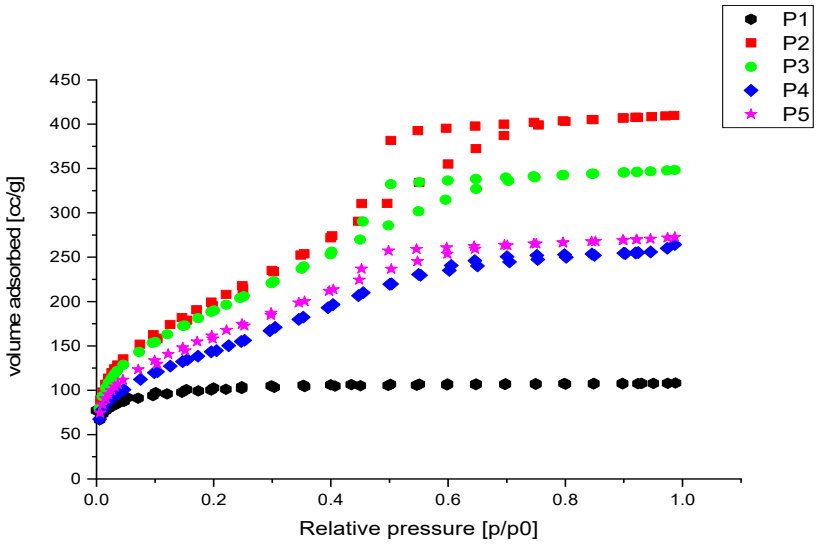

Figure 5. N_2 adsorption -desorption isotherms of silica nanoparticles

According to the International Union of Pure and Applied Chemistry (IUPAC) [45], N_2 adsorption-desorption isotherms of silicate xerogels produced are Type Ib in case of sample P1, Type IVa for samples P2, P3, P5 and Type IVb for sample P4. The type Ib isotherms are specific for materials with wider micropores and possibly narrow mesopores under 2.5 nm. In case of type IVa isotherms, the materials are characteristic for mesoporous materials and capillary condensation is accompanied by hysteresis [45, 46]. The hysteresis obtained for samples P2, P3 and P5 showed H2b type of hysteresis loops characteristic for complex pore with larger neck widths. In case of sample P4 the type IV b isotherm is specific for mesopores with smaller width. **Table 2** shows the parameters obtained from isotherms for the silicate xerogels prepared.

Table 2. Textural parameters and data obtained from isotherms

Sample name	DFT Pore width, [nm]	BJH Desorption Pore diameter [nm]	Multi-BET surface area [m^2/g]	Total pore volume [cm^3/g]
P1	2.50	3.068	316	0.17
P2	5.09	3.853	750	0.63
P3	4.89	3.450	702	0.54
P4	4.89	3.451	529	0.41
P5	3.40	3.443	591	0.43

Using DFT method, pore size distribution profiles of prepared silicate xerogels are given in **Figure 6**.

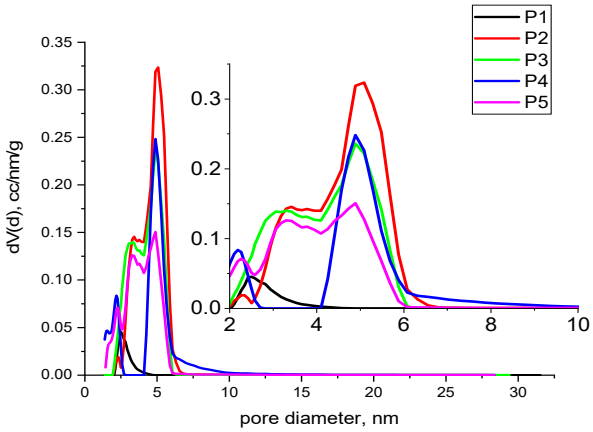

Figure 6. Pore size distribution of silica nanoparticles

From **Figure 6** we can observed that in case of sample P1 the material presents a large unimodal distribution with an average of 2.5 nm and for sample P4, the material presents a bimodal distribution with an average of 4.89 nm. In case of the all-other samples the distribution of pores is multimodal confirming the type of isotherms.

The sample P2 has the highest surface area and a total pore volume of 750 m^2/g and 0.63 cc/g respectively. Pore size distribution was affected by the gelation pH (high content of sodium silicate). The sample P2 presents also the largest pore size of 5.09 nm.

CONCLUSIONS

Silica xerogels with high surface area, highly uniform pore structure and high silanol group content were successfully synthesized using low-cost silica source ($Na_2Si_3O_7$) and TEOS in the presence of acetic acid and hydrochloric acid via sol–gel process. The use of acetic/HCl acid in sodium silicate sol-gel process was important because them produce high surface area of mesoporous materials without addition of any template agent.

The simultaneous addition of acetic/HCl acid as catalysts and used of acetone as solvent, made possible to synthesize amorphous silica nanomaterials with high surface area and pore volume. The highest BET surface area of 750 m^2/g and pore volume 0.63 cm^3/g was registered for P2

sample. Also, all xerogels silicate samples were kept at room temperature for gelling, the temperature being another parameter satisfactory to obtain the high surface area. FTIR spectra reveal the main characteristic bands for porous SiO_2 nanoparticles. Raman spectra certifies the structure of porous SiO_2 nanoparticles and emphasizes the presence of both hydrolysis and condensation processes which are also confirmed by the FTIR spectra. Laser confocal images put in evidence the influence of the TEOS/$Na_2Si_3O_7$ amount on the crystal size and rugosity.

EXPERIMENTAL SECTION

Materials

Tetra-ethyl-orthosilicate (TEOS, 98% Merck), acetone (CHIMREACTIV SRL, 99.92%), $Na_2Si_3O_7$ (Loba Feinchemie), acetic acid (Chimopar, reactive analysis), Hydrochloric acid (HCl, EMSURE ^{R}, ACS, ISO, Reag Ph. EUR 37%), distilled water without further purification.

Xerogels synthesis

A series of five sample of silica was prepared using different quantities of sodium silicate ($Na_2Si_3O_7$) by replacing TEOS and maintaining the total ratio for SiO_2 at 1.8g. We solubilized the $Na_2Si_3O_7$ in different amounts of distilled water in order to obtain a molar ratio of 1:722. Then, TEOS was solubilized in acetone and form a second solution and added drop wise onto the first solution. We added a 1: 9 solution of CH_3COOH/HCl in order to adjust the pH at 5. The precursors for the synthesis are shown **in Table 3**.

Table 3. Synthesis parameters

Samples	P1	P2	P3	P4	P5
TEOS (g)	6.5	3.3	1.9	0.6	0
$Na_2Si_3O_7$ (g)	0	1.25	1.75	2.25	2.5
Acetone (g)	10	10	10	10	10
CH_3COOH(g)	3	3	3	3	3
HCl (mL)	0.1	0.1	0.1	0.1	0.1
H_2O (g)	3	65	91	117	130

The solutions were left to gel and were stored for 28 days at room temperature for ageing. The obtained materials were washed in excess with water for 5 times and 2 times with ethanol. The obtained materials were dried at 100 ^{o}C and further analyzed.

Characterization

The chemical structure of sodium silicate xerogels was confirmed by using FT-IR spectrometry (JASCO 430 apparatus) in the wave number range of 4000 to 400 cm^{-1}. Raman spectra was done with Shamrock 500i Spectrograph from Andor United Kingdom.

Imaging and roughness data were obtained with LEXT – 3D measuring laser microscope OLS4000 with 405 nm laser light source.

Nitrogen adsorption measurements were carried out at 77 K with a Surface Area and Pore Size Distribution Analyzer (Quantachrome Nova 1200e) to determine the pore size, pore volume and specific surface area of the xerogels obtained. Specific surface area was calculated by the Brunauer-Emmett-Teller (BET) method. Total pore volume was estimated from the adsorbed N2 volume at ~1 relative pressure (P/Po) values. Barrett-Joyner-Halenda (BJH) method was used to estimate pore size and pore volume by using desorption branch of the isotherm.

ACKNOWLEDGMENTS

The authors thank to „Coriolan Dragulescu" Institute of Chemistry of Romanian Academy for the financial support: Program 4. Inorganic compounds and hybrids with relevance in nanostructured materials science, precursors for advanced materials.

REFERENCES

1. N.P. Rizky; A.B. Herny; M.H. Agus; Sekartedjo and D.R. Doty; *Proc. Eng.,* **2017**, *170,* 93
2. G.H. Bogush; M.A. Tracy and C.F. Zukosky; *J. Non-Cryst. Solids* **1988**, *104,* 95
3. M. Sadeghi; M. Dorodian and M. Rezaei; *J. of Adv. In Chem.*, **2013**, *6*, 917-922
4. G. Herbert; *J. Eur. Ceram. Soc.* **1994**, *14*, 205-214
5. A.-M. Putz; L. Almasy; A. Len; C. Ianasi, *Fuller. Nanotub. Car. N.*, **2019**, *27,* 323-332
6. A.-M. Putz; C. Savii; C. Ianasi; Z. Dudás; K.N. Székely; J. Plocek; P. Sfârloagă; L. Săcărescu; L. Almásy, *J. Porous Mater.,* **2015**, *22*, 321-331
7. D. Nagao; H. Osuzu; A. Yamada; E. Mine; Y. Kobayashi; M. Konno; *J. Colloid Interface Sci.* **2004**, *279*, 143-149
8. S. Vemury; S.E. Pratsinis; L. Kibbey; *J. Mater. Res.,* **1997**, *12*, 1031-1042
9. T. Tani; N. Watanabe; K. Takatori; *J. Nanoparticle Res.,* **2003,** *5*, 39-46
10. G.H. Bogush and C.F. IV Zukoski *J. Colloid Interface Sci*, **1991**, *142*, 19-34
11. L.T. Arenas; C.W. Simm; Y. Gushikem; S.L.P. Dias; C.C. Moro; T.M.H. Costa, E.V. Benvenutti; *J. Braz. Chem. Soc.*, **2007**, *18*, 886-890
12. R.S. Dubey; Y.B.R.D. Rajesh; M.A. More; *Mater. Today Proc.*, **2015**, *2*, 3575-3579
13. S. Lazareva; N. Shikina; L. Tatarova and Z. Ismagilov; *Eurasian Chem.-Technol. J.*, **2017**, *19*, 295-302
14. Q. Guo; D. Huang; X. Kou; W. Cao; L. Li; L. Ge; J. Li; *Ceram. Int.,* **2017**, *43*, 192-193
15. A.A. Hamouda and H.A.A. Amiri; *Energies* **2014**, *7* 568-590

16. H.C. Liu; J.X. Wang; Y. Mao; R.S. Chen; *Colloid Surf. A Physicochem. Eng. Asp*., **1993**, *74*, 7
17. M.F. Zawrah; A.A. EL-Kheshen; H.M. Abd-El-Aal, *J. Ovonic Resear.,* **2009**, *5,* 129-133
18. S.-W. Ui; I.-S. Choi; S.-C. Choi; *Int. Sch. Res.*, **2014**, Article ID 834629, 1-6
19. S.S. Hayrapetyan; H.G. Khachatryan; *Microporous Mesoporous Mater*., **2005**, *78*, 151-157
20. N. Yu; Y. Gong; D. Wu; Y. Sun; Q. Luo; W. Liu; F. Deng; *Microporous Mesoporous Mater.* **2004**, *72,* 25-32
21. B.S. Chun; P. Pendleton; A. Badalyan; S.-Y. Park; *Korean J. Chem. Eng.,* **2010**, *27*, 983-990
22. M.C.A. Fantini, C.F. Kanagussuko; G.J. M. Zilioti; T.S. Martins; *J. Alloys Compd*., **2011**, *509,* S357-S360
23. T.H. Chiang; S.-L. Liu; S.-Y. Lee; T.-E. Hsieh; *Thin Solid Films*, **2009**, *517,* 6069-6075
24. P. Innocenzi; P. Falcaro; D. Grosso; F. Babonneau; *J. Phys. Chem. B*, **2003**, *107,* 4711-4717
25. E.C. de O. Nassor; L.R. Ávila; P.F. dos S. Pereira; K.J. Ciuffi; P.S. Calefi, & E.J. Nassar; *Mater. Res.*, **2011**, *14*, 1–6
26. H. El Rassy; A.C. Pierre; *J. Non- Cryst. Solids,* **2005**, *351*, 1603-1610
27. S.R. Ryu; M. Tomozawa; *J. Non-Cryst. Solids*, **2006**, *352*, 3929-3935
28. F. Rubio; J. Rubio; J.L. Oteo, *Spectroscopy Lett*., **1998**, *31*, 199-219
29. C.J. Brinker; J. Non Cryst. Solids, **1988**, *100*, 31-50
30. S.S. Prakash; C.J. Brinker; A.J. Hurd; *J. Non Cryst. Solids*, **1995**, *190*, 264-275
31. S. Musić; N. Filipović-Vinceković and L. Sekovanić; *Braz. J. Chem. Eng*., **2011**, *28,* 89-94
32. X. Ying-Mei, Q. Ji; H. De-Min; W. Dong-Mei; C. Hui-Ying; G. Jun and Z. Qiu-Min; *Oil Shale,* **2010***, 27*, 37-46
33. D. Geetha; A. Ananthiand and P. S. Ramesh; *J. Pure Appl. Phys.,* **2016***, 4,* 20-26
34. V.H. Le; C.N.H. Thuc and H.H. Thuc; Nanoscale Res. Lett., **2013**, *8*, 58
35. W. Thongthai and C. Metta; *Songklanakarin J. Sci. Technol*., **2012**, *34*, 403-407
36. I. Halasz; A. Kierys; J. Goworek; H. Liu; R.E. Patterson; *J. Phys. Chem. C*, **2011**, *115*, 24788-24799
37. G. Marcin; J.-S. Małgorzata; K. Mikko; S. Janne; *Proceedings, XVII IMEKO World Congress*, 2003, June 22 – 27, Dubrovnik, Croatia
38. G. Socrates; Infrared and Raman Characteristic Group Frequencies Tables and Charts, *John Wiley & Sons*, **2001**
39. T. Jin; Z. Shanrong; W. Weifeng; D. Gordon; M. Xuanxue; *Mater. Sci. Eng. B*, **2004**, *106*, 295
40. O.V. Khavryuchenko; V.D. Khavryuchenko; J.O. Roszinski; A.I. Brusilovets; B. Friede; V.V. Lisnyak; *Thin Solid Films,* **2006**, *515,* 1280
41. A. Jitianu; G. Amatucci; L.C. Klein; *J. Mater. Res*., **2008**, *23,* 2084
42. H. Haryadi; *IPTEK,* **2007**, *18*, 74
43. I. Halasz, R. Li; M. Agarwal and N. Miller; *Stud. Surf. Sci. Catal.*, **2007**, *170A*, 800
44. D. Cebeci; A. Alam; P. Wang; R. Pinal; D. Ben-Amotz; *Eur. Pharm. Rev*., **2017**, *22*, 18-21
45. K.S. W. Sing; D.H. Everett; R.A.W. Haul; L. Moscou; R.A. Pierotti; J. Rouquerol; T. Siemieniewska; *Pure Appl. Chem.,* **1985**, *57,* 603
46. M. Thommes; K. Kaneko; A.V. Neimark; J.P. Olivier; F. Rodriguez-Reinoso; J. Rouquerol and K.S.W. Sing; *Pure Appl. Chem*., **2015**, *87,* 1051

STUDIA UBB CHEMIA, LXVI, 1, 2021 (p. 49-61)
(RECOMMENDED CITATION)
DOI:10.24193/subbchem.2021.1.04

BEHAVIOR IN AC POLARIZATION OF HIGH-SILICON CAST IRONS

CSABA BARTHA[a], VIRGIL MARINESCU[b], MONICA JIPA[a*], BEATRICE-GABRIELA SBARCEA[b], ATTILA TÓKOS[a], ALINA-RUXANDRA CARAMITU[b], IOSIF LINGVAY[a]

ABSTRACT. The behavior of high-silicon cast irons in AC polarization was studied in terms of elementary composition and morphological structure to find suitable materials for inert anodes used in various electrochemical processes with polarization in AC or DC with superimposed AC signal. Experimentally, through optical emission spectrometry, XRD, and SEM-EDAX techniques, the investigated samples' morphology and composition were determined. The behavior in AC polarization at J_{ac} current density between 1 and 300 A/m^2 was assessed through electrochemical and gravimetric methods. The results showed that the mass losses in AC polarization at J_{ac} less than 10 A/m^2 are insignificant (below 8.5x10^{-5} g/Ah), and at J_{ac} 100 A/m^2, samples with a Si content higher than 8% were below 3.75x10^{-4} g/Ah (approx. 150x less than in the case of similar anodically polarized materials in DC). It was also noted that the main processes that occur in the AC polarization of silicone cast iron in aqueous media consist of the anodic oxidation of iron with the formation of iron oxide films and the anodic dissolution with the formation of soluble compounds of some metals from the composition of silicone cast irons (Mn, Cr, Cu, etc.). Furthermore, these anodic processes are coupled with the cathodic processes, which in natural environments consist most probably in reducing the dissolved oxygen.

Keywords: *silicon cast iron, corrosion, AC polarization, mass loss, inert anodes*

[a] *Research-Development Institute for Environmental Protection Technologies and Equipment, Str. Parcului, Nr. 7, 420035, Bistrița, România*

[b] *National Institute for Research and Development in Electrical Engineering INCDIE ICPE-CA,313 Splaiul Unirii, RO-030138, Bucharest, Romania*

[*] *Corresponding author: monica.jipa@icpebn.ro*

INTRODUCTION

In the view of sustainable development, maintaining a clean environment and conserving natural resources is a priority issue [1-3]. In this background, the development and characterization of new materials, with functional characteristics suitable for various applications, ensuring sustainable exploitation without toxic waste at the end of their life span, are always current research topics [4].

The development of any chemical synthesis process is conditioned thermodynamically by the activation energy required for the process. Thermal control of chemical processes (ensuring the activation energy required to initiate and carry out the process through thermal transfer) has many disadvantages, compared to the electrochemical control (energy losses in the production chain, transport and transfer of thermal energy, high response time, and hysteresis of regulation/automation systems, complicated equipment/reactors with high material consumption). In the case of electrochemical syntheses, the process control is relatively simple by overvoltage η, respectively, by controlling the current density J [A/m^2], which crosses the surface of the electrodes- Taffel's law (1):

$$\eta = a + blnj, \tag{1}$$

where a and b are constants specific to the process/electrochemical system and depend on the temperature [5].

Development and advanced characterization (including electrochemical behavior) of materials suitable for the production of electrodes, which under specific operating conditions exhibits stability and adequate electrochemical behavior in anodic [6-12] or cathodic [13-16] polarization, limits the widespread application of the electrochemical technologies. A particular case is the applications of polarized electrodes in AC or DC superimposed with AC signal, such as grounding systems of electrical power systems [17], electrical and corrosion protection of underground pipelines interfered by induced AC stray currents [18, 19].

Recent studies show that the microorganisms' biochemical activity, including those in the activated sludge from wastewater treatments, can be stimulated by exposing the biomass to an extremely low-frequency electric field (ELF) [20-28].

High-silicon cast irons present high stability under anodic polarization conditions (low dissolution rate) [29, 30] and are used frequently in the production of anodes for cathodic protection systems of underground or underwater metallic structures [31, 32].

Therefore, for the development of suitable materials used in various applications, such as long-lasting (lifetime over 100 years) earthing plats for electrical grids or passive electrodes for bioreactors with electromagnetic field stimulation, the paper aims to study the behavior of high-silicon cast irons in AC polarization.

RESULTS AND DISCUSSION

Table 1 covers the chemical composition, determined experimentally, and the assigned code for the high-silicon cast iron samples.

Table 1 shows that the samples obtained are iron alloys with high silicon content (between 2.98 and 17.77%- depending on the dosed metallurgical silicon, and a series of elements from the used raw materials (steel scraps and metallurgical silicon).

Table 1. Composition and coding of high-silicon cast iron samples

Sample code	Content [%]									
	Si	Fe	C	Mn	Cr	Mo	Cu	S	P	Others
Si3	2.98	90.1	1.06	0.33	0.23	0.03	0.43	0.04	0.05	Balance
Si8	8.12	84.9	1.14	0.55	0.49	0.06	0.49	0.02	0.04	
Si11	11.21	86.3	0.85	0.64	0.51	0.09	0.16	0.03	0.03	
Si14	14.1	81.1	1.05	0.98	0.83	0.14	0.56	0.06	0.07	
Si18	17.77	79.3	1.03	0.49	0.21	0.04	0.91	0.04	0.06	

Figure 1 illustrates the XRD diffractogram recorded for the Si3 sample.

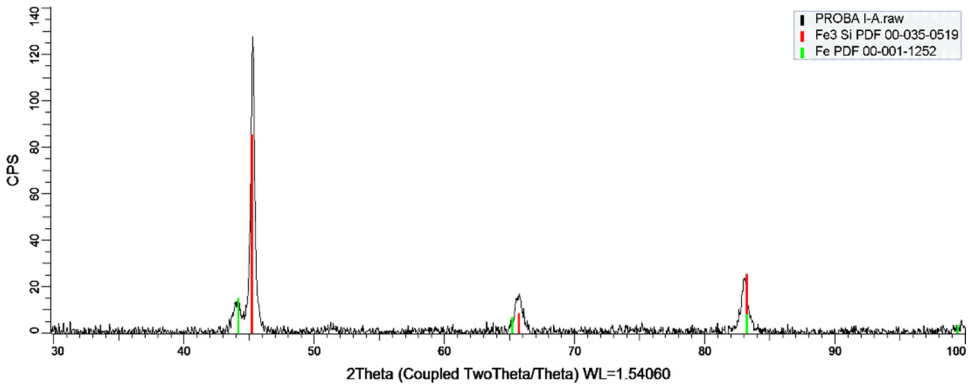

Figure 1. XRD diffractogram recorded on sample Si3.

Figure 1 show that the Si3 sample contains two crystalline phases Fe_3Si and Fe.

The XRD diffractograms recorded on the Si8, Si11, Si14, and Si18 samples were similar and presented in Figure 2.

Figure 2 reveals that the investigated samples with Si content between 8 and 18% contain a single crystalline phase, respectively Fe_3Si (cementite), result in compliance with those reported in [33].

Figure 3 illustrates the results recorded on the Si8 sample regarding the evolutions of the open circuit potentials (E_{OCP}= E_{corr} at J_{ac}= 0) and the polarization potential E_{AC} in 50 Hz AC, at J_{ac} current densities between 1 and 300 A/m^2 in 0.1M KCl solution.

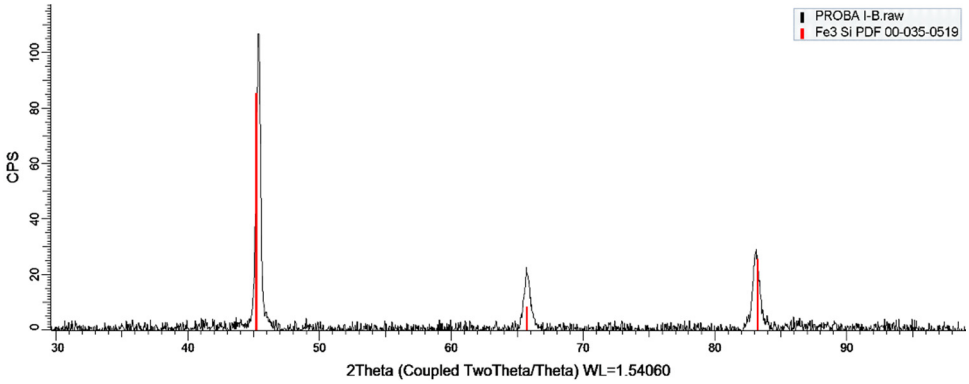

Figure 2. XRD diffractogram recorded on samples Si8, Si11, Si14, and Si18

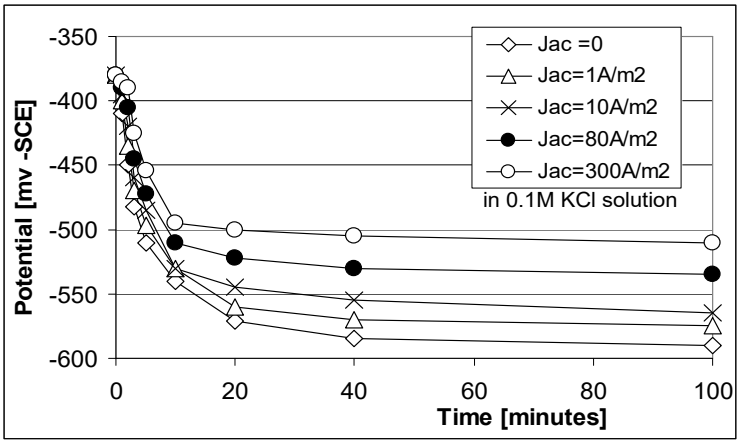

Figure 3. Time evolutions of E_{corr} and E_{AC} recorded on the Si8 sample.

Figure 3 analysis shows that at the immersion of the sample in 0.1M KCl solution, the open circuit potential of the metal display a continuous migration trend towards more electronegative values After an initiation/ stabilization time (approx. 20 minutes, in which the variations are significant) it tends asymptotically to the value of -590 mV, expressing the mixed E_{corr} corrosion potential of the sample. This value is determined by the electrolytic system's nature (given primarily by the metal's electronegativity, the electrolyte's composition, temperature, and dissolved oxygen/partial oxygen pressure). Further, following the sample polarization in AC, the electrode potential migration trend towards more electropositive values is more pronounced, and the value at which the EAC potential stabilizes is determined by the density of the Jac polarization current.

Annotating with Δ_E, the value wherewith the mixed corrosion potential migrates to more electropositive values, under the influence of the E_{AC} polarization current, we have (2):

$$\Delta_E = E_{AC} - E_{corr} = f(J_{ac}), \quad (2)$$

wherein $\mathrm{f(J_{ac})}$ expresses the variation function of the potential under polarization in alternating current.

The evolution of the potential under the action of the polarization current in AC can be explained by Figure 4, which graphically illustrates the response of a metal/electrolyte electrochemical system, characterized by the polarization curve *i= f(E)* to equilibrium disturbance by applying in E_{corr} of a sinusoidal polarization voltages in AC having the period *T*.

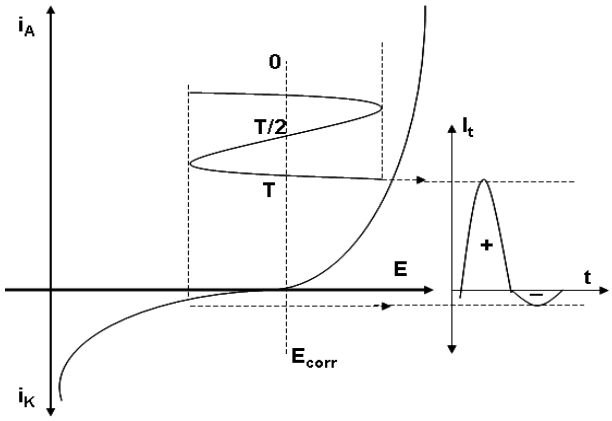

Figure 4. The metal/electrolyte system response at polarization through an AC disturbing signal overlapped in E_{corr}; i_A - global anodic current; i_K - global cathodic current; E_{corr}- mixed corrosion potential; *T*- duration of one period of disturbing sinusoidal signal; I_t- evolution of the AC polarization current

Figure 4 shows that the electrochemical system responds to polarization in sinusoidal AC with a distorted alternating current, in which the share of the anodic half-period (+) is higher than that of the cathode half-period (-), which globally leads to an anodic polarization of the system and implicitly to the migration with Δ_E towards more electropositive values of the electrode potential.

Thus, considering that the value of Δ_E indicates the effect of AC polarization on the metallic material's electrochemical stability, it can be considered a parameter in evaluating the material's passivity to polarization in AC. Time evolutions of E_{corr} and E_{AC} recorded on samples Si3, Si11, Si14, and Si18 are similar to those of sample Si8 (Figure 3), the differences found being in the values of E_{corr} and Δ_E.

The values in Table 2 show that as the Si content of the samples increases (Table 1), the E_{corr} values become more electronegative, and the Δ_E value decreases, which indicates that the corrosivity of the material decreases (passivity increases in AC polarization).

Table 2. E_{corr} and Δ_E values recorded (100 minutes) for the investigated samples at J_{ac} current densities (50 Hz AC)

J_{ac} [A/m^2]	**Samples**									
	Si3 (3 %Si)		**Si8** (8 %Si)		**Si11** (11 %Si)		**Si14** (14 %Si)		**Si18** (18 %Si)	
	E_{OPC}= E_{corr} [mV$_{SCE}$]	Δ_E [mV]	E_{OPC}= E_{corr} [mV$_{SCE}$]	Δ_E [mV]	E_{OPC}= E_{corr} [mV$_{SCE}$]	Δ_E [mV]	E_{OPC}= E_{corr} [mV$_{SCE}$]	Δ_E [mV]	E_{OPC}= E_{corr} [mV$_{SCE}$]	Δ_E [mV]
0	–562	0	–590	0	–590	0	–594	0	–599	0
0.1		10		5		4		3		2
1		25		20		15		7		5
10		51		35		25		16		12
80		88		63		55		45		41
300		115		81		72		63		61

Figure 5 shows the average mass losses recorded on the sample pairs after exposure for 240 hours to AC polarization *vs.* current density (J_{ac}).

Figure 5 shows that for all samples investigated at a current density of up to 10 A/m^2, the mass losses are insignificant (below 0.2 g, respectively, below 8.3x10^{-5} g/Ah). At a current density of 100 A/m^2, for samples with a Si content higher than 8%, the mass losses are less than 0.9 g, respectively 3.75x10^{-4} g/Ah (about 150x less than in the case of similar, polarized materials in DC [31]). The results on the AC polarization behavior of silicone

cast iron samples in 0.1M KCl solution can be explained by Figure 4, which shows that the investigated electrochemical system responds to AC polarization through an anodic global current, results that are consistent with those reported for the electrochemical behavior of similar materials [29].

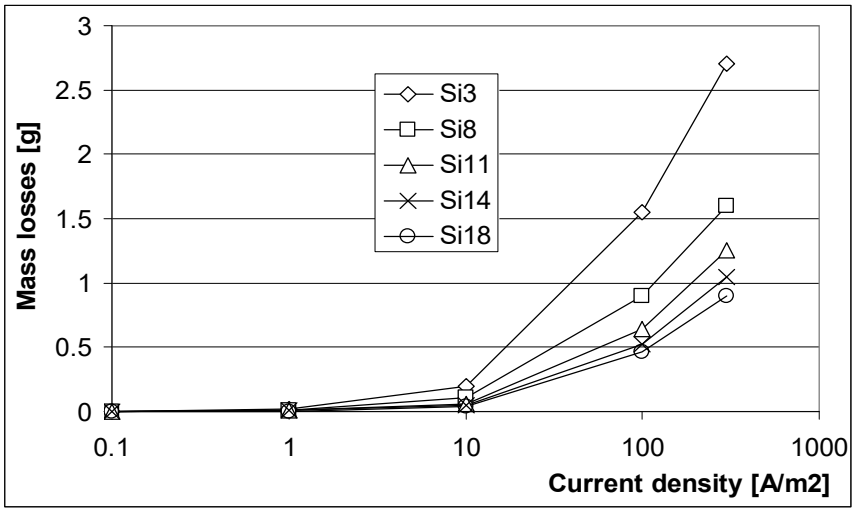

Figure 5. Mass losses *vs.* current density of the investigated samples.

Figure 6 illustrates the representative SEM images regarding the investigated samples' morphology, according to the Si content: 3% Si, 8% Si, and 18% Si.

Comparative analysis of images a, b, c, and d in Figure 6, highlights as a common element the presence of graphite spherical precipitations, specific to silicon cast iron with silicon content higher than 3% [33, 34]. The Si3 sample (Figure 6 a- approx. 3% Si) presents a structure in which the two major crystalline structures (distributed relatively homogeneously) are distinguished, identified by XRD (Figure 1- Fe and Fe_3Si cubically crystallized). The Si8 sample (Figure 6 b- 8% Si) shows a homogeneous structure, uniformly crystallized (Fe_3Si- according to Figure 2), which explains the unique mechanical characteristics reported [29]. The Si18 sample (Figure 6c, d- 18% Si) shows a tense structure in which small crystals of Fe_3Si prevail (Figure 2), and the presence of intercrystalline cracks is noticed (explains the high fragility reported [29]).

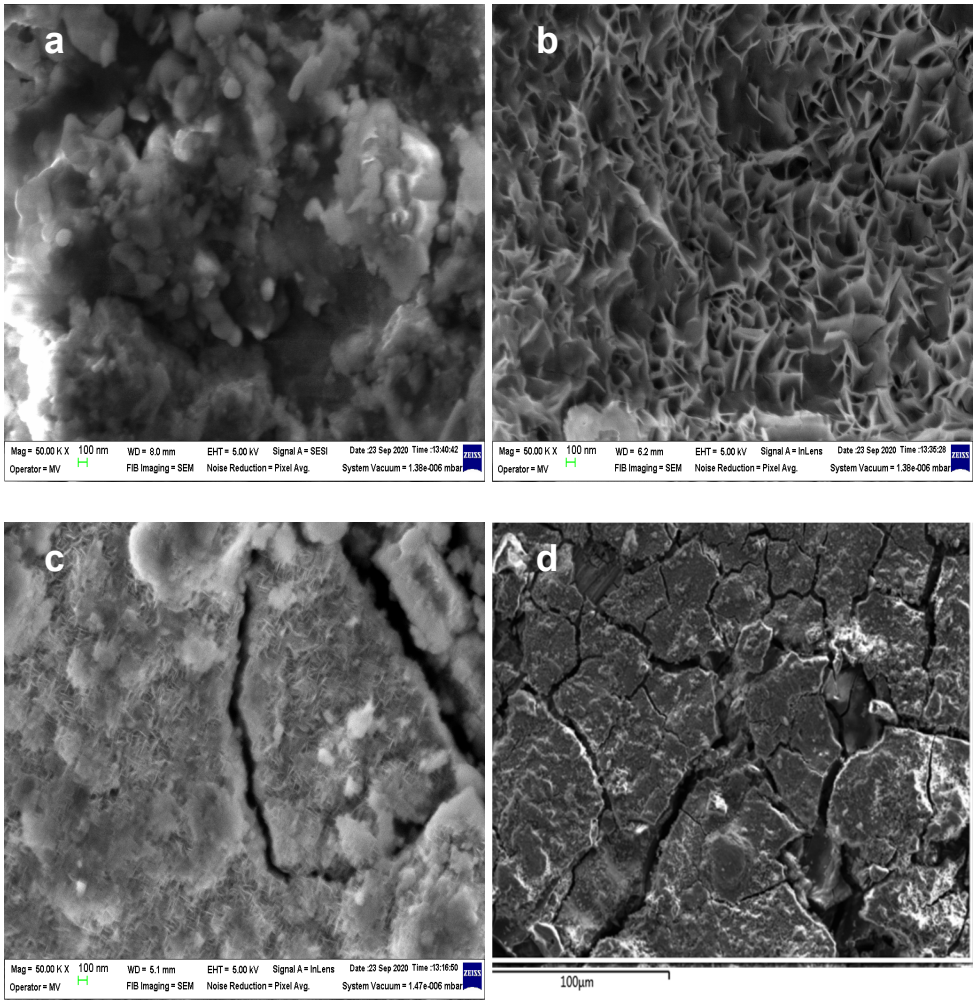

Figure 6. SEM images of the samples: **a**- 3% Si, **b**- 8% Si, and **c, d**- 18% Si.

Table 3 summarizes the results of EDAX measurements (superficial elementary compositions- average values for 5 spectra recorded in 5 different locations) obtained on surface A (unexposed to polarization in AC) compared to surface B (exposed to polarization in 50 Hz, AC 300 A/m^2, for 240 hours), normalized for the main elements identified (100% specified components).

The analysis of the data presented in Table 3 shows that, following the polarization of the investigated samples in 50 Hz AC with 300 A/m^2, the oxygen content of the investigated surface layer (surface B) increases significantly as compared to that of the samples not exposed to AC polarization (surface A). The oxygen content of surfaces exposed to AC polarization decreases with increasing Si content of the investigated samples.

Table 3. The value of 50 Hz AC polarization (240 hours at J_{ac} 300 A/m^2) of the exposed (B) and unexposed (A) samples surface

Elements	Sample- content Wt [%]									
	Si3		Si8		Si11		Si14		Si18	
	A	B	A	B	A	B	A	B	A	B
Si	3.4	3.38	8.82	8.92	11.25	11.26	14.31	14.43	17.27	17.28
Fe	94.1	63.40	87.95	61.88	86.39	63.36	82.01	62.79	79.66	61.77
0	0.10	31.95	0.15	27.9	0.20	24.52	0.25	21.72	0.35	19.88
C	1.26	1.27	1.29	1.30	0.85	0.86	1.05	1.06	1.05	1.07
Mn	0.41	0	0.75	0	0.64	0	0.98	0	0.52	0
Cr	0.13	0	0.51	0	0.51	0	0.83	0	0.22	0
Cu	0.6	0	0.53	0	0.16	0	0.57	0	0.93	0

Also, during polarization in AC, the metallic elements Mn, Cr, and Cu are entirely dissolved from the samples' surface. These findings, in context with Figure 4, suggest that the main processes that occur in AC polarization of silicone cast iron in aqueous media consist of anodic oxidation of iron with the formation of iron oxide films (3):

$$xFe + 2yOH^- \rightarrow Fe_xO_y + yH_2O + 2ye^-, \quad (\mathbf{3})$$

and the anodic dissolution of some metals *Me* from the composition of silicon cast irons (such as Mn, Cr, Cu), with the formation of soluble compounds (4):

$$Me \rightarrow Me^{z+} + ze^-, \quad (\mathbf{4})$$

where z^+ represents the valence of the dissolved metal, and e^- the elementary charge (electron) released.

The anodic processes (3) and (4) are coupled with the cathodic process- probably to reduce the dissolved oxygen in the solution, respectively (5):

$$O_2 \rightarrow 2\ O;\ O + 2e^- \rightarrow O^{2-};\ H_2O + O^{2-} \rightarrow 2\ OH^- \quad (\mathbf{5})$$

Experimental results indicate that silicon cast irons with Si content above 8% present high stability to AC polarization. Thus, such materials can be used successfully to achieve long-lasting (life over 100 years) earthing plats for power systems [17-19], durable electrodes for the protection of the

underground gas pipelines exposed to AC stray currents [19], inert electrodes for the electrochemical processes, including bioelectrochemical technologies (stimulation of biological processes for wastewater treatment [28], acceleration and control of fermentation processes to obtain biogas [26]). When used as inert electrodes in electrochemical processes, it is necessary to consider the effects of electrolyte impurity with metal ions found in the composition of silicon cast iron used (Fe, Cr, Cu, and Mn).

CONCLUSIONS

Through electrochemical, gravimetric, XRD, and SEM-EDAX investigations, silicone cast irons with silicon content between 3 and 18% were characterized. Analysis of the obtained experimental data shows that:

-in the microstructure of the investigated samples, for the samples with Si content of approximately 3%, Fe and Fe_3Si crystals prevail, unlike samples with Si content higher than 8%, in which XRD highlighted only cubically crystallized Fe_3Si;

-the Si content of the samples determines the electronegativity (the open circuit potential- E_{corr}) of the investigated samples, immersed in 0.1M KCl solution (between –562 mV_{SCE} for Si3 and –599 mV_{SCE} for Si18), and increases with the Si content of the sample;

-at the AC polarization of the investigated samples, their potential becomes more electropositive than E_{corr}, the migration to more electropositive values of Δ_E is determined by the density J_{ac} of the polarization current (increases with increasing J_{ac}) and by the Si content of the samples (increases with decrease in Si content);

-mass losses at AC polarization are determined by J_{ac} (increases with increasing J_{ac}) and the Si content of the samples (increases with decreasing Si content); at J_{ac}, less than 10 A/m^2, the losses are insignificant (below $8.5x10^{-5}$ g/Ah) for all samples, and at J_{ac} 100 A/m^2, samples with Si content higher than 8%, below $3.75x10^{-4}$ g/Ah (approx. 150x less than in the case of similar anodized polarized materials in DC);

-the main processes that occur in AC polarization of silicon cast irons in aqueous media consist of the anodic oxidation of iron with the formation of iron oxide films and the anodic dissolution with the formation of soluble compounds of some metals from the composition of silicon cast irons (Mn, Cr, Cu), probably coupled with the cathodic process of reducing dissolved oxygen in solution.

Based on these findings, silicone cast irons with Si content higher than 8% present high stability to AC polarization and can be successfully used to achieve long-lasting earthing plats for power systems, protective electrodes for

underground gas pipelines exposed to AC stray currents, inert electrodes with applications in electrochemical and bioelectrochemical technologies (stimulation, acceleration, and control of biological processes with industrial applications).

EXPERIMENTAL SECTION

Samples of high-silicon cast irons were obtained by usual metallurgical techniques from steel scraps and metallurgical silicon (ferrosilicon). After casting, the samples were sandblasted with sand, washed, and dried in an oven at 90±50° C, preceding the experimental determinations. The elemental analysis of the obtained alloys was performed through optical emission spectrometry technique, with a specialized equipment type LAVWA 18 A from SPECTRO Analytical.

XRD and SEM-EDAX techniques were employed in the morpho-structural analysis of the obtained high-silicon cast iron samples. XRD measurements were performed with D8 Discover equipment (from Bruker), configured on primary optics with a Cu tube with primary radiation (λ = 1.540598 Å), Göebel mirror, and on secondary optics with a 1D LynxEye detector. SEM-EDAX measurements were performed using an energy dispersive X-ray spectrometer (EDS), INCA Energy 250, Oxford Instruments, combined with Zeiss field emission scanning electron microscope (FESEM).

In a parallelepiped vessel, two samples (approx. 100x100 mm with a thickness of approx. 5 mm) were fixed in a parallel plane position (distance between samples approximately 16 cm) and immersed in 0.1 M KCl solution. The samples were connected to the output of a 50 Hz power supply with an adjustable voltage between 1 and 20 V, thus ensuring polarizations in AC at J_{ac} between 1 and 300 A/m^2. Time evolution of the potentials in the open circuit (E_{corr} at J_{ac}=0) and the evolution of the E_{AC} polarization potential in 50 Hz AC were determined at J_{ac} current densities between 1 and 300 A/m^2, against a saturated calomel electrode (SCE) with a PM2517E type multimeter manufactured by Philips (input impedance higher than 10 MΩ).

Sample mass losses were calculated by measuring the samples before and after AC polarization (at various J_{ac} for 240 hours). Measurements were performed with a digital analytical scale with an accuracy of ± 0.0001g (type Precisa 320 XR -model XR125SM from Precisa Gravimetrics AG). For each sample, measurements were performed on the surface unexposed to polarization in AC compared to the surface exposed to polarization in 50Hz AC (240 hours at 300A/m^2, in 0.1M KCl solution).

ACKNOWLEDGMENTS

This work was financially supported by a grant of the Romanian Ministry of Education and Research, CCCDI – UEFISCDI, under the scientific Programme PN III - PTE, Contract 12 PTE/2020– ESELFBio.

REFERENCES

1. A. Świercz; E. Zajęcka; *Carpathian J. Earth Environ. Sci.*, **2018**, *13 (1)*, 249-266.
2. G.M. Ispas; C. Roba; R. Bâlc; D.M. Gligor; *Carpathian J. Earth Environ. Sci.*, **2020**, *15 (2),* 415–428.
3. M.R. Niță; C.I. Ioja; *Carpathian J. Earth Environ. Sci.*, **2020**, *15 (2)*, 471–479.
4. E.A. Stere; I. Popa; *Electroteh. Electron. Autom.,* **2018**, *66 (4)*, 127-134.
5. T. Erdey-Grúz; *Kinetics of electrode processes*, Akadémiai kiadó, Budapest, Hungary, **1969**, pp. 15-45.
6. Y. Xianjin; Z. Lipeng; D. Yunhui; Z. Zengdian; *J. Rare Earths*, **2006**, *24 (1)*, 352-354.
7. F. Zaza; C. Paoletti; R. Lo-Presti; E. Simonetti; M. Pasquali; *J. Power Sources*, **2010**, *195 (13)*, 4043-4050.
8. R.D. Xu; L.P. Huang; J.F. Zhou; P. Zhan; Y.Y. Guan; Y. Kong; *Hydrometallurgy*, **2012**, *125–126*, 8-15.
9. W. Yun-Hai; C. Qing-Yun; L. Guo; L. Xiang-Lin; Anodic materials with high energy efficiency for electrochemical oxidation of toxic organics in waste water, in: *Industrial waste*, K. Y. Show, X. Guo Eds; IntechOpen, Rijeka, Croatia, **2012**, Chapter 2, pp. 33-50
10. I. Gallino; M.E. Kassner; R. Busch; *Corros. Sci.*, **2012**, *63*, 293-303.
11. D. Jia; K. Wang; J. Huang; *Chem. Eng. J.*, **2017**, *317*, 673-686.
12. H. Chu; Q. Wu; J. Huang; *Colloids Surf. A Physicochem. Eng. Asp.*, **2018**, *558*, 495-503.
13. S. Permeh; K. Lau; M.E. Boan; B. Tansel; M. Duncan; *J. Mater. Civ. Eng.*, **2020**, *32 (7)*, 04020184.
14. O.G. Kuznetsova; A.M. Levin; O.I. Tsybin; M.A. Sevostyanov; V.A. Bryukvin; A.O. Bolshikh; *Russ. Metall.*, **2018**, *2018 (7)***,** 651–654.
15. K.V. Hansen; M. Chen; T. Jacobsen; K.T.S. Thydén; S.B. Simonsen; S. Koch; M.B. Mogensen; *J. Electrochem. Soc.,* **2016**, *163 (10)*, 1217- 1227.
16. S. Geißler; H. Tiainen; H.J. Haugen; *Mater. Sci. Eng. C.*, **2016**, *63*, 359-366.
17. I. Lingvay; C. Homan*; C.* Lingvay*; Rev. Chim.,* **2007***, 58 (11)*, 1051-1054.
18. I. Lingvay; A. Voina; C. Lingvay; C. Mateescu**;** *Rev. Roum. Sci. Techn.–Électrotechn. Énerg*, **2008**, *53 (2)*, 95-112.
19. I. Lingvay; A.M. Bors; D. Lingvay; L. Radermacher; V. Neagu*; Rev. Chim.,* **2018**, *69 (12)*, 3593-3599.
20. D. Sandu; I. Lingvay; S. Lányi; D.D. Micu; C.L. Popescu; J. Brem; L.C. Bencze; C. Paizs; *Studia UBB Chemia*, **2009**, *54 (4)*, 195-201.

21. R.W. Hunt; A. Zavalin; A. Bhatnagar; S. Chinnasamy; K.C. Das; *Int. J. Mol. Sci.,* **2009**, *10*, 4515-4558.
22. M. Gao; J. Zhang; H. Fen; *Bioelectromagnetics*, **2011**, *32*, 73-78.
23. C. Stancu; M. Lingvay; I. Szatmári; I. Lingvay; *The 8th Int. Symp.on ATEE,* Bucharest, Romania, May 23-25, **2013**, 1-4.
24. E. Radu; D. Lipcinski; N. Tănase; I. Lingvay; *Electroteh. Electron. Autom.*, **2015**, *63 (3)*, 68-74.
25. M. Lingvay; A.R. Caramitu; A.M. Bors; I. Lingvay; *Studia UBB Chemia*, **2019**, *64 (2)*, 279-288.
26. C. Mateescu; I. Lingvay; A. Caramitu; N. Tanase; E. Radu, RO Patent RO132199 B1, **2020**.
27. C. Bartha; A. Caramitu; M. Jipa; D.M. Ignat; A. Tókos; *Studia UBB Chemia*, **2020**, *65 (4)*, 85-93.
28. C. Bartha; M. Jipa; A.R. Caramitu; A. Voina; A. Tókos; D.M. Ignat; I. Lingvay; *Rev. Roum. Sci. Techn.– Électrotechn. Énerg,* ***2020***, in press
29. M. Stawarz; W. Kajzer; A. Kajzer; M. Dojka; *Arch. Foundry Eng*., **2017**, *17 (2)*, 101-106.
30. U. de la Torre; A. Loizaga; J. Lacaze; J. Sertucha; *J. Mater. Sci. Technol.*, **2014**, *30 (12)*, 1425-1431.
31. Specialist Castings Limited; *High Silicon Cast Iron Anode*, (n.d.).
32. I. Lingvay; C. Lingvay; G. Rus; I. Laţa; V. Pavlovschi; L. Ancas; RO Patent 120717 B1, **2001**.
33. R. González-Martínez; U. de la Torre; J. Lacaze; J. Sertucha; *Mater. Sci. Eng. A*, **2018**, *712*, 794- 802.
34. P. Rubin; R. Larker; E. Navara; M.L. Antti; *Metallogr. Microstruct. Anal.*, **2018**, *7*, 587–595.

STUDIA UBB CHEMIA, LXVI, 1, 2021 (p. 63-71)
(RECOMMENDED CITATION)
DOI:10.24193/subbchem.2021.1.05

BISMUTH DOPED ZnO/MoO_2 COMPOSITES FOR THE CATALYTIC DEGRADATION OF METHYLENE BLUE

MUBBARA MUSHTAQ[a], SHOOMAILA LATIF[b*], MUHAMMAD IMRAN[a], AYESHA JAVAID[a], LIVIU MITU[c*]

ABSTRACT. From past years, the demand of clean water has been increased due to shortage of portable fresh water. Parallel, the use of composite materials for the catalytic degradation of pollutants particularly dyes in industrial effluents has attracted good attention. In this work, bismuth doped ZnO/MoO_2 composites were synthesized by co-precipitation method using bismuth chloride, zinc sulphate and sodium molybdate as starting precursors. The structural/morphological studies of these composites were accomplished by UV–Visible spectroscopy, Fourier Transform Infrared Spectroscopy and Scanning Electron Microscopy. The catalytic activity of the bismuth doped ZnO/MoO_2 composites was investigated by degradation of methylene blue (MB) dye. The degradation of MB was observed to be 75% at only 45 sec and enhanced catalytic activity was observed by increasing Bi content in synthesized composites.

Keywords: *ZnO/MoO_2 composites; Bismuth doping; Methylene blue; Catalytic degradation*

INTRODUCTION

Metal oxides have recently attained rapid attention for remediation and environmental protection. The degradation of dyes in waste water from textile industry is really a challenging task and such dyes are a huge source of water contamination. To cope with this challenge, significant consideration has been paid to resolve this issue and as such catalytic properties of metal oxides were improved by doping them with variety of metals [1].

[a] *Institute of Chemistry, University of the Punjab, Lahore 54000, Pakistan*
[b] *School of Physical Sciences, University of the Punjab, Lahore 54000, Pakistan*
[c] *Department of Nature Sciences, University of Pitesti, Pitesti, 110040, Romania*
**Corresponding author: shoomaila_latif@yahoo.com; ktm7ro@yahoo.com*

Among several metal oxides used for this purpose, TiO_2 and ZnO have been broadly reported for degradation process of dyes due to their remarkable properties. ZnO has recently been reported more advantageous over TiO_2 because of its low cost and high catalytic activity. Moreover, it has similar conduction and valence bands to that of TiO_2 [2]. ZnO is also a good semiconducting material of II–VI type, with a wide band gap (3.37 eV) and a large excitation binding energy (60 meV) at room temperature thus making it good for photocatalytic applications [3].

Catalytic properties of zinc oxide have been enhanced either by doping or by developing ZnO based composites such as ZnO/metal [4], ZnO/metal oxide [5] and ZnO/polymer [6]. Doping is considered to be more useful in this regard. A large number of dopants such as transition metals as well as rare earth elements have been reported to enhance the catalytic properties of ZnO [7-10]. Combination of different metal oxides can reduce the band gap, hence, extending the absorbance range to visible region to achieve a higher photocatalytic activity [11-14]. Some notable examples of such combinations are CuO–TiO_2 [15], WO_3–TiO_2 [16], ZnO/TiO_2 [17], ZnO/SnO_2 [11], TiO_2/MgO [18], and SnO_2/ZnO [19].

$NaBH_4$ supported by a catalyst is a well-known reducing agent for the reduction of MB dye. Composites synthesized by doping have been reported to assist $NaBH_4$ [20, 21]. Keeping in view the literature background, in this study, molybdenum oxide is chosen for modifying ZnO [22, 23] while bismuth ion is selected as a dopant because of its previously reported role in enhancing catalytic properties of ZnO [24]. According to accessible literature, there is no work reported on the synthesis of Bi-doped ZnO/MoO_2 composite material for catalytic degradation of MB. Therefore, in this study, we report the preparation of Bi-doped ZnO/MoO_2 composite material together with its catalytic reduction efficiency.

RESULTS AND DISCUSSION

Bismuth doped ZnO/MoO_2 composites were synthesized by co-precipitation method followed by annealing process. These composites were subsequently characterized by different spectroscopic techniques. UV-Visible Spectrum of the composite was recorded by UVD-T90+ Spectrophotometer in the range 200-800 nm and exhibit maximum wavelength at 255 nm (Figure 1). The single absorption indicates homogeneity across the sample of composite.

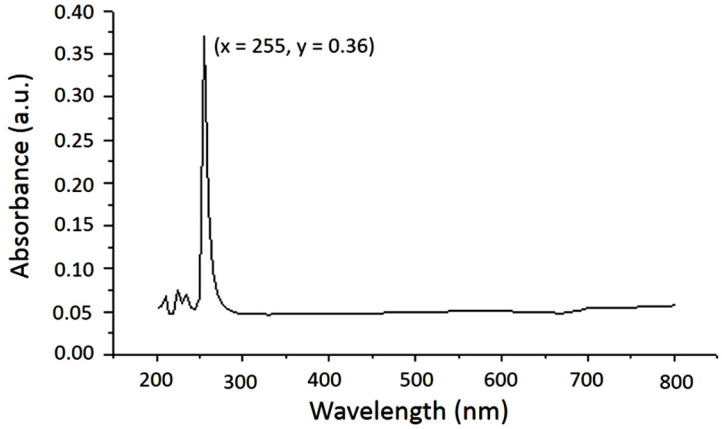

Figure 1. UV-Vis spectrum of Bi-doped ZnO/MoO_2 (1%) composites

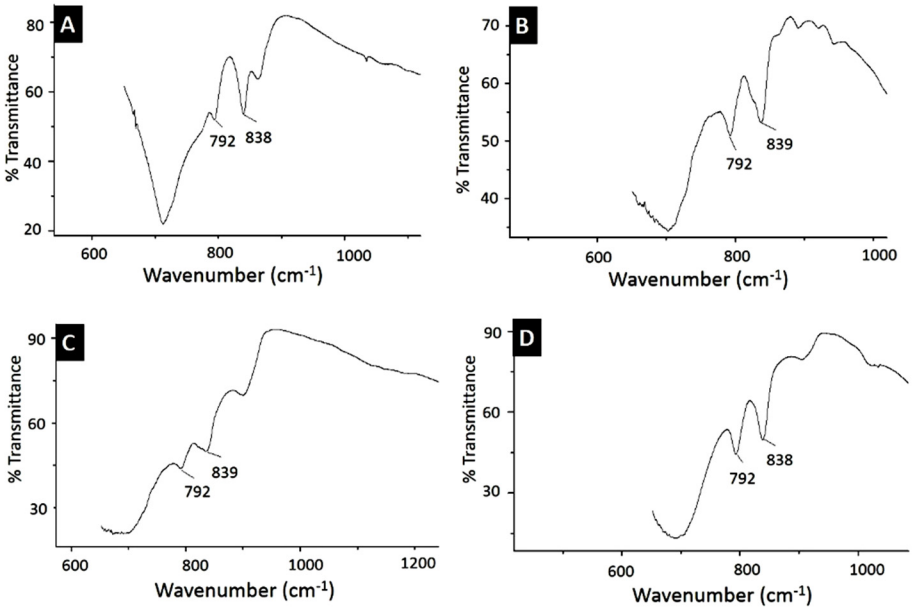

Figure 2.A: FT-IR Spectrum of 0.4% Bi-doped ZnO/MoO_2 composite;
B: FT-IR Spectrum of 0.6% Bi-doped ZnO/MoO_2 composite;
C: FT-IR Spectrum of 0.8% Bi-doped ZnO/MoO_2 composite;
D: FT-IR Spectrum of 1% Bi-doped ZnO/MoO_2 composite

FT-IR spectral data provided valuable information about the functional groups present in the synthesized bismuth doped ZnO/MoO_2 composites. The FT-IR spectra of Bi-doped ZnO/MoO_2 composites were recorded in the range 4000-400 cm^{-1}. The spectrum of bismuth doped metal oxide composites showed a broad band at 740-990 cm^{-1} which was assigned to Bi-O stretching mode vibrations [25] while the peak observed at 792 cm^{-1} is assigned to Mo-O in MoO_2 [26]. The band observed around 400-650 cm^{-1} is attributed to the zinc oxide bending vibrations [27]. FT-IR spectra of ZnO/MoO_2 composites with variable concentrations of dopant i.e. bismuth were recorded and compared. All the spectra showed bands around same frequency which confirmed the formation of bismuth doped ZnO/MoO_2 composite (Figure 2).

The surface morphology of Bi-doped ZnO/MoO_2 appears to be dense globular and rod-like structures with high porosity as shown by the SEM micrograph of the prepared composite (Figure 3).

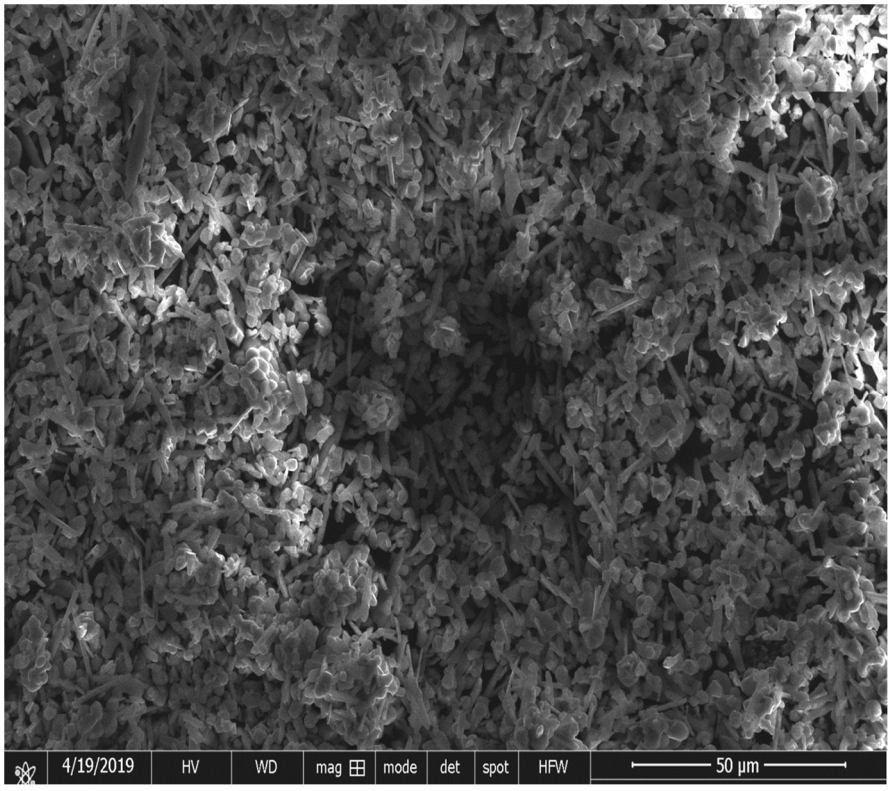

Figure 3. SEM micrograph of the prepared Bi-doped ZnO/MoO_2 composite (1%)

Catalytic degradation of MB by synthesized composites

To investigate the role of bismuth doped ZnO/MoO_2 composites as catalyst, degradation of MB was studied in the presence of $NaBH_4$ by adding variable concentration of composites as well as in the absence of composite. $NaBH_4$ is a well-known reducing agent and its efficiency is associated with its high electron injection capacity [28]. The rate of degradation was observed in the range 400-800 nm at room temperature. Overall, Bi doped ZnO/MoO_2 composites have shown enhanced catalytic activity for the degradation of MB. The different color of MB in its oxidized and reduced form make it good candidate for catalytic study. Figure 4A contains

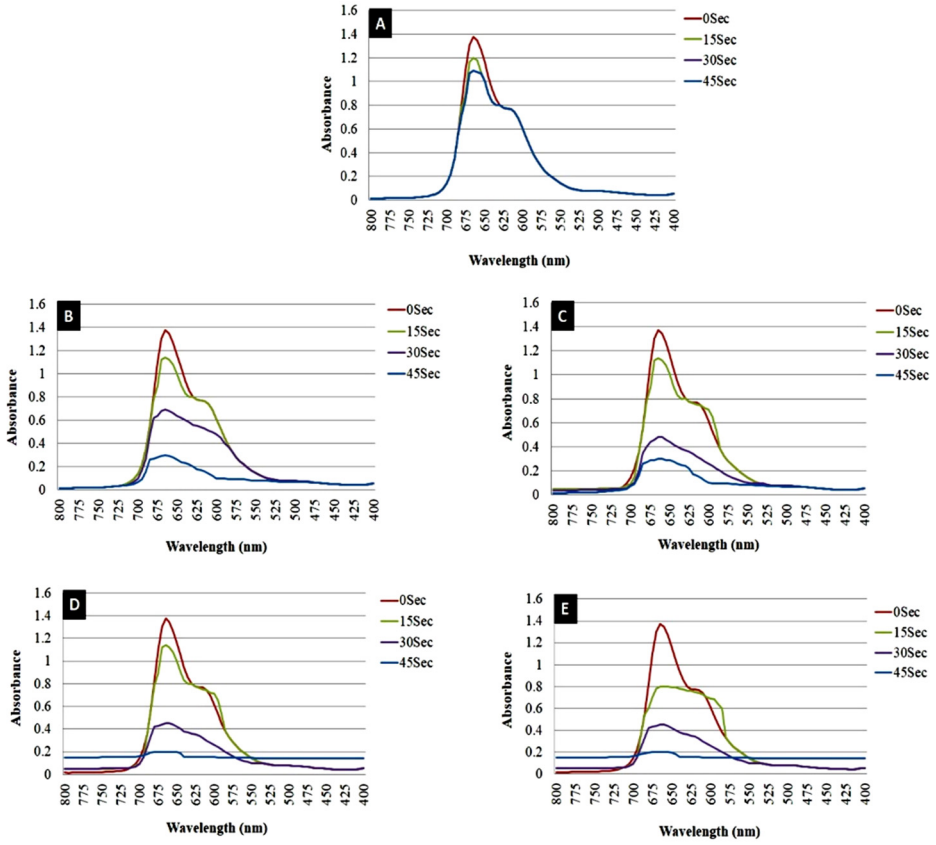

Figure 4. Catalytic degradation of MB using $NaBH_4$ with Bi-doped ZnO/MoO_2 composites **A:** without composites; **B:** Bi-doped ZnO/MoO_2 composites (0.4%); |**C:** Bi-doped ZnO/MoO_2 composites (0.6%); **D:** Bi-doped ZnO/MoO_2 composites (0.8%); **E:** Bi-doped ZnO/MoO_2 composites (1%)

absorption spectra of MB in the absence of composite and shows that absorption peaks of the MB solution diminish gradually with time and finally solution becomes colorless. Moreover, in this case, the absorption peak of MB at 665 nm was found to decrease slowly with the increase in the reaction time indicating a slow degradation rate in the absence of composite.

In the same manner degradation of MB was investigated by adding variable concentration (0.4% to 1.0%) of synthesized composite as catalyst. The results are graphically represented in Figure 4(B-E). Generally, it has been observed that by increasing the concentration of Bi doping in composite, rate for MB degradation was completed in less time interval. So, it can be concluded that the addition of bismuth composite enhances the degradation of the dye and maximum efficiency was observed especially in case of 1% bismuth doped ZnO/MoO_2 composite as compared to other compositions. This enhanced reduction efficiency is might be due to provision of large surface by the Bi doped ZnO/MoO_2 composites which cannot be achieved in its absence. Moreover, these findings are in agreement with previously reported catalytic property of Bi doped ZnO composites [24].

CONCLUSIONS

The bismuth doped ZnO/MoO_2 composites were successfully synthesized by a facile, simple, and low cost co-precipitation method. The catalytic efficiencies of bismuth doped ZnO/MoO_2 composites for degradation of MB were reported. Bismuth doped ZnO/MoO_2 was found to be an efficient catalyst to degrade MB dye, an environmental hazard.

EXPERIMENTAL SECTION

Chemicals used

Zinc sulphate $ZnSO_4 \cdot 7H_2O$, Sodium molybdate Na_2MoO_4, Bismuth chloride $BiCl_3$, Sodium hydroxide NaOH, Tetrahydrofuran C_4H_8O used were of analytical grade and purchased from sigma Aldrich. These were used as such without any further purification. Spectroscopic analysis of the composites was performed by mean of UV-Vis spectrophotometer (Labomed spectrophotometer system; model UVD-T90+), FT-IR spectrometer (Agilent FTIR spectrophotometer; model CARY-630; range 4000-650 cm^{-1}) and SEM (Nova Nano 450-SEM field emission scanning electron microscope (FESEM).

Fabrication of Bismuth doped ZnO/MoO_2 composites

Bi^{3+} doped ZnO/MoO_2 composites were successfully prepared by simple co-precipitation method (Figure 5). Appropriate amounts of zinc sulphate (1 mM), sodium molybdate (1 mM) and bismuth chloride (0.4 – 1.0 %) were dissolved in 10 mL deionized water separately and stirred for few minutes until solutions became transparent. To the solution of bismuth chloride, solutions of zinc sulphate and sodium molybdate were added together with stirring on hot plate. Then, NaOH (2 mol %) was added drop wise in the above resulting mixture and stirred again vigorously by keeping the pH at 7. This resulted yellow colored precipitates, which were filtered, washed several times with deionized water, ethanol and finally dried in oven at 80°C for 2 hours. The dried precipitates were crushed with mortar and pestle to obtain fine powder and then placed in muffle furnace at 650°C for 4 hours to anneal at the rate of (5 °C/min).

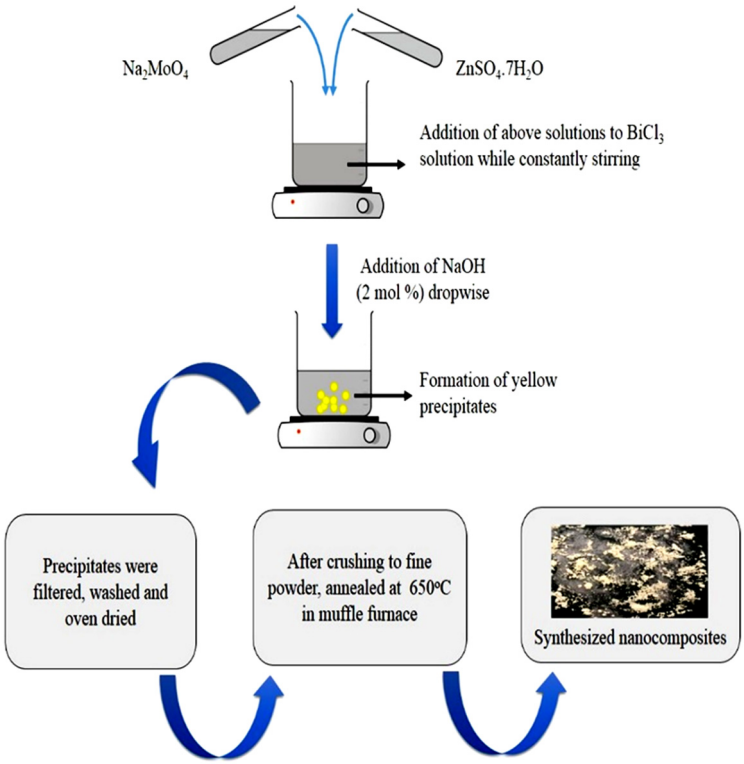

Figure 5. Schematic representation for the synthesis of Bi doped ZnO/MoO_2 composites

Degradation of MB using Bi doped ZnO/MoO_2 composites

MB solution (2.0 mmol, 5 mL) was mixed with $NaBH_4$ (0.2 g) in the presence of variable amount (0.4 – 1.0%) of Bi-doped ZnO/MoO_2 catalyst at room temperature. The degradation of dye was noted by UV/Visible Spectrometer after every 15 seconds. The degradation rate of MB dye was calculated by using the following equation:

$$\text{Degradation rate} = \frac{Ao-A}{A} x100$$

where A_o shows initial absorbance, and A corresponds to variable absorbance.

ACKNOWLEDGMENTS

The authors are grateful to University of the Punjab, Lahore, Pakistan, for funding this project.

REFERENCES

1. a) M.M. Khan; J. Lee; M.H. Cho; *J.Ind.Eng.Chem.,* **2014**, *20(4)*, 1584-1590. b) S. Sfaelou; L.C. Pop; O. Monfort; V. Dracopoulos; P. Lianos; *Int.J.Hydrogen Energ.*, **2016**, *41(14)*, 5902-5907. c) R. Gusain; K. Gupta; P. Joshi; O.P. Khatri; *Adv.Colloid Interface Sci.*, **2019**, *272*, 102009. d) Z. Pap; É. Karácsonyi; L. Baia; L.C. Pop; V. Danciu; K. Hernádi; K. Mogyorósi; A. Dombi; *Phys.Status Solidi B*, **2012**, *249(12)*, 2592-2595.
2. S.K. Yadav; S.R. Madeshwaran; J.W. Cho; *J.Colloid Interface Sci.*, **2011**, *358(2)*, 471-476.
3. S. Anandan; N. Ohashi; M. Miyauchi; *Appl.Catal.B: Environ.*, **2010**, *100(3-4)*, 502-509.
4. R. Qiu; D. Zhang; Y. Mo; L. Song; E. Brewer; X. Huang; Y. Xiong; *J.Hazard.Mater.*, **2008**, *156(1-3)*, 80-85.
5. Q. Yu; J. Li; H. Li; Q. Wang; S. Cheng; L. Li; *Chem.Phys.Lett.,* **2012**, *539*, 74-78.
6. C. Hariharan; *Appl.Catal. A-Gen.*, **2006**, *304*, 55-61.
7. T. Jia; W. Wang; F. Long; Z. Fu; H. Wang; Q. Zhang; *J.Alloys Compd.*, **2009**, *484(1-2)*, 410-415.
8. C. Wu; Q. Huang; *J.Lumin.*, **2010**, *130(11)*, 2136-2141.
9. B. Donkova; D. Dimitrov; M. Kostadinov; E. Mitkova; D. Mehandjiev; *Mater. Chem.Phys.*, **2010**, *123(2-3)*, 563-568.
10. S. Gao; X. Jia; S. Yang; Z. Li; K. Jiang; *J.Solid State Chem.*, **2011**, *184(4)*, 764-769.
11. W. Cun; Z. Jincai; W. Xinming; M. Bixian; S. Guoying; P. Ping'an; F. Jiamo; *Appl.Catal.B-Environ.*, **2002**, *39(3)*, 269-279.

12. K. Gopidas; M. Bohorquez; P.V. Kamat; *J.Phys.Chem.*, **1990**, *94(16)*, 6435-6440.
13. M. Long; W. Cai; J. Cai; B. Zhou; X. Chai; Y. Wu; *J.Phys.Chem.B,* **2006**, *110(41)*, 20211-20216.
14. M. Xue; L. Huang; J.Q. Wang; Y. Wang; L. Gao; J.H. Zhu; Z.G. Zou; *Nanotechnology*, **2008**, *19(18)*, 185604.
15. G. Li; N.M. Dimitrijevic; L. Chen; T. Rajh; K.A. Gray; *J.Phys.Chem.C*, **2008**, *112(48)*, 19040-19044.
16. Y. He; Z. Wu; L. Fu; C. Li; Y. Miao; L. Cao; H. Fan; B. Zou; *Chem.Mater.*, **2003**, *15(21)*, 4039-4045.
17. G. Marci; V. Augugliaro; M.J. Lopez-Munoz; C. Martin; L. Palmisano; V. Rives; M. Schiavello; R.J. Tilley; A.M. Venezia; *J.Phys.Chem.B,* **2001**, *105(5)*, 1033-1040.
18. J. Bandara; S. Kuruppu; U. Pradeep; *Colloids Surf.A Physicochem. Eng.Asp.*, **2006**, *276(1-3)*, 197-202.
19. L. Zheng; Y. Zheng; C. Chen; Y. Zhan; X. Lin; Q. Zheng; K. Wei; J. Zhu; *Inorg.Chem.,* **2009**, *48(5)*, 1819-1825.
20. N. Gupta; H.P. Singh; R.K. Sharma; *J.Mol.Catal.A:Chem.,* **2011**, *335(1-2)*, 248-252.
21. K. Mallick; M. Witcomb; M. Scurrell; *Mater.Chem.Phys.*, **2006**, *97(2-3)*, 283-287.
22. Z.J. Jiang; C.Y. Liu; L.W. Sun; *J.Phys.Chem.B*, **2005**, *109(5)*, 1730-1735.
23. Y. Chen; C. Lu; L. Xu; Y. Ma; W. Hou; J.J. Zhu; *Cryst.Eng.Comm.,* **2010**, *12(11)*, 3740-3747.
24. V. Chandraboss; J. Kamalakkannan; S. Prabha; S. Senthilvelan; *RSC Adv.*, **2015**, *5(33)*, 25857-25869.
25. V. Fruth; M. Popa; D. Berger; C. Ionica; M. Jitianu; *J.Eur.Ceram.Soc.*, **2004**, *24(6)*, 1295-1299.
26. C. Barraclough; J. Lewis; R. Nyholm; *J.Chem.Soc.*, **1959**, *713*, 3552-3555.
27. V. Chandraboss; L. Natanapatham; B. Karthikeyan; J. Kamalakkannan; S. Prabha; S. Senthilvelan; *Mater.Res.Bull.*, **2013**, *48(10)*, 3707-3712.
28. L. Yu; J. Xi; H.T. Chan; T. Su; D.L. Phillips; W.K. Chan; *Phys.Chem. Chem.Phys.*, **2012**, *14(10)*, 3589-3595.

20. N. Gupta; H.P. Singh; R.K. Sharma; *J.Mol.Catal.A:Chem.,* **2011**, *335(1-2)*, 248-252.
21. K. Mallick; M. Witcomb; M. Scurrell; *Mater.Chem.Phys.*, **2006**, *97(2-3)*, 283-287.
22. Z.J. Jiang; C.Y. Liu; L.W. Sun; *J.Phys.Chem.B*, **2005**, *109(5)*, 1730-1735.
23. Y. Chen; C. Lu; L. Xu; Y. Ma; W. Hou; J.J. Zhu; *Cryst.Eng.Comm.,* **2010**, *12(11)*, 3740-3747.
24. V. Chandraboss; J. Kamalakkannan; S. Prabha; S. Senthilvelan; *RSC Adv.*, **2015**, *5(33)*, 25857-25869.
25. V. Fruth; M. Popa; D. Berger; C. Ionica; M. Jitianu; *J.Eur.Ceram.Soc.*, **2004**, *24(6)*, 1295-1299.
26. C. Barraclough; J. Lewis; R. Nyholm; *J.Chem.Soc.*, **1959**, *713*, 3552-3555.
27. V. Chandraboss; L. Natanapatham; B. Karthikeyan; J. Kamalakkannan; S. Prabha; S. Senthilvelan; *Mater.Res.Bull.*, **2013**, *48(10)*, 3707-3712.
28. L. Yu; J. Xi; H.T. Chan; T. Su; D.L. Phillips; W.K. Chan; *Phys.Chem. Chem.Phys.*, **2012**, *14(10)*, 3589-3595.

STUDIA UBB CHEMIA, LXVI, 1, 2021 (p. 73-88)
(RECOMMENDED CITATION)
DOI:10.24193/subbchem.2021.1.06

ALUMINUM PILLARED BENTONITE – CHARACTERIZATION AND SYNTHESIS OPTIMIZATION BY RESPONSE SURFACE METHODOLOGY

GABRIELA MUNTIANU[a*], ANDREI-IONUȚ SIMION[a*], CRISTINA-GABRIELA GRIGORAȘ[a], NICOLETA PLATON[a], ILEANA-DENISA NISTOR[a], GHEORGHIŢA JINESCU[b]

ABSTRACT. Bentonite is a clay mineral whose chemical structure can be easily modified by pillaring process for introduction of various cations such as aluminum, chromium, nickel, zinc etc. fact that conducts to attractive and versatile products suitable for diverse applications going from gas separation to pollutants removal or excipients for food industry for example.

This paper deals with the synthesis of aluminum pillared bentonite based on a process involving bentonite suspension and pillaring agent preparation, bentonite intercalation and calcination. The raw material and the obtained products were analyzed by X-ray diffraction, nitrogen adsorption-desorption technique, ammonia-temperature programmed desorption and scanning electronic microscopy. Three ratios of aluminum cations – amount of bentonite (5 mmol/g, 12.5 mmol/g, 20 mmol/g) and three calcination temperatures (300 °C, 400 °C, 500 °C) were used according to a Response Surface Methodology program aiming to attain the highest interlamellar distance, specific surface area and surface acidity. Collected data were fitted to second order polynomial equations. An aluminum cation – bentonite amount ratio of 12.5 mmol/g and a calcination temperature of 400 °C were found as appropriate conditions for bentonite pillaring process. Tests conducted on these settings showed that mathematical models were in good agreement with the experimental values presenting a high degree of accuracy.

Keywords: *bentonite, mathematical modelling, pillared clay, Response Surface Methodology*

[a] *"Vasile Alecsandri" University of Bacau, Department of Chemical and Food Engineering, 157 Calea Marasesti, 600115, Bacau, Romania*

[b] *Politehnica University of Bucharest, Department of Chemical and Biochemical Engineering, 1-7 Polizu, 011061, Bucharest, Romania*

**Corresponding authors: muntianu.gabriela@ub.ro, asimion@ub.ro*

INTRODUCTION

Clays are common natural minerals which, due to their specific properties [1, 2], are valuable in chemicals, pharmaceuticals, medical, cosmetics, ceramics, foods, agriculture or mining industries being used as catalysts [3], as drug carriers, gene vehicles [4], active ingredients or excipients [5], as intelligent food nanopackaging materials [6], as binding or dispersing agents, for clarification, deodorizing, neutralization and purification of petroleum products, removal of fats [7, 8] etc.

With layers consisting of one Al^{3+} octahedral sheet placed between two Si^{4+} tetrahedral sheets [9] and having montmorillonite as major constituent, raw bentonite is one of the most abundant 2:1 type clay minerals [10]. Depending on the more frequent encountered cation of crystal lattice, this material can be classified as sodium bentonite or as calcium bentonite [11]. It possesses high porosity, high specific surface, important hydration and swelling capacities, adsorption and ion exchange capacity etc. which make it suitable especially as adsorbent material for removal organic or inorganic polluting substances such as heavy metals [12, 13], dyes [14-16], chemicals [17, 18] etc. from wastewater, air or soil.

Bentonite adsorption capacity is based on two different mechanisms: *i)* an ion exchange reaction at permanent charged sites and *ii)* formation of complexes with surface hydroxyl groups [10, 19] and it can be enhanced by pillaring processes [9] which increase the basal spacing and adsorption surface area leading to more numerous active sites dispersed on the product surface [20].

The methods to modify the internal bentonite structure by pillaring in order to obtain three-dimensional microporous materials while maintaining the same thermal stable structure include: chemical modification (activation with mineral acids [21-23], alkaline activation, ion exchange etc.), physical modification (mechanic ways of operating on particle size), or thermal modification (also called thermal activation). The mentioned methods can be applied alone or in different combinations [24-26].

Final properties of the modified bentonite can be influenced by the selection of various work parameters. One of them is represented by the choice of cations used for pillaring process. Simple cations namely aluminum [25-29], iron, chromium [30, 31], nickel, zinc, magnesium, titan, copper, gallium [28, 30, 32, 33] and mixed cations such as aluminum – iron [31, 34], aluminum – chromium, aluminum – zirconium, aluminum – gallium [30, 33], aluminum – lanthanum – cerium, chromium – iron – zirconium or inorganic / organic compounds [32, 35] are successfully employed for this purpose.

The ratio of hydroxyl groups – metal (responsible for the material alkalinity) and the amount of cations reported at bentonite mass (metal/clay ratio) affect also the pillaring due to the fact that they control the *p*H value and the nature of cations species [32-34].

The final and the more important part of bentonite pillaring process is the thermal treatment achieved by calcination step to form fixed metal oxide pillars [35].

In this context, in the present paper, an experimental program was developed using different variations for two of the sodium bentonite pillaring process main parameters: aluminum cations – bentonite amount ratio and calcination temperature. The Response Surface Methodology was employed to establish the appropriate values of these parameters in order to achieve high basal spacing (also called interlamellar distance), an important specific surface area and a good surface acidity.

The raw material and the aluminum pillared bentonite were analyzed by X-ray diffraction, nitrogen adsorption-desorption technique, ammonia-temperature programmed desorption technique and by scanning electronic microscopy the registered results revealing that the obtained products possess properties making them suitable for various purposes (adsorption or catalysis being only two of them).

RESULTS AND DISCUSSION

Sodium bentonite and Al-PILCs characterization

X-ray diffractograms for sodium bentonite and for obtained aluminum pillared bentonites shown in Figure 1 reveal major changes in raw material structure after pillaring.

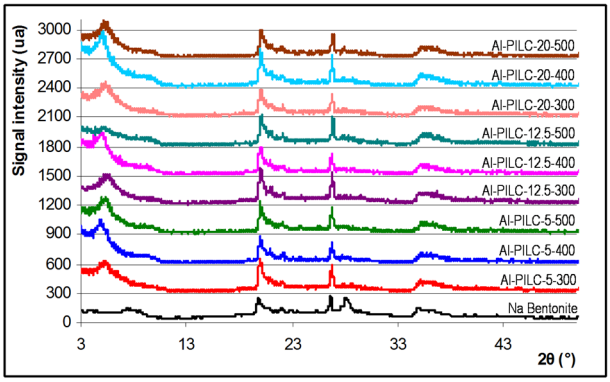

Figure 1. XRD patterns of sodium and Al-PILCs

With the help of Bragg's law applied on XRD data, the interlamellar distance was calculated for each pillared bentonite. According to values presented in Table 1, Al-PILCs obtained after calcination at 300 °C (Al-PILC-5-300, Al-PILC-12.5-300, Al-PILC-20-300) have low ID values of 1.65 – 1.7 nm which can be due to the fact that, at this temperature, the oxido-metallic pillars are not completely formed. The highest basal spacing (1.78 – 1.79 nm) was recorded for samples treated at 400 °C (Al-PILC-5-400, Al-PILC-12.5-400, Al-PILC-20-400). In these cases, the d_{001} peaks are relatively uniform which signifies that the pillaring process took place and led to rigid and homogeneous distributed pillars. At the temperature of 500 °C, aluminum pillared bentonite samples (Al-PILC-5-500, Al-PILC-12.5-500, Al-PILC-20-500) presented also lower ID values (1.66 – 1.67 nm). Moreover, characteristic peaks for pillared bentonite disappeared and the obtained products had tendencies to become amorphous.

Table 1. Experimental and predicted results obtained for Al-PILCs

Run	***Experimental code***	***ID [nm] (Mean ± Standard Deviation)***	
		Experimental results	***Predicted results***
1	Al-PILC-5-300	1.65 ± 0.0058	1.64
2	Al-PILC-5-400	1.78 ± 0.0076	1.79
3	Al-PILC-5-500	1.67 ± 0.0153	1.68
4	Al-PILC-12.5-300	1.64 ± 0.0321	1.65
5	Al-PILC-12.5-400	1.79 ± 0.0473	1.79
6	Al-PILC-12.5-500	1.70 ± 0.0153	1.69
7	Al-PILC-20-300	1.63 ± 0.0173	1.63
8	Al-PILC-20-400	1.78 ± 0.0100	1.77
9	Al-PILC-20-500	1.66 ± 0.0503	1.67

Run	***Experimental code***	***S^{BET} [m^2/g] (Mean ± Standard Deviation)***	
		Experimental results	***Predicted results***
1	Al-PILC-5-300	100.12 ± 0.5460	95.39
2	Al-PILC-5-400	129.05 ± 0.0289	134.62
3	Al-PILC-5-500	102.23 ± 0.7312	101.39
4	Al-PILC-12.5-300	104.63 ± 0.5056	111.17
5	Al-PILC-12.5-400	146.30 ± 0.6807	140.98
6	Al-PILC-12.5-500	99.55 ± 0.5008	98.33
7	Al-PILC-20-300	133.97 ± 0.5600	132.16
8	Al-PILC-20-400	152.80 ± 0.5292	152.55
9	Al-PILC-20-500	98.40 ± 0.2309	100.47

Run	*Experimental code*	*SA [mmol H^+/g] (Mean ± Standard Deviation)*	
		Experimental results	*Predicted results*
1	Al-PILC-5-300	0.339 ± 0.0055	0.348
2	Al-PILC-5-400	0.406 ± 0.0561	0.401
3	Al-PILC-5-500	0.222 ± 0.0053	0.218
4	Al-PILC-12.5-300	0.384 ± 0.0035	0.374
5	Al-PILC-12.5-400	0.437 ± 0.0051	0.431
6	Al-PILC-12.5-500	0.236 ± 0.0081	0.252
7	Al-PILC-20-300	0.390 ± 0.0058	0.391
8	Al-PILC-20-400	0.443 ± 0.0051	0.454
9	Al-PILC-20-500	0.291 ± 0.0061	0.279

Our data are consistent with those reported by Xu *et al.* [20] and by Gil *et al.* [36]. They show that when a temperature of 200-300 °C is used, the polycations are dehydrated. At temperatures between 300 °C and 600 °C, the polycations are dehydroxylated and the obtained materials possess a microporous [37] and rigid structure provided by formed oxido-metallic pillars separating adjacent silicate arrangements and thus increasing the distance between the bentonite layers. Chae *et al.* [38] stipulate that at higher temperatures (more than 700 °C), the resulted pillared products are progressively and irreversibly degraded and they cannot be used for retention processes.

Textural characteristics of sodium bentonite and Al-PILCs were determined by nitrogen adsorption/desorption isotherms at temperature of 350.45 °C. The results for raw material and for the three Al-PILCs having the highest interlamellar distances (Al-PILC-5-400, Al-PILC-12.5-400 and Al-PILC-20-400) are depicted in Figure 2. They were compared with the standardized forms proposed by International Union of Pure and Applied Chemistry (IUPAC) and they are similar type IV with H1 hysteresis this shape being encountered in materials that contain mainly mesoporous and small amounts of microporous particles. Between 0.02 and 0.03, the p/p_0 domain is occupied with nitrogen molecules. After the inflection point, the molecules adsorption is carried in mono molecular and poly molecular layers. Nitrogen capillary condensation begins in mesoporous zone and the hysteresis is evidenced in p/p_0 domain of 0.4 to 0.5. PILCs adsorption capacity fallows the sequence Al-PILC-20-400 > Al-PILC-12.5-400 > Al-PILC-5-400 being considerably greater than that of the natural bentonite.

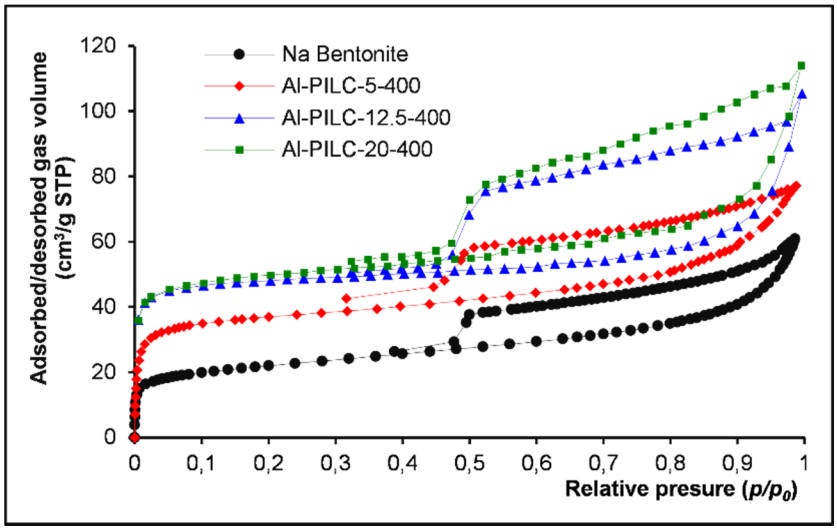

Figure 2. Nitrogen adsorption-desorption isotherms of raw and pillared sodium bentonite

From data summarized in Table 1, a significant S^{BET} amplification can be remarked compared to that of sodium bentonite which was of 31.1 m^2/g. When an aluminum cations – bentonite amount ratio of 5 mmol/g was used for pillaring process, the Al-PILCs specific surface areas were the lowest ones (100.12 m^2/g for Al-PILC-5-300) while the increase of this ratio to 12.5 mmol/g or to 20 mmol/g led to important S^{BET} augmentation (more than 146.30 m^2/g for Al-PILC-12.5-400 and more than 152.80 m^2/g for Al-PILC-20-400). In terms of calcination, the obtained results are consisting with the idea that the appropriate temperature for sodium bentonite pillaring process is of 400 °C since the best specific surface area (of 152.80 m^2/g) was registered for Al-PILC-20-400.

Beside to the high porosity, the prepared PILCs possess also an intensified surface acidity due to bentonite structure modification by the aluminum oxide pillars. Acid centers interact with ammonia in order to form NH_4^+ ions which fixe to the bentonite surface leading to a SA going from 0.222 mmol H^+/g for Al-PILC-5-500 to a least double one (0.443 mmol H^+/g for Al-PILC-20-400) of that recorded for initial sodium bentonite (0.180 mmol H^+/g).

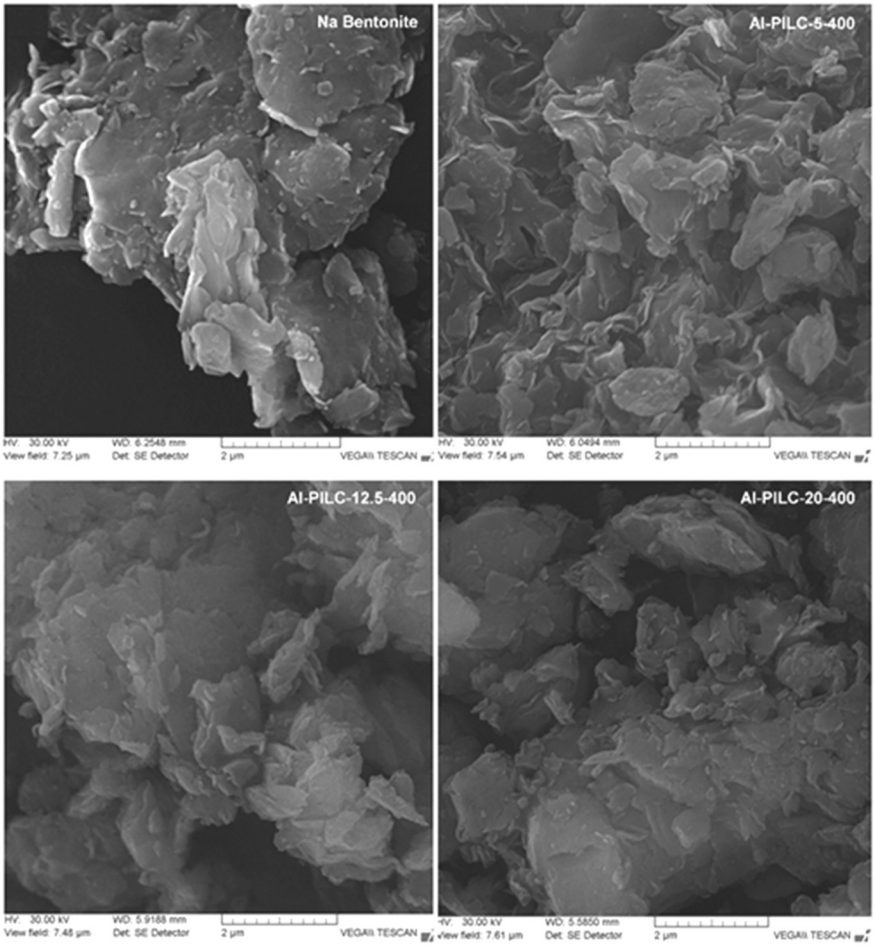

Figure 3. SEM micrographs of raw sodium bentonite and pillared materials

Similar results were emphasized also by other researches. Aluminum cations in pillaring agent insures higher molecular weight species that provide hydrothermal stability of pillared clays [39]. The nature of pillaring agent strongly depends of OH/metal ratio ($0.5 < OH/Al^{+3} < 2.5$) affecting the micropore volume and the surface area of pillared clay [37]. The Al^{+3}/g clay ratio plays a determinant role in the future properties of the obtained materials. For 30 and 90 mmol Al^{+3}/g clay the microporosity increases. At a Al^{+3}/g clay ratio of 180 mmol, an excess of aluminum oxide is introduced between the clay layers and, in spite, of a large distance, the micropore volume and area decreased [40].

Regarding the materials morphology, SEM images illustrated in Figure 3 show a clear evolution caused by the pillaring process.

The initial sodium bentonite presents a stratified, lamellar structure with visible layers mixed with big aggregates while in Al-PILCs products, the morphology is changed due to the aluminum greater amounts. The particles are smaller, finer and clearer and tend to form aggregates with a porous structure. These findings can be explained by the fact that the physio-chemical properties including microporosity of pillared clay increased with aging time of the pillaring solution due to the transformation of Al_{13} into $Al_{24}O_{72}$ (Al_{13} dimer) and other polynuclear cations [37, 41, 42]. It can be applied both for pillaring agent and for intercalated bentonite and consists of letting the reaction media to rest in a dark place at temperatures between 15 °C and 90 °C for periods going from one hour to one week in which the pillaring agent reacts with solution anions by hydrolysis, polymerization and complexation.

The obtained Al-PILCs structure sustains the possibility of materials ability to retain different molecules between their layers insuring by consequence the possibility to use them to different purposes one of them being as pollutants adsorbents.

Experimental design and optimization

Based on the experimental data and with the help of Expert Design 7.0 software, the obtained second order polynomial equations for three studied functions (ID, S^{BET}, SA) as affected by aluminum cations – bentonite amount ratio and calcination temperature parameters are presented below.

$$ID = 1.79 - 0.0058 \cdot A + 0.018 \cdot B + 0.0025 \cdot A \cdot B - 0.014 \cdot A^2 - 0.13 \cdot B^2 \quad (1)$$

$$S^{BET} = 140.98 + 8.96 \cdot A - 6.42 \cdot B - 9.42 \cdot A \cdot B + 2.60 \cdot A^2 - 36.23 \cdot B^2 \quad (2)$$

$$SA = 0.43 + 0.026 \cdot A - 0.061 \cdot B + 0.0045 \cdot A \cdot B - 0.0038 \cdot A^2 - 0.12 \cdot B^2 \quad (3)$$

In equations 1-3, the negative and positive signs of the coefficients indicate the effect of the studied parameters on the considered response.

Table 2 synthesizes the results of the quadratic model fitting in the form of analysis of variance (ANOVA).

Table 2. ANOVA for response surface quadratic models

Statistical parameter	***Response functions***		
	ID	S^{BET}	*SA*
p-value	0.0054	0.0054	0.0057
F-value	42.8742	16.6318	41.5201
Determination coefficient (R^2)	0.98619	0.96518	0.98575
Adjusted determination coefficient (Adj-R^2)	0.96319	0.90714	0.96201
Predicted determination coefficient (Pred. Adj. R^2)	0.83774	0.65388	0.83281
Coefficient of variation (CV), %	0.74854	5.64396	4.62402
Adequate Precision	16.11585	10.46069	17.85821
Predicted residual error sum of squares (PRESS)	0.00571	1335.27637	0.00921

The *p*-values inferior of 0.05 point out that the models terms are significant. The calculated *F*-values for the regressions were much greater than the values from Fisher tables ($F_{5, 3}$ = 9.01, for a 95% confidence level), confirming that the models fit to the experimental data. For all the established equations, there are only reduced chances that *F*-values this large could occur due to noise.

The determination coefficients R^2 of the quadratic regression models were close to unit indicating how much of the variability in data can be explained by the mathematical equations. The adjusted determination coefficient (Adj-R^2) which measures also the models goodness of fit has values were close to the corresponding determination coefficients values. The predicted determination coefficients for all the studied response functions are in reasonable agreement with the Adj-R^2.

At the same time, the low values of the coefficients of variation imply that the variation in the mean values were acceptable. Furthermore, adequate precision measures the signal to noise ratio and a ratio greater than 4 is generally desirable and designate satisfactory signals for the models to be used to navigate the design space.

The predicted residual sum of squares (PRESS) cross-validation technique identifies the model with better prediction. Its lower values sustain this hypothesis for ID and SA response functions. The high PRESS for S^{BET} could be explained by the fact that the model does not fit very well the edges of the studied domain. For example, if the experimental data recorded for Al-PILC-5-300 is ignored in the model generation process, the PRESS descends to 365.20846. In the same time, better results can be obtained for R^2 (0.99442), Adj-R^2 (0.98048), Pred. Adj. R^2 (0.89491) and for coefficient of variation (2.57534 %). Nonetheless, since in both cases, the calculated

relative error between the experimental data and those generated by the proposed equations is lower than 6 % for the Al-PILC-5-300 run, it can be considered that both the mathematical models express a good accuracy.

The three-dimensional response surface plots obtained from the RSM – CCD equations are illustrated in Figure 4. As it can be seen from this figure, both aluminum cations – bentonite amount ratio and calcination temperature affect the bentonite pillaring process. One can observe that an increase of the aluminum cations – bentonite amount ratio and of the calcination temperature from the 5 to 20 mmol/g and from 300 to 400 °C respectively impairs positively the values of the response functions while a temperature higher than 400 °C has a negative impact.

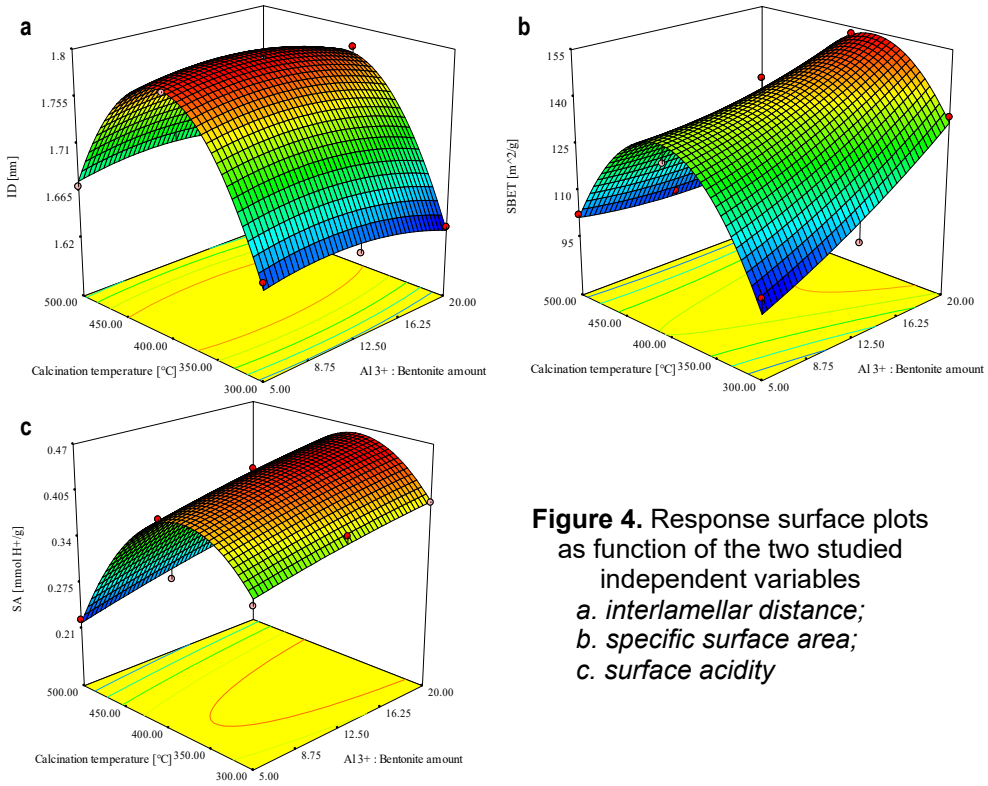

Figure 4. Response surface plots as function of the two studied independent variables
a. interlamellar distance;
b. specific surface area;
c. surface acidity

The developed mathematical models permitted to found the optimum values for the studied parameters as being 19.85 mmol/g for aluminum cations – bentonite amount ratio and 396.25 °C for the calcination temperature.

In these conditions, according to data furnished by the software, a maximum interlamellar distance of 1.77 nm, a specific surface area of 152.08 m^2/g and a surface acidity of 0.45 mmol/g H^+ could be obtained. Even though, while it is recommended to use a temperature of 400 °C for the calcination step, for aluminum cations – bentonite amount ratio a lower value of 12.5 mmol/g could be considered for two different reasons: firstly, because very similar values can be attained for the followed response functions and secondly, especially for economic causes. In this last case, the pillaring process is easier to handle because it implies the use of lower volumes of reagents and of prepared solutions and, in the same time, the entire procedure is less time and energy consuming.

Several experiments were carried using the stipulated optimal factors. The results (1.8 ± 0.0152 nm for ID; 145 ± 1.2678 m^2/g for S^{BET} and 0.439 ± 0.0032 mmol H^+/g for SA) revealed that the mathematical hypothesis is in a good agreement with the collected real data.

MATERIALS AND METHODS

Reagents

Hexahydrate aluminum chloride ($AlCl_3$ 6 H_2O), sodium hydroxide (NaOH) and silver nitrate ($AgNO_3$) involved as reagents in the experiments were of analytical grade and were purchased from PanReac AppliChem ITW Reagents (Germany), Lach-Ner (Czech Republic) and respectively from Chemical Company (Romania).

Sodium bentonite with a bulk density of 2400 kg/m^3, with 5 % humidity and particle size of 2 μm was supplied by Sigma Aldrich Romania and it was used as received, without purification and pretreatment.

In order to check their reproducibility, all the described analysis were carried out in triplicate and presented as mean values.

Sodium bentonite characterization

Sodium bentonite structure and interlamellar distance (ID) (d_{001}) were examined by X-ray diffraction (XRD) with a Siemens D5000 Diffractometer (Cu-K_α) (LabX, Canada) on a 2θ range between 3° and 50° with 0.02° step size using a 30 mA current and a 40 kV voltage.

Its adsorption/desorption isotherms and its specific surface area (S^{BET}) were determined by *Brunauer*, *Emmet* and *Teller* (BET) analysis performed with a Beckman Coulter SA 3100 Surface Area Analyser (Beckman Coulter GmbH, Germany). Prior to the analysis, the sample was degassed at 120 °C for 4 hours in order to eliminate any impurities and water traces. The studied gas was nitrogen of 99.9 % purity at a temperature of 350.45 °C.

Surface acidity (SA) was determinate by ammonia-temperature programmed desorption method. With the help of a gas carrier (nitrogen), ammonia vapors passed for 10 minutes through the aliquots of 0.2 g bentonite fixed bed. The sample was than repeatedly washed with nitrogen to remove the physiosorbed ammonia. Desorption step was carried out between 150 °C and 500 °C. The surface acidity was established as being the total ammonia amount desorbed per gram of bentonite.

Scanning electronic microscopy (SEM) analyses, realized with a Vega Tescan LSH II equipment (Tescan Orsay, France), was employed for sodium bentonite morphological characterization.

Aluminum pillared bentonite (Al-PILC) synthesis

For pillaring agent preparation, a 0.2 mol/L hexahydrate aluminum hydroxide solution was introduced in a Berzelius flask placed on a Nahita Blue 692 magnetic stirrer (Auxilab, Spain) set at 600 rpm, at room temperature. A 0.2 mol/L sodium hydroxide solution was added at constant flow of 1 mL/min in order to avoid aluminum hydroxide precipitation known as affecting the pillaring agent quality. The basicity relationship OH^-/Al^{+3} was maintained constant at a value of 2.2. The *p*H was adjusted at 4 with sodium hydroxide using a *p*H meter 315i Set (WTW, Germany).

A 2 % (w/w) bentonite suspension was prepared with distilled water and stirred for 2 hours at 800 rpm.

Resulted pillaring agent was added, drop by drop, at the same constant flow of 1 mL/min, into the bentonite suspension under agitation at 800 rpm, at room temperature. The obtained intercalated bentonite was let to rest for 12 hours for aging in a dark place and separated from the pillaring agent solution by simple decantation. The resulting bentonite slurry was repeatedly washed with distilled water. The removal efficiency of undesirable constituents was considered satisfactory when no precipitation was registered in the presence of silver nitrate.

The intercalated bentonite was then filtrated under vacuum and submitted to stabilization by drying at 120 °C for 4 hours in an Air Performance AP60 drying oven (Precisa, Romania) and calcinations for 2 hours at different temperatures using a Caloris L1003 laboratory furnace (Caloris Group, Romania).

Al-PILCs characterization

The obtained products were analyzed using the same methods and conditions as those specified for raw material characterization (see dedicated section previously presented).

Experimental design and optimization

The optimization of two of the main parameters influencing the bentonite pillaring process was conducted using a RSM costumed Central Composite Design (CCD). Design Expert 7.0 software was employed for experimental program setup, data analysis, mathematical model development and graph plotting. The different levels of variation tested are presented in Table 3.

Table 3. Experimental setup used for Al-PILCs

Run	*Experimental code*	*Aluminum cations - amount ratio*		*Calcination temperature*	
		Variation levels	*Real values [mmol/g]*	*Variation levels*	*Real values [°C]*
1	Al-PILC-5-300	- 1	5.0	- 1	300
2	Al-PILC-5-400	- 1	5.0	0	400
3	Al-PILC-5-500	- 1	5.0	1	500
4	Al-PILC-12.5-300	0	12.5	- 1	300
5	Al-PILC-12.5-400	0	12.5	0	400
6	Al-PILC-12.5-500	0	12.5	1	500
7	Al-PILC-20-300	1	20.0	- 1	300
8	Al-PILC-20-400	1	20.0	0	400
9	Al-PILC-20-500	1	20.0	1	500

Three studied response functions (interlamellar distance, specific surface area and surface acidity) were fitted with second order polynomial models expressed in the equation (4):

$$Y = a + b \cdot A + c \cdot B + d \cdot A \cdot B + e \cdot A^2 + f \cdot B^2 \quad (4)$$

where *Y* is the response function; *a* is the equation intercept, *b* and *c* are the linear coefficients, *d* is the cross-coefficient, *e* and *f* are the quadratic coefficients; *A* is the coded value for aluminum cations – bentonite amount ratio; *B* is the coded value for calcination temperature.

CONCLUSIONS

Sodium bentonite was used in this study as raw material for obtaining aluminum pillared materials. To this purpose, a process including bentonite suspension and pillaring agent preparation, bentonite intercalation and product stabilization was conducted in different experimental conditions.

Aluminum cations – bentonite amount ratio and calcination temperature were varied between 5 mmol/g and 20 mmol/g and between 300 °C and 500 °C according to a response surface methodology program. Both initial sodium bentonite and pillared clays were analyzed by X-ray diffraction, nitrogen adsorption-desorption technique, ammonia-temperature programmed desorption and scanning electronic microscopy and the resulted data were employed to develop mathematical models. A ratio of 12.5 mmol/g aluminum cations – bentonite amount and a calcination temperature of approximately 400 °C were found as appropriate for the clay pillaring process. In these conditions, the acquired interlamellar distance was of 1.79 nm, the specific surface area was of 146.3 m^2/g and the surface acidity attained 0.43 mmol H^+/g all the followed response functions having values considerable higher than those of the used raw material indicating that the established models were accurate presenting high confidence levels.

REFERENCES

1. A.V. Ursu; G. Jinescu; F. Gros; I.D. Nistor; N.D. Miron; G. Lisa; M. Silion; G. Djelveh; A. Azzouz; *J. Therm. Anal. Calorim.*, **2011**, *106(3)*, 965-971.
2. F. Rouquerol; J. Rouquerol; K. Sing; *Adsorption by powders and porous solids. Principles, methodology and applications,* Academic Press, London, **1999**, pp. 357-378.
3. R.A. Schoonheydt; *Appl. Clay Sci.*, **2016**, *131*, 107-112.
4. C.H. Zhou; L.Z. Zhao; A.Q. Wang; T.H. Chen; H.P. He; *Appl. Clay Sci.*, **2016**, *119*, 3-7.
5. P.S.C. Silva; S.M.B. Oliveira; L. Farias; D.I.T. Fávaro; B.P. Mazzilli; *Appl. Clay Sci.*, **2011**, *52(1)*, 145-149.
6. T.J. Gutiérrez; A.G. Ponce; V.A. Alvarez; *Mater. Chem. Phys.*, **2017**, *194*, 283-292.
7. J. Konta; *Appl. Clay Sci.*, **1995**, *10(4)*, 275-335.
8. F.J. Galindo-Rosales; F.J. Rubio-Hernández; *Appl. Clay Sci.*, ***2006***, *33(2)*, 109-115.
9. L. Gu; J. Xu; L. Lv; B. Liu; H. Zhang; X. Yu; Z. Luo; *Desalination*, **2011**, *269(1)*, 206-213.
10. M. El Bouraie; A.A. Masoud; *App. Clay Sci.*, **2017**, *140*, 157-164.
11. Z. Vryzas; V.C. Kelessidis; L. Nalbantian; V. Zaspalis; D.I. Gerogiorgis; Y. Wubulikasimu; *Appl. Clay Sci.*, **2017**, *136*, 26-36.
12. M.K. Uddin; *Chem. Eng. J.*, **2017**, *308*, 438-462.
13. J.N. Putro; S.P. Santoso; S. Ismadji; Y.-H. Ju; *Microporous Mesoporous Mater.*, **2017**, *246*, 166-177.

14. I. Belbachir; B. Makhoukhi; *J. Taiwan Institute Chem. Eng.*, **75**, 2017, 105-111.
15. N. Belhouchat; H. Zaghouane-Boudiaf; C. Viseras; *Appl. Clay Sci.*, **2017**, ***135***, 9-15.
16. X. Liang; Y. Lu; Z. Li; C. Yang; C. Niu; X. Su; *Microporous Mesoporous Mater.*, **2017**, *241*, 107-114.
17. K. Styszko; K. Nosek; M. Motak; K. Bester; *C. R. Chim.*, **2015**, *18(10)*, 1134-1142.
18. J. Fan; W. Yang; A. Li; *React. Funct. Polym.*, **2011**, *71(10)*, 994-1000.
19. T. Ngulube; J.R. Gumbo; V. Masindi; A. Maity; *J. Environ. Manag.*, **2017**, *191*, 35-57.
20. T. Xu; Y. Liu; F. Ge; L. Liu; Ouyang, Y., *Appl. Surf. Sci.*, **2013**, *280*, 926-932.
21. A.V. Ursu; C. Jinescu; I.D. Nistor; V.A. Aruș; G. Isopencu; M.A. Mareș; *Rev. Chim.*, **2010**, *(61)12*, 1226-1230.
22. S. Nousir; V.A. Aruș; T.C. Shiao; N. Bouazizi; R. Roy; A. Azzouz; *Microporous and Mesoporous Mater.*, **2019**, *290*, DOI: 10.1016/j.micromeso.2019.109652.
23. F. Boudissa; D. Mirilă; V.A. Aruș; T. Terkmani; S. Semaan; M. Proulx; I.D. Nistor; R. Roy; A. Azzouz; *J. Hazard. Mater.*; **2019**, *364(15)*, 356-366.
24. R.A. Schoonheydt; T. Pinnavaia; G. Lagaly; N. Gangas; *Pure Appl. Chem.*, **1999**, *71(12)*, 2367-2371.
25. R.A. Schoonheyat; T. Pinnavia; G. Lagaly; N. Gangas; *Pure Appl. Chem.*, **1999**, *71*, 2367-2371.
26. S. Nousir; V.A. Aruș; T.C. Shiao; N. Bouazizi; R. Roy; A. Azzouz; *Microporous Mesoporous Mater.*, **2019**, *290*, 109652.
27. G. Muntianu; N. Platon; A. Mardaru; I.D. Nistor; N.D. Miron; G. Jinescu; *U.P.B. Sci. Bull., Series B*, **2015**, *77(3)*, 151-164.
28. D.C. Mirilă; M.Ș. Pîrvan; N. Platon; A.M. Georgescu; V. Zichil; I.D. Nistor; *Acta Chem. Iași*, **2018**, *26(2)*, 263-280.
29. R. Azzallou; R. Mamouni; Y. Riadi; M. El Haddad; Y. El Mouzdahir; R. Mahboub; A. Elmchaouri; S. Lazar; G. Guillaumet; *Rev. Chim.*, **2010**, *61(12)*, 1155-1157.
30. A.-M. Georgescu; G. Brabie; I.D. Nistor; C. Penot; F. Nardou; *J. Porous Mater.*, **2015**, *22(4),* 1009-1019.
31. D.C. Mirilă; M.S. Pârvan; A.M. Roșu; V. Zichil; I.D. Nistor: *Sci. St. Res. Chem. Chem. Eng. Biotechnol. Food Ind.*, **2018**, *19(1)*, 63-72.
32. M.L. Chavez-Garcia; L. De Pablo-Galan; M.P. Saucedo-Ramirez; *J. Mex. Chem. Soc.*, **2006**, *50(1)*, 36-41.
33. P. Cañizares; J.L. Valverde; M.R. Sun Kou; C.B. Molina; *Microporous Mesoporous Mater.*, **1999**, *29(3)*, 267-281.
34. J.T. Kloprogge; L.V. Duong; R.L. Frost; *Environ. Geol.*, **2005**, *47(7)*, 967-981.
35. S. Sivakumar; S.K. Ghosh; A.D. Damodaran; K.G.K. Warrier; *Mater. Lett.*, **1997**, *31(1)*, 113-118.
36. S. Vercauteren; J. Luyten; R. Leysen; E.F. Vansant; *J. Membr. Sci.*, **1996**, *119(1)*, 161-168.
37. A.A.G. Tomlinson; *J. Porous Mater.*, **1998**, *5(3)*, 259-274.
38. A. Gil; L.M. Gandía; *Chem. Eng. Sci.*, **2003**, *58(14)*, 3059-3075.

39. H.J. Chae; I.-S. Nam; S.W. Ham; S.B. Hong; *Catal. Today*, **2001**, *68(1)*, 31-40.
40. M.N. Timofeeva; S.T. Khankhasaeva; Y.A. Chesalov; S.V. Tsybulya; V.N. Panchenko; E.T. Dashinamzhilova; *Appl. Catal., B*, **2009**, *88(1)*, 127-134.
41. A. Gil; M. Montes; *Langmuir*, **1994**, *10(1)*, 291-297.
42. A.-M. Georgescu; F. Nardou; I.D. Nistor; *Sci. Study Res. Chem. Chem. Eng., Biotechnol., Food Ind.*, **2016**, *17(3)*, 261-269.

STUDIA UBB CHEMIA, LXVI, 1, 2021 (p. 89-104)
(RECOMMENDED CITATION)
DOI:10.24193/subbchem.2021.1.07

MODELING AND SIMULATION OF PRESSURE, TEMPERATURE AND CONCENTRATION FOR THERMAL EXPLOSIONS

OLIMPIA BUNTA[a], MIHAELA-LIGIA UNGUREŞAN[b,*], VLAD MUREŞAN[c], OVIDIU STAN[c]

ABSTRACT. In this paper is presented a simple possible model which can explain the thermal explosion problem, the existence of an induction period and a sudden rapid temperature rise. As state variables used for modeling are: the pressure, the temperature and the concentration. The time evolutions of these state parameters are analogically modeled using ordinary differential equations. The numerical simulations of the obtained model are made in Matlab/Simulink™. The validation of the model is realized by comparison between experimental data and simulation results, presenting a good accuracy.

Keywords: *thermal explosion, analogical modeling, numerical simulation, state Parameters*

INTRODUCTION

Thermal explosions are events of high complexity which typically involve several processes from the fields of chemistry and physics, such as temperature rises [1], expansion, phase transition, chemical processes and reactions, and finally momentum transfer [2]. The analysis of an explosion phenomena may involve the description of the physical and chemical initial states of the material, its rate of heating, rate of decomposition kinetics [3], changes in the chemical and mechanical explosive properties, rate of burning, transfer rate of explosive energy into thermal and mechanical energy (hydrodynamics), and, finally, amount of damage (violence) [4,5].

[a] *Iuliu Hatieganu University of Medicine and Pharmacy, Orthodontics Department, 31 Avram Iancu st., 400117, Cluj-Napoca, Romania*
[b] *Technical University of Cluj-Napoca, Physical and Chemistry Department, 103-105 Muncii st., 400641, Cluj-Napoca, Romania*
[c] *Technical University of Cluj-Napoca, Department of Automation, 15 C-tin Daicoviciu st., 400020, Cluj-Napoca, Romania*
** Corresponding author: mihaela.unguresan@chem.utcluj.ro*

In a thermal explosive reaction, the rate of reaction rapidly varies with temperature and the moment of explosion takes place at some finite temperature [6,7].

The value of the critical temperature, below which the thermal explosion of a chemical cannot occur, is indispensable to prevent such a chemical from exploding. To determine the critical temperature, it has so far been necessary to measure the value in explosion experiments [8].

The problem of the critical regimes evaluation, perceived as separating regimes of the explosive regions and nonexplosive ways of the chemical reactions, is the most important mathematical aspect within the thermal explosion theory. Many authors, such as N. N. Semenov [9], D. A. Frank-Kamenetsky [10], O. M. Todes and P. V. Melent'ev [11], A. G. Merzhanov and F. I. Dubovitsky [12], B. Grey [13], have investigated the critical phenomena of the thermal explosion theory.

A solution for modelling the real phenomena, including, using fractional order differential equations (which can describe the mathematical models of the fractional order systems), is presented.[14] The fractional order models have the main advantage of generating a wider spectrum of possible approximations for the behaviour of the approached phenomena. This aspect implies the possibility to obtain more accurate models than using integer order models. However, the fractional order models have to main disadvantages: firstly, these types of models present more parameters than the integer order ones, fact that make the identification of the approached phenomena dynamics more difficult (the applied identification methods are based, mainly, on iterative algorithms); secondly, the numerical simulation of fractional order models involve complex problems (the necessity of their approximation using integer order models occurs, using, for example, the Oustoloup filter, but the resulted approximation have, in general, significantly high orders, their simulation becoming laborious), aspect which make difficult their usage in practice.

Some interesting dependency functions between the parameters of the phenomenon of recombination of Oxygen and nitrogen atoms on quartz are presented in [15]. However, the proposed functions, describing static mathematical dependences, cannot be used for the accurate modelling of the explosion dynamics. In [16], a predictive modelled is used for the lower flammability limits of $H_2/O_2/CO_2$ mixture in order to prevent the explosion.

Examples of analytically determined mathematical models based on usage of ordinary differential equations and partial differential equations.[17] However, these models are valid for particular types of thermal explosions and, in the case when experimental data are available, their usage questionable.

In this paper, an original and general method for the modelling and simulation of the thermal explosions is presented. The numerical simulation method based on Taylor series generates high accuracy and it can be efficiently applied both if the considered thermal explosion is modelled as lumped parameter process or as distributed parameter model. In the case of modelling the explosions as lumped parameter models, the ordinary differential equations are use and in the case of modelling the explosions as distributed parameter models, the partial differential equations are used. The proposed method is efficient in the case when experimental data must be used in the modelling procedure. To prove the proposed method efficiency, the case of thermal explosion of oxyhydrogen gas initiated by the wall of a quartz reactor [18] is considered.

RESULTS AND DISCUSSION

Mathematical modeling

It is a known fact that the usual linear processes can be expressed through the following analytical model:

$$\dot{\mathbf{x}} = \mathbf{A}\mathbf{x} + \mathbf{B}\mathbf{u} \tag{1}$$

$$\mathbf{y} = \mathbf{C}\mathbf{x} + \mathbf{D}\mathbf{u} \tag{2}$$

where: **u** = **u**(t), **x** = **x**(t) and **y** = **y**(t) represent the input, the state and the output vectors, and (**A**), (**B**), (**C**), and (**D**) correspond to the state, the input-state, the state-output, and the input-output matrix. The matrices are constant if the process is time invariant and variable if the process varies in time. The initial conditions (IC), for t = t_0, respectively $\mathbf{x}_{IC}$ = **x**(t_0) are known. In the hypothesis in which the known **u** = **u**(t) input vector presents a continuous evolution in relation to time, the solution in its vectorial form (1) of the ordinary differential equation (ode), respects the conditions of continuity of the Cauchy sense.

Taking into consideration a limited number of successive derivatives which consider the time variable for (1), respectively:

$$\dot{\mathbf{x}} = \mathbf{A}\mathbf{x} + \mathbf{B}\mathbf{u} \tag{3}$$

$$\ddot{\mathbf{x}} = \dot{\mathbf{A}}\mathbf{x} + \mathbf{A}\dot{\mathbf{x}} + \dot{\mathbf{B}}\mathbf{u} + \mathbf{B}\dot{\mathbf{u}} \tag{4}$$

$$\dddot{\mathbf{x}} = \ddot{\mathbf{A}}\mathbf{x} + 2\dot{\mathbf{A}}\dot{\mathbf{x}} + \mathbf{A}\ddot{\mathbf{x}} + \ddot{\mathbf{B}}\mathbf{u} + 2\dot{\mathbf{B}}\dot{\mathbf{u}} + \mathbf{B}\ddot{\mathbf{u}} \tag{5}$$

$$\ddddot{\mathbf{x}} = \dddot{\mathbf{A}}\mathbf{x} + 3\ddot{\mathbf{A}}\dot{\mathbf{x}} + 3\dot{\mathbf{A}}\ddot{\mathbf{x}} + \mathbf{A}\dddot{\mathbf{x}} + \dddot{\mathbf{B}}\mathbf{u} + 3\ddot{\mathbf{B}}\dot{\mathbf{u}} + 3\dot{\mathbf{B}}\ddot{\mathbf{u}} + \mathbf{B}\dddot{\mathbf{u}} \tag{6}$$

It can be observed that ($\dot{\mathbf{x}}$) in (4) derives from (3), ($\ddot{\mathbf{x}}$) in (5) derives from (4), and finally ($\dddot{\mathbf{x}}$) in (6) derives from (5), and so on, which simplifies the operation of progressive derivatives which regard the time variable of the state vector (**x**).

The present paper proposes the method of the complete Taylor series for the numerical estimation of the ($\mathbf{x}_k$) vector:

$$\mathbf{x_k} \cong \mathbf{x_{k-1}} + \sum_{m=1}^{\omega} \frac{\Delta t^m}{m!} \overset{(m)}{\mathbf{x}}_{k-1} \tag{7}$$

The right side of the equation is considered at the $t_{k-1} = (k-1)\cdot\Delta t$ moment, where (k-1) stands for the regressive sequence, and the sufficiently undersized (Δt), stands for the integration step. Therefore, the estimated solution at the $t_k = k\cdot\Delta t$ moment, where (k) represents the current sequence, corresponds to:

$$x_k \cong x_{k-1} + \sum_{m=1}^{\omega} \frac{\Delta t^m}{m!} (A \cdot x_{(k-1)}^{(m-1)} + B \cdot u_{(k-1)}^{(m-1)}) \tag{8}$$

where (ω) marks the maximum derivatives number with respect to the time variable, which limits the truncated evolution of the Taylor series, for the situation of the minimal $\omega \geq 2$ condition. Obviously: $\mathbf{u}_{k-1} = \mathbf{u}(t_{k-1})$, $\mathbf{x}_{k-1} = \mathbf{x}(t_{k-1})$, $\mathbf{x}_k = \mathbf{x}(t_k)$, and $u_{(k-1)}^{(m-1)} = \left[\frac{d^{m-1}}{dt^{m-1}}(u)\right]_{k-1}$, $x_{(k-1)}^{(m-1)} = \left[\frac{d^{m-1}}{dt^{m-1}}(x)\right]_{k-1}$ respectively with the remark that for m = 1, respectively (m - 1) = (0), correspond $\overset{(0)}{\mathbf{u}}_{k-1} = \mathbf{u}_{k-1}$ and $\overset{(0)}{\mathbf{x}}_{k-1} = \mathbf{x}_{k-1}$.

In order to ensure the starting of the calculation, at the initial $t_0 = t_{k-1}$, respectively k = 1 moments, the investigated initial conditions are expressed by using the ($\mathbf{x}_0$) state vector, to which the ($\mathbf{u}_0$) input vector is associated.

The vector ($\mathbf{x}_k$) approximated at the $t_k = k\cdot\Delta t$ moment, corresponds to:

$$\mathbf{x}_k \cong \mathbf{x}_{k-1} + \frac{\Delta t}{1!}(\mathbf{A}\mathbf{x} + \mathbf{B}\mathbf{u})_{k-1} + \frac{\Delta t^2}{2!}(\dot{\mathbf{A}}\mathbf{x} + \mathbf{A}\dot{\mathbf{x}} + \dot{\mathbf{B}}\mathbf{u} + \mathbf{B}\dot{\mathbf{u}})_{k-1} +$$
$$+ \frac{\Delta t^3}{3!}(\ddot{\mathbf{A}}\mathbf{x} + 2\dot{\mathbf{A}}\dot{\mathbf{x}} + \mathbf{A}\ddot{\mathbf{x}} + \ddot{\mathbf{B}}\mathbf{u} + 2\dot{\mathbf{B}}\dot{\mathbf{u}} + \mathbf{B}\ddot{\mathbf{u}})_{k-1} +$$
$$+ \frac{\Delta t^4}{4!}(\dddot{\mathbf{A}}\mathbf{x} + 3\ddot{\mathbf{A}}\dot{\mathbf{x}} + 3\dot{\mathbf{A}}\ddot{\mathbf{x}} + \mathbf{A}\dddot{\mathbf{x}} + \dddot{\mathbf{B}}\mathbf{u} + 3\ddot{\mathbf{B}}\dot{\mathbf{u}} + 3\dot{\mathbf{B}}\ddot{\mathbf{u}} + \mathbf{B}\dddot{\mathbf{u}})_{k-1} + \ldots \tag{9}$$

The $(\ )_{k-1}$ notation highlights the fact that the whole expression between the parenthesis is considered at the (k-1) sequence and at the $t_{k-1} = (k-1)\cdot\Delta t$ moment.

For the considered process the time evolution of the three state parameters, respectively the pressure (Figure 1), the temperature (Figure 2) and the concentration (Figure 3) are approximated by the periodical exponential functions in the form:

$$y_{AN}(t) = \left(1 - \frac{T_1}{T_1 - T_2}\varepsilon^{-t/T_1} - \frac{T_2}{T_2 - T_1}\varepsilon^{-t/T_2}\right) \cdot K \cdot u \tag{10}$$

for the increasing evolutions in Figure 1 and 2, respectively in the form:

$$y_{AN}(t) = \left(\frac{T_1}{T_1 - T_2}\varepsilon^{-t/T_1} + \frac{T_2}{T_2 - T_1}\varepsilon^{-t/T_2}\right) \cdot K \cdot u \tag{11}$$

for the decreasing evolution in Figure 3. The input signal u_0 = constant is considered to be the one to induce the explosion, and (K) represents a proportionality coefficient.

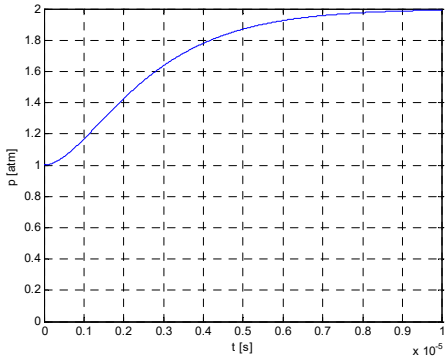

Figure 1. The evolution of pressure

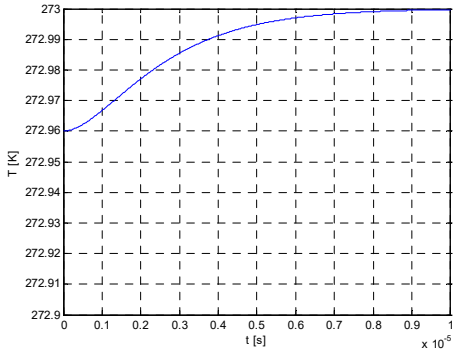

Figure 2. The evolution of temperature

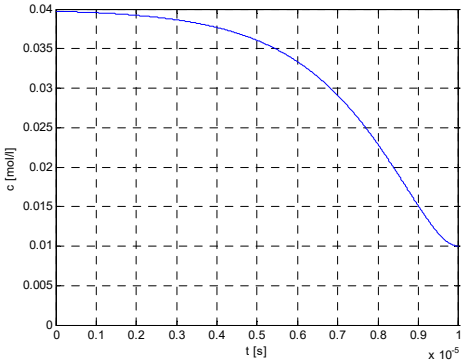

Figure 3. The evolution of concentration

The two-time constants (T_1) and (T_2) are specific for each of the state parameters, respectively:

$$T_2 = \lambda \cdot T_1 \tag{12}$$

and the final $t_f = 10^{-5}$ time is approximated by:

$$t_f = \mu \cdot (T_1 + T_2) = \mu \cdot (1 + \lambda) \cdot T_1 = \mu \cdot (1 + \frac{1}{\lambda}) \cdot T_2 \tag{13}$$

where μ=5 and λ=2 are considered.

The point of inflexion of these curves results at the time:

$$T_i = \frac{T_1 T_2}{T_2 - T_1} \cdot ln\left(\frac{T_1}{T_2}\right) = \mu \cdot \frac{\lambda + 1}{\lambda - 1} \cdot ln\,\lambda \cdot t_f \tag{14}$$

so that the decrease of λ>1 restricts the progressive decrease of the inflexion moment (t_i).

The analogical model associated to functions (1) and (2) can be expressed using the ordinary differential equation:

$$A_0 \cdot y + a_1 \frac{dy}{dt} + a_2 \frac{d^2 y}{dt^2} = a_0 y_0 + a_1 y_1 + a_2 y_2 = K \cdot u_0 \tag{15}$$

where $a_0 = 1$; $a_1 = T_1 + T_2$ and $a_2 = T_1 \cdot T_2$.

The initial conditions considered at the $t = t_0 = 0$ moment are:

- for Figure 1: $y_{0IC} = 1$; $y_{1IC} = 0$; $u_0 = 1$;
- for Figure 2: $y_{0IC} = 272.96$; $y_{1IC} = 0$; $u_0 = 0.04$;
- for Figure 3: $y_{0IC} = 0$; $y_{1IC} = 0$; $u_0 = 0.03$.

This model stood at the base of the software elaborated in order to obtain the numerical simulation.

The numerical simulation

Using the presented method, for the present application results the following algorithm:

$$y_0 = y_{0I} \tag{16}$$

$$y_1 = y_{1I} \tag{17}$$

$$y_2 = \frac{1}{a_2}\left[Ku_0 - \left(a_0 y_0 + a_1 y_1\right)\right] \tag{18}$$

$$y_3 = \frac{1}{a_2}\left[Ku_1 - \left(a_0 y_1 + a_1 y_2\right)\right] \tag{19}$$

$$y_4 = \frac{1}{a_2}\left[Ku_2 - \left(a_0 y_2 + a_1 y_3\right)\right] \tag{20}$$

$$y_5 = \frac{1}{a_2}\left[Ku_3 - \left(a_0 y_3 + a_1 y_4\right)\right] \tag{21}$$

where K = 1, $u_0 = 1$; $u_1 = 0$; $u_2 = 0$ and $u_3 = 0$.

The above iterations continue with two Taylor Series, which will replace (16) and (17), respectively:

$$y_{0K} = y_0 + \frac{\Delta t}{1!} y_1 + \frac{\Delta t^2}{2!} y_2 + \frac{\Delta t^3}{3!} y_3 + \frac{\Delta t^4}{4!} y_4 + \frac{\Delta t^5}{5!} y_5 \tag{22}$$

and

$$y_{1K} = y_1 + \frac{\Delta t}{1!} y_2 + \frac{\Delta t^2}{2!} y_3 + \frac{\Delta t^3}{3!} y_4 + \frac{\Delta t^4}{4!} y_5 \tag{23}$$

where $\Delta t = t_f/100$ is the integration step.

The indicator for this numerical integration performance is expressed by “the relative error cumulated in percentages” [19], denoted with:

$$Crep\ y_0 = 100 \cdot \frac{\sum_{K=0}^{K_f} \Delta y_{0K}}{\sum_{K=0}^{K_f} y_{AN,K}} \tag{24}$$

where $K_0=0$, respectively $K_f = t_f/\Delta t$ are the initial and final sequences of calculation. The sums ($\sum_{K=0}^{K_f} y_{AN,K}$) result from (1) and (2) and:

$$\sum_{K=0}^{K_f} \Delta y_{0K} = \left| \sum_{K=0}^{K_f} \left(y_{0K} - y_{0AN,K} \right) \right| \tag{25}$$

The indicator (15) is established at each calculus iteration, and the ($t = t_f$) final values are in the range of the (10^{-4}) % order, which proves the remarkable accuracy of this numerical integration method.

The above algorithm was implemented in Matlab™ software. The simulation results are presented in Table 1, successively grouped on Figures 1, 2 and 3 for the time interval $t_0 = 0$, up to $t_f = 10^{-5}$, with the extraction step of the results of $\Delta t = 10 \cdot \Delta t = 10^{-6}$.

Table 1. Simulation results of thermal explosion state variables

t/s	10^{-7}	$1.1 \cdot 10^{-6}$	$2.1 \cdot 10^{-6}$	$3 \cdot 10^{-6}$	$4 \cdot 10^{-6}$	$5 \cdot 10^{-6}$
Pressure/(atm)	1.0052	1.3155	1.628	1.800	1.903	1.953
Temperature (K)	272.9602	272.9789	272.9852	272.992	272.9961	272.9982
Concentration (mol/l)	0.03984	0.03053	0.02113	0.01599	0.01291	0.01139
Crep (%)	10^{-4}	10^{-4}	10^{-4}	10^{-4}	10^{-4}	10^{-4}

t/s	$6 \cdot 10^{-6}$	$7 \cdot 10^{-6}$	$8.1 \cdot 10^{-6}$	$9.1 \cdot 10^{-6}$	10^{-5}
Pressure/(atm)	1.979	1.990	1.995	1.9978	1.9989
Temperature (K)	272.9992	272.9996	272.9998	272.9999	273
Concentration (mol/l)	0.010615	0.0103	0.010137	0.010065	0.0100307
Crep (%)	10^{-4}	10^{-4}	10^{-4}	10^{-4}	10^{-4}

The used parameters were:

- the integration step $\Delta t = 10^{-9}$;
- the calculus coefficients for the time constants: $\mu = 5$; $\lambda = 2$;
- the time constants: $T_1 = 6.67 \cdot 10^{-7}$; $T_2 = 1.33 \cdot 10^{-6}$;
- the coefficients of the equation (15): $a_0 = 1$; $a = 2 \cdot 10^{-6}$; $a_2 = 8.88 \cdot 10^{-7}$;
- crep y_0 is of the order 10^{-4}, which proves the remarkable performance of the numerical integration.

The inflexion moment (t_i) in (14) can be changed in wide limits. For this particular study and using the corresponding software, it was obtained $t_i = 9.24 \cdot 10^7$, for a number of 1000 integration steps.

Example: The thermal explosion of oxyhydrogen gas initiated by the wall of a quartz reactor

The experimental data obtained during a thermal explosion of oxyhydrogen gas initiated by the wall of a quartz reactor are given. The experimental data are referring to the pressure variation and to the temperature variation during the explosion. The data associated to the pressure variation (the derivative of pressure in relation to time) are given in Table 2.

Table 2. The pressure variation

t	0	1	2	3	5	7	10	12	15	18	20	22	25	28	30
$\frac{dp}{dt}$ [torr/s]	0	0.2	0.5	0.8	1.4	1.8	2.6	2.7	2.8	2.7	2.1	1.9	1.4	1	0.8

The experimental variation of the pressure in relation to time [dp/dt](t) is presented, also, in Figure 4.

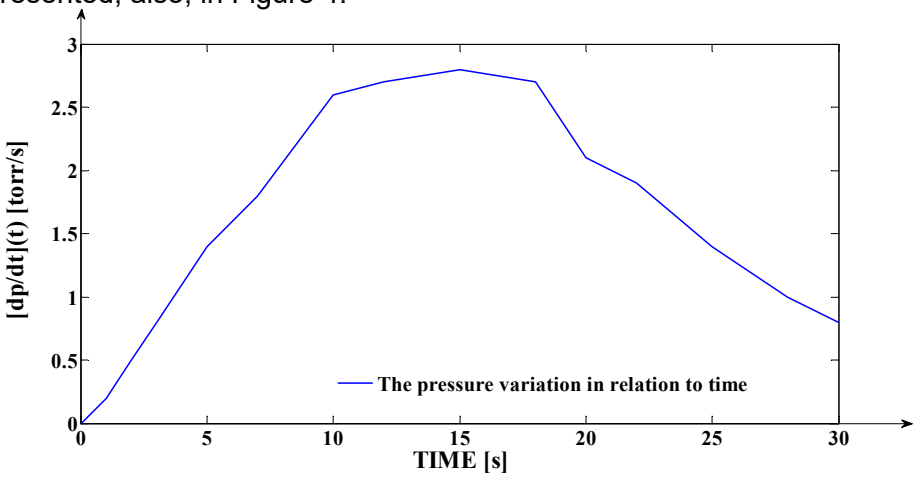

Figure 4. The [dp/dt](t) function

Using the experimental data from Table 2, the pressure evolution p(t) in relation to time (over the initial condition), during the experiment, can be determined according to Table 3.

Table 3. The pressure evolution in relation to time

t	0	1	2	3	5	7	10	12	15	18	20	22	25	28	30
$\sum \frac{dp}{dt} \cdot \Delta$ [torr]	0	0.2	0.7	1.5	2.9	4.7	7.3	10	12.8	15.5	17.6	19.5	20.9	21.9	22.7

In order to approximate the transformation of $\frac{dp}{dt}$ (t) in p(t), the graph-analytical integration of the data from Table 2 is being applied, by using the following equation:

$$p(t) \cong \sum_{i=0}^{14} \frac{dp}{dt}(t_i) \cdot \Delta t_i \tag{26}$$

where (Δt_i) is the graph-analytical integration step, for i = 0, 1, 2, …14. Due to the fact that the curve in Figure 4 is referring to $\frac{dp}{dt}$ (t), the initial pressure (associated to the initial conditions) become null through differentiation. Knowing the initial pressure of p_0 = 585 torr. the real pressure is given by:

$$p_1(t) = p_0 + p(t) \tag{27}$$

Consequently, p(t) represents an over-pressure in relation to p_0. The p(t) evolution is presented in Figure 5 (using the data from Table 3).

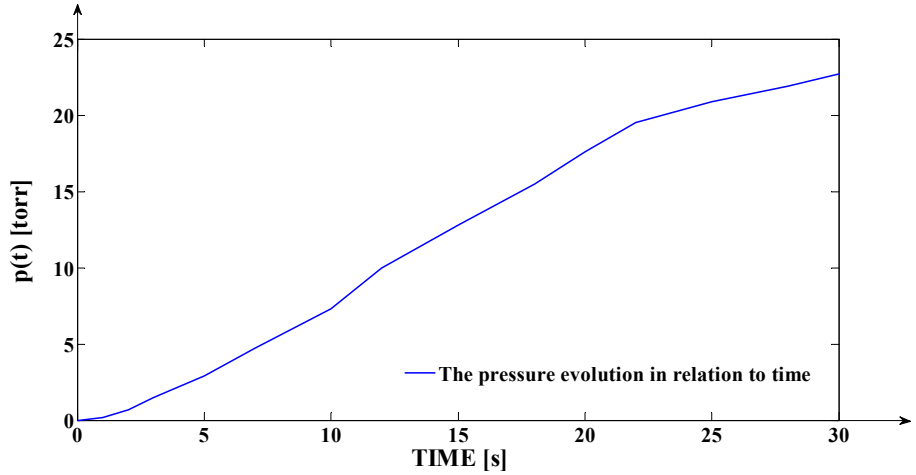

Figure 5. The p(t) evolution

According to Figure 4, the maximum value of [dp/dt](t) function is reached for t =15 s, aspect which implies the fact that the inflection point of the curve presented in Figure 5 (p(t)) is given by t = 15 s, too.

The experimental data associated to the evolution of the temperature $\Delta T(t)$, over the initial temperature of T_0 = 870 K and in relation to time, are presented in Table 4.

Table 4. The temperature evolution in relation to time, over T_0

t [s]	0	13.25	14.4	14.9	15.01	15.05	15.1	15.16	15.21
ΔT [K]	0	100	200	300	400	500	600	700	800

Also, considering the initial temperature, too, the temperature evolution in relation to time is presented in Table 5.

Table 5. The temperature evolution in relation to time

t [s]	0	13.25	14.4	14.9	15.01	15.05	15.1	15.16	15.21
T [K]	870	970	1070	1170	1270	1370	1470	1570	1670

Using the data from Table 5, the temperature evolution is presented in Figure 6.

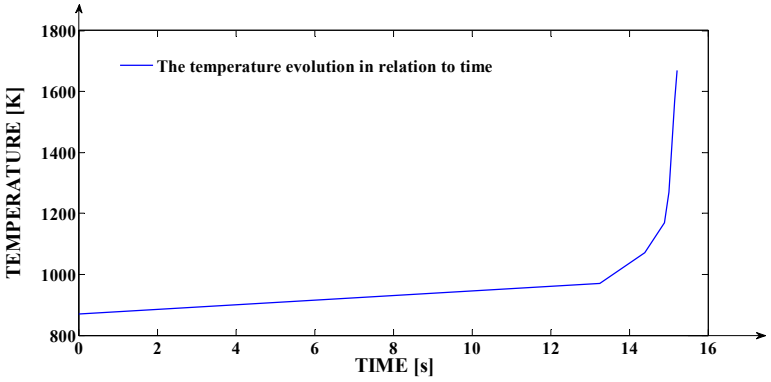

Figure 6. The T(t) evolution

In Figure 6, the explosion is highlighted around the moment t =15 s through the high temperature values.

For modelling-simulation the thermal explosion of oxyhydrogen gas initiated by the wall of a quartz reactor, the proposed method is applied. The approximating analytical solutions for the p(t) and T(t) evolutions, are given by:

- for the p(t) overpressure (in relation to the initial conditions):

$$y_{pAN}(t) = (1 - \frac{T_{p1}}{T_{p1} - T_{p2}} \cdot e^{-\frac{t}{T_{p1}}} - \frac{T_{p2}}{T_{p2} - T_{p1}} \cdot e^{-\frac{t}{T_{p2}}}) \cdot K_p \cdot u_p(t)$$

- for the T(t) temperature:

$$y_{TAN}(t) = T_0 + (e^{-\frac{t}{T_{T1}}} + e^{-\frac{t-t_1}{T_{T2}}}) \cdot u_T(t)$$

In the first equation T_{p1} = 8 s and T_{p2} = 10 s are the time constants of the pressure dynamics, K_p = 26.8 torr/s is the proportionality constant of the pressure dynamics and $u_p(t)$ is the input signal (this signal is a step unit signal which presents the commutation at the moment t_0 = 0, it being introduced in the model the moment of finalizing the reactor preparation for the experiment).

In the second equation T_{T1} = 2.89 s and T_{T2} = 0.298 s are the time constants of the temperature dynamics, T_0 = 870 K is the initial temperature, $u_T(t)$ is the input signal having a similar form and modelling the same action as $u_p(t)$, respectively t_1 = 13.3 s is a delay constant.

The mentioned structure parameters (the mentioned constants) values are identified using iterative identification algorithms based on processing the experimental data.

The comparative graph between the experimental p(t) curve and the simulated one (obtained by applying the proposed simulation method) is presented in Figure 7.

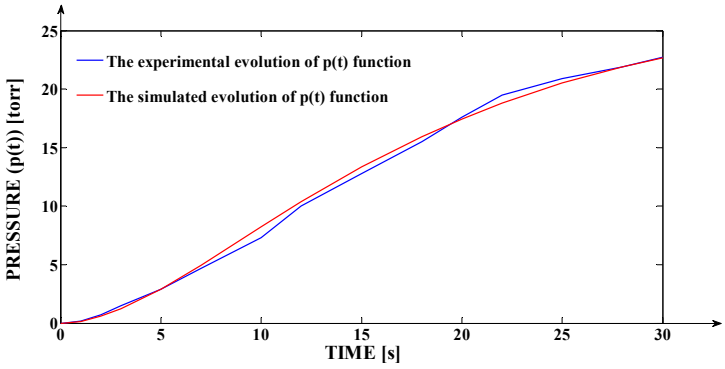

Figure 7. The comparative graph between the experimental p(t) evolution and the simulated one

From Figure 7, the high efficiency of the proposed modelling-simulation method results through the good superposition of the simulated curve over the experimental one. The high precision is, also, proven through the insignificant value of the cumulated error in percentage computed for the simulated curve in relation to the experimental one: $CREP_P$ = 0.4903 % (error which in absolute values is proportional with 10^{-3} ($4.903 \cdot 10^{-3}$).

Also, based on using the proposed model for the p(t) dynamics in relation to time, the pressure variation [dp/dt](t) can be simulated. Hence, the comparative graph between the experimental pressure variation ([dp/dt](t)) curve and the simulated one (obtained by applying the proposed simulation method) is presented in Figure 8.

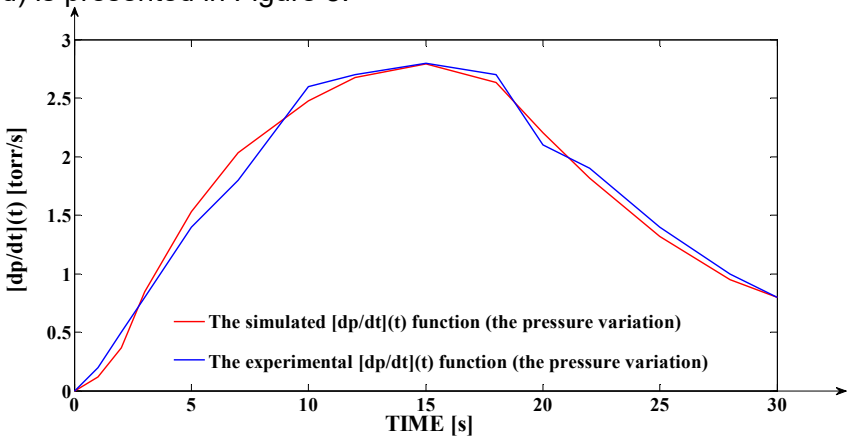

Figure 8. The comparative graph between the experimental pressure variation [dp/dt](t) evolution and the simulated one

The same conclusions as in the case of the comparison presented in Figure 7 result. The conclusions are proven through the insignificant value of the cumulated error in percentage computed for the simulated curve in relation to the experimental one: $CREP_{DP}$ = 0.6408 % (error which in absolute values is proportional with 10^{-3} ($6.408 \cdot 10^{-3}$).

The comparative graph between the experimental T(t) curve and the simulated one (obtained by applying the proposed simulation method) is presented in Figure 9. As in the previous two simulations, the same conclusions result. In this case, too, the value of the cumulated error in percentage computed for the simulated curve in relation to the experimental one is an insignificant one: $CREP_T$ = 1.8478 % (error which in absolute values is proportional with 10^{-2} ($1.8478 \cdot 10^{-3}$). The sensible higher value of $CREP_T$ than $CREP_P$ and $CREP_{DP}$ is due to the consistent higher absolute values of the temperature T(t) than the values of the other signals (p(t) and

[dp/dt](t)). Practically, by descending scaling of the $CREP_T$ error with 100 (the approximate proportion between the mentioned values), in the case of the temperature modelling-simulation we have obtained even better results than in the cases of pressure, respectively of pressure variation.

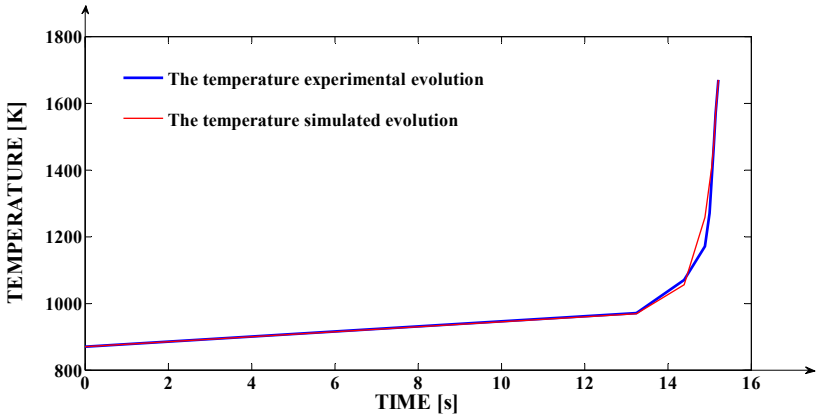

Figure 9. The comparative graph between the experimental temperature evolution and the simulated one

CONCLUSIONS

For certain cases, mathematical modeling is the only available predictive tool, and for other cases, mathematical modeling is one of the effective approaches. The usefulness of the results depends firstly on accuracy of mathematical model.

The explosions are non-linear phenomena and the modeling procedures which can be applied for obtaining their mathematical model are complex ones. Also, the identification methods used for determining the structure parameters of non-linear processes are laborious due to the fact that they are complex extensions of the identification methods which can be applied in the case of linear processes. Considering these aspects, in many cases, when other possibilities are available, the direct modelling of non-linear processes using non-linear models should be avoided. In this context, we have proposed a solution to solve and simplify the modelling of explosions by “avoiding of using a complex non-linear model. This solution is based on dividing the time period associated to the explosion in two intervals, the first interval corresponding to the increasing stage of the explosion (as intensity) and the second one corresponding to the decreasing

one. Practically, both stages can be modelled separately as linear processes, but the entire explosion phenomenon remains non-linear. More exactly, the explosion model is non-linear on the entire time period but is linear on intervals and we model separately each interval. In this paper, as study case, only the increasing stage of the approached explosions are modelled, but the decreasing stage modelling is similar as applied procedures. However, the proposed algorithm can be modified in order to have the possibility to apply it in order to model-simulate the explosion as a unitary non-linear phenomenon, but the associated computations are more complex: (1) has to be modified at the form $\dot{x}=f(x,u)$ and (2) has to be modified at the form $y=g(x,u)$, where both f and g functions are non-linear).

For the studied process, the thermal explosion, it can be concluded that the algorithm presented by this research contributes to a high interpretation of the extremely short period of the explosion phenomena, analyzed from the perspective of pressure, temperature and concentration evolution in time, both in steady and transient states. The accuracy of the model is proved by the very small values of the relative error cumulated in percentages.

REFERENCES

1. V. Novozhilov; *Sci Rep,* **2016**, 6, 29730.
2. A.N. Campbell; *Phys Chem Chem Phys*, **2015**, 17(26), 16894-906.
3. V. Novozhilov; *Sci Rep,* **2018**, 8(1), 4030.
4. A.K. Oppenheim; *Chemical Kinetic Aspects, Dynamics of Combustion Systems,* 2 nd ed.; Springer Berlin Heidelberg Publisher, **2008**, 81-113.
5. E. Glascoe; H. Keo Springer; J.W. Tringe; L. Maienschein; *Bull Am Phys Soc,* **2011**, 56 (6), 347-351.
6. C.Y. Chan; P.C. Kong; *Appl Math Comput*, **1995**, 71(2-3), 201-210.
7. G.N. Gorelov; V.A Sobolev; *Combust Flame,* **1991**, 87 (2), 203-210.
8. K. Takashi; *Critical Temperatures for the Thermal Explosion of Chemicals*, Hardbound, **2005**, 406.
9. N.N. Semenov; *AN SSSR,* **1959**.
10. D.A. Frank-Kamenetsky; *Diffusion and Heat Transfer in Chemical Kinetics*, Moscow, Nauka, **1967**.
11. O.M. Todes; P.V. Melent'ev; *J Phys Chem*,**1939,** 13 (7), 52–58.
12. A.G. Merzhanov; F.I. Dubovitsky; *UChN,* **1966**, 35(4), 656–683.
13. B.F. Gray; *Combust Flame,* **1973,** 21, 317–325.
14. R. Almeida; N.R.O. Bastos; M.T.T. Monteiro; *Math. Methods Appl. Sci.*, **2016**, 39(16), 4846-4855.

15. B.E. Zhestkov; S.N. Kozlov; E.N. Alexandrov; *High Temp*, **2019**, 57(3), 329-334.
16. X. Hu; Q. Xie; J. Zhang; Q. Yu; H. Liu; Yasong Sun; *Int. J. Hydrog. Energy*, **2020**, 45(51), 7837-27845.
17. K. Allali; Y. Joundy; A. Taik; *Mathematical Modelling of Natural Phenomena*, **2019**, 14, 602-614.
18. E.N. Aleksandrov, N.M. Kuznetsov, S.N. Kozlov; *Combust. Explos. Shock Waves*, **2010**, 46, 533–540.
19. T. Coloşi; M. Abrudean; M.-L. Ungureşan; V. Mureşan; *Numerical Simulation Method for Distributed Parameters Processes using the Matrix with Partial Derivatives of the State Vector*, Ed. Springer, **2013**, pg. 343.

STUDIA UBB CHEMIA, LXVI, 1, 2021 (p. 105-113)
(RECOMMENDED CITATION)
DOI:10.24193/subbchem.2021.1.08

CITRUS BUTANOL ESTERS HAVING PLASTICIZING AND LUBRICANT CHARACTERISTICS OBTAINED IN A BUBBLE COLUMN TYPE REACTOR

SORINA BORAN[a], GIANNIN MOSOARCA[a] *, SABINA NITU[a] *, COSMIN VANCEA[a]

ABSTRACT. The aim of this paper was the synthesis of some citric esters with potential biodegradable properties and their use as plasticizers or PVC lubricants. Citric esters were obtained in a bubbling column-type esterification reactor, using citric acid as the acid component, and monoethylene glycol, n-butanol, t-butanol as the hydroxyl components. The esters were characterized by FT-IR spectrometry to reveal the existence of the esteric bonds. Esters present a good thermal stability. The TCS criterion shows a level of compatibility specific to secondary plasticizers. There is a similarity between the values of the tested compounds and the standard DOF regarding hardness. The breaking strength are better and the values of elongation at break are close to the considered standards. The esters prove a very good migration towards rubber and are comparable to tribological fluids. The four balls test showed that without additives and at a test level of 40 daN for 60 min time period, the diameters of the wear spot are generally very good, being in the range of 0.43-0.62 mm. By adding oils, their behavior improves. The welding load values are also good (200-220 daN). The synthesized citrus esters have clear characteristics of plasticizers and/or lubricants for PVC.

Keywords: *citrus esters, bubble column reactor, plasticizer, lubricant*

INTRODUCTION

Currently, special emphasis is placed on the low-energy technologies where the synthesis of environmentally friendly products that have plasticizer and/or lubricant properties are obtained.

[a] *Politehnica University Timisoara, Faculty of Industrial Chemistry and Environmental Engineering, 6 Vasile Pârvan Bd., RO-300223, Timisoara, Romania*
** Corresponding authors: giannin.mosoarca@upt.ro; sabina.nitu@upt.ro*

Esters represent a particular importance both in the field of auxiliaries for polymer processing (plasticizer or lubricants) as well as in the field of fluids with applications in tribology.

Citric acid (2-hydroxypropane-1,2,3-tricarboxylic acid) is a weak tribasic organic acid. In nature it is found in citrus fruits and in the human and animal body as metabolic intermediate in citric acid cycle. The uses of citric acid as an acidifier, flavoring, chelating agent [1] and active ingredient in some commercial cleaning products have led to the industrial production of about two tons per year. Citric acid esters have technical applications in the field of lubricants, hydraulic fluids or transformer oils [2].

Citrus esters with potential biodegradable properties, synthesized by classical esterification methods, have clear characteristics of plasticizer and lubricant, respectively [3-6].

Column reactors with bubbling are used at present in many chemical processes [7-10] because they may intensify the heat exchange and may diminish the energy consumption [11-16].

The industrial development leads to an increase in pollution, thus environmental protection represents an important and actual concern [17-20]. In this context, energy efficiency is the most cost-effective way of cutting carbon dioxide emissions and improvements environmental quality [21].

The present paper presents the obtaining of some citrus esters in a low energy consuming bubble column reactor. The products were tested as possible lubricants and plasticizer, revealing that they have adequate or even superior properties to traditional ones.

REZULTS AND DISCUSSION

Physical-chemical properties of the synthesized citrus esters are presented in Table 1, where P1 – citric ester with monoethylene glicol and *n*-butanol and P2 - citric ester with monoethylene glicol and *t*-butanol.

Table 1. Physical-chemical properties of the synthesized citrus esters

Property	P1	P2
Aspect	viscous	viscous, transparent
Color	yellow	colorless
Acid index, mg KOH g^{-1}	< 1	< 1
Refractive index, (20°C)	1.2546	1.2247
Density (25°C), g cm^{-3}	1.2275	1.2311

It may be noticed that although the both esters are viscous, as expected, the other physical-chemical properties are slightly different. P1 is yellow (a very light color) and P2 is colorless, the refractive index of P1 is greater with 2.4%, while its density is smaller only with 0.3% than of the P2. Acid index is below 1 for the both citrus esters.

FT-IR spectra reveal the presence of citrus esters. As an example the FT-IR spectrum for the P1 is presented in Figure 1. The compound structure was confirmed by the presence of the main characteristic bands: 2979 cm^{-1} ($\nu_{CH_3}^{as}$), 1165 cm^{-1} (ν_{COC}^{as}), 1324 cm^{-1} (ν_{COC}^{as}), 1720,3 cm^{-1} ($\nu_{C=O}^{as}\ in\ ester$).

TG/DTG, DSC/DDSC analysis were also performed and presented in Figure 2 for P1, as an example. The TG curve reveal a continuous mass loss in the studied temperature range. The steps are difficult to separate on the TG curve but the decomposition steps can be distinguished by analyzing the DSC and DDSC curves. One is at 294.4°C and the other over 600°C. The major mass loss at the inflection point is 45.29%, and the maximum occurs before 500°C. After the characterization of the obtained citrus esters as organic compounds, they were investigated as plasticizers and lubricants for PVC.

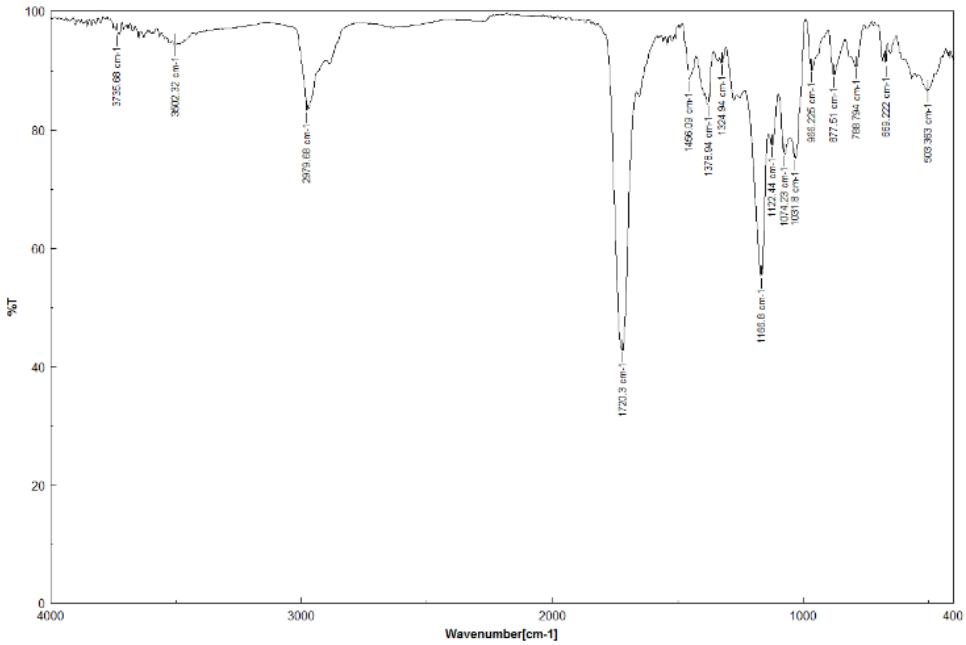

Figure 1. FT-IR spectrum for the citrus ester P1

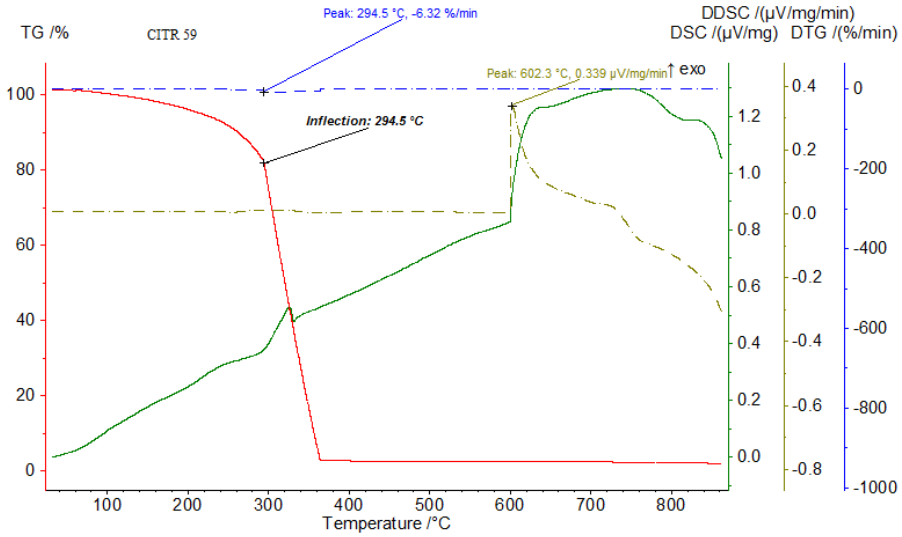

Figure 2. TG/DTG, DSC/DDSC curves obtained for citrus ester P1

Plasticizer investigations. In order to analyze the plasticizer properties, tests were performed that define the compatibility, namely the TCS criterion. Results are presented in Table 2. For comparison meaning, four classic DOF, DOA, DOS and DBF plasticizers were tested under the same conditions.

Table 2. Compatibility tests value of the TCS criterion

Test	P1	P2	DOS	DOF	DOA	DBF
TCS, ^{0}C	148-150	149-150	157-158	117	142	89

There is a level of compatibility specific to secondary plasticizers.

In order to appreciate the products efficiency, Shore A hardness and traction test (100% modulus, elongation at break and breaking strength) were performed, results being presented in Table 3.

In terms of hardness there is a similarity between the values of the tested compounds and the values entered for DOF (standard, a classic representative of the class of primary plasticizers).

The 100% module has values much higher than the value corresponding to the DOF, which indicates a relatively low level of efficiency from this point of view. Very good values of breaking strength are found, compared to the considered standards (DOF and DOA), while the values of elongation at break are close to those of DOA and DOF.

Table 3. Test efficiency for the citrus esters

Tests		P1	P2	DOF	DOA
Shore A Hardness, ^{0}Sh	3"	82.6	89.6	85.0	68.6
	10"	81.7	89.0	84.0	65.3
Traction tests	100 % Modulus, kgf cm^{-2}	182	247	88	112
	Elongation at break, %	249	253	324	333
	Breaking strength, σ_r, kgf cm^{-2}	340	426	156	192

Tests for permanence, which define the plasticizers anchoring capacity in the polymer matrix were also performed, results being presented in Table 4.

Table 4. Test for permanence for the citrus esters

Proprieties		P1	P2	DOF	DOA
Migration towards rubber, 24h / 70^{0}C, %, -		2.25	3.7	4.86	3.21
Water rezistance, 24h / 20^{0}C	Absorbtion, %, +	0.42	0.36	0.19	1.55
	Extraction, %, -	0.55	0.12	0.17	3.42

The migration towards rubber values are slightly smaller than the DOF, but comparable to DOA. The water resistance is placed at the same level as DOF. All the products tested in this respect prove a very good migration towards rubber, the values obtained being between the necessary ones and the standards. The resistance to extraction with water and oil is also very good. Thus, from this point of view we can say that the analyzed compounds have the characteristics of a primary plasticizer.

Concluding it may be affirmed that the citrus esters present plasticizer properties, especially as a secondary plasticizer used in polymer processing.

Physical constants and rheology. Analyzing some of the physical properties and of the rheology of the obtained products reveal that they are comparable to tribological fluids, that is high flammability points and the flow points values and kinematic viscosity that have similar variation (Table 5).

Table 5. Values of the main physical constants and rheology of the citrus esters

Citrus esters	Kinematic viscosity, mm^2/s		Flammability points, ^{0}C	Flow points, ^{0}C
	40 ^{0}C	100 ^{0}C		
P1	200.0	17.4	261	-18
P2	187.3	12.6	261	-20

Lubricant investigations. In order to determine the lubricant capacity of the obtained citrus esters, the four balls test was performed, results being presented in Table 6.

Table 6. Ware stain diameter and four ball test for the citrus esters

Citrus esters	Without additives	With aditive of 1.5% Zn dithiophosphat		With aditive of 1.5% Zn dithiocarbonate	
	Ware stain diameter, mm, 40 daN, 60 min	Ware stain diameter, mm 40 daN 60 min	Welding, daN	Ware stain diameter, mm 40 daN 60 min	Welding, daN
P1	0.48	0.48	200	0.46	200
P2	0.71	0.62	260	0.65	240

The results show that in the case of species without additives and at a test level of 40 daN for 60 min time period, the diameters of the wear spot are generally very good, placing in the range of 0.43-0.62 mm. Adding oils in all cases leads to a slight improvement in behavior. The welding load values are also good and a level of 200-220 daN is constantly reached. The results for the compounds with additives show a good compatibility of these synthetic oils with anti-wear additives.

CONCLUSIONS

The aim of this paper was the synthesis of some esters based on citric acid and their evaluation in order to be used as plasticizers and as lubricants for PVC. Citric esters were obtained in a bubbling column-type esterification reactor, using citric acid as the acidic component and monoethylene glycol as the hydroxyl component in conjunction with *n*-butanol, *t*-butanol.

Due to the intrinsic biodegradability characteristics brought by the citrus skeleton, it is accepted that the synthesized citrus esters have the ability not to negatively influence the environment. The obtained esters were characterized by FT-IR spectrometry in order to reveal the existence of the esteric bonds - 1720,3 cm^{-1} ($\nu_{C=O}^{as}\ in\ ester$). The TG/DTG, DSC/DDSC analysis was used to determine their thermal stability and degradability, revealing a remarkable thermal stability. The TCS criterion presents a level of compatibility specific to secondary plasticizers. There is a similarity between the values of the tested compounds and the standard DOF in terms of

hardness. The 100% module indicates a relatively low level of efficiency from this point of view. The breaking strength are better and the values of elongation at break are close to the considered standards (DOF and DOA). The esters also prove a very good migration towards rubber and that they are comparable to tribological fluids, because of their high flammability points and the flow points values and kinematic viscosity that have similar variation. The lubricant capacity of the obtained citrus esters was performed using the four balls test, revealing that without additives and at a test level of 40 daN for 60 min time period, the diameters of the wear spot are generally in the range of 0.43-0.62 mm. By adding oils, their behavior improves. The welding load values are also good and a level of 200-220 daN being constantly reached. The obtained results certify that the synthesized citrus esters have clear characteristics of plasticizers and/or lubricants for PVC, in particular as secondary plasticizers used in the polymers processing.

EXPERIMENTAL SECTION

Ester synthesis. The synthesis takes place in two stages. First, the citric acid, the monoetylene glicol, the other hydroxyl components (in the proportions 1:2:1) and the catalyst (*p*-toluenesulphonic acid) – 0.1%, are introduced into a flask equipped with a water-cooled rising refrigerant and a thermometer, where a pre-esterification reaction takes place under continuous stirring in a preheating nest (Figure 3).

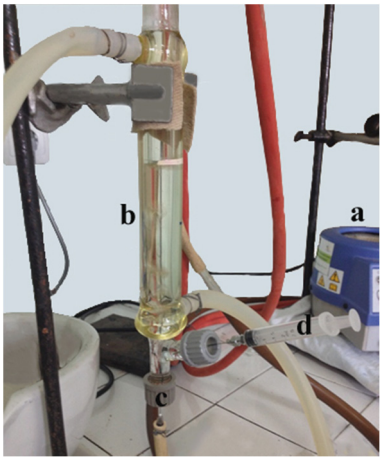

Figure 3. Ester synthesis experimental installation
(a) preheating nest; **(b)** bubble column reactor; **(c)** bubbling nozzle; **(d)** sampling

After one hour, the reaction mass is cooled to 80°C, and the resulting product is transferred directly into the esterification column reactor with bubbling (Figure 3), which was preheated to 80°C. The synthesis takes place at reflux temperature, without removing the reaction water from the system. The esterification reaction is monitored by periodically determining the acid index throughout the synthesis.

Analyzing methods. *Physical-chemical properties*: Aspect – visual; Refractive index – Abbe refractometer; Density, at 20°C – pycnometer; Acid number - according to SR ISO 3682.

FT-IR spectra were recorded with a Bruker Vertex 70 spectrometer (Bruker Daltonik GmbH, Germany) equipped with a Platinium ATR spectrometer, Bruker Diamond type A225/Q.I.

Thermogravimetric analysis (TG)/(DTG) and differential scanning calorimetry (DSC) were performed with NETZSCH STA apparatus STA449F1A 449F1-0220-M. A quantity of between 3 ÷ 7 mg sample was heated in a crucible of Al2O3, with the rate of 5^0C/min., under a nitrogen atmosphere in the temperature range of 25 ÷ 900^0C.

Evaluation of P1 and P2 synthesized esters as plasticizer: TCS criterion was determined with the Boetius microscope, using a PVC suspension Kw = 67. In order to evaluate the other tests, PCV foils were realized, which were roundly or squarely cut of 5 cm – according to SR EN ISO 2898-2:2003. The Shore A hardness and the traction tests were performed according to SR EN ISO 846:2000. For the water resistance investigation, the square foil was immersed in distilled water at 20±2°C for 24 hours. The volatiles were determined at 100±2°C for 24 hours. The plasticizer migration was determined with the round foils at 70±2°C for 24 hours using rubber absorbent discs. Oil stability was determined at 20±2^0C for 168 hours.

Evaluation of P1 and P2 synthesized esters as lubricants. Flammability point was determined according to ASTM D 92, in a tank of 50 mm in diameter, buried in the sand, over which the flame is passed. Flow disorder point was determined according to ASTM D 97. The kinematic viscosity and the viscosity index were determined using the Ubbelohde viscometer, according to ASTM 445.

ACKNOWLEDGEMENTS

The research was supported by POS CCE Nr. PO102418 12/5124 / 22.05.2014 grant.

REFERENCES

1. F.H. Verhoff; *Citric Acid. Ullmann's Encyclopedia of Industrial Chemistry*, Wiley-VCH: Weinheim, Germany, **2005**; pp. 7-8.
2. Patent Germany; https://patents.google.com/patent/DE102011079558A1/en.
3. L. Mirci; S. Boran; *Mater. Plast.*, **2004**, *41(4)*, 231-239.
4. L. Mirci; S. Boran; P. Luca; V. Boiangiu; *J. Synth. Lubr.*, **2003**, *20(1)*, 39-52.
5. L. Mirci; S. Boran; *Mater. Plast.*, **2000**, *37(3)*, 145-153.
6. L. Mirci; J. Herdan; S. Boran; *J. Synth. Lubr.*, **2000/2001**, *17(4)*, 295-307.
7. S. Popa; C. Csunderlik; V. Jascanu; D. Jurcau; N. Plesu; *Mater. Plast.*, **2004**, *41(2)*, 62-65.
8. S. Popa; C. Csunderlik; V. Jascanu; D. Jurcau; N. Plesu; *Mater. Plast.,* **2003**, *40(4)*, 177-181.
9. S. Popa; V. Jascanu; D. Jurcau; N. Plesu; *Rev. Chim.-Bucharest*, **2003**, *54(7)*, 595-598.
10. S. Popa; C. Csunderlik; S. Florea; V. Jascanu; N. Plesu; *Rev. Chim.-Bucharest,* **2002**, *53(4)*, 259-263.
11. S. Popa; S. Boran; *Mater. Plast.*, **2016**, *53*, 410-413.
12. S. Popa; S. Boran; *Rev. Roum. Chim.*, **2015**, *60*, 991-995.
13. S. Popa; S. Boran; G. Mosoarca; C. Vancea; *Stud. U. Babes-Bol. Che.*, **2019**, *64(3)*, 143-152.
14. S. Popa; S. Boran; *Therm. Sci.*, **2017**, *21(5)*, 2031-2037.
15. D. Kohn, S. Popa, *Exp. Heat Transfer,* **1999**, 12(3), 193.
16. S. Popa, S. Boran, *Rev. Roum. Chim.*, **2016**, 61, 851.
17. G. Mosoarca; P. Negrea; C. Vancea; M. Motoc; M. Anghel; D. David; *Rev. Chim.-Bucharest*, **2010**, *61*, 983-985.
18. C. Vancea; M. Gheju; G. Mosoarca; *Rev. Rom. Mater.*, **2017**, *47(4)*, 435-441.
19. C. Vancea; R.M. Jurca; M. Gheju; G. Mosoarca; *Rev. Rom. Mater.*, **2018**, *48(3)*, 308-314.
20. C. Vancea; G. Mosoarca; A. Negrea; A. Latia; R.M. Jurca; *Rev. Rom. Mater.*, **2016**, *46(3)*, 296-302.
21. A.M. Omer; *J. Renew. Sustain. Energ.*, **2009**, *1*, 053101.

STUDIA UBB CHEMIA, LXVI, 1, 2021 (p. 115-125)
(RECOMMENDED CITATION)
DOI:10.24193/subbchem.2021.1.09

THE WATER QUALITY OF SOME SHALLOW WELLS FROM HARGHITA COUNTY (SÂDOMINIC COMMUNE), ROMANIA

SILVIA BURCĂ[a], CERASELLA INDOLEAN[a]*

ABSTRACT. This study includes the most important physico-chemical parameters monitoring of the shallow wells from Sândominic commune, Harghita County, Romania, in order to establish if the water sources can be used as drinking water. The pH, dH_T, acidity, alkalinity, CCO-Mn, NO_2^-, NO_3^-, NH_4^+, Cl^- and Fe_{total} parameters were determined using appropriate standard methods and compared with allowable values for drinking water, according to Romanian legislation. Based on the determined parameter values, most of the samples were characterized by a moderate or high mineralization (288-980 mg/L), and for some of them there was a contamination with organic substance and nitrate ions.

Keywords: *groundwater, monitoring, shallow wells, pollution*

INTRODUCTION

It is difficult to imagine any clean and sanitary environment without water. Invariably, the progress of sanitation throughout the world has been closely associated with the availability of water; and, the larger the quantity and the better the quality of the water, the more rapid and extensive has been the advance of public health.

Romania is a country with reduced water resources compared to the rest of Europe. Despite the achievement of numerous accumulations, the volume of surface water is modest and the rivers have a relatively small flow. Romania's total water resources are estimated at 40×10^9 m^3 / year of which inland rivers have only 5×10^9 m^3 / year and 3×10^9 m^3 / year are groundwater. The water potential is approximately 1750 m^3 / inhabitant / year, compared to the European average of 4800 m^3 / inhabitant / year [1].

[a] *Babeş-Bolyai University, Faculty of Chemistry and Chemical Engineering, Department of Chemical Engineering, 11 Arany Janos str., RO-400028, Cluj-Napoca, Romania*
**Corresponding author e-mail: liliana.indolean@ ubbcluj.ro*

The water from Danube is used in small quantity (as water-source), but, even with this, the volume of Romanian water resources per capita remains modest compared to the average in Europe.

The water reserves differ geographically, being rich in mountain areas and low in Bărăgan and Dobrogea, as well as some karst areas, where the population uses even rainwater for some household needs. To reduce these discrepancies, various inter-basin adductions have been built, but they do not increase significantly the water amount, fact that make us have extra-reasons to take care of Romanian water reserves, which is a problem not only quantitatively but also qualitatively [2-5].

The regulatory agency in the water sector in Romania is "Autoritatea Națională de Reglementare pentru Serviciile Comunitare de Utilități Publice" – "National Romanian Regulator for Public Services" (ANRSC). As there was no more recent data available at a national level, a report published by ANRSC states that in 2011 a total number of 1021 entities were administrating water services [6], including mostly private 44 regional operators who accounted for 86,3% of the market share. The utilities usually manage all the existing stages of drinking water cycle, from abstraction, potable water treatment, transport and distribution to the collection, treatment and discharge of wastewater [7].

In Romania, on large areas, drinking water supply is represented by the groundwater, particularly from wells, more than 45% of the population lives in rural and benefit from centralized water supply system [8,9].

Groundwater may contain impurities or contaminants, which can originate from watershed or soil. Water moving through underground rocks and soils may pick up magnesium, calcium, iron, manganese, chlorides, selenium, boron, arsenic or radon. Groundwater is often polluted due to human activities, such as: fertilizers usage, animal manures, pesticides, improperly built and located septic systems for household wastewater, storm-water drains that discharge chemicals to groundwater, improper disposal or storage of wastes, chemical spills at local industrial sites [10-12]. These natural contaminants can produce various health problems depending on their amount.

Oxidizable substances in water or chemical oxygen consumption are substances that can oxidize both cold and hot under the action of an oxidant (organic substances are oxidized hot and inorganic cold). The increase in the amount of organic substances in the water or their appearance at a given time indicates a water pollution with germs that usually accompany the organic substances [8, 9,13,14].

A special problem is generated by the presence of high nitrate/nitrite ions quantities. Ammonia results in water from the incomplete degradation of organic substances that contain nitrogen or may come from the soil. It represents the first stage of decomposition of organic substances with

nitrogen content and therefore, indicates a recent pollution (hours, days) and consequently, is very dangerous. Nitrogen in water comes from incomplete oxidation of ammonia in the presence of nitrifying bacteria. They represent a more advanced stage of the decomposition processes of organic substances containing nitrogen and consequently, their presence or increase in concentration indicates an older pollution, so, less dangerous. The concomitant presence of ammonia and nitrite shows us a continuous pollution. The susceptibility to nitrite ions of new-born children and animals is due to the fetal hemoglobin, which has more affinity for oxygen, therefore forms methemoglobin, quicker than in adult organisms [15-21].

Iron can be found in water in the form of soluble ferric salts (in the ferrous form as bicarbonates and less as sulphates, phosphates or silicates), insoluble ferric salts (in the form of hydroxide) or in colloidal form, complexed with organic substances. Iron in water promotes the development of ferrobacteria, which obstruct the pipes. In excess, it gives the water a metallic taste, a reddish-brown colour, stains the laundry, it settles on the pipes, on the kitchen utensils, etc. [22, 23].

This paper includes a case study on the water quality from some shallow wells located in Sândominic commune, Harghita County, a place at the foot of the Hășmaș Mountains. In this commune there is no drinking water distribution network, it is obtained from wells.

RESULTS AND DISCUSSION

Sândominic commune is the largest commune in the Ciucu de Sus area, with a number of 6300 inhabitants.

The population density is high, the distance between the households being relatively small, there being no sewerage system for taking over the domestic water, the own pollution sources are close to the wells.

Evaluating the water samples collected from the wells from the commune perimeter, the following conclusions were reached: the water from the W1 is drinkable, but, there is probably still a drainage that achieves a partial communication with the Olt river, because a certain iron content was found in the samples taken from this well; the water from the W2 well is drinkable, with moderate to hard hardness, so it is necessary to add some water softener, when it is used for washing, to prevent the limescale deposition in the washing machine. In situations where it is desired to use water in the thermal power plant, it is advisable to add a cationic filter for calcium and magnesium ions retaining.

The water from the W3 well is not drinkable, having a content above the limit allowed by the Romanian legislation in force for the chemical consumption of oxygen (presence of the organic substances) and, for the high content of NH_4^+ NO_3^- and chloride ions, also. Exceeding these limits for the mentioned indicators can be attributed to the chemical fertilizer depot located in the vicinity of this well.

Based on water hardness, expressed in German degree, water can be classified as very soft (0 - 4 °d), soft (4-8 °dH), moderately hard (12 -18 °dH), hard (18 – 30 °dH) and very hard (>30 °dH) [14, 24].

Total hardness values, Table 1 and Table 2, showed that all well water samples have moderately hardness and can be included in the category of moderately hard. Values showed in Table 1 suggest that there are no major changes in this indicator for March compared to May. Higher hardness values were recorded for samples collected from the W2 area respectively W3 area, figure 1.

Table 1. The recorded values of surface water and well water quality indicators, for March 2020, Sândominic Commune, Harghita, Romania.

Measured indicator	Olt	W1	W2	W3	Lunca Mare	Maximum allowed value (law 458)
pH	7.4	6.6	7.0	7.0	6.8	6.5-8.5
CCO-Mn (mg/L) O_2	3.40	1.51	0.80	**9.95**	2.37	**5.0**
NH_4^+ (mg/L)	**1.42**	0	0	0.23	0.1	**0.5**
NO_2^- (mg/L)	0.025	0	0	0	0	0.5
NO_3^- (mg/L)	4.5	11	24	**90**	**58**	**50**
Cl^- (mg/L)	8.85	8.85	12.03	70.8	8.85	250
Acidity, (mval/ml)	0.65	0.43	0.78	1.57	0.74	-
Alkalinity, (mval/ml)	2.94	2.52	5.26	10.09	2.52	-
Hardness d^0	12.10	9.36	18.5	18.5	11.42	min. 5
Fe_{tot} (mg/L)	0.95	0.1	-	-	-	0.2
Fixed residue (mg/L)	225	288	420	980	301	-

Table 2. The registered values of surface and groundwater water indicators for May 2020, Sândominic commune, Harghita, Romania.

Measured indicator	Olt	W1	W2	W3	Lunca Mare	Maximum allowed value (law 458)
pH	7.4	6.5	7.0	7.0	6.9	6.5-8.5
CCO-Mn (mg/L) O_2	3.50	1.50	0.85	**10.05**	2.30	**5.0**
NH_4^+ (mg/L)	1.76	0	0	0.38	0.13	0.5
NO_2^- (mg/L)	0.020	0	0	0	0	0.5
NO_3^- (mg/L)	4.8	12	23.9	**94**	**55**	**50**
Cl^- (mg/L)	8.85	8.85	11.94	71.8	8.85	250
Acidity, (mval/ml)	0.60	0.48	0.80	1.37	0.84	-
Alkalinity (mval/ml)	2.64	2.02	5.00	10.29	2.78	-
Hardness d^0	13.10	9.08	18.67	18.67	12.32	min. 5
Fe_{tot} (mg/L)	1.25	0.08	-	-	-	0.2
Fixed residue (mg/L)	230	269	428	992	299	-

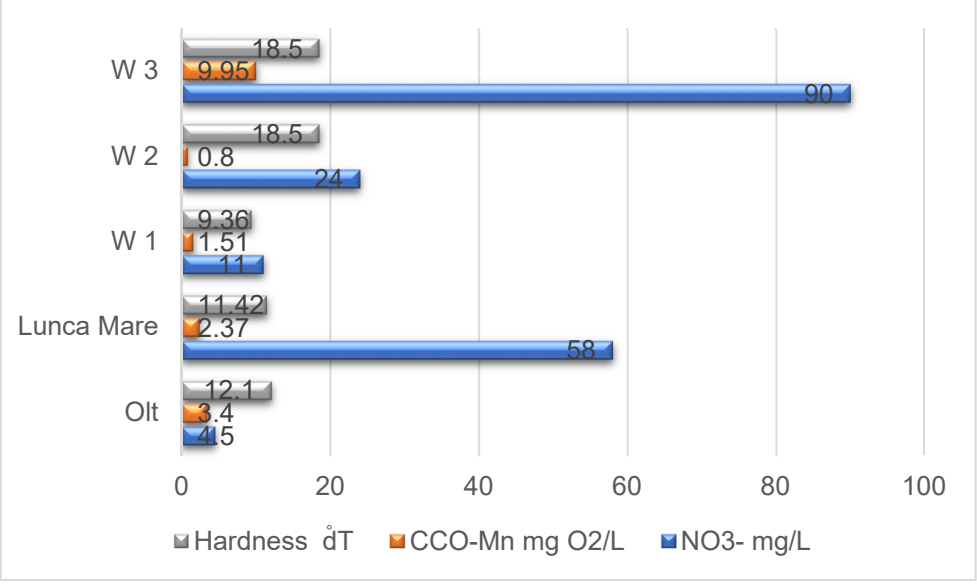

Figure 1. The CCO-Mn, total hardness and nitrate concentration values for the groundwater surface water samples - Sândominic Commune, Harghita County, Romania, March 2020

For the samples taken from the Olt River, it is found pollution from the waters of copper mines in the town of Balan, as well as a relatively high content of NH_4^+ and NO_3^- ions (indicating a continuous pollution) and the presence of Fe_{tot} ions, also.

In addition, for the Lunca Mare River, the analysed samples suggest that there is a moderate pollution, due to the presence of organic substances and NO_3^- ions, which is due to the discharge of untreated wastewater (from sewage).

CONCLUSIONS

Based on the monitoring of the physico-chemical properties carried out (the pH, dH_T, acidity, alkalinity, CCO-Mn, NO_2^-, NO_2^-, NH_4^+, Cl^- and Fe_{total} parameters) from samples taken (shallow well waters, Sândominic commune, Harghita County, Romania), it was found that, in general, the groundwater is characterized by a moderate to high mineralization (W3), but the water from this source isn't drinkable.

In the case of the water from the W2 well, this is drinkable, with moderate to hard hardness, so it is necessary to add some water softener, for household's consumption.

The water from the well W1 is drinkable, having a moderate hardness, but, the presence of the iron ions, probably due to an underground communication with the water from the Olt River, makes it not o superior and pleasant water to taste, so, of average quality for human consumption.

For the water samples taken from Olt River, there is a pollution of them with copper ions coming from mines in the nearby town of Balan and also, a relatively high content of NH_4^+ and NO_3^- ions (indicating a continuous pollution), as well as the presence of Fe_{tot} ions.

Regarding the Lunca Mare River, there is a more moderate pollution, the presence of organic substances and NO_3^- ions is due to the discharge of untreated domestic waters.

EXPERIMENTAL SECTION

Collection site and water sampling

The water samples were collected from wells (Figure 2) located in Sândominic, Harghita County, Romania, in March and May 2020.

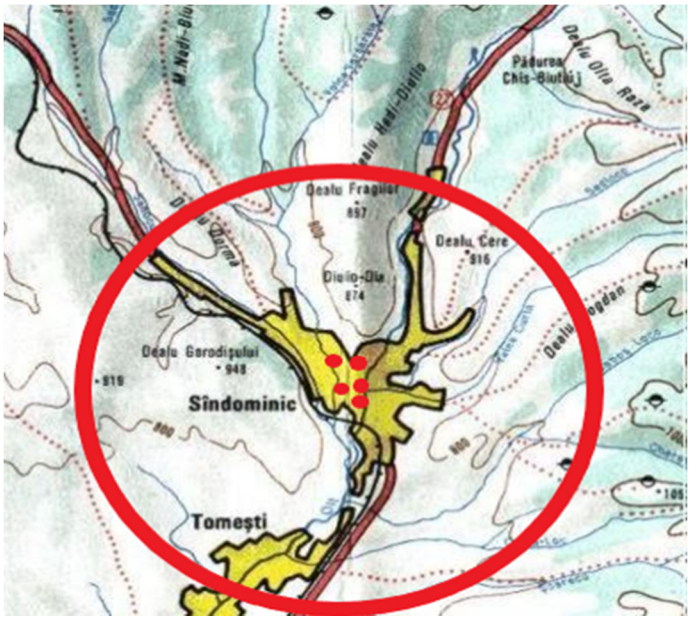

Figure 2. Sândominic commune, Harghita County, Romania; the water sampling points [26].

Sândominic commune is located at the intersection of latitude 46° 35 N, with the length of 25° 48 E, at 640 m above sea level. Specific to this region is the mountainous relief whose elevations vary between 840 m in the Olt Valley and 1792 m in the peak of Hășmașu Mare [25].

The mesometamorphic complex and the sedimentary rock system of the Hășmașu Mare massif

The western part is dominated by a high relief coming from the Neogene volcanic eruptions, made up of the Gurghiu and Harghita massifs, with characteristic volcanic morphology [28].

In this area the relief forms heights that reach up to 1800 m. In the crystalline-Mesozoic area, at the eastern limit of the perimeter, a rugged relief with steep slopes is specific. In the mesometamorphic lens, the rugged terrain forms are maintained, while in the epimetamorphic complex the aspects become more attenuated, with small variations in altitude. The contrast of the epimetamorphic-mesometamorphic lands can be observed conclusively on the Olt Valley [25-28].

Climate

The region is characterized by a temperate subalpine continental climate, with an average annual temperature of 5-6°C, The winds are closely related to major atmospheric circulations and relief conditions. Winds generally blow from the northwest, and spring and autumn are easterly, sometimes southerly winds [29].

Hydrography

Hydrographically, the region belongs to the upper basin of the Olt hydrographic network. The subalpine climate with relatively abundant annual precipitation determined the formation of a dense hydrographic network, characterized by small watercourses, with variable flow, but generally low. The flow of watercourses varies depending on the precipitations level. The hydrographic network is tributary to the Olt River, which has as main tributaries from the west: Szanduj brook, Sipos brook with Virgo tributaries, Jindieșul de Sus, Jindieșul de Jos, Ruțoc, Minei stream, Salamaș stream, Vărășoaia brook with tributaries Magasbukk, Voroc, Fagul Cetății Mici, Fagul Cetății Mari and Drumul Coastei [30].

It can be appreciated that the network in the western part is less developed than in the eastern part (despise the mesozone), where the water flows are higher. The tributaries from this zone are: Meggyes stream (with Vaspatak, Csofronkako, Csofronka tributaries), Nagyag stream, Mesteacăn stream, Szekpataka stream (with Gyengemenes tributary), Kovacs stream, Mihaly stream, Szimina stream, Galkut, Borviz, Szabók and Kurta stream. The rest of the valleys are torrential, with intermittent watercourses [26-30].

The groundwater samples were taken between the Olt River and Lunca Mare from Sândominic commune, and the surface water samples were taken from the Olt River and Lunca Mare stream.

Sources of groundwater and surface water pollution in Sâdominic commune

The main pollution sources for groundwater in Sândominic commune are: wastewater from septic tanks in households, the location of stables, latrines, landfills are located at a relatively short distance from wells, the existence of a chemical fertilizer depot.

For surface waters (Olt and Lunca Mare) the main sources of pollution are: wastewater resulting from the industrial technological process at copper mines (operated until 2006 in Balan city), the location of stables, latrines, landfills too close to the river Olt and Lunca Mare stream and meteoric waters.

Water samples were taken from wells located in the following areas: Sândominic no.1016 area (W1), Marton Aron General School (W2) and Gall

Sândominic no.1693 area (W3). The fountains have a depth between 6 and 8 m, the water depth in the fountain is 1-2.5 m, the variation of the water level after precipitation is 30-40 cm – for the fountain located on W1 and 4-5 cm for the fountain located in the W3 area. The distance to the nearest source of pollution is between 9-15 m, see table 3.

Water samples were collected in plastic containers, previously rinsed 2-3 times with the water sample, completely filled, and then closed so that no air bubbles remain inside the bottle. On wells equipped with pumps, the water sample was collected after a minimum of 10 minutes run, while from wells with extraction the samples collection was made introducing the bucket at 10-30 cm below the water mirror. After collection, bottles were placed in dark boxes.

Until the analyses were run water samples were kept at temperatures below 5°C and processed within 6 h from collection.

Table 3. The characteristics of the groundwater source.

Well water samples	Depth well (m)	Depth of the water in the well (m)	Variation of water level after precipitation (cm)	Distance to the nearest source of pollution (m)
W1	7	2.5	30-40	15
W2	8	2	-	9
W3	6	1	4-5	15

Water samples analysis

For the collected water samples, the following indicators were determined: the pH, acidity, alkalinity, total hardness, ammonia concentration, nitrite concentration, nitrate concentration, chemical oxygen consumption, iron ion concentration, Cl^- ion concentration and the fixed residue.

Wells water samples were characterized using the physico-chemical methods according to Romanian legislation (Laws 458/2002, 311/2004).

The pH were determined using a Consort C863 pH meter (SR ISO 10523/96), total dissolved solids (TDS) were determined using gravimetric method (Romanian STAS 3638/76). Total hardness and chemical oxygen demand were determined by volumetric method (Romanian STAS 3326-76, STAS 3002-85). Concentration of Fe_{total}, NO_2^- $NO_3^-$and NH_4^+ ions were determined using molecular absorption spectroscopy (SR 13315/96, STAS 3048/2-96, SR ISO 7890-3:2000, STAS 6328/85) using an UV VIS Spectrometer Jenway 6305.

Each sample was measured three times, the averaged values were presented.

REFERENCES

1. A. Cineti; “Resursele de ape subterane ale României”, Ed. Tehnica, București, **1999**, pp. 296-299.
2. M. Mănescu; “Poluarea apelor subterane: studii de caz”, Ed. Orizonturi Universitare, Timișoara, **2002**, pp. 240-251.
3. S. Manescu; M. Cucu; M. L. Diaconescu; “Chimia sanitară a mediului”, Ed. medicală, București, **1994**, pp. 40-158.
4. M. Chiba; A. Sinohara; M. Sekine; *J. Radioanal. Nucl. Chem.*, **2006**, *269*, 519-526.
5. Ordin nr. 161 din 16/02/2006 pentru aprobarea Normativului privind clasificarea calităţii apelor de suprafaţă în vederea stabilirii stării ecologice a corpurilor de apă.
6. Autoritatea Națională de Reglementare pentru Serviciile Comunitare de Utilități Publice – Raport de activitate, **2013**.
7. A. Delcea, I. Bitir-Istrate, R. Pătrașcu, C. Gheorghiu, *E3S Web of Conferences 85, 06008 (2019), EENVIRO 2018*, **2019**, 1-15.
8. M. Sabio; F. Zamora; J. Gañan,; C.M. González-García; J.F. González; *Water Res.*, **2006**, *40*, 3053-3060.
9. Y.S. Li; *Arch. Environ. Contam.Toxicol.*, **1996**, *31*, 557-562.
10. S. Cater; M. Stefan; J. Bolton; A. Safarzadeh-Amiri; *Environ. Sci. Technol.,* **2000**, *34*, 659-662.
11. Y. Ranran; C. Baoshan; *Procedia Environ. Sci.*, **2010**, *2*, 1745-1749.
12. M.A. Barron; L. Haber; A. Maier; J. Zhao; M.Burron; “Toxicological review of phenol” EPA/635/R-02/006, **2002**.
13. M. Stanca; A. Măicăneanu; C. Indolean; “Caracterizarea, valorificarea şi regenerarea principalelor materii prime din industria chimică şi petrochimică, Ed. Presa Universitară Clujeană, Cluj-Napoca, **2007**, pp. 6-28.
14. S. Burcă, C. Indolean, A. Măicăneanu, *Studia UBB Chem.*, **2015**, *3(3)*, 247-255.
15. M. Ielenicz; “Dealurile şi podişurile României”, Editura Fundaţiei „România de mâine”, București, **1999**, pp. 34-167.
16. C. Baciu; “Hidrogeologie. Elemente teoretice şi aplicaţii practice”, Ed. Cărţii de Ştiinţă, Cluj-Napoca, **2004**, pp. 151-158.
17. N. Mészáros; O. Clichici; “Pe poteci cu bănuţei de piatră: ghid geologic al zonei Cluj”, Ed. Tipored, București, **1967**, pp. 60-68.
18. M. Tokumura; A. Ohta; H. Znad; Y. Kawase; *Water Res.*, **2006**, *40*, 3775-3784.
19. J. Casado,;J. Fornaguera; M.I. Galán; *Water Res.*, **2006**, *40*, 2511-2516.
20. Z. Kassam; L. Yerushalmi; S. Guiota; *Water, Air, & Soil Pollution*, **2003**, *143*, 179-192.
21. Sanchez-Polo; J. Rivera-Utrilla; U. Gunten; *Water Res.*, **2006**, *40*, 3375-3384.
22. World Healt Report **2007**, “A safer future: global public health security in the 21st century“, World Health Organization, 1211 Geneva 27, Switzerland.
23. C. Nertan; C. Rosu, *Environ. Prog.*, **2010**, *12*, 293-298.

24. B. Almăşan, et col., Studiu complex al condiţiilor geologice şi minerale ale zăcământului pirito-cuprifer de la Bălan, în vederea optimizării metodelor de exploatare''. Universitatea Bucureşti, **1986,** pp. 3-48.
25. I.S. Atanasiu; "Cercetări geologice în împrejurimile Tulgheşului''; Anuarul I.G.al R.S.R., vol. XIII, **1928**.
26. www.carpati.org_harta_muntii_Hasmas_83_LI
27. I.Băncilă; "Geologia Carpaţilor Orientali''; Ed. St. Bucureşti; **1958**.
28. I. Bercia; E. Bercia; H.G. Krautner; "Unităţile tectonice structurale şi stratigrafice a formaţiunilor metamorfice din zona Cristalino-mezozoică a Munţilor Bistriţei''; D.S. vol III/1, **1996**.
29. A. Chelărescu; "Note sur legisement cuprifere Bălan. (Transylvanie)''; C.R.Inst. des Sci.Romanie, Acad. Des Sci III./2, **1939**.
30. D. Codarcea; ,,Noi date asupra stratigrafiei terenurilor cristalofiliene din România''; Studii şi cercetări Tom.12 Bucureşti, **1967**.

STUDIA UBB CHEMIA, LXVI, 1, 2021 (p. 127-142)
(RECOMMENDED CITATION)
DOI:10.24193/subbchem.2021.1.10

SURFACE WATER QUALITY ASSESSMENT IN SEMI-ARID REGION (EL HODNA WATERSHED, ALGERIA) BASED ON WATER QUALITY INDEX (WQI)

AMEL FERAHTIA[a,b], MOHAMMED TAHAR HALILAT[c], FATEH MIMECHE[d]*, ETTAYIB BENSACI[a,b]

ABSTRACT. The present study was aimed to assess the surface water pollution sources in a semiarid region of Algeria by characterizing the physicochemical quality of the water of the main Wadis of the El Hodna watershed and determining the water quality index according to the uses of drinking water, irrigation, and aquatic life. This index is calculated in purpose to communicate information on the water quality for concerned citizens and policymakers. The calculated WQI values of the studied Wadis were higher than 100, which indicates that the waters of the El Hodna watershed are unfit for human consumption, irrigation, and aquatic life. The obtained results have shown that different types of pollution (industrial, domestic and agricultural) affect the waters of the El Hodna watershed, which lead to degrade the water quality of this aquatic ecosystem and consequently its biodiversity and public health.

Keywords: *Water quality index, surface water quality, El Hodna watershed, Pollution, semiarid region, Algeria.*

INTRODUCTION

Water is a natural resource, and it forms the principal component of all living organisms in this world [1], which plays a massive role in different vital and structural activities. It is familiar that water is an essential source for industrial development, irrigation, hydroelectric production, drinking purposes, and domestic uses for human survival [2].

[a] *Department of Natural and Life Sciences, Faculty of Sciences, M'Sila University, M'Sila 28000, Algeria*
[b] *Biology, Water and Environment Laboratory (LBEE), University 8 Mai 1945 Guelma, BP 401, Guelma, 24000, Algeria*
[c] *Faculty of Natural and Life Sciences, University of KasdiMerbah, 30000, Ouargla, Algeria*
[d] *Department of Agricultural Sciences, M'Sila University, M'Sila, 28000, Algeria,*
** Corresponding author: fateh.mimeche@univ-msila.dz*

The requirement for water increased due to the expansion of agriculture and industry, urbanization, and the increase in the population demographic. In many countries, people depend on piped water supplied from reservoirs as well as private wells for their water needs [3]. Therefore, with an increased understanding of the importance of drinking water quality to public health and raw water quality to aquatic life, there is a great need to assess surface water quality [4].

Water quality indicates the relation of all hydrological properties including physical, chemical and biological characteristics of the water body. Hence, water quality assessment involves the analysis of physicochemical and biological parameters that reflect the biotic and abiotic status of the aquatic ecosystem [5]. The abundance of particular element might suggest the unstable or unfavorable ecosystem which can have a negative or positive impact on the population [6].

Many approaches have been applied to assess the water chemistry and status of the water quality in the river. The water indexes are the most effective tools to convey information about water quality to communities of users, those responsible for the management, decision-making authorities, and the public [7].The water quality index (WQI) can tell us whether the overall quality of water bodies possesses a potential threat to various uses of water, such as habitat for aquatic life, irrigation water for agriculture and livestock, recreation, esthetics, and drinking water supplies [8].WQI can reduce the bulk of the information into a single value to express the data in a simplified and logical form, it takes information from several sources and combines them to develop an overall status of a water system [1]. Many studies around the world have been using the WQI to survey the evolution of the surface water quality as well as in India [9], Benin [10], Nigeria [11], Turkey [12] and Egypt [13].

In Algeria, most studies have focused on the effects of industrial and urban discharges on surface water quality like [14], [15], [16], [17], [18] and [19]. The watershed of the El Hodna, with its large area located in a semi-arid region, its passage between the Tellian domain to the north and the Sahara to the south, promotes the diversity of bioclimatic environments that strongly influences the socioeconomic activity of these regions. This study area is highly influenced by human pressure resulting to domestic, agricultural, and partially industrial activities. In the aim to improve our knowledge on the water pollution resources of the El Hodna watershed, we tried to characterize the physicochemical quality and determine the WQI of the main Wadis of this watershed to verify their ability for consumption, their use in agriculture irrigation and for aquatic life referring to acceptable norms.

RESULTS AND DISCUSSION

Surface water properties

Table 1 shows the physico-chemical parameters per Wadi with the mean, standard deviation (SD), minimum and maximum.

The spatial differences between the TS, Salinity, Turbidity, NO_3^-, NO_2, Cl^- and SO_4^{2-} variables were significant ($p < 0.05$). No spatial differences were observed for the remaining of the physicochemical parameters.

The surface water temperature ranged between (12.5 C°- 27C°) at all the nine studied Wadis (Table 1). The minimum value (12.5C°) was observed in Wadi El Ham (01) and the maximum value (27C°) was observed in Wadi Khobana. The temperature modified by the climatic conditions, the sampling time humidity, and sunlight exposure [20].

The recorded values of electrical conductivity were shown notable variations from Wadi to another. The maximum value of 7767.36 µS/ cm was recorded in Wadi El ham (01). According to [21] the high conductivity could be interpreted by domestic and industrial effluent discharges transport a lot of dissolved conducting minerals into the water bodies. The minimum value of 786 µS/ cm was recorded in Wadi Lougmen, this can be explained to the dilution of the water by the addition of rainwater [22]. Important changes in conductivity can be an indicator that some other source of pollution has entered the stream [23].

The pH of the water samples ranged between 6.56 to 8.90, these values were found to be nearly neutral or alkaline, which characterize the calcareous soils of the El Hodna region. The minimum value of 6.56 was observed in Wadi El Khobana and the maximum value of 8.90 was found in Wadi Bousâada. The increase in the pH could be related to the photosynthesis and the growth of aquatic plants, where the photosynthesis consumes CO_2 and leads to a raising in the pH values [13].

The Dissolved oxygen concentration results varied from one station to another, depending on the nature of the microclimatic conditions and pollution extent. Almost all the water samples collected from the Wadis had considerably low DO values. The maximum value was recorded in Wad M'cif (7.34 mg/l), and the minimum value was noted in Wadi Bousâada (1.25 mg/l). The lowest concentrations were due to the additional discharge of sewage and other waste combined with the microbial decomposition of the organic matter [17].

Table 1. Mean ± SD (standard deviation), min and max of physico-chemical parameters per Wadi.

	Wadi M'Sila	Wadi Logmen	Wadi Djnen	Wadi K'sob	Wadi M'cif	Wadi khobana	Wadi Bousâada	Wadi ELHam 1	Wadi EL Ham 2
T (°C)	23.10 ± 2.85 (20.3, 26.00)	21.16±3.62 (24.3, 17.20)	19.8±1.31 (21,18.40)	20.87±3.17 (24.50, 17)	20±7.07 (25 ,15)	23.80 ±4.53 (20.60, 27)	19.83 1.62 (21.10, 18)	16.06± 3.45 (19.40, 12.50)	17.55±4.88 (21, 14.10)
pH	7.5±1,12 (8.83, 6.5)	7.71±0.66 (8.33,7)	8.04 ±0.56 (8.63 , 7.5)	8.06 ±0.46 (8.72, 7.60)	7.60 ±0.57 (8 ,7,20)	6.79±0.32 (7.01, 6.56)	8.10± 1.24 (8.90, 8.75)	7.94± 0.74 (8.35, 7.08)	7.72 ± 0.99 (8.42, 7.02)
CE (µs/cm)	2459,79± 1176,53 (3649 .50,1296.62)	1906±1552.62 (3678.5, 786)	(2563,66±1445,9) (4210, 1500)	1743,5±121,43 (1856, 1575)	1817.26 ± 3530 (4815 , 2245)	2441.53 ± 645.12 (2897.70, 1985.36)	1935.3± 462.66 (2290,1412)	5765.75± 2273.82 (7767.36 ,3293.4)	5374.25±3198.60 (7636,3112.5)
TDS (mg/l)	1801,66±866,73 (2647 ,915)	1724,33±410,75 (2120, 1300)	2205.66 ±837.94 (3167,1630)	1124,07±382,37 (1595,794)	1067.25± 1100.61 (289,1845.5)	2450.50±1898.58 (3793, 1108)	1404.16±353.62 (1812.50, 1200)	2849 ± 1648.19 (4620, 1360)	2937 ±1581.09 (4055 ,1819)
HCO_3^- (mg/l)	367.88±90.5 (445-,268.25)	300,8±71,44 (378,237)	552.6±1189.87 (755.378,4)	388,72±142,27 (586,257.50)	283.90±56.43 (323.80, 244)	102.39±330.20 (402.60, 257.80)	516.33±234.22 (710, 256)	232.16 ± 65.94 (305, 176.5)	222.50±142.13 (323, 122)
Ts (mg/l)	1230,94 ±395,46 (1687,982.83)	1467,33±864,81 (2465,931)	1778.66±1118.80 (3145,981)	1284,17±138,24 (1406, 1087.7)	3153.88±701.28 (3649.77, 2658)	1685.95± 256.04 (1867,1504.9)	1581.66±286.37 (1345,1900)	4416.63±1706.29 (5887,65,2546)	2649.02±1067.05 (3403,54,1894,5)
Salinity (‰)	12 ±7 (7,20)	3,03±2.58 (5, 0.1)	9,26±1.75 (11,7.5)	7.2 ±4.44 (11 ,0.8)	19,5 ±13,43 (29 ,10)	9.5 ±2.12 (11, 8)	22.33± 7.5 (30,15)	36±10.58 (48.28)	38.5 ±12.02 (47.30)
OD (mg / l)	3,49±0,62 (4.13,2.9)	4.63± 0.96 (5.70,3.83)	4.23±1.76 (2.8,6.2)	3,93±1,60 (6.23, 2.79)	6.41±1.32 (7.34,5.48)	2.85 ±1.48 (3.90,1.80)	2.48 ±1.76 (4.50, 1.25)	4.39 ±1.03 (3.23, 5.22)	3.22 ±1.10 (4 , 2.44)
Turb (NTU)	96.93 ±28.61 (125, 67.80)	15.50±8.31 (25,9.51)	14.44±15.25 (32, 4.45)	25,33±18,37 (45.03, 3.02)	5.78± 5.79 (9.87, 1.68)	26.41±23.51 (43.03, 9.78)	30.95±21.59 (52,8.85)	63.66± 53.50 (124, 22)	13.30± 10.05 (2040, 6.19)
TH (f°)	99.13±46.02 (150, 60.40)	324,6 ±262,33 (620 ,118.8)	418.66±304.33 (704.5, 98.70)	264.2±337,25 (769, 70)	194.25± 39.95 (222.50, 166)	19.45±101.75 (115.50, 88)	446.83 ± 145.48 (600, 310.5)	487.66± 337.61 (840, 167)	126 ± 70.71 (176, 76)
NO_3^- (mg/l)	8.14 ±10 .47 (19.42,0.38)	7.14 ± 6.20 (12.56,0.37)	6.12±5.81 (12.14, 0.53)	9,14 ± 7,81 (17.8, 0.62)	1.88± 1.71 (3.09, 0.67)	14.53±5.70 (18.56, 10.50)	1.73 ±1.80 (3 ,0.45)	2.22± 1.86 (4.09 ,0.36)	0.54± 0.48 (0.88, 0.20)
NO_2^- (mg/l)	0.69±0.23 (0.90, 0.44)	3.85±2.86 (6.70, 0.97)	1.67±1.17 (2.41 ,0.32)	1,04 ± 1,02 (2.41, 0.22)	0.13 ± 0.11 (0.20, 0.05)	1.13±1.56 (2.23 , 0.02)	0.26 ± 0.19 (0.38 , 0.03)	0.33 ±0.31 (0.70, 0.10)	0.10±0.09 (0.17, 0.03)
NH_4^+ (mg/l)	1.02±0.65 (1.48,0.56)	1.03 ±1.24 (2.43 , 0.03)	2,06±1,78 (3.6, 0.10)	0,39± 0,39 (0.95 , 0.05)	0.55± 0.75 (1.08,0.02)	0.77±0.95 (1.44, 0.09)	1.69± 1.42 (2.87, 0.1)	1.48± 2.36 (4.21, 0.08)	0.78 ±1.02 (1.50, 0.06)
Po_4^{-3} (mg/l)	0.27±0.08 (0.35, 0.20)	7.34 ± 10.15 (19.02 ,0 .60)	0.95±0.92 (5.6,0.3)	0.30 ± 0.24 (0.03 , 0.52)	0.63± 0.85 (1.23 ,0.03)	1.03±1.17 (1.85, 0.20)	0.76 ± 0.5 (1.30, 0.3)	0.23 ±0.15 (0.40 ,0.09)	0.83 ±1.10 (1.6, 0.05)
Cl^- (mg/l)	315 .5 ±70.47 (388.20,247.50)	215.43± 144.64 (367.8,80)	302.9±145.61 (436.2, 147.5)	282,35± 75,57 (395.1 , 234.5)	273.65 ± 760.50 (954, 567)	326.29± 86.42 (387.40, 265.18)	206.43 ± 87.23 (263.3, 106)	2926.45±2616.26 (5745,67.576,7)	1633.90±1463.85 (2669, 598.8)
SO_4^{-2} (mg/l)	504.3±207.96 (743.40, 365.5	287,56 ±50.46 (324.2, 230)	255.5±216.33 (410, 102.5)	538.70± 224.44 (697.40, 380)	406.40± 26.73 (425.30, 387.50)	623.15± 192.55 (759.30 ,487)	267.66± 74 (320, 183)	969.66± 381.88 (1391.50, 647.50)	877.65 ± 214.04 (1029, 726.3)
Ca^{+2} (mg/l)	154.17±50.28 (211, 115.50)	163.74± 63.86 (231.4, 104.50)	295.71 ± 322.10 (531.20, 113)	141,20 ± 24,40 (187.22 , 101)	190.55±97.09 (259.20 ,121.90)	228.70±51.90 (265.40 ,192.00)	358.46± 74.84 (473.4, 170)	670.13 ± 381.38 (1104, 387.80)	386.25± 392.80 (108.5, 664)
Mg^{+2} (mg/l)	80.55±19.42 (102, 64.15)	(84.95 ±24.57) (112, 64)	365.32.±311.12 (699.48, 84)	77,62 ± 24,40 (103.5 ,46)	170.50± 06.77 (246, 95)	99.10± 2.69 (101, 97.20)	151.41±74.84 (195.65, 65)	635.87 ± 762.69 (1516.32 , 178)	41.14 ± 22.44 (57 ,25.27)
DBO	48 ± 13.11 (60,34)	30.33± 2.51 (33,28)	35 ± 5.56 (40 ,29)	37 ± 10,13 (50.28)	31.5 ± 7.7 (37 ,26)	57.5 ±3.53 (60, 55)	60 ± 26.45 (80 ,30)	34.33 ± 9.29 (45,28)	35 ± 7.07 (40, 30)

The properties of the TDS, TS and salinity of all the studied samples were ranged between 289- 4620 mg/l,931- 5887.65 mg/l and 0.1- 48‰ respectively. The highest concentrations of these parameters were found in Wadi El Ham (01) (Table 1). The lowest TDS was found in Wadi M'cif (289 mg/l), while the lowest TS and salinity were found respectively in Wadi Lougmen (931 mg/l, 0.1‰). The ecological imbalance in the aquatic ecosystem caused by the technical abrasive action of total solids [24]. The excess of dissolved solids affects the water quality for all its uses; drinking, agricultural and industrial purposes. Many problems caused by high concentrations of TDS like a bad odor and taste, hardness, corrosion, and scaling in the water supply system [23]. Salinity, TS, and TDS augmentation are original to the effluent discharges from several industrial establishments around the El Hodna basin, also they are due to the domestic activities, lithologic composition, and evaporation effects under the arid climate of this region, which can promote the concentration of salts in water.

The turbidity values in the present study are exhibited between (1.68-125 NTU). The maximum value was observed at Wadi M'Sila (125 NTU) and the minimum value was reported in Wadi M'cif (1.68 NTU). The high turbidity in M'Sila Wadi may be explained by the discharge of the wastewater and the waste construction materials, because it crosses several urban agglomerations and industrial zones of M'Sila. The high turbidity causes reduced transparency of water due to the presence of particles such as clay or silt, finely divided organic matter, plankton, or other microscopic organisms [20]. Besides, raised values of turbidity lowering the biological productivity of aquatic organisms [25].

The total hardness from the water samples are ranged between 60.40 f° and 840 f°. The lowest amount of total hardness was recorded in Wadi M'Sila, this decreaseis due to the low concentration of calcium and magnesium [10], while the highest total hardness was recorded in Wadi El Ham (01) due to the addition of large quantities of urban sewage discharged in this Wadi [26]. According to [27] the variation of the total hardness in the water can be related to the nature of the soil traversed.

The chloride values are high almost in all the studied Wadis, the minimum value was recorded in Wadi Lougmen (80 mg/l) and the maximum value (5745.67 mg/l) was recorded in Wadi EL Ham (01). The high chloride concentration is due may be to the disposal of sewage water of Baniou city in this Wadi. Human and other animals release a very high quantity of chloride together with nitrogenous compound (urine and feces) [2]. The concentration of these chemical element considered an important parameter for the detection of contamination by the domestic sewage [28-29].

The phosphate values in the present study were ranged between 19.02 to 0.03 mg/l, where the minimum values were observed at Wadi M'cif, and the maximum values were noted at Wadi Lougmen, due probably to the augmentation of pollution loaded by organic matter and agricultural runoff around this station. Phosphate is one of the limiting nutrients causing the eutrophisation [30]. The major sources of phosphate in the water are domestic sewage, agriculture effluents, and industrial wastewaters. Thus, the high concentration of phosphate considered as a pollution indicator [31].

The concentration of sulphate in the present investigation varied from 102.5 to 1391.5 mg/l. All the stations reported high concentrations of sulphate. The minimum concentration was recorded in Wadi Djnen (102.5 mg/l) and the maximum concentration was recorded in Wadi El Ham (01) (1391.5mg/l). These high levels of sulphates are due to wastewater and domestic discharges. Sulphates come from run-off, fertilizers containing relatively large amounts of organic and inorganic sulfur compounds, SO_4^{-2} ions in water under natural conditions [32].

The values of bicarbonate fluctuated between 122 and 755 mg/l.The maximum value was found in Wadi Djnen, and the minimum value was observed in Wadi El Ham (02). The highest bicarbonate concentration in Wadi Djnen was explained by the evacuation of domestic effluents and solid waste, which attributed to the presence of a large amount of organic matter accessible to bacterial decomposition [33], during which CO_2 is liberated and dissolves in water and accelerates the formation of HCO_3^-[34].

The nitrate varied between 0.2 mg/l in Wadi EL Ham (2) and 19.41mg/l in Wadi M'Sila. The higher concentration of No^-_3 maybe due to the influx of nitrogen in the floodwater and the discharge of domestic, industrial wastewaters and runoff from agricultural fields settled across the El Hodna watershed, which can lead to excessive proliferation of algae in the water body and can lead to eutrophication of the environment [35].

However, the nitrite was relatively low, except Wadi Lougmen, which marked a high value (6.7 mg / l) that could be explained by the incomplete oxidation of organic matter, particularly in summer denitrifying bacteria break up nitrates into nitrites and ammonia. Nitrite in water bodies is derived essentially from industrial waste and domestic waste [36].

Ammonium levels ranged between 0.02 mg/l and 4.21 mg/l. The low concentrations of ammonium in all Wadis can be explained by the transformation of the ammonium in nitrate by the nitrifying bacteria, also by the assimilation of the ammonium ion by the aquatic plants [37]. Generally, it comes from the biodegradation of waste and inputs from domestic, agricultural and industrial [38]. The presence of NH_4^+ with high concentrations in a stream or a lake can result in algae blooming and eventually the destruction of the aquatic ecosystem [39].

The minimum of the Calcium concentration was registered in Wadi El K'sob (101 mg/l) and the maximum value is in Wadi El Ham (01) (1104 mg/l). Calcium is responsible for contaminating the water, where the disposal sewage of industrial waste is considered an important source of calcium [2].

The minimum value of Magnesium concentration is 25.27 mg / l in Wadi El Ham (02), while the maximum value recorded at Wadi El Ham (01) (1516.32 mg/l), it might be due to the illegal elimination of domestic and industrial wastewater [40] in this Wadi. The high magnesium values can be toxic to aquatic life [37].

Biochemical oxygen demand (BOD) is used to determine the level of organic pollution of the water. The BOD recorded from all the nine Wadis ranged between (26 - 80 mg/l). The highest BOD value was observed at Wadi Bousaada, and the lowest was in Wadi M'cif. This increase of BOD5 in Wadi Bousaada is due to disposal of domestic, industrial effluents, and slaughterhouse operations, it is the most commonly used parameter for determining the oxygen demand on receiving water of a municipal and industrial discharge [40]. The higher the amount of BOD, the higher will be the amount of pollution in the water [41].

Relationships between water physicochemical parameters

The Pearson correlation matrix obtained from our study for each parameter is showed in the (Table 2). The temperature showed positive correlation with NO_3^- (r = 0.743). While the pH showed positive correlation with HCO_3^- (r =0.782) and TH (r = 0.690). Positive correlations observed between conductivity and salinity, TDS, TS Cl^-, Ca $^{+2}$and So_4-^{2} (r between 0.703 and 0.945). It can be seen that TDS ,TS and salinity are positively correlated with each other and with the minerals Cl^-, So_4^{+2} ,Ca^{+2} and Mg^{+2}, also the concentration of chloride has a significant positive relation with So_4^{2-}, Ca^{+2}, Mg^{+2}, this, indicates a large presence of inorganic dissolved solids due either to human influences or to the geological nature of the terrain crossed. However, the strong positive correlation of calcium with Mg^{2+} (r = 0.827) may be indicate the common origin [42].

The results of the Principal Component Analysis reveal that the first two axes account for 57.45% of the variability in the influence of physicochemical parameters on the sites. The F1 axis has a variance of 37.52 % and the F2 axis has 19.93%. Based on PCA, three groups were identified: 1, 2, and 3. The factorial axes shows that the group 1 (cluster 1) formed by the site of Wadi EL Ham 1, Wadi EL Ham 2 and Wadi Djnen (Figure 1).

Table 2. Coefficient of the water quality correlation of Wadis in El Hodna watershed.

	T(°C)	pH	CE(µs/cm)	TDS (mg/l)	Ts (mg/l)	Salinity (%)	HCO_3^- (mg/l)	DO (mg / l)	Turbid (NTU)	TH (F°)	NO_3^- (mg/l)	NO_2^- (mg/l)	NH_4^+ (mg/l)	Po_4^{-3} (mg/l)	Cl^- (mg/l)	SO_4^{-2} (mg/l)	Ca^{+2} (mg/l)	Mg^{+2} (mg/l)	BDO_5 (mg/l)
T(°C)	1																		
pH	0.324	1																	
CE (µs/cm)	-0.529	-0.523	1																
TDS (mg/l)	-0.252	-0.286	**0.776***	1															
Ts (mg/l)	-0.363	-0.485	**0.925****	**0.676***	1														
Salinity (%)	-0.393	-0.374	**0.945****	**0.722***	**0.887****	1													
HCO_3^- (mg/l)	0.659	**0.782***	-0.659	-0.378	-0.559	-0.466	1												
D O (mg / l)	-0.235	0.235	0.150	-0.098	0.392	0.210	0.018	1											
Turbidity (NTU)	0.255	-0.388	0.240	0.351	0.373	0.190	-0.224	0.172	1										
TH (F°)	0.337	**0.690***	-0.030	0.287	0.114	0.026	0.519	0.321	-0.001	1									
NO_3^- (mg/l)	0.743*	0.115	-0.374	-0.219	-0.348	-0.380	0.429	-0.608	-0.060	0.166	1								
NO_2^- (mg/l)	-0.190	0.296	-0.370	-0.124	-0.319	-0.459	-0.067	0.231	-0.155	0.206	-0.382	1							
NH_4^+ (mg/l)	0.391	-0.553	-0.318	-0.250	-0.305	-0.355	-0.079	-0.498	0.427	-0.633	0.351	-0.215	1						
Po_4^{-3} (mg/l)	-0.229	-0.185	-0.103	0.168	-0.229	-0.228	-0.338	-0.452	-0.305	-0.160	-0.084	0.647	0.107	1					
Cl^- (mg/l)	-0.217	-0.418	**0.877****	**0.868****	**0.918****	**0.804****	-0.481	0.204	0.528	0.280	-0.209	-0.253	-0.245	-0.123	1				
SO_4^{-2} (mg/l)	0.113	-0.514	**0.703***	**0.707***	**0.760***	0.619	-0.415	-0.133	0.487	0.193	0.248	-0.396	0.042	-0.042	**0.865****	1			
Ca^{+2} (mg/l)	-0.172	-0.154	**0.787***	**0.883****	**0.803****	**0.811****	-0.155	0.227	0.362	0.435	-0.245	-0.315	-0.382	-0.218	**0.897****	0.679*	1		
Mg^{+2} (mg/l)	0.072	-0.088	0.487	0.599	**0.680***	0.461	0.040	0.413	0.518	0.568	-0.061	-0.209	-0.236	-0.359	**0.779***	0.632	**0.827****	1	
BDO_5 (mg/l)	0.352	-0.077	-0.269	-0.281	-0.273	-0.027	0.280	-0.206	-0.084	-0.417	0.040	-0.248	0.489	-0.008	-0.388	-0.265	-0.226	-0.365	1

*Correlation is significant at the 0.05 level (2-tailed)

**Correlation is significant at the 0.01 level (2-tailed)

Thus cluster record high values of turbidity, HCO_3^-, SO_4^{-2}, TDS, TS, Cl^-, Ca^{2+}, Mg^{+2}, CE, pH and NH^{+4}. This shows an inorganic pollution in the water related to the domestic activities in these stations. The BDO_5, NO_3^- and temperature are located on the same side of the (cluster 2) formed from the following sites: Wadi M'Sila, Wadi khobana, Wadi Bousaada which shows an urban, industrial and agricultural organic pollution. Therefore, the sites: Wadi M'cif, Wadi K'sob, Wadi EL Khobana (cluster 3) have high values of NO_2^-, PO_4^- associated with the impacts of agricultural activities (leaching of fertilizers) in the areas surrounding these Wadis.

*Correlation is significant at the 0.05 level (2-tailed)
**Correlation is significant at the 0.01 level (2-tailed)

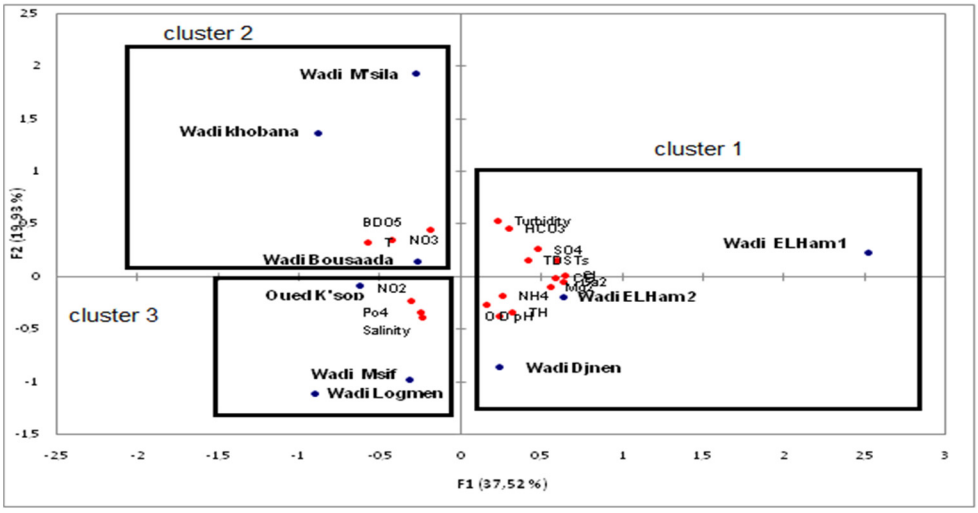

Figure 1. Projection of physico-chemical parameters on the factorial planes axes 1 and 2, with the stations and groups.

Water quality index

The Water Quality Index (WQI) gives the overall quality of water based on large number of physico-chemical characteristics of water [43].

Table 03 illustrate the values of the WQI of the studied Wadis that flow in across the El Hodna basin and dump at the chott El Hodna. The WQI score for Drinking water was calculated using guidelines of [44] and [45] for irrigation water. While, aquatic life index was calculated using CCME guideline [46]. Only 09, 10 and 8 variables were used for the calculation of WQI according to Dinking, irrigation and aquatic life criteria respectively.

The selected parameters for drinking water are TDS, pH, NO_2^-, NO_3^-, Cl^-, SO_4^{-2}, Ca^{+2}, PO^{-3}_4, Mg^{+2}. However, TDS, pH, CE, NO_3^-, PO^{-3}_4, HCO_3, Cl^-,

SO_4^{-2}, Ca^{+2} and Mg^{+2} were selected for irrigation. The selected variables for Aquatic life are T, TDS, pH, DO, BOD_5, NO_2^-, NO_3^- and Cl^-.

The calculated WQI values for the studied Wadis ranged between 23.7- 633.95 for the drinking water, 6.30-97.72 for the irrigation water and 18.09-10616.35 for the aquatic life guidelines (Table 3).

Table 3. WQI and its categorization of different Wadis of El Hodna basin for drinking, irrigation, and aquatic life utilization.

WADIS	WOI Irrigation	WQR	WQI Aquatic life	WQR	WQI DW	WQR
Wadi M'Sila	18.06	excellent	712.6	unfit	146.45	unfit
Wadi Lougmen	97.72	very poor	10616.35	unfit	633.95	unfit
Wadi K'sob	55.35	poor	18.09	excellent	349.02	unfit
Wadi M'cif	6.30	excellent	327.08	unfit	23.27	excellent
Wadi EL Khobana	83.86	very poor	53.79	poor	557.12	unfit
Wadi Bousaada	31.16	good	79.95	very poor	124.82	unfit
Wadi EL Ham 1	28.592	good	171.36	unfit	159.29	unfit
Wadi EL Ham 2	59.38	poor	280.87	unfit	339.35	unfit
WadiDjnen	39.45	good	52.63	unfit	172.13	unfit

WQI: water quality index. *WQR:* water quality rating.

Our study indicates that the fluctuation of the water quality index varied from excellent to very poor for water irrigation utilizations, where the highest value of WQI was registered at Wadi Lougmen (97.72), Wadi K'sob (55.35), Wadi Khobana (83.86) and Wadi El Ham (01) (59.38) which indicate poor and very poor water quality.

Based on WQI values, the water quality categorized from very poor to unfit for aquatic life guidelines. However, the water at Wadi K'sob was found excellent. Although, as recommendations on drinking water, except Wadi M'cif (23.27; excellent), all the other Wadis have unfit quality, with a quality index greater than 100, that make them inappropriate for any domestic purposes. A high concentration of EC, TDS, HCO_3, Cl^-, DBO_5, PO_4^{-3}, NO^-_3, NO_2^-, Cl^- and SO_4^{-2}could explain the high values of the water quality index (WQI) in these Wadis. The results of our study also indicate a large pollution load in the Wadis of the El Hodna basin. The high WQI values are contributed mainly by various

anthropogenic activities such as discharge of untreated wastewater, sewage water, industrial effluents and agricultural runoff lead by many Wadis. Hence, our study concludes that the continuous pollution of the water sources by the human activities can lead to the degradation of the surface water quality (Chott El Hodna) and the ground water of this basin which considered the main water supply of the population of this semi-arid region.

CONCLUSIONS

The evaluation of the physicochemical quality of the water of the El Hodna basin Wadis that discharge in Chott El Hodna has allowed us to identify the pollution sources and the degree of contamination that affects this wetland of international importance. Overall, the obtained results revealed that most water quality parameters exceeding acceptable limits.

The direct discharge of urban waste and sewage water in the Wadis of the El Hodna basin and the intensive use of fertilizers in agriculture along the watershed make these waters very vulnerable to pollution and consequently the degradation of these waters, which leads to the loss of biodiversity of these aquatic ecosystems. Although, the results of the WQI show that the quality of the water of the different studied Wadis changed from excellent to very poor for irrigation, poor to unfit for consumption for aquatic life, except Wadi K'sob (excellent), and unfit for the human consumption for drinking water except Wadi M'cif (excellent). The value of the WQI indicates the extent of pollution when the domestic discharges and the agricultural activities constituted the major threat to the water quality of these Wadis. In order to preserve the water quality (surface and groundwater) of the El Hodna basin against further degradation effective pollution monitoring should be taken shortly.

For this purpose, strict precautions should be taken along these Wadis and within the El Hodna basin to ensure safe human activities. Also, regular monitoringof the water quality of these Wadis and takes into account all protection measures by the concerned members and the local authorities.

EXPERIMENTAL SECTION

Study Area

The Hodna basin is with a drainage area of 26 000 km², and it is the fifth largest basin in Algeria, it is located between 36°11' and 34°29' N latitude and between 3°2' and 6°11' E longitude (Figure 2). This basin straddles two

distinct geological and geomorphological domains. To the north and north-east is the Tellian Atlas, and to the South, the Saharan Atlas. The situation of this basin between two series of mountains to the north and the south, organizes it as an endorheic basin around an almost flat bowl at 400 m altitude. At the center of this basin, the dry salt lake named “Chott El Hodna” covers around 1150 km². This area receives the water and the sediment yields of the whole Wadis of the region [47].

The El Hodna watershed is characterized by a semi arid climate, with annual mean rainfall less than 200mm per year and high temperatures in the summer and low in the winter [48]. The lowest temperature is reached during January with a value of 1.44 °C, while the maximum is 37.92°C in August (Meteorological station of M’Sila from 1988 to 2014).

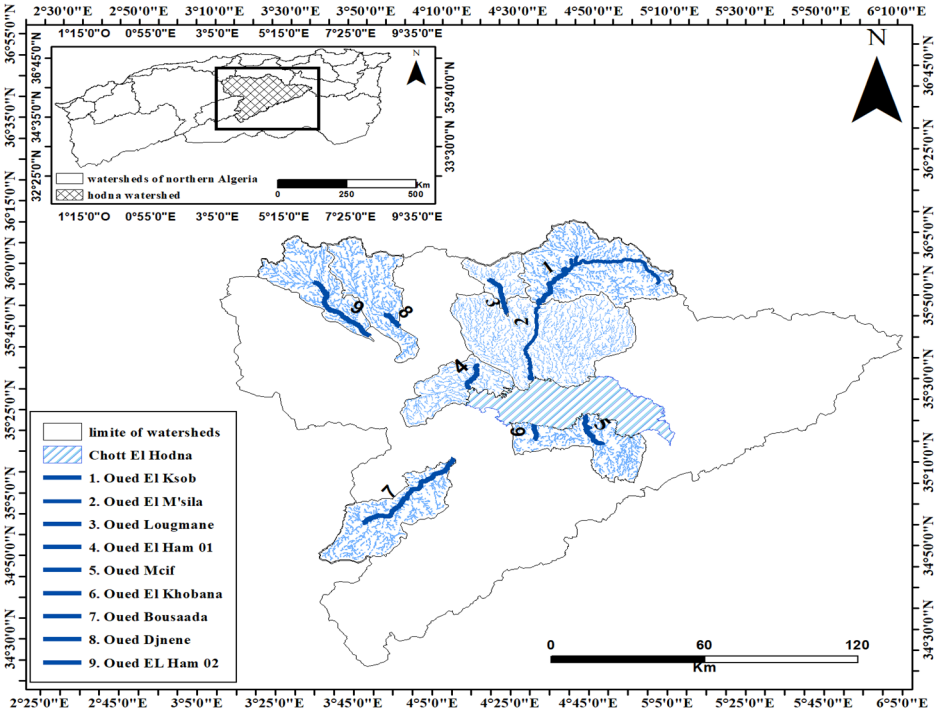

Figure 2. Situation of studied Wadis in El Hodna basin.

Water sampling and analysis

Nine Wadis of the Hodna basin are chosen as sampling sites, which they flow into Chott El Hodna.

The water samples were collected during April 2018 by clean polyethylene bottles, where they rinsed thrice before sample collection. Parameters such as pH, dissolved oxygen, temperature, salinity, conductivity and TDS were measured in situ by using a portable multiparameter. All samples are labeled properly after that they transported in cooler boxes at a temperature below 4 C° immediately to the laboratory for analysis of other physicochemical parameters. Biochemical oxygen demand (BOD_5) was measured using an OxiTop IS12. Chloride was measured using Mohr's method. TS was determined by the drying and the weighing method, while bicarbonate was detected by titration method using 0.01 N (HCl), Turbidity measured by Turbidimeter (HACH 2100N). The total Calcium and magnesium hardness were analyzed by volumetric titration methods. Nitrates, nitrites, phosphates, and ammonium have been dosed by a flame spectrophotometer [49].

Statistical Analysis

ANOVA test was performed to search for a possible variation it was employed for each parameter and each Wadi.

Pearson's correlation coefficient was applied to calculate the relationship between various physicochemical parameters. Significance levels of tests were taken as $p < 0.05$ and highly significant as $p < 0.01$. Also, the Principal Component Analysis (PCA) biplot was employed to show tendencies or clustering patterns. All the statistical analyses were performed with SPSS statistical software (2012 version 18.0).

Water quality index

WQI is one of the most effective tools to monitor surface and ground water pollution. In the formulation of the water quality index the relative importance of the various parameters depends on the intended use of water [50].

WQI has been calculated to evaluate the water quality of Wadis the El Hodna basin through several steps of the weighted arithmetic index method given by [51]:

$$WQI = \sum Q_i W_i / \sum W_i$$

where Q_i is the sub quality index of the i^{th} parameter (or Qi is the quality rating scale of each parameter), W is the weight unfit of each parameter, and n is the number of parameters.

Calculation of Qi : $\mathbf{Q_i=100[(V_i-V_0/S_i-V_0)]}$

Where, Vi is the estimated concentration of i^{th} parameter in the analyzed water, Vo is the ideal value of this parameter in pure water, Vo = 0 (except pH = 7.0 and DO=14.6mg/l), S_i is the recommended standard value of i^{th} parameter.

Calculation of Wi

Calculation of unfit weight (*Wi*) for water quality parameters is inversely proportional to the recommended standards for the corresponding parameters.

$$\boldsymbol{W_i= K/S_i}$$

Where, (K) = the proportionality constant and it can also be calculated by using the following equation: $\boldsymbol{K= 1/\sum (1/S_i)}$
WQI has been classified into 5 classes, the water quality is rated between excellent, good, poor, very poor and unfit consumption when the value of the index lies between 0-25, 26-50, 51-75, 76-100 and >100, respectively (Table 4).

Table 4. Water Quality Index (WQI) range and status [50].

Water Quality index	Water Quality Status
0-25	Excellent
26-50	Good
51-75	Poor
76-100	Very poor
>100	Unfit for Consumption

ACKNOWLEDGMENTS

We thank the technical staff of biology laboratory of M'Sila University for their help in water analyzing.

REFERENCES

1. R. Subramanian; R. Vidhya; V.N. Mariappan; *Eco. Env. Cons.,* **2018**, *24*, S392-S402.
2. S. Bhasin; A.N. Shukla; S. Shrivastava; U. Mishra; *Haya: Saudi. J. Life Sci*., 2016, *1*, 51-64.
3. K. Brindha; R. Kavitha; *Environ. Earth Sci.*, **2015**, *73(9)*, 5383–5393.
4. Y. Ouyang; *Wat. Res.*, **2005**, *39(12)*, 2621-2635.
5. A.D. Smitha; P. Shivashankar; *Int. Res. J. Enviro. Sci.*, 2013, *2(8)*, 59-65.

6. S.G. Patil; S.G. Chonde; A.S. Jadhav; P.D. Raut; *Res. J. Recent Sci*., **2012**, *1(2)*, 56 - 6.
7. E.R. Salcedo-Sánchez; S.E.G. Hoyos; M.V.E. Alberich; M.M. Morales; *Environ. Monit. Assess*., **2016**, *188 (10)*, 1-2.
8. N.C. Kankal; M.M. Indurkar; S.K. Gudadhe; S.R. Wate; Asian. *J. Exp. Bio, Sci*., **2012**, *26(1)*, 39-48.
9. D. Tyagi; D.S. Malik; *Int. J. Curr. Res. Life. Sci*., 2018, *7(8)*, 1234-1239.
10. J.E.B. Zandagba; F.M. Adandedji; B.E. Lokonon; A. Chabi; O. Dan; D. Mama; *Am. J. Environ. Sci. Eng*., **2017**, *1(4)*, 117–127.
11. A.E. Donald; U.A. Blessing; *Int. J. Fish. Aquat. Stud.,* 2019, *7(1),* 153-159.
12. Ş. Şener; E. Şener; A. Davraz; *Sci. Total Environ*., 2017, *584*, 131-144.
13. A.D.G. Al-Afify; A.A. Othman; M.F. Ramadan; *Rend. Lincei. Sci. Fis. Nat.* 2018, *29(3)*, 725–736.
14. S. Bouaroudj; A. Menad; A. Bounamous; H. Ali-Khodja; A. Gherib; D.E. Weigel; H. Chenchouni; *Chemosphere,* **2019**, *219*, 76-88.
15. N. Bougherira; A. Hani; F. Toumi; N. Haied; L. Djabri; *Hydrol. Sci. J*., **2015**, *62(8),*1290-130.
16. A. Toumi; A. Reggam; H. Alayat; M. Houhamdi; *J. Mater. Environ. Sci*., **2016**, *7(1)*,139-147.
17. A. Reggam; H. Bouchelaghem; M. Houhamdi; *J.Mater. Environ. Sci.,* 2015, *6(5)*, 1417-1425.
18. A. Bengherbia; F. Hamaidi; R. Zahraoui; M.S. Hamaidi; S. Megateli; *Leban Sci J*., 2014, *15(2),*39–51.
19. S. Benrabah; H. Bousnoubra; N. Kherici; M. Cote; *Rev. Sci. Technol., Synthese*, **2013**, *26*, 30-39.
20. S.M. Ezzat; H.M. Mahdy; M.A. Abo-State; E.H. Abd El Stakour; M.A. El-Bahnasawy; *Middle-East. J. Sci. Res*., 2012, *12(14)*, 413-423.
21. W.M.A.W.M Khalik; M.P. Abdullah; N.A. Amerudin; N. Padli; J. Mater. *Environ. Sci*., **2013**, *4(4)*, 488-495.
22. F. Mimeche; M. Biche; A. Ruiz-Navarro; F.J. Oliva-Paterna; *Limnetica*., **2013**, *32 (2),* 391-404.
23. S. Acharya; S.K. Sharma; V. Khandegar; *Poll.Res*, **2018**, *37(1)*, 209-22.
24. R. Bhutiani; F. Ahamad; V. Tyagi; K. Ram; Environ. Conserv. J.,2018, 19(1& 2), 191–201.
25. Y.B. Gideon; F.B. Fatoye; J.I. Omada; *Int. J. Sci. Technol*., **2013**, *2(12)*, 891-899.
26. S. Sanyal; D.K. Paul; J. Appl. *Nat. Sci*, **2019**, *11*(2), 492-502.
27. W. Ayad; M. Kahoul; *J. Mater. Environ*. Sci, 7, 1288–1297.
28. O.S. Brraich; S.K. Saini; *Int. J. Adv. Res*., **2015**, *3(12)*, 1498-1509.
29. V. Pradeep; C. Deepika; G. Urvi; S. Hitesh; *Int. J. Res. Chem. Environ*., **2012**, *2(1)*,105-111.
30. S. Saha; A. Mandal; D. Sahoo; Int*. J. Fish. Aquat. Stud.,* **2017**, *5(6),* 23-27.
31. D.N. Saksena; R.K. Garg; R.J. Rao; *J. Environ. Biol*., 2008, *29(5),*701-71.
32. K.K. Sharma; S. Kour; K. Sharma; *Int. J. Appl. Res*., **2017**, *3(7)*, 686-691.
33. A.M. Abdel-Satar; *J. Aquat. Res.*, **2005**, *31(2)*,200-223.

34. M.H. Abdo; Afr J. Biol. Sci., **2010**, 6 (2), 143-158.
35. N. Chaib; B. Samraoui; *Sécheresse,* **2011***; 22,* 171-177.
36. H. Effendi, B. Romanto; Y. Wardiatno; *Procedia. Environ. Sci*., **2015**, *24*, 228-237.
37. R. Bhateria; D. Jain; *Rev. Sustainable Water. Res. Manage,* ***2016****, 2*(*2*), 161-173.
38. A. Barakat; M. El Baghdadi; J. Rais; B. Aghezzaf; M. Slassi; *Int. Soil. Water. Conserv. Res*., **2016**, *4*, 284–292.
39. H. Jeong; J. Park; H. Kim; *J. Chem*., **2013**, 1-9.
40. N.R. Ilavarasan; R. Ilangovan; P.R. Prasanna; *J. Environ. Biol.*, **2016**, *37,* 1463-1472.
41. M. Jeyaraj; G. Nirmaladevi; P.N. Magudeswaran; *Int. J. Res. Dev. Technol*., **2014**, *2(4)*, 1-4.
42. S.N. Brinis; A. Boudoukha; A.A. Hamel; *LARHYSS J*., **2015**, *22*, 123–137.
43. B. Desai; H. Desai; *Int. J. Agric. Environ. Sci*., **2018**, *5(3)*, 53-65.
44. W.H.O.; *Guidelines for drinking water quality' incorporating first addendum,* 3 rd ed.; Electronic version for the Web, **2006**, [http://www.who.int/water sanitation healt h/dwq/gdwq0 506.pdf]
45. R.S. Ayers; D.W. Westcot; *Food, Agriculture Organization of the Unfited Nations (FAO), water quality for agriculture, irrigation and drainage*, FAO, Rome, Paper No. 29. Rev1, M-56, **1994**.
46. C.C. M.E. (Canadian Council of Ministers of the Environment); 2007. A protocol for the derivation of water quality guidelines for the protection of aquatic life. Winnipeg, Manitoba: Canadian Council of Ministers of the Environment, 2007, PP 37
47. F. Boudjemline; A. Semar; *J. Wat. Land Dev*., **2018**, *36(1)*, 17-26.
48. E. Bensaci; S. Bendjama; S. Telli; S. Reguig; A. Zoubiri; M. Houhamdi; *Int J Environ Water*., **2014**, *3*, 61-68.
49. J. Rodier; B. Legube; N. Merlet; R. Brunet; *L'analyse de l'eau*, 9thed, Dunod, Paris, France, **2009**, pp. 160.
50. C.S. Rao; B.S. Rao; A.V.L.N.S.H. Hariharan; N.M. Bharathi; *Int. J. Appl. Bio Pharm. Tech.*, **2010**, *1(1)*, 79-86.
51. R.M. Brown; N.J. McCleiland; R.A. Deininger; M.F. O'Connor; *Poll. Res.*, **1972**, *6,* 787-797.

STUDIA UBB CHEMIA, LXVI, 1, 2021 (p. 143-152)
(RECOMMENDED CITATION)
DOI:10.24193/subbchem.2021.1.11

A VIABLE STRATEGY FOR THE BIODEGRADATION OF HALOGENATED ORGANIC COMPOUNDS FROM THE WASTEWATER MEDIATED BY *PSEUDOMONAS PUTIDA*

DIANA IONELA STEGARUS[a], CONSTANTIN PALADI[b], ECATERINA LENGYEL[c], CORNELIU TANASE[d], ANAMARIA CĂLUGĂR[e], VIOLETA-CAROLINA NICULESCU[a,*]

ABSTRACT. Microbial degradation is to be considered a perspective solution in the elimination of microporous organic compounds in the environment. Various studies attest to the *Pseudomonas putida* species as being capable of aerial biodegradation of numerous organic compounds including chlorinated aromatic compounds. The aim of this study was to demonstrate the ability of *Pseudomonas putida* to grow on various organic substrates, being a possible candidate for dehalogenation of various chlorinated organic compounds Water samples were prepared by contamination with a solution containing 1,1,1-trichloroethane, 1,1,1,2-tetrachloroethane, trichloromethane and tetrachloromethane. The concentrations of halogenated organic compounds, before and after inoculation, were determined by gas chromatographic method. The results obtained showed the reduction, in the presence of *Pseudomonas putida*, of various halogenated organic compounds such as 1,1,1-trichloroethane, 1,1,1,2-tetrachloroethane, trichloromethane and tetrachloromethane with values ranging from 23% to 45% over a time interval of 120 days. The present study demonstrates the ability of *Pseudomonas putida* to grow on various organic substrates, being a possible candidate for dehalogenation of various types of chlorinated organic compounds.

Keywords: *biodegradation, dehalogenation, groundwater, halogenated organic compounds, Pseudomonas putida*

[a] *National Research and Development Institute for Cryogenic and Isotopic Technologies – ICSI Ramnicu Valcea, 4th Uzinei Street, 240050 Ramnicu Valcea, Romania;*
[b] *Nicolae Testemitanu University of Medicine and Pharmacy of Chisinau, 165 Ștefan cel Mare and Sfint Blvd, 2004 Chisinau, Moldova*
[c] *Lucian Blaga University of Sibiu, 9th Victoriei Street, 550024, Sibiu, Romania;*
[d] *Department of Pharmaceutical Botany, George Emil Palade University of Medicine, Pharmacy, Sciences and Technology of Târgu Mureș, 38 Gheorghe Marinescu Street, Târgu Mureș, Mureș, 540139, Romania*
[e] *Faculty of Horticulture, Advanced Horticultural Research Institute of Transylvania, Viticulture and Oenology Department, University of Agricultural Sciences and Veterinary Medicine Cluj-Napoca, 3-5 Manastur Street, 400372, Cluj-Napoca Romania*
** Corresponding author: violeta.niculescu@icsi.ro*

INTRODUCTION

Remediation of wastewater has always been a major environmental and economic issue, being a complex process, which involves massive financial expenses [1], [2]. From this point of view, the use of bacteria able to biodegrade *in situ* the chlorinated compounds could potentially be an effective approach [3], [4]. This is possible as long as the availability of bacteria strains and the facility of introducing them leaves the promise of a reasonable working environment both ecologically and financial. Emission of pollutants into the environment does not only describe an ecologically fundamental problem, but it is continuously dichotomized by forming a cascade that reflects in various fields of everyday life, starting with agriculture, food industry or medicine. Water quality is a widely debated issue and its assessment is increasingly complex [5], [6].

Extensive use of halo-aromatic compounds as odorous solvents or pesticides has led to their massive release in the environment. Many of these compounds used to be considered non-degradable, but, due to the continuous evolution of microbial enzyme mechanisms, new methods for their mineralization are constantly discovered [7]. Microbial degradation is considered a perspective solution in order to eliminate the micro-porous organic compounds in the environment and it can be improved by creating genetically modified or isolated bacteria by various selection methods.

These processes may influence the soils and waters decontamination process in various industrial regions of the world [8], [9].

The hydrocarbons degradation in either soil or water is primarily conditioned by the presence or absence of strains corresponding to the chemical compound [10], [11]. The main factor in the bacteria presence becomes the accessibility of the pollutant. In order to have a positive effect on mineralization, the bacterium should come into direct contact with the pesticide / compound, either by chemotactic response or by transporting it to the contaminated area [12]. Thus, too low pollutant concentration can inoculate the soil with ineffective bacteria, as long as the amount of nutrient is inadequate [4], [13]. Various studies demonstrated that hydrocarbons from the solid tar are resistant to microbial decomposition, but, recently, the enzyme activity of aerobic and anaerobic microorganisms in the degradation of organ chlorinated compounds was investigated [7], [14]. Due to the surface/volume ratio unfavorable for the microbial growth, the substrate remains insoluble. The smaller the volume/area ratio is, the faster the microbial decomposition process of organic compounds becomes.

Another important factor in the process of the aromatic compounds microbial degradation is the temperature. Various studies confirm the hypothesis that, at low temperatures, low hydrocarbons toxicity leads to a more prolific increase of the colonies [15], [16]. In winter, however, during frost, bacterial efficiency tends to drastically decrease.

The chemical compounds such as phosphorus or nitrogen are indispensable for the aromatic hydrocarbons biodegradation [3]. Thus, at a temperature of 14°C, an absorption of 4 nmol N/mg oil was found. The maximum efficiency in decomposition of aromatics is achieved when 3.2 mg phosphate/L is introduced. In addition, the presence of phosphate and nitrogen is a limiting factor, and their addition can stimulate the biodegradation process [17], [18], [19]. Normally, bacterial metabolism also involves a certain oxygen consumption, due to the fact that both saturated and aromatic hydrocarbons involve the presence of oxygenase and molecular oxygen in the chemical decomposition process. Although aromatic compounds biodegradation in anaerobic conditions is possible, it is slower and less efficient [17].

A recent study emphasizes the enormous impact that iron oxide ions can play in the dynamics of biodegradation [20]. This can positively interact with certain *Dehalobacter* cultures in a groundwater remediation process, favoring the dichloromethane and chloroform decomposition. The same study demonstrates a three-time faster conversion of dichloromethane in the presence of iron ion [20].

Although many studies demonstrate significant biodegradation capabilities in laboratory conditions, the effectiveness of their use *in situ* (where the multitude of organic compounds present might interfere with biodegradation) is still poorly studied [21], [22], [23], [24], [25], [26], [27], [28],[29].

The aim of this study was to demonstrate the ability of *Pseudomonas putida* to grow on various organic substrates, being a possible candidate for dehalogenation of various chlorinated organic compounds (such as 1,1,1-trichloroethane, 1,1,1,2-tetrachloroethane, trichloromethane or tetrachloromethane).

RESULTS AND DISCUSSION

The results revealed that the *Pseudomonas* strain needed a fairly long period of accommodation with the organic compounds from the water, consequently, the determined values varied on a case-by-case basis. Figure 1 presents the degradation of the 1,1,1-trichloroethane over a period of 120 days, in the presence of *Pseudomonas putida* strain.

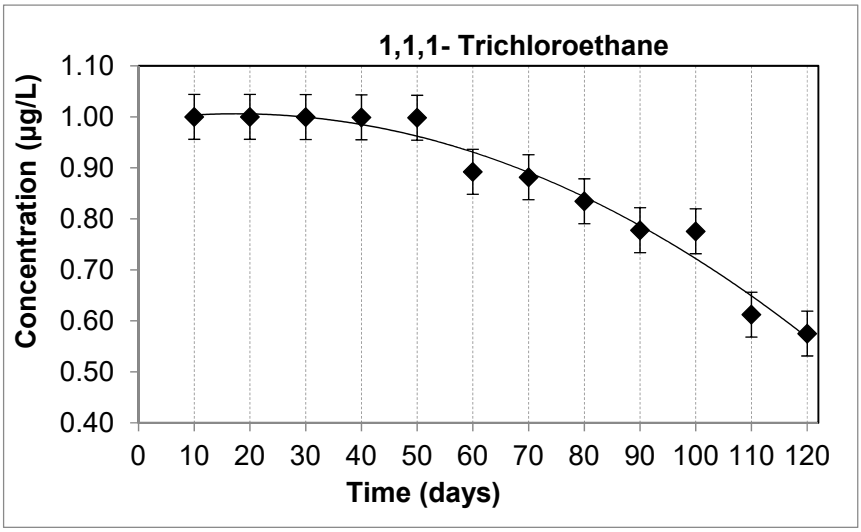

Figure 1. The graphic representation of temporal pattern of 1,1,1-trichloroethane degradation by *Pseudomonas putida* strain. Error bars indicate the ranges for triplicate samples.

The biodegradation of 1,1,1-trichloroethane was observed after 30 days, with a small decrease in concentration of only 0.0004 µg/L. The concentration of this compound decreased successively with values ranging from 0.0004 µg/L to 0.1077 µg/L, reaching a concentration of 0.8923 µg/L after the first 60 days. Between the 60 and 90 days, the 1,1,1-trichloroethane concentrations were between 0.88923 µg/L and 0.7777 µg/L, demonstrating the action of the *Pseudomonas putida* strain. Within 90 and 120 days period, the concentrations of 1,1,1-trichloroethane diminished by 23.00% to 42.49%, reaching a concentration of 0.5751 µg/L. After 120 days, the 1,1,1-trichloroethane compound has stopped the decrease in concentration.

Figure 2 reveals the degradation of the 1,1,1,2-tetrachloroethane over a period of 120 days, in the presence of *Pseudomonas* strain. As it can be seen, 1,1,1,2-tetrachloroethane undergoes a successive decomposition but the accommodation takes more than a month. Thus, after 60 days, the 1,1,1,2-tetrachloroethane concentrations were reduced with 23.7% by the action of *Pseudomonas putida* bacteria, reaching values of 0.9237 µg/L. The decrease concentration was more visible in the 60-90 days period, with values reaching 0.6572 µg/L. After 110 days, the concentration reached 0.5501 µg/L. After this period, the concentration of 1,1,1,2-tetrachloroethane remained constant, the bacteria losing its decomposition capacity.

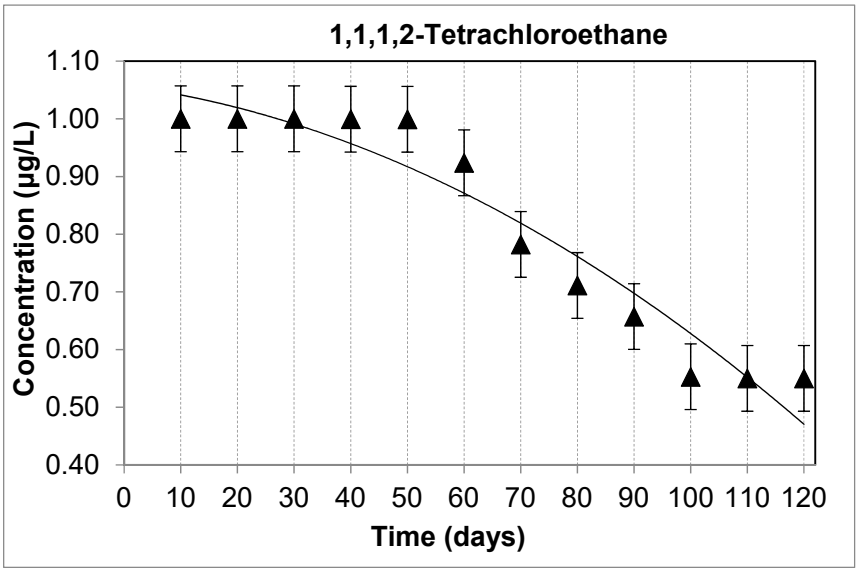

Figure 2. The graphic representation of temporal pattern of 1,1,1,2-tetrachloroethane degradation by *Pseudomonas putida* strain. Error bars indicate the ranges for triplicate samples.

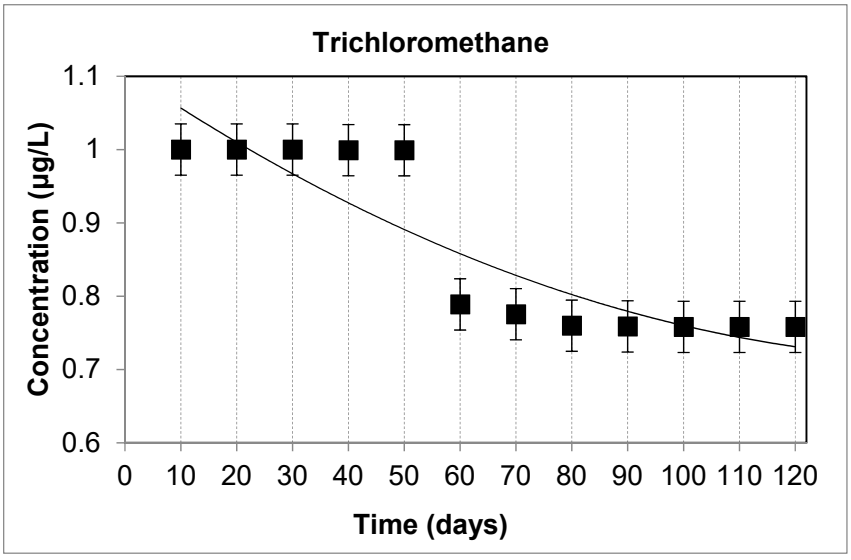

Figure 3. The graphic representation of temporal pattern of trichloromethanetime degradation by *Pseudomonas putida* strain. Error bars indicate the ranges for triplicate samples.

The other two chlorinated compounds (trichloromethane and tetrachloromethane) were also monitored, the results being displayed in Figure 3 and Figure 4. In the case of trichloromethane [30], it must be noted that the bacterial strain was accommodated with the higher contaminated environment after 40 days. Only after this period the first signs of a decrease in their concentrations appeared (0.9992 µg/L for trichloromethane and 0.9989 µg/L for tetrachloromethane). For trichloromethane, biodegradation is more significant in the 60-100 days range and the values of this compound concentration reached 0.7588 µg/L. Subsequent concentration determinations after 110 or 120 days did not show diminishes, the values remaining constant.

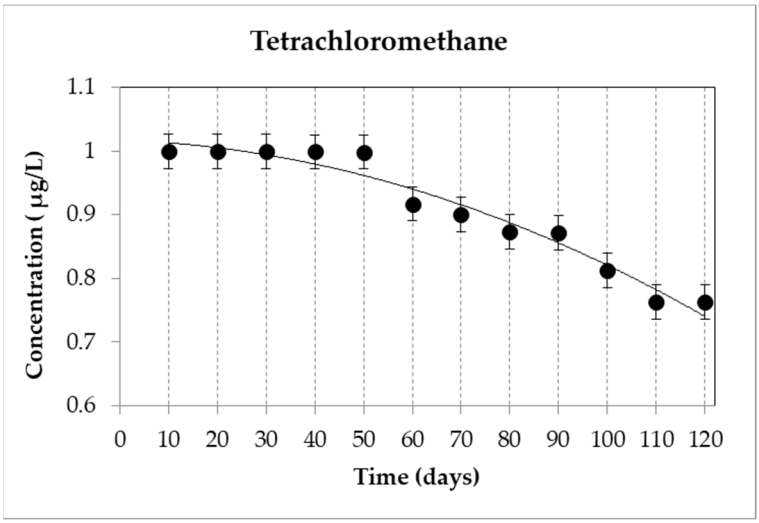

Figure 4. The graphic representation of temporal pattern of tetrachloromethane degradation by *Pseudomonas putida* strain. Error bars indicate the ranges for triplicate samples.

The biodegradation of tetrachloromethane led to the values of 0.8722 µg/L after 90 days and 0.7628 µg/L after 120 days. After 110 days there were no changes in the biodegradation of this compound in the presence of *Pseudomonas putida*.

Analysing all the results, it may be stated that, by far, the highest activity was measured for the degradation of the chlorinated ethane compounds, their concentrations being reduced at half of the initial values after the test period. Also, in their case, the accommodation of the *Pseudomonas putida* type strain was shorter than in the case of methane derivates.

An important aspect of the chlorinated compounds degradation is the formation of toxic oxidation products. For example, there were studies that reported the formation of acyl chlorides resulting from the hydroxylation of a

di-chlorinated carbon followed by elimination of one of the chlorines [31]. Acyl chlorides can act as protein modifying agents. However, during the assays used to determine the degradation rates of the different chlorinated hydrocarbons, we did not observe any decline in degradation rates. Apparently, the amounts of potentially toxic intermediates produced were too low to significantly inactivate the co-metabolic degradation.

Chlorinated aliphatics behave as unique source of carbon and energy to various bacteria. Chlorinated compounds are electron deficient, acting as electron acceptors and the energy is produced by a respiratory process in anaerobic media. In the best scenario, the chlorinated compound is degraded only if another substrate is present, due to the broad-specificity enzymes from the bacteria [32]. Future studies regarding the biodegradation of chlorinated compounds should target both basic and applied aspects of the bioremediation.

CONCLUSIONS

The use of bacteria capable of chlorinated compounds biodegradation ultimately yields convincing results under experimental conditions, and the bacterial sources facility could be an economic advantage. On the other hand, the multifactorial nature of the process (involving various environmental factor such as temperature, humidity, chemical composition of the water used as substrate) could create potential difficulties in applying the methods tested in the laboratory *in situ*. Also, irrational application of the methods in situ could lead to the accumulation of intermediary toxic compounds in microbial metabolism.

The capacity of the *Pseudomonas putida* strain to degrade 1,1,1-trichloroethane, 1,1,1,2-tetrachloroethane, trichloromethane and tetrachloromethane was reached at low concentrations, but it must be taken into consideration the variety of compounds present in polluted waters that may affect the viability of the bacterium. The biodegradation rate of the chlorinated ethane derivates was reduced to 23.72% after 60 day. The lowest biodegradation rate was for methane derivates with only 45% decrease in concentration, mainly between 60 and 100 day after inoculation with Pseudomonas putida strains.

EXPERIMENTAL SECTION

Sampling

Pseudomonas putida was isolated from a wastewater lagoon in South Carolina and deposited to the ATCC (*Pseudomonas putida* ATCC 31483) by Sybron Biochemical Corp. (Salem, VA, US) and it was activated in tryptic soy broth TSB culture media (Sigma Aldrich, Darmstadt, Germany) for 24 hours

at 30ºC. Water samples were prepared by contamination with a solution containing 1 µg/mL of 1,1,1-trichloroethane, 1,1,1,2-tetrachloroethane, trichloromethane and tetrachloromethane, using a standard mixture solution of 10 µg/mL from each compound (LGC Standards GmbH, Wesel, Germany).

Working protocol

1000 mL water were inoculated with 1 mL suspension containing 106 Pseudomonas putida cells. The cells number per mL was established by reading the suspension optical density at 660 nm with Cecil 1200 spectrophotometer (Cecil Instruments, Cambridge, UK).

The temperature was kept at 28°C and monitored for 120 days, the samples being incubated in a Memmert IPP 300 equipped with incubator Peltier system (Memmert GmbH + Co. KG, Schwabach, Germany). In order to preserve bacterial viability in water samples, $C_{12}H_{17}N_4OS^+$ (thiamine) (Sigma Aldrich, Darmstadt, Germany) was periodically introduced (once a week) at a concentration of 1 mg/L.

The identification and quantification analysis

The concentrations of 1,1,1-trichloroethane, 1,1,1,2-tetrachloroethane, trichloromethane, tetrachloromethane, before and after inoculation, were determined by a gas chromatographic method, according to ISO 10301:1997 standard, in order to establish the efficiency of the bacterial strain for the compounds degradation [33].

In order to achieve the compounds identification and quantification, the samples were prepared by taking 500 mL water which was extracted twice with 50 mL hexane (Sigma Aldrich, Darmstadt, Germany). The combined extracts were dried over sodium sulphate (Sigma Aldrich, Darmstadt, Germany) and concentrated to a volume of 2 mL with a TURBOVAP 500 concentrator (Biotage AB, Uppsala, Sweden).

The identification and quantification analysis was achieved using a 240 MS 450 GC Varian gas chromatograph coupled with a mass spectrometer (Varian, Inc., Palo Alto, CA, United States).

For the chromatographic Separation, a TG-WAXMS polar column (Thermo Fisher Scientific, Waltham, Massachusetts, United States) (dimensions: 60 m x 0.32 mm x 0.25 µm) was used. The oven temperature was maintained at 70 °C for 0.8 min, then it was increased to 110 °C, with a rate of 3°C/min, then to 140°C with 3°C/min and finally to 160°C by 1.2°C/min, where it was maintained for 2 min. Injection port and detector temperatures were maintained at 240°C and 270°C respectively, whereas the injection volume was 2 µL (splitless injection), the column being cleaned with 1.80 mL/min.

The calibration curves were designed by using 7 calibration levels: 0,01; 0,03; 0,05; 0,1; 0,3; 0,5; 0,8; 1 µg/mL from the 10 µg/mL stock standard mixture solution of 1,1,1-trichloroethane, 1,1,1,2-tetrachloroethane, trichloromethane and tetrachloromethane (LGC Standards GmbH, Wesel, Germany). Each compound was identified and quantified with a ratio of at least 3 m/z with a similarity of at least 70% compared to the spectra of similar compounds in the NIST 08 spectral library.

Analyses were conducted in triplicate and the results were expressed as average ± SD.

ACKNOWLEDGMENTS

The work has been funded by the Romanian Ministry of Education and Research under the projects PN 19110301 and PN 19110302, grant no. 9N/2019 and Operational Programme Human Capital of the Ministry of European Funds through the Financial Agreement 36355/23.05.2019, HRD OP 380/6/13 - SMIS code 123847.

REFERENCES

1. M. Anjum; R. Miandad; M. Waqas; F. Gehany; M.A. Barakat; *Arab. J. Chem.*, **2019**, *12*, 4897–4919.
2. K. Rehman; A. Imran; I. Amin; M. Afzal; *Chemosphere*, **2019**, *217*, 576–583.
3. G. Fuchs; M. Boll; J. Heider; *Nat. Rev. Microbiol.*, **2011**, *9*, 803–816.
4. M. Kronenberg; E. Trably; N. Bernet; D. Patureau; *Environ. Pollut.*, **2017**, *231*, 509–523.
5. L.C. Oprean; I. Oprean; O. Danciu; G. Ciortea; *Republican Technical-Scientific Library,* **2012**, *1*(1-3), 580-590.
6. R. Iancu, *Transylv. Rev. Syst. Ecol. Res.*, **2013**, *15,* 91–116.
7. A.A. Sari; N. Ariani; S. Tachibana; Y. Sudiyani; *AIP Conf. Proc.,* **2016**, *1744*, 020003.
8. K.F. Reardon; D.C. Mosteller; J.D. Bull Rogers; *Biotechnol. Bioeng.,* **2000**, *69,* 385–400.
9. M. Farhadian; D. Duchez; C. Vachelard; C. Larouche; *Water Res.*, **2008**, *42,* 1325–1341.
10. P.J. Hernes; R. Benner; *J.G.R. Oceans*, **2003**, *108*, doi.org/10.1029/ 2002JC001421.
11. M.S. Fuentes; C.S. Benimeli; S.A. Cuozzo; M.J. Amorosso; *Int. Biodeterior. Biodegradation*, **2010,** *64*, 434–441.

12. D. Paul; *Microbial Technology for Health and Environment*, Springer, Singapore; **2020**; 303–325. doi.org/10.1007/978-981-15-2679-4_12.
13. C.A. Pettigrew; B.E. Haigler; J.C. Spain; *Appl. Environ. Microbiol.,* **1990**, *57*(1), 157-162.
14. K.R. Sowers; H.D. May; *Curr. Opin. Biotechnol,* **2013**, *24*, 482–488.
15. M.S. Díaz-Cruz; D. Barceló; *Chemosphere.* **2008**, *72*, 333–342.
16. A. Chebbi; D. Hentati; H. Zaghden; N. Baccar; F. Rezgui; M. Chalbi; S. Sayadi; M. Chamkha; *Int. Biodeterior. Biodegradation*, **2017**, *122,* 128–140.
17. A.K. Haritash; C.P. Kaushik; *J. Hazard Mater.*, **2009**, *169*, 1–15.
18. P.K. Arora; H. Bae; *Microb. Cell. Fact*, **2014**, *13,* 31–31.
19. B. Biswas; B. Sarkar; R. Rusmin; R. Naidu; *Environ. Int*. **2015**, *85,* 168–181.
20. M. Lee; E. Wells; Y.K. Wong; J. Koenig; L. Adrian; H.H. Richnow; M. Manefield; *Environ. Sci. Technol.,* **2015**, *49,* 4481–4489.
21. P. Mirleau; R. Wogelius; A. Smith; M.A. Kertesz; *Appl. Environ. Microb.*, **2005**, *71,* 6571–6577.
22. N.J. Palleroni; *Bergey's Manual of Systematic Bacteriology*, Springer, New York, **2005**, pp. 323-373.
23. A Dechesne; G. Wang; G. Gülez; D. Or; B.F. Smets; *Proc. Natl Acad. Sci. U S A,* **2010**, *107,* 14369–14372.
24. J.A. Cray; A.N.W. Bell; P. Bhaganna; A.Y. Mswaka; D.J. Timson; J.E. Hallsworth; *Microb. Biotechnol.,* **2013**, *6,* 453–492.
25. M.S. Munna; Z. Zeba; R. Noor; *S. J. Microbiol.*, **2016**, *5*(1), 9-12.
26. M. Yoshikawa; M. Zhang; K. Toyota; *Microbes Environ.*, **2017**, *32,* 188–200.
27. P. Dvořák; V. de Lorenzo; *Metab. Eng.*, **2018**, *48,* 94–108.
28. F.D. Bora; C.I. Bunea; R. Chira; A. Bunea; *Molecules,* **2020**, *25*, 750; doi:10.3390/molecules25030750.
29. A. Donici; C.I. Bunea; A. Calugar; E. Harsan; I. Racz; F.D. Bora; *Bulletin UASVM Horticulture*, **2018**, *75* (2), 127-132.
30. Christian Penny, Stephane Vuilleumier & Francoise Bringel; *FEMS Microbiol Ecol,* **2010**, *74*, 257–275.
31. ISO 10301:1997: Water quality - Determination of highly volatile halogenated hydrocarbons - Gas-chromatographic methods. 1st ed. (reviewed and confirmed in **2013**).
32. Ana B. Rios Miguel, Mike S.M. Jetten, Cornelia U. Welte; *Water Research,* **2020**, X, 100065.
33. M.E. Rasche; M.R. Hyman; D.J. Arp; *Appl. Environ. Microbiol.,* **1991**, *57,* 2986–2994.

STUDIA UBB CHEMIA, LXVI, 1, 2021 (p. 153-163)
(RECOMMENDED CITATION)
DOI:10.24193/subbchem.2021.1.12

RADIOCARBON INVESTIGATION OF THE BIG BAOBAB OF OUTAPI, NAMIBIA

ADRIAN PATRUT[a,b]*, ROXANA T. PATRUT[a], LASZLO RAKOSY[c], DEMETRA RAKOSY[d], ILEANA-ANDREEA RATIU[a,b], KARL F. VON REDEN[e]

ABSTRACT. The article reports the AMS (accelerator mass spectrometry) radiocarbon dating results of the Big baobab of Outapi, which is the largest African baobab of Outapi, Namibia. The investigation of this monumental baobab revealed that it consists of 8 fused stems, out of which 4 are false stems. The Big baobab exhibits a closed ring-shaped structure. Three stems build the ring, which is now incomplete due to previous damage to the false cavity. Three wood samples were collected from the false cavity and from the longest false stem. Seven segments were extracted from the samples and dated by radiocarbon. The oldest investigated sample segment had a radiocarbon date of 820 ± 17 BP, corresponding to a calibrated age of 780 ± 10 calendar years. According to dating results, the Big baobab of Outapi is 850 ± 50 years old.

Keywords: *AMS radiocarbon dating, Adansonia digitata, dendrochronology, age determination, false cavity, multiple stems.*

INTRODUCTION

The African baobab (*Adansonia digitata* L.) is the most widespread and utilized of the eight or nine species of the *Adansonia* genus, which belongs to the Bombacoideae subfamily of Malvaceae. The African baobab is endemic to the arid savanna of mainland Africa [1–6].

[a] *Babeş-Bolyai University, Faculty of Chemstry and Chemical Engineering, 11 Arany Janos, RO-400028, Cluj-Napoca, Romania.*
[b] *Babeş-Bolyai University, Raluca Ripan Institute for Research in Chemistry, 30 Fantanele, RO-400294 Cluj-Napoca, Romania.*
[c] *Babeş-Bolyai University, Faculty of Biology and Geology, 44 Republicii, RO-400015, Cluj-Napoca, Romania.*
[d] *AG Spatial Interaction Centre, German Centre for Integrative Biodiversity Research, 5e Deutscher Platz, D-04103 Leipzig, Germany.*
[e] *NOSAMS Facility, Dept. of Geology & Geophysics, Woods Hole Oceanographic Institution, Woods Hole, MA 02543, U.S.A.*
** Corresponding author: apatrut@gmail.com*

In 2005, we initiated an extended research project to clarify several controversial aspects related to the architecture, growth and age of the African baobab. The research is based on AMS radiocarbon investigation of very small wood samples collected from inner cavities, deep incisions in the stems, fractured stems and from the outer part/exterior of large baobabs [7–15]. According to the research results, all large and old baobabs are multi-stemmed and exhibit preferentially closed or open ring-shaped structures. The oldest specimens were found to have ages up to 2,500 years [9,10,12,13].

Namibia is one of the African countries with the highest number of baobabs, which show different local abundance and distribution in the 12 regions [16]. The highest number and density of baobabs can be found in the Omusati region, in the north-central part of Namibia (26,573 km^2). According to a recent survey, the mean density of baobabs in Omusati is 6.7 (± 2.5) trees/ha, which corresponds to a total number of 17.80 (± 6.64) million individuals [17].

The climate of Omusati is described as semi-arid, with the rainfall restricted to summer months (November to April). The vegetation in the Omusati region belongs to the Mopane savanna, according to Giess classification of vegetation zones [17].

Our survey in Omusati identified a number of 11 superlative baobabs, with a circumference of over 20 m, out of which 6 are located in and around Outapi, 3 in Onesi and one each in Tsandi and Okahao. The high density of baobabs and the number of superlative specimens is also due to large areas with sandy soils, rich in sodium and calcium.

Outapi (also called Uutapi and Ombalantu), located close to the border with Angola, is the capital of the Omusati region. It hosts 6 superlative baobabs in an area of less than 10 km^2. The most famous is the Ombalantu baobab, which is part of a national heritage site. However, the largest specimen is the Big baobab.

Here we present the investigation and AMS radiocarbon dating results of the Big baobab of Outapi.

RESULTS AND DISCUSSION

The Big baobab of Outapi and its area. Ten years ago, the large baobab was situated on a vacant land with sandy soil at the intersection of Nakakanda Mukatala and Natanael Mahwilili streets in Outapi, close to the Outapi Town Hotel. The baobab is currently in the yard of a newly built social shelter for young people. They use it for trash and waste disposal. This tree is known only to nearby residents as a large baobab in the area. Because it is the largest baobab in town, we named it the Big baobab of Outapi.

The GPS coordinates of the tree are 17º30.141' S, 014º58.982' E and the altitude is 1116 m. The mean annual rainfall in the area is 467 mm, while the mean annual temperature reaches 21.1 °C (Outapi station). The Big baobab has a maximum height of 22.1 m, the circumference at breast height (cbh; at 1.30 m above ground level) is 31.01 m and the overall wood volume is around 330 m^3 (**Figure 1**). The horizontal dimensions of the canopy are 33.6 x 32.8 m. In terms of circumference, the Big baobab of Outapi ranks sixth in the world, after Holboom, Sagole big tree, Makuri Lê boom, Dorslandboom and Sir Howard baobab at Tsandi, all from Namibia, except Sagole big tree, which is from South Africa [9, 12, 18].

The monumental baobab consists of 8 stems, out of which 4 are false ones [19]. It also has several buttress branches. The baobab exhibits a closed ring-shaped structure, with a false cavity defined by three stems. The false cavity opened some time ago, by the splitting of two stems. The resulting opening occupies an angle of more than 30° of the circumference. The false cavity has a bell shape with a height of 2.95 m and an ellipsoidal base with the axes of 2.24 x 1.88 m (**Figure 2a** and **2b**). On the other hand, two false stems are disposed in V-shape with an opening of around 50°. Their lengths at ground level are 2.80 and 3.61 m (**Figure 3**). Such false stems disposed in V-shape provide better stability in sandy soils.

Figure 1. General view of the Big baobab of Outapi from the south-west.

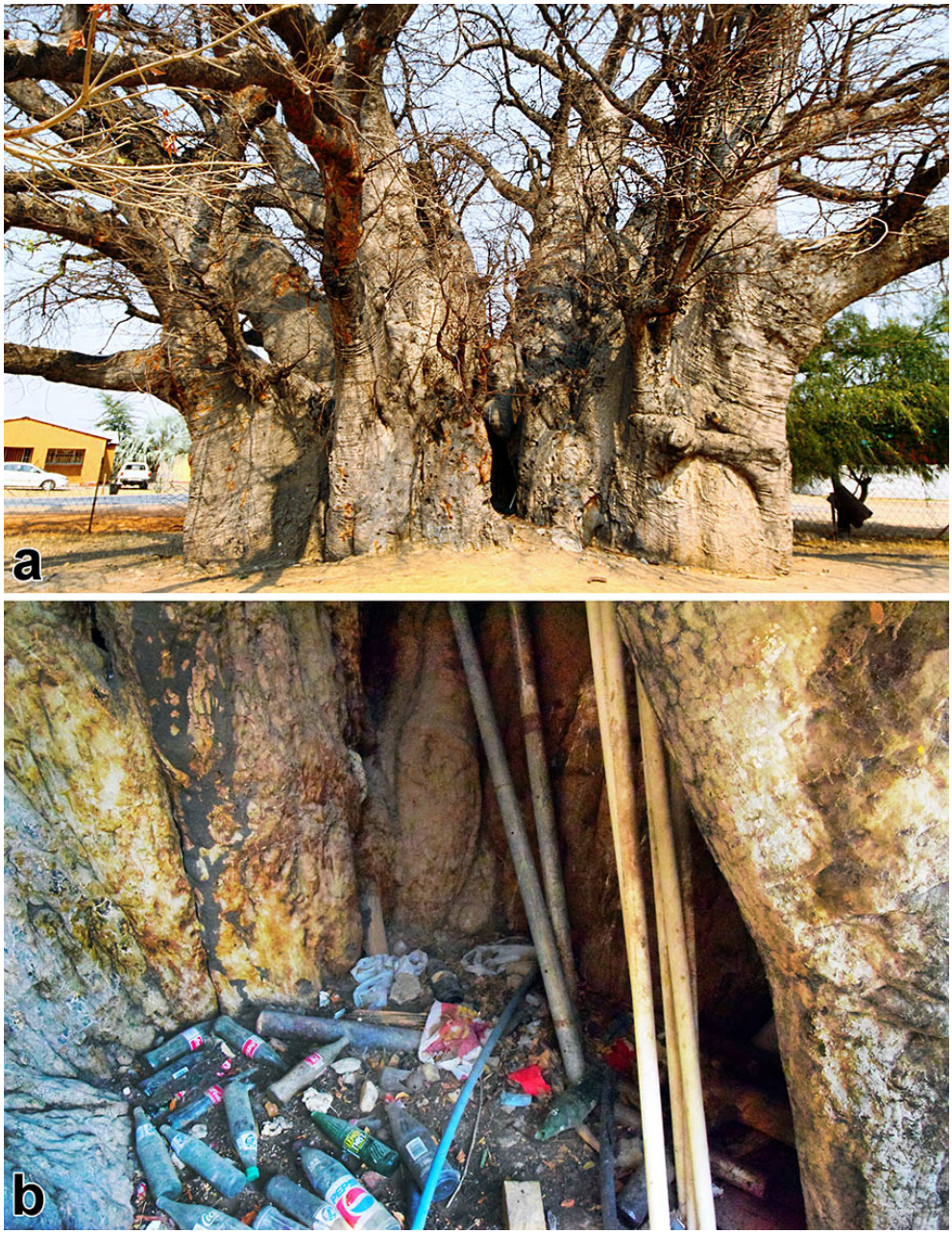

Figure 2.a. View of the Big baobab from the south-east, showing in the centre the entrance to the false cavity; **b.** The base of the false cavity covered by trash and waste.

Wood samples. Three wood samples were collected with an increment borer. One wood sample (labeled BB-1) was collected from the inner walls of the false cavity. Other two samples (labeled BB-2 and BB-3) were collected from the deepest end/origin and from the middle of the longest false stem of the pair disposed in V-shape. All samples were collected at convenient heights, between 1.20 and 2.10 m.

A number of seven tiny segments were extracted from determined positions of the three samples. Five segments (marked from 1a to 1e) were extracted from sample BB-1, while one segment each (marked 2x and 3x) was extracted from samples BB-2 and BB-3.

AMS results and calibrated ages. Radiocarbon dating results of the 7 sample segments are listed in Table 1. The radiocarbon dates are expressed in ^{14}C yr BP (radiocarbon years before present, i.e., before the reference year 1950). Radiocarbon dates and errors were rounded to the nearest year.

Calibrated (cal) ages, expressed in calendar years CE (CE, i.e., Common Era), are also presented in Table 1.

Table 1. Radiocarbon dating results and calibrated ages of samples collected from the Big baobab of Outapi.

Sample/ segment code	Depth[1] [height[2]] (m)	Radiocarbon date [error] (^{14}C yr BP)	Cal CE range 1σ [confidence interval]	Assigned year [error] (cal CE)	Sample/ segment age [error] (cal CE)
BB-1a	0.01 [1.20]	-	-	>1950	>Modern
BB-1b	0.10 [1.20]	101 [± 18]	1816-1830 (22.8%) **1892-1922 (45.4%)**	1907 [± 35]	115 [± 15]
BB-1c	0,25 [1.20]	308 [± 18]	1517-1538 (17.4%) **1627-1654 (50.8%)**	1640 [± 15]	380 [± 15]
BB-1d	0.40 [1.20]	438 [± 17]	**1452-1488 (68.3%)**	1470 [± 20]	550 [± 20]
BB-1e	0.54 [1.20]	820 [± 17]	**1230-1250 (45.7%)** 1260-1271 (22.5%)	1240 [± 10]	780 [± 10]
BB-2x	0.40 [2.10]	331 [± 16]	**1512-1546 (43.2%)** 1624-1643 (25.1%)	1529 [± 15]	480 [± 15]
BB-3x	0.60 [2.10]	310 [± 19]	1516-1540 (21.3%) **1627-1654 (46.9%)**	1640 [± 15]	380 [± 15]

[1]Depth into the wood.
[2]Height above ground level.

The 1σ probability distribution (68.3%) was selected to derive calibrated age ranges. For one segment (BB-1d), the 1σ distribution is consistent with one range of calendar years. For other five segments (BB-1b, BB-1c, BB-1e, BB-2x, BB-3x), the 1σ distribution corresponds to two ranges of calendar years. In these cases, the confidence interval of one range is considerably greater than that of the other; therefore, it was selected as the cal CE range of the sample for the purpose of this discussion. For obtaining single calendar age values of samples, we derived a mean calendar age of each sample from the selected range (marked in bold). Sample ages represent the difference between the year 2021 CE and the mean value of the selected range, with the corresponding error. Sample ages and errors were rounded to the nearest 5 yr. We used this approach for selecting calibrated age ranges and single values for sample ages in our previous articles on AMS radiocarbon dating of large angiosperms, especially baobabs [7-15, 18-22].

Figure 3. The photograph presents the two false stems disposed in V-shape.

Dating results of samples. For the five segments extracted from sample BB-1, which was collected form the inner walls of the false cavity, segment ages increase with the depth in the wood, i.e., from BB-1a to BB-1e.

For the first segment BB-1a, the age falls after 1950 CE (0 BP), namely the ^{14}C activity, expressed by the ratio $^{14}C/^{12}C$, shows a higher value than the standard activity registered in the reference year 1950. This result, that corresponds to a negative radiocarbon date, is termed greater than Modern (>Modern). Such cases indicate a very young age of the dated wood, which was formed after 1950 CE. In the case of segment BB-1a, the result shows that the baobab is still growing in the direction of the false cavity.

The oldest segment BB-1e represents the sample end and corresponds to a distance of 0.54 m from the cavity walls toward the exterior. Its radiocarbon date of 820 ± 17 BP amounts to a calibrated age of 780 ± 10 calendar yr. The continuous increase of segment ages shows that sample BB-1 has not reached the point of maximum age in the sampling direction. The depth of the cavity walls in the sampling direction is around 1.10 m. Because for the false cavity walls, the point/area of maximum age is always located closer to the cavity than to the exterior, one can estimate that this point is positioned at a distance of at least 0.60 m from the sampling point.

We also dated two segments BB-2a and BB-3a, which originate from samples collected from the deepest end/origin of the longest false stem, i.e., its emergence point from the adjacent ordinary stem and from the middle of this false stem, respectively. Their radiocarbon dates are 331 ± 16 and 310 ± 19 BP. These values correspond to calibrated ages of 480 ± 15 and 380 ± 15 calendar yr.

Age of the Big baobab. The age of the baobab can be calculated by extrapolating the age of the oldest segment BB-1e, which represents the deepest end of sample BB-1, i.e., 780 ± 10 calendar yr, to the point of maximum age inside the cavity walls. This gives us an age of 850 ± 50 years for the oldest part of the Big baobab. According to this value, the Big baobab of Outapi started growing around the year 1170 CE.

Ages of segments BB-2x and BB-3x, namely 480 ± 15 and 380 ± 15 calendar years, are associated with the age and growth of the largest false stem. These values indicate that the longest false stem emerged from the adjacent ordinary stem around 480–500 years ago and that it grew very fast, around 1.80 m in length in the first 100 years.

Architecture of the Big baobab. Our research based on radiocarbon dating has identified a new very stable architecture that enables African baobabs to reach large sizes and old ages. We named it ring-shaped structure (RSS). In this multi-stemmed architecture, the stems describe at ground level

a circle or an ellipse. The most frequent is the closed RSS, in which the stems are pointed upward and are fused almost completely. The fused stems are disposed in a ring with a natural empty space inside, which was named false cavity [9, 11]. As mentioned, the Big baobab of Outapi exhibits a closed RSS, with a damaged false cavity, whose walls are covered by bark.

All large baobabs are multi-stemmed. The vast majority are common stems, which shoot from the roots or emerge from fallen stems. Some baobabs have peculiar structures, which are trapezoidal or triangular in horizontal section. According to radiocarbon dating, the oldest age can be found toward the upper contact with the larger adjacent ordinary stem, from which the false stem emerges. The age decreases toward the opposite sharp extremity. This false stem plays the role of an anchor and is a special type of buttress, very different from the so-called buttress branch. Certain baobabs have two adjacent false stems disposed in V-shape, with an opening of 30–60º [19]. The Big baobab possesses 4 false stems, out of which two are disposed in V-shape.

PROTECTION AND CONSERVATION

Although Namibia has strict laws for protection and conservation of the vegetation and fauna, its monumental baobabs, which are among the largest and oldest in the world, are practically unattended and unprotected. Even if Outapi is the capital of the Omusati region, the largest tree in town, the Big baobab, is used as trash and waste disposal. This action deteriorates even further the false cavity, which is already damaged. Another large baobab (cbh = 23.05 m), located very close to the central market, is used as a public toilet by both men and women. It is known by locals as the “Market Toilet tree”.

CONCLUSIONS

The research discloses the AMS radiocarbon dating results of the Big baobab of Outapi, which is the largest African baobab from Outapi, Namibia. The aim of the research was to determine the architecture and the age of this monumental baobab. The Big baobab consists of 8 stems, out of which 4 are ordinary and 4 are false stems. Two false stems are disposed in V-shape. The tree exhibits a closed ring-shaped structure, with a damaged false cavity inside.

Three wood samples were collected from the false cavity and from the longest false stem, out of which seven segments were extracted, processed and radiocarbon dated. The oldest investigated sample segment had a radiocarbon date of 820 ± 17 BP, which corresponds to a calibrated age of 780 ± 10 calendar yr. According to dating results, the Big baobab of Outapi started growing of 850 ± 50 years ago. The longest false stem is 480 ± 15 years old and it grew very fast during the first 100 years.

EXPERIMENTAL SECTION

Sample collection. The three small wood samples were collected with a Haglöf CH 800 increment borer (0.80 m long, 0.0054 m inner diameter). A number of seven segments of the length of 0.001 m were extracted from predetermined positions along the wood samples. The segments were processed and investigated by AMS radiocarbon dating.

Sample preparation. The standard acid-base-acid pretreatment method was used for removing soluble and mobile organic components [23]. The pretreated samples were combusted to CO_2 by using the closed tube combustion method [24]. Next, CO_2 was reduced to graphite on iron catalyst, under hydrogen atmosphere [25]. Eventually, the resulting graphite samples were investigated by AMS.

AMS measurements. AMS radiocarbon measurements were done at the NOSAMS Facility of the Woods Hole Oceanographic Institution (Woods Hole, MA, U.S.A.), by using the Pelletron ® Tandem 500 kV AMS system. The obtained fraction modern values, corrected for isotope fractionation with the normalized $\delta^{13}C$ value of -25 $^{0}/_{00}$, were finally converted to a radiocarbon date.

Calibration. Radiocarbon dates were calibrated and converted into calendar ages with the OxCal v4.4 for Windows [26], by using the SHCal20 atmospheric data set [27].

ACKNOWLEDGEMENTS

The investigation and sampling of the baobab was authorized by the Ministry of Environment and Tourism of Namibia under the Research/Collecting Permit No. 1934_2014. The research was funded by the Romanian Ministry of Education and Research CNCS-UEFISCDI under grant PN-III-P4-ID-PCE-2020-2567, No. 145/2021.

REFERENCES

1. G.E. Wickens, *Kew Bull.*, **1982**, *37(2)*, 172-209.
2. D.A. Baum, *Ann. Mo. Bot. Gard.*,**1995**, *82*, 440-471.
3. G.E. Wickens, P. Lowe, "The Baobabs: Pachycauls of Africa, Madagascar and Australia", Springer, Dordrecht, **2008**, pp. 232-234, 256-257, 295-296.
4. J.D. Pettigrew, L.K. Bell, A. Bhagwandin, E. Grinan, N. Jillani, J. Meyer, E. Wabuyele, C.E. Vickers, *Taxon*, **2013**, *61*, 1240-1250.
5. G.V. Cron, N. Karimi, K.L. Glennon, C.A. Udeh, E.T.F. Witkowski, S.M. Venter, A.E. Assobadjo, D.H. Mayne, D.A. Baum, *Taxon*, **2016**, *65*, 1037-1049.
6. A. Petignat, L. Jasper, “Baobabs of the world: The upside down trees of Madagascar, Africa and Australia”, Struik Nature, Cape Town, **2015**, pp. 16-86.
7. A. Patrut, K.F. von Reden, D.A. Lowy, A.H. Alberts, J.W. Pohlman, R. Wittmann, D. Gerlach, L. Xu, C.S. Mitchell, *Tree Phys.*, **2007**, *27*, 1569-1574.
8. A. Patrut, K.F. von Reden, R. Van Pelt, D.H. Mayne, D.A. Lowy, D. Margineanu, *Ann. Forest Sci.*, **2011**, *68*, 93-103.
9. A. Patrut, S. Woodborne, R.T. Patrut, L. Rakosy, D.A. Lowy, G. Hall, K.F. von Reden, *Nat. Plants*, **2018**, *4(7)*, 423-426.
10. A. Patrut, K.F. von Reden, D.H. Mayne, D.A. Lowy, R.T. Patrut, *Nucl. Instrum. Methods Phys. Res. Sect. B*, **2013**, *294*, 622-626.
11. A. Patrut, S. Woodborne, K.F. von Reden, G. Hall, M. Hofmeyr, D.A. Lowy, R.T. Patrut, *PLOS One*, **2015**, *10(1): e0117193.*
12. A. Patrut, S. Woodborne, K.F. von Reden, G. Hall, R.T. Patrut, L. Rakosy, J-M. Leong Pock Tsy, D.A. Lowy, D. Margineanu, *Radiocarbon*, **2017**, *59(2)*, 435-448.
13. A. Patrut, R.T. Patrut, L. Rakosy, D.A. Lowy, D. Margineanu, K.F. von Reden, *Studia UBB Chemia*, **2019**, *LXIV, 2 (II)*, 411-419.
14. A. Patrut, S. Woodborne, R.T. Patrut, G. Hall, L. Rakosy, C. Winterbach, K.F. von Reden, *Forests*, **2019**, *10*, 983-993. doi:10.3390/f10110983.
15. A. Patrut, A. Garg, S. Woodborne, R.T. Patrut, L. Rakosy, I.A. Ratiu, *PLOS One*, **2020**, *15(1): e0227352.*
16. K. Lisao, C.J. Geldenhuys, P.W. Chirwa, *Glob. Ecol. Conserv.*, **2018**, *14*: e00386.
17. F. Munyebvu, I. Mapaure, E.G. Kwembeya, *S. Afr. J. Bot.*, **2018**, *119*, 112-118.
18. R.T. Patrut, A. Patrut, D. Rakosy, L. Rakosy, D.A. Lowy, J. Bodis, K.F. von Reden, *Studia UBB Chemia*, **2020**, *LXV, 2*, 149-159.
19. A. Patrut, S. Garnaud, O. Ka, R.T. Patrut, T. Diagne, D.A. Lowy, E. Forizs, J. Bodis, K.F. von Reden, *Studia UBB Chemia*, **2017**, *LXII, 1*, 111-120.
20. A. Patrut, K.F. von Reden, P. Danthu, J-M. Leong Pock Tsy, R.T. Patrut, D.A. Lowy, *PLOS One*, **2015**, *10(3): e0121170.*
21. A. Patrut, K.F. von Reden, P. Danthu, J-M. Leong Pock-Tsy, L. Rakosy, R.T. Patrut, D.A. Lowy, D. Margineanu, *Nucl. Instrum. Methods Phys. Res. Sect. B*, **2015**, *361*, 591-598.

22. A. Patrut, R.T. Patrut, P. Danthu, J.-M. Leong Pock-Tsy, L. Rakosy , D.A. Lowy, K.F. von Reden, *PLoS ONE*, **2016**, *11(1)*, e0146977.
23. N.J. Loader, I. Robertson, A.C. Barker, V.R. Switsur, J.S. Waterhouse, *Chem. Geol.*, **1997**, 136(3), 313–317.
24. Z. Sofer, *Anal. Chem.*, **1980**, *52(8)*, 1389-1391.
25. J.S. Vogel, J.R. Southon, D.E. Nelson, T.A. Brown, *Nucl. Instrum. Methods Phys. Res. Sect. B*, **1984**, *5*, 289-293.
26. C. Bronk Ramsey, *Radiocarbon*, **2009**, *51*, 337-360.
27. A.G. Hogg, T.J. Heaton, Q. Hua, J.G. Palmer, C.S.M. Turney, J. Southon, A. Bayliss, P.G. Blackwell, G. Boswijk, C.B. Ramsey, C. Pearson, F. Petchey, P.J. Reimer, R.W. Reimer, L. Wacher, *Radiocarbon*, **2020**, *62(4)*, 759-778.

STUDIA UBB CHEMIA, LXVI, 1, 2021 (p. 165-178)
(RECOMMENDED CITATION)
DOI:10.24193/subbchem.2021.1.13

IMMOBILIZATION OF PHENYLALANINE AMMONIA-LYASE ON HYDROXYAPATITE AND HYDROXYAPATITE COMPOSITES

JUDITH-HAJNAL BARTHA-VARI[a], RENÁTA ELEKES-DARABONT[a], LAURA-EDIT BARABÁS[a], RÉKA BARABÁS[a,*]

ABSTRACT. A new and efficient immobilization method of phenylalanine ammonia-lyase was obtained using hydroxyapatite (HAP) and hydroxyapatite - carbon nanotube, gelatin and chitosan - composites (HAP-CNT, HAP-GEL and HAP-CS) as support material. HAP and HAP composites were characterized by transmission electron microscopy (TEM), laser diffraction particle size analyzer and XRD measurements. The obtained nanobioconjugates were tested in the ammonia elimination reactions from L-phenylalanine (L-**1**). The reusability and the time-course profile of the immobilized enzyme preparation was also tested. While the biocatalyst obtained by using HAP-CS-15 as support material provided the highest conversion rate in the ammonia elimination reaction from L-**1** (98,1% compared to 98,5% obtained using the non-immobilized enzyme), the most stable biocatalyst proved to be HAP-PAL, which maintained more than 80% of its initial activity even after 5 cycles of reuse.

Keywords: *hydroxyapatite, composites, carbon nanotubes, gelatin, chitosan, phenylalanine ammonia-lyase, immobilization, ammonia elimination*

INTRODUCTION

Due to the increasing interest for natural resources and reduced pollution, biocatalytic routes are gaining more importance [1]. Enzymes are obtained from renewable sources, they are biocompatible, thus the enzymatic processes are cost effective and environmentally friendly [2]. However, their application on industrial scale is hampered by their instability and difficulty of retain and reuse [3]. These drawbacks can be overcome by immobilization, when biocatalysts with improved stability and reusability are obtained [4].

[a] Babeş-Bolyai University, Faculty of Chemistry and Chemical Engineering, 11 Arany Janos str., RO-400028, Cluj-Napoca, Romania,
** Corresponding author: breka@chem.ubbcluj.ro*

Hydroxyapatite (HAP) is the principal mineral component of bone [5]. HAP has unique properties as biocompatibility, bioactivity, osteoconductivity and affinity to biopolymers [6]. Due to its biocompatibility and structural similarity with human hard tissue its widely used as inorganic biomaterial [7]. It founds applications in drug delivery [8], biomedicine [9] or medical devices [10]. Their use is however hampered by their poor fracture toughness and resistance. HAPs mechanical properties can be improved with materials such as carbon nanotubes [11], graphene oxide [12], gelatin [13], or chitosan [14].

Ammonia-lyases are acting on C-N bonds and catalyse the formation of α, β unsaturated bonds by elimination of ammonia from their substrates [15]. Phenylalanine ammonia-lyases (PAL EC 4.3.1.24, EC 4.3.1.25) are homotetrameric enzymes performing the non-oxidative deamination of L-phenylalanine into (E)-cinnamic acid [16] (Scheme 1). Cinnamic acid is the precursor of various phenylpropanoids, such as lignins, flavonoids and coumarins [17]. These derivatives are also widely used in cosmetics [18]. Several immobilized PAL preparates have been reported on various support materials [19] [20] [21]. Our previous successful immobilization of *Pc*PAL on carboxylated and aminated carbon nanotubes drove our interest to the immobilization of the same enzyme on hydroxyapaptite and its composites. These support materials could present a promising alternative, since they are cost effective and environmentally friendly.

In this study our aim was the immobilization of phenylalanine ammonia-lyase from *Petroselinum crispum* (*Pc*PAL) on HAP and HAP composites obtained with carbon nanotubes (HAP-CNT), gelatin (HAP-GEL) and chitosan (HAP-CH), and to test the stability and reusability of the obtained nanobioconjugates.There are several studies which reported the immobilization of enzymes on HAP and HAP composites [22],[23],[24], but according to our knowledge the immobilization of *Pc*PAL on these materials has not been investigated.

RESULTS AND DISCUSSION

The aim of the study was the immobilization of *Pc*PAL on hydroxyapatite (HAP) and HAP composites obtained by using carbon naotubes (HAP-CNT), gelatine (HAP-GEL) and chitosan (10, 15 and 20%) (HAP-CS-10, HAP-CS-15 and HAP-CS-20), and testing the activity and stability of the obtained immobilized enzyme preparations.

The immobilized enzymes were tested in the ammonia elimination reaction from L-phenylalanine, L**-1 (Scheme 1)**.

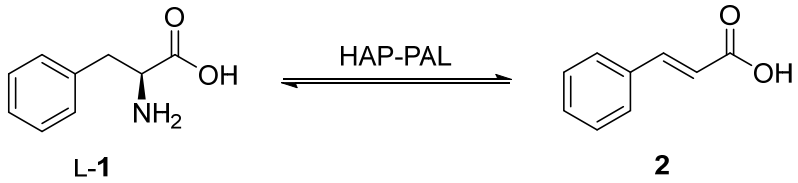

L-**1** **2**

Scheme 1. PAL immobilized on hydroxyapatite and its composites for ammonia elimination reaction from L-phenylalanine

Preparation of HAP and HAP based nanocomposites

HAP and HAP composites were obtained by coprecipitation, the most straightforward and frequently used method for the preparation of these materials [25].

Even though being used on a large scale, HAPs poor tensile strength and fracture toughness makes it unsuitable for a wide range of applications. HAPs mechanical structures can be improved by using different additives, such as carbon nanotubes, gelatin or chitosan [26], [27]. Due to the CNTs excellent mechanical properties, HAP can be toughen and strengthen [28].

HAP-gelatin composites have high porosity and interconnectivity, great biocompatibility and good mechanical properties [29].

The polymeric composites of HAP have improved properties, including modulus, strength and stiffness compared to pure HAP [30]. The HAP/chitosan composites are good candidates for tissue engineering, bone and cartilage scaffolds [31].

Characterization of the support material

Particle size distribution

Several characteristics, such as chemical reactivity, opacity, texture, viscosity, density, porosity or material strength of materials are affected by the size of their particles [32]. The particle size and surface area greatly influence the properties of HAP. Depending on the growth conditions the particle size of HAP is usually between 10 and 500 nm [33].

The particle size of the obtained HAP and HAP composites was determined by laser diffraction particle size analyzer.

By adding the additives to the HAP a slight increase of the particle size can be observed. This could be due to the ease of aggregation of the particles in presence of polymers. The smallest particles are obtained by using carbon nanotubes as additive (**Fig. 1**).

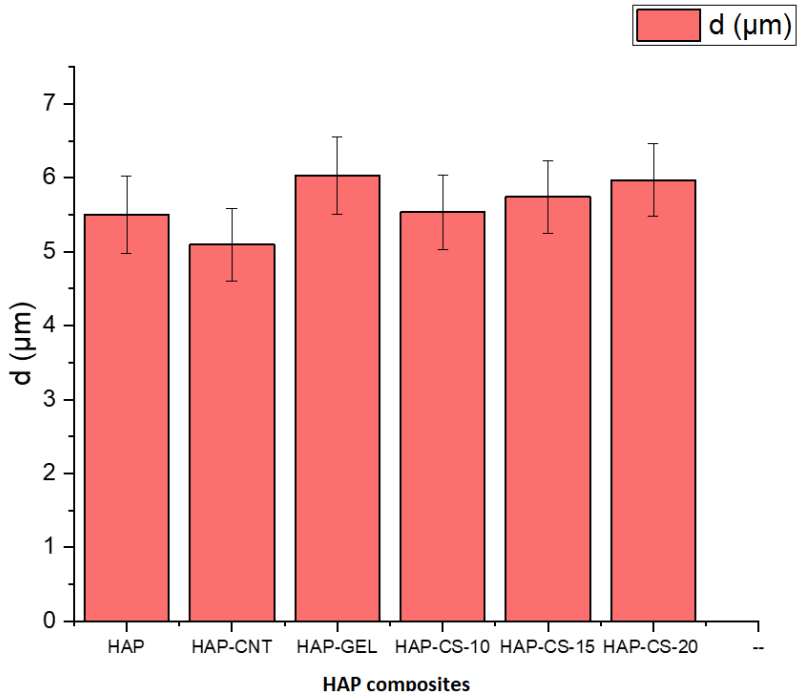

Figure 1. Particle size distribution of HAP and HAP-composites

Transmisson electron microscopy (TEM)

The morphology of the obtained composites was examined by transmission electron microscopy. As expected, in case of the HAP (**Fig. 2** (1)) a good homogeneity can be observed, property which characterizes this support. The carbon nanotube particles are integrated between the HAP crystals (**Fig. 2** (2)). The composites obtained by the addition of gelatin (**Fig. 2** (3)) and chitosan **Fig 2** (4), (5), (6)), loses the prism shape characteristic to HAP, instead they have a round shape. Thus, the gelatin and chitosan have a strong influence upon the morphology of the composites, they disable the formation of the crystals. The morphology and the size distribution in case of HAP-CS are evan. A difference between the HAP (**Fig. 2** (1)) and HAP coated by APTES (**Fig. 2** (7)) can also be observed on the TEM images, since APTES creates a silica coating of HAP.

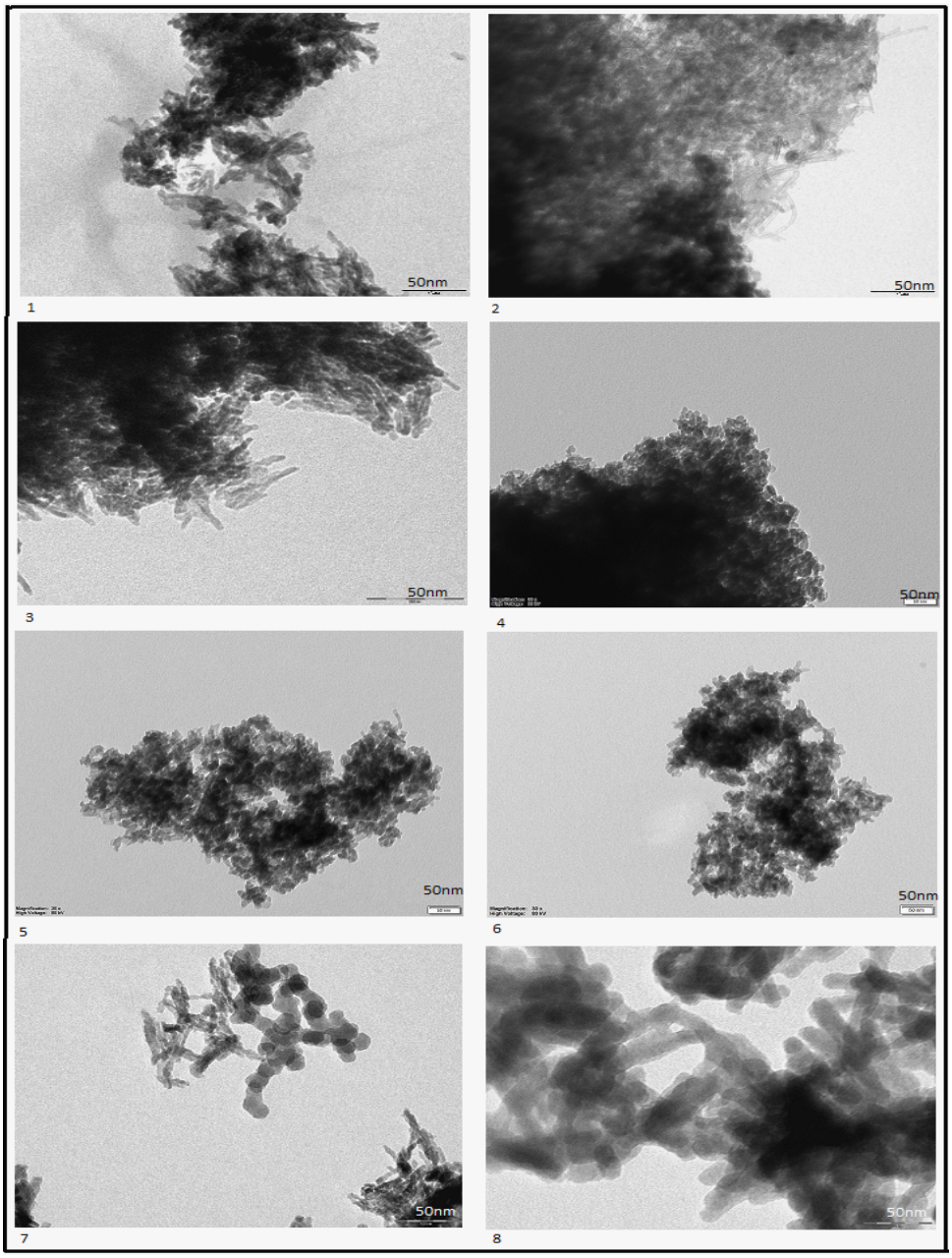

Figure 2. TEM images of: (1) HAP, (2) HAP-CNT, (3) HAP-GEL, (4) HAP-CS-10, (5) HAP-CS-15, (6) HAP-CS-20, (7) HAP+APTES, (8) HAP-GEL+APTES (The resolution of the images is 50nm)

XRD measurements

The composites were also analyzed by x-ray diffraction. There is no significant difference between the phase composition and crystallinity of HAP, HAP-GEL, HAP-CS and HAP-CNT. The peaks marked with star are characteristic for the hydroxyapatite. In case of all composites other phases besides HAP can not be identified (**Figure 3**).

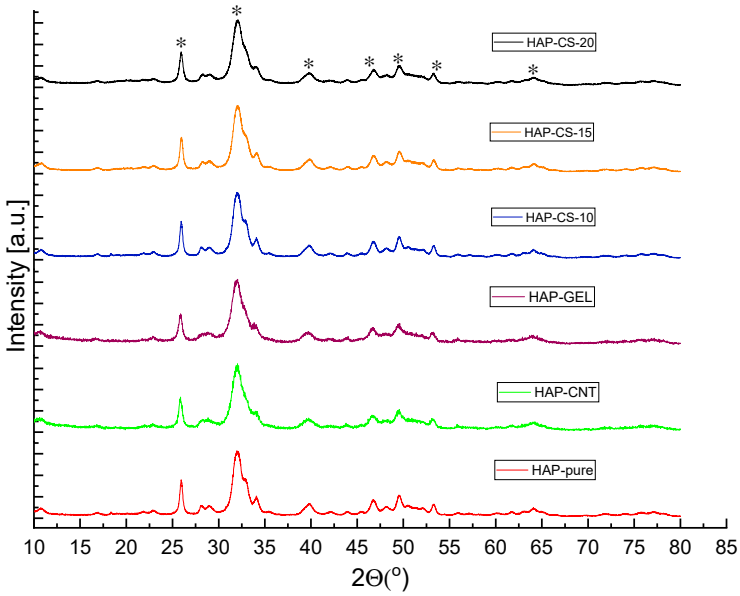

Figure 3. XRD measurements of HAP and HAP composites

Immobilization of *Pc*PAL on hydroxyapatite and its composites

For the immobilization of the enzyme on the HAP and its composites obtained with carbon nanotubes and gelatin first a surface modification of the support material was achieved using aminopropyl triethoxy silan (APTES), followed by the addition of glycerol diglycidyl ether a crosslinker which was recently successfully used for the stable, covalent attachment of *Pc*PAL on the surface of carbon nanotubes [21]. The enzyme was immobilized on the surface of the modified support material (**Scheme 2A**). For the HAP composites obtained with chitosan the direct linkage of the enzyme on the support material

was achieved by using GDE (**Scheme 2B**). For control experiments also the adsorption of the enzyme on the surface of HAP was achieved. The obtained products were characterized by reproducibility (immobilization reactions were performed in duplicate) and high immobilization yields (**Table 1**.)

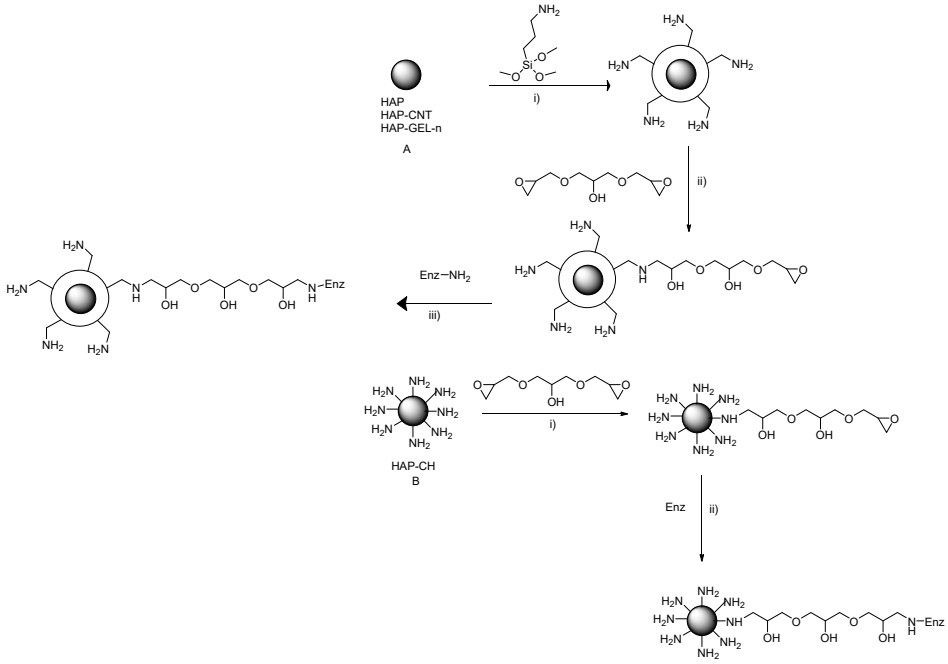

Scheme 2. Immobilization of *Pc*PAL on **A**. HAP, HAP-CNT and HAP-GEL, *i*) APTES in EtOH, *ii*)GDE in EtOH, *iii*) *Pc*PAL in Tris buffer, 0.1M, pH 8.8 and **B** HAP-CH, *i*) GDE in EtOH, *ii*) *Pc*PAL in Tris buffer, 0.1M, pH 8.8

Table 1. Immobilization yield of the enzyme preparations

SUPPORT MATERIAL	IMMOBILIZATION YIELD (%)
HAP	99
HAP-CNT	99.9
HAP-GEL	99.7
HAP-CS-10	91.9
HAP-CS-15	99.6
HAP-CS-20	92.4
HAP-ADS	99.6

Biocatalytic behavior of the obtained enzyme preparation in the ammonia elimination reaction from L-phenylalanine

The biocatalyst obtained by adsorption and by the covalent attachment of *Pc*PAL on the HAP and HAP composites were tested in the ammonia elimination reactions from L-phenylalanine. The highest activity was achieved using the enzyme preparation obtained by HAP with 15% chitosan as support material (**Table 2**, entry 6), where the conversion was comparable with the conversion of the reaction catalyzed by the native enzyme (**Table 2**, entry 1), followed by HAP (**Table 2**, entry 2) and HAP-GEL (**Table 2**, entry 4). The lowest enzyme activity was achieved using HAP-CNT as biocatalyst (**Table 2**, entry 3). In order to further increase the conversion rates, different chitosan content was used as additive in the HAP. But by increasing or decreasing the chitosan content above or under 10%, the enzyme activity decreased dramatically (**Table 2,** entry 5 and 7). The adsorbed enzyme preparation also showed high enzymatic activity (**Table 2**, entry 8).

Table 2. Conversion of the reactions catalyzed by the immobilized *Pc*PAL on HAP and HAP composites (rt, 22h)

ENTRY	ENZYME PREPARATION	CONVERSION (%)
1	**PCPAL**	98.5
2	**HAP**	87.9
3	**HAP-CNT**	77.7
4	**HAP-GEL**	80.8
5	**HAP-CS-10**	49.5
6	**HAP-CS-15**	98.1
7	**HAP-CS-20**	53.97
8	**HAP-ADS**	72.6

Next, the *reusability* of the best performing enzyme preparations (HAP-PAL, HAP-CS-15-PAL, HAP-GEL-PAL, HAP-CNT-PAL, HAP-ads-PAL) was tested in repeated batch cycles. In case of all preparations the enzyme activity showed a decreasing tendency. The most stable enzyme preparation in the reusability test was the one obtained using HAP as support material, followed by the HAP-CS-15. In case of the HAP-GEL the first three cycles show a stability in the enzyme activity, followed by a drastic decrease.

The less efficient biocatalyst proved to be the one obtained with HAP-CNT. The enzyme adsorbed on the surface of the support material showed a drastic decrease at the second reuse, the obtained conversion being only 14%. This could be due to the leaking of the enzyme from the support material when immobilized by adsorption (**Figure 4**).

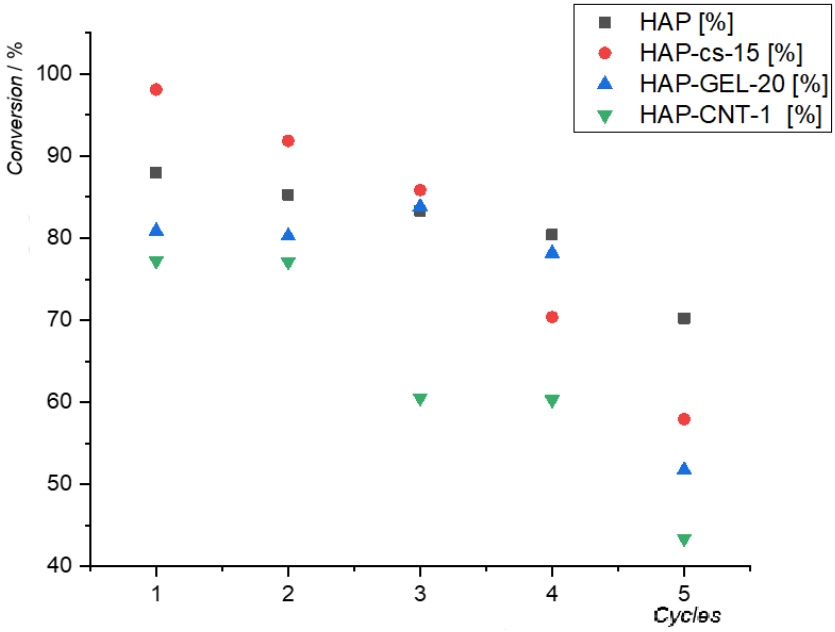

Figure 4. Reusability of the best performing immobilized enzyme preparations (rt, 22h)

Time-course profile

The time course profile of the ammonia elimination reactions from L-**1** mediated by the two best performing enzyme preparations (HAP-PAL and HAP-CS-15-PAL) was investigated. Samples were withdrawn from the reaction mixtures after 1, 2, 4, 7, and 24 hours. In both cases an almost linear increase of conversion can be observed, however, in case of HAP-PAL the maximum conversion (91%) was achieved faster (**Figure 5**).

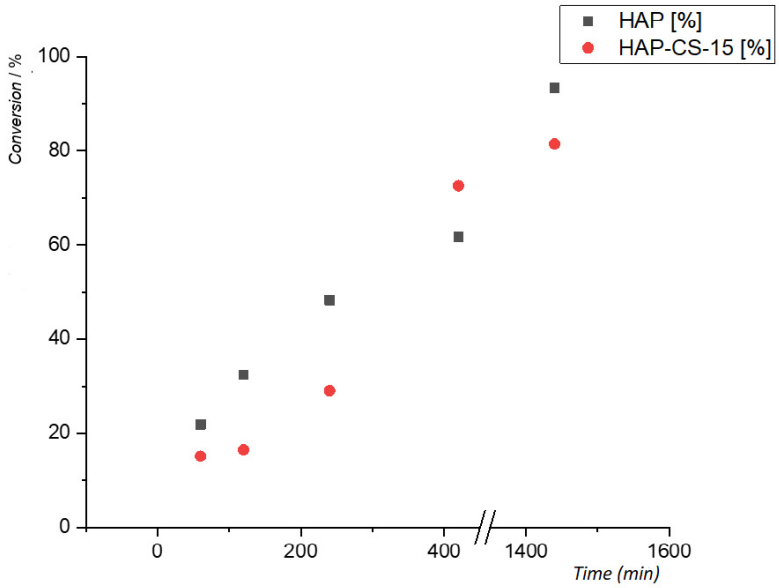

Figure 5. Time course profile of the reactions catalyzed by HAP-PAL and HAP-CS-15-PAL

CONCLUSIONS

This study demonstrates that hydroxyapatite and its composites obtained with carbon nanotubes, gelatin, and chitosan can be used as support material for the immobilization of phenylalanine ammonia lyase. The support materials were obtained by coprecipitation method and were characterized by transmission electron microscopy, laser diffraction particle size analyzer and XRD measurements. The obtained nanoparticles were further used for the immobilization of phenylalanine ammonia lyase. The nanobioconjugates were tested in the ammonia elimination reaction from L-phenylalanine. The most durable immobilized enzyme preparations were HAP-CS-15-PAL and HAP-PAL. The highest conversion rates were obtained with HAP-CS-15 (98,1%), while in the reusability studies HAP-PAL had the best performance, it maintained more than 80% of its initial activity even after 5 cycles of reuse. Although these enzyme preparations show lower catalytic activity then other *Pc*PAL preparations previously obtained, by further optimization procedures hydroxyapatite could be a promising alternative as support material for the immobilization of PAL.

EXPERIMENTAL SECTION

Materials

Enzyme

Phenylalanine ammonia-lyase from parsley (*Pc*PAL) was overexpressed in E. coli and purified according to the method described by Dima et al[34]

Chemicals

Single walled carbon nanotubes were purchased from Chengdu Organic Chemicals Co. Ltd (Chengdu, China). All other reagents were of analytical grade (Merck, Germany) and used without further purification. The technical grade solvents were dried and/or freshly distilled prior to use.

Equipments

Transmission electron microscopy (TEM) was performed using an automatic H-7650 TEM, Hitachi (Tokyo, Japan) with accelerating voltage 40-120 kV, zoom 200x-600000x, by dipping a holey-carbon TEM grid into a suspension of the immobilized enzyme. Sample was imaged using an Olympus KeenView G2 camera, transmission electron microscope operating at 120kV.

For the Bradford protein assay, an 8453 UV-Vis spectrophotometer, Agilent (Santa Clara, CA, USA) was used.

Ultrasonications during enzyme immobilization were performed in a Transsonic 460/H ultrasonic bath, Elma Schmidbauer GmbH (Singen, Germany) at 100W, 40 kHz.

The shaking and incubation of enzymatic reactions was performed using a Titramax 1000 instrument, equipped with a heating module.

The particle size distribution was measured with a Shimadzu WING SALD-7101 (Japan).

The XRD analysis was performed on a Shimadzu XRD 6000 (Japan) using CuKα radiation at 40Kv, 30mA, at λ=1.542 Å. X-Ray images were prepared for each material. The red lines indicates the caraceristic signs of the HAP crystals 25,8 32,05 39,84 46,78 49,53 53,13 63,97. The spectrum was identified by the ICPDS 09-0432 code in database.

The enzymatic reactions were monitored with an Agilent (Santa Clara, CA, USA) HPLC.

Methods

Preparation of HAP and HAP composites

Pure HAP and HAP-based NCs were prepared as previously described [35]. The used precursors were $Ca(NO_3)_2$ as a source of Ca^{2+} and $(NH_4)_2HPO_4$ as a source of PO_4^{3-}. An aqueous solution of 0.9 mol/L $(NH_4)_2HPO_4$ was added

dropwise with a feed rate of 25 ml/min, using a peristaltic pump, into a stirred aqueous solution of 1.5 mol/L $Ca(NO_3)_2 \cdot 4H_2O$, at room temperature. The appropriate quantities of additives, 1% carbon nanotube, 20% gelatin, were added to the $Ca(NO_3)_2$ solution while chitosan (10/15/20%) was added to the $(NH_4)_2HPO_4$ solution. The pH was adjusted to 11 by adding 25% ammonia solution under constant stirring at room temperature. The suspension was matured for 22 h, filtered and washed.

Immobilization of the enzyme on HAP and HAP composites

Immobilization of PcPAL on HAP, HAP-GEL and HAP-CNT

HAP and HAP composites (HAP-GEL, HAP-CNT 20mg) were added to a solution of APTES (120 mg in 5 mL ethanol, **Scheme 2A** step *i*)). The obtained suspension was sonicated to avoid bundled HAP formation, and incubated at room temperature for 1 hour shaking at 1300 rpm. After 1 hour of incubation the reaction mixture was filtered and GDE (100mg in 5mL EtOH) was added (**Scheme 2A step** *ii*)). The reaction mixture was incubated for 4 hours at room temperature shaking at 1300 rpm. After activation the sample was filtered. To the GDE activated support *Pc*PAL (2 mg in Tris buffer, 0.1M, pH 8.8) was added and the reaction mixture was shaken at 1300 rpm for 4 hours at room temperature (**Scheme 2A** step *iii*)). After the immobilization the resulted biocatalyst was filtered and washed with distilled water (3x10 mL). The amount of PAL immobilized on the support material was determined from the total mass of the enzyme in the solution before the immobilization and in the unified filtrates after the immobilization (measured spectrophotometrically using the Bradford method).

Immobilization of PcPAL on HAP-CS

HAP-CS (20 mg) was added to a solution of GDE (100mg in 5mL EtOH) shaking at 1300 rpm at room temperature for 4 hours (**Scheme 2B** step *i*)). The activated HAP-CS was filtered and *Pc*PAL (2 mg in Tris buffer, 0.1M, pH 8.8) was added (**Scheme 2B** step *ii*)). The reaction mixture was incubated for 4 hours at 1300 rpm at room temperature. The reaction mixture was filtered and the obtained enzyme preparation was washed with distilled water (3x10 mL). The amount of PAL immobilized on the support material was determined from the total mass of the enzyme in the solution before the immobilization and in the unified filtrates after the immobilization (measured spectrophotometrically using the Bradford method).

Immobilization of PcPAL on HAP-CS by adsorption

HAP (20 mg) was added to a solution of *Pc*PAL (2 mg in Tris buffer, 0.1M, pH 8.8). The reaction mixture was incubated for 4 hours at 1300 rpm at room temperature. The reaction mixture was filtered and the obtained

enzyme preparation was washed with distilled water (3x10 mL). The amount of PAL immobilized on the support material was determined from the total mass of the enzyme in the solution before the immobilization and in the unified filtrates after the immobilization (measured spectrophotometrically using the Bradford method).

*Ammonian elimination reaction from L-**1** mediated by the obtained enzyme preparations*

HAPs-PAL (1 mg) was added to a solution of L-phenylalanine (**1**, 0.8 mg, 4.7 mM) in Tris buffer (0.1 M, pH 8.8, 1 mL). The resulting mixture was shaken (1250 rpm) at room temperature for 22 h. The reaction mixture was filtered and analyzed by high performance liquid chromatography.

Reusability of the immobilized enzyme preparations

For the recycling experiments the reactions were performed as described at the previous section. The enzyme was recovered from the reaction mixture after each cycle by centrifugation at 13400 rpm for 1 min and washed with buffer solution (3 x 1 mL) and reused in the following experiment.

The time course profile of the reactions

The time course profile of the reaction was obtained by performing the ammonia elimination reactions with reaction times of 1, 2, 4, 7 and 24h.

ACKNOWLEDGMENTS

This work was supported by a grant of the Romanian National Authority for Scientific Reasearch CNCS-UEFISCDI, project number PN-III-P2-2.1-PED-2019-3664.

REFERENCES

1. L.M. Pera; M.D. Baigori; A. Pandey; G.R. Castro, *Biocatalysis*. Elsevier B.V., **2015**.
2. R.A. Sheldon; S. Van Pelt, *Chem. Soc. Rev.*, **2013**, *42,* , 6223–6235.
3. M. Hartmann; X. Kostrov, *Chem. Soc. Rev.*, **2013**, *42*, 15, 6277–89.
4. C. Mateo; J.M. Palomo; M. Fuentes; L. Betancor; V. Grazu; F. López-Gallego; B.C.C. Pessela; A. Hidalgo; G. Férnandez-Lorente; R. Férnandez-Lafuente; J. M. Guisan, *Enzyme Microb. Technol.*, **2006**, *39*, 2, 274–280.
5. W.C. Liu; H.Y. Wang; L.C. Chen; S.W. Huang; C. Wu; R.J. Chung, *Ceram. Int.*, **2019**, *45*, 5, 5668–5679.
6. R. Barabás; E. de Souza Ávila; L.O. Ladeira; L.M. Antônio; R. Tötös; D. Simedru; L. Bizo; O. Cadar, *Arab. J. Sci. Eng.*, **2020**, *45*, 1, 219–227.
7. S. Mondal; G. Hoang; P. Manivasagan; H. Kim; J. Oh, *Ceram. Int.*, **2019**, *45*, 14, 17081–17093.

8. P. Yang; Z. Quan; C. Li; X. Kang; H. Lian; J. Lin, *Biomaterials*, **2008**, *29*, 32, 4341–4347.
9. S. Mondal; U. Pal; A. Dey, *Ceram. Int.*, **2016**, *42*, 16, 18338–18346.
10. J.S. Cho; D.S. Yoo; Y.C. Chung; S. H. Rhee, *J. Biomed. Mater. Res. - Part A*, **2014**, *102*, 2, 455–469.
11. K. Balani; Y. Chen; S.P. Harimkar; N.B. Dahotre; A. Agarwal, *Acta Biomater.*, **2007**, *3*, 6, 944–951.
12. M. Li; P. Xiong; F. Yan; S. Li; C. Ren; Z. Yin; A. Li; H. Li; X. Ji; Y. Zheng; Y. Cheng, *Bioact. Mater.*, **2018**, *3*, 1, 1–18.
13. R.K. Brundavanam; Z.T. Jiang; P. Chapman; X.T. Le; N. Mondinos; D. Fawcett; G. E. J. Poinern, *Ultrason. Sonochem.*, **2011**, *18*, 3, 697–703.
14. J. Venkatesan; S. K. Kim, *Mar. Drugs*, **2010**, *8*, 8, 2252–2266.
15. L. Poppe; J. Rétey, *Curr Org Chem*, **2003**, *7*, 13, 1297–1315.
16. L. Poppe; J. Rétey, *Angew. Chemie - Int. Ed.*, **2005**, *44*, 24, 3668–3688.
17. H. Ritter; G.E. Schulz, *Plant Cell*, **2004**, *16*, 12, 3426–3436.
18. A. Gunia-Krzyżak; K. Słoczyńska; J. Popiół; P. Koczurkiewicz; H. Marona; E. Pękala, *Int. J. Cosmet. Sci.*, **2018**, *40*, 4, 356–366.
19. D. Weiser; L.C. Bencze; G. Bánõczi; F. Ender; R. Kiss; E. Kõkai; A. Szilágyi; B. G. Vértessy; Ö. Farkas; C. Paizs; L. Poppe, *ChemBioChem*, **2015**, *16*, 16, 2283–2288.
20. D. Weiser; A. Varga; K. Kovács; F. Nagy; A. Szilágyi; B.G. Vértessy; C. Paizs; L. Poppe, *ChemCatChem*, **2014**, *6*, 5, 1463–1469.
21. J.H. Bartha-Vári; M.I. Toşa; F.D. Irimie; D. Weiser; Z. Boros; B.G. Vértessy; C. Paizs; L. Poppe, *ChemCatChem*, **2015**, *7*, 7, 1122–1128.
22. K.H. Jang; K.B. Song; J.S. Kim; C.H. Kim; B.H. Chung; S. K. Rhee, *Bioprocess Eng.*, **2000**, *23*, 1, 89–93.
23. C. Marzadori; S. Miletti; C. Gessa; S. Ciurli, *Soil Biol. Biochem.*, **1998**, *30*, 12, 1485–1490.
24. B. Wang; J.J. Zhang; Z.Y. Pan; X.Q. Tao; H. S. Wang, *Biosens. Bioelectron.*, **2009**, *24*, 5, 1141–1145.
25. A. Fihri; C. Len; R.S. Varma; A. Solhy, *Coord. Chem. Rev.*, **2017**, *347*, 48–76.
26. T.A. Dick; L.A. dos Santos, *Mater. Sci. Eng. C*, **2017**, *77*, 874–882.
27. M. Prakasam; J. Locs; K. Salma-Ancane; D. Loca; A. Largeteau; L. Berzina-Cimdina, *J. Funct. Biomater.*, **2015**, *6*, 4, 1099–1140.
28. R. Rajesh; N. Senthilkumar; A. Hariharasubramanian; Y. Dominic Ravichandran, *Int. J. Pharm. Pharm. Sci.*, **2012**, *4*, SUPPL. 5, 23–27.
29. R. Munirathinam; J. Huskens; W. Verboom, 1–32, **2015**.
30. C. Zhou; Q. Wu, *Colloids Surfaces B Biointerfaces*, **2011**, *84*, 1, 155–162.
31. M.R. Nikpour; S.M. Rabiee; M. Jahanshahi, *Compos. Part B Eng.*, **2012**, *43*, 4, 1881–1886.
32. R. Barabás; M. Czikó; I. Dékány; L. Bizo; E. S. Bogya, *Chem. Pap.*, **2013**, *67*, 11, 1414–1423,.
33. Z. Xu; G. Qian; M. Feng, *Results Phys.*, **2020**, *16*, 102991,.
34. N.A. Dima; A. Filip; L.C. Bencze; M. Olah; P. Satorhelyi; B.G. Vertessy; I.Poppe; C. Paizs, *Studia UBB Chemia*, **2016**, *61*, 2, 21-34.
35. E.S. Bogya; R. Barabás; A. Csavdári; V. Dejeu; I. Bâldea, *Chem. Pap.*, **2009**, *63*, 5, 568–573.

STUDIA UBB CHEMIA, LXVI, 1, 2021 (p. 179-194)
(RECOMMENDED CITATION)
DOI:10.24193/subbchem.2021.1.14

LC-MS/MS METHOD FOR THE DETERMINATION OF DIAZOLIC ANTHELMINTIC DRUG LEVELS FROM SHEEP AND HUMAN PLASMA FOR USE IN PHARMACOKINETIC AND BIOAVAILABILITY STUDIES

LÉNÁRD FARCZÁDI[a,b], SILVIA IMRE[b,c*], LAURIAN VLASE[a]

ABSTRACT. A new high-throughput, inexpensive and selective LC-MS method for determining fenbendazole, albendazole and albendazole sulfoxide from human and ovine plasma was developed and validated in accordance with current guidelines in bioanalysis. Analytes (fenbendazole, albendazole, albendazole sulfoxide) and internal standard (fluconazole) were separated on a Gemini NX-C18 analytical column in reversed phase chromatography in gradient elution using mobile phase composed of acetonitrile and aquenous 0.2% formic acid with a flow rate of 0.6 mL/min. After positive electrospray ionization analytes were detected in the mass spectrometer in selected reaction monitoring mode, monitoring fragment ion m/z 268.05 from m/z 300.08 for fenbendazole, ion m/z 234.07 from m/z 266.09 for albendazole, ion m/z 240.04 from m/z 282.09 for albendazole sulfoxide and ion m/z 220.06 from m/z 307.60 for fluconazole. Sample preparation was performed using protein precipitation. Validation of the analytical method was performed with respect to selectivity, stability, linearity (r>0.9901), precision (RSD<12.9%) and accuracy (bias<12.7%) over the concentration ranges of 5-250 ng/mL for each analyte (lower limit of quantification was 5 ng/mL for all analytes). The analytical method is simple, versatile and suitable for bioanalysis of these azole anthelmintic drugs from human and ovine samples, and applicable in pharmacokinetic studies involving fenbendazole and albendazole.

Keywords: *fenbendazole, albendazole, pharmacokinetics, bioavailability, LC-MS*

[a] *Iuliu Hatieganu University of Medicine and Pharmacy, Faculty of Pharmacy, Department of Pharmaceutical Technology and Biopharmaceutics, 8 Victor Babes street, RO-400012, Cluj-Napoca, Romania*

[b] *George Emil Palade University of Medicine, Pharmacy, Science, and Technology of Targu Mures, Center for Advanced Medical and Pharmaceutical Research, 38 Gheorghe Marinescu street, RO-540142, Targu Mures, Romania*

[c] *George Emil Palade University of Medicine, Pharmacy, Science, and Technology of Targu Mures, Faculty of Pharmacy, Department of Analytical Chemistry and Drug Analysis, 38 Gheorghe Marinescu str., RO-540142, Targu Mures, Romania*

**Corresponding author, email: silvia.imre@umfst.ro*

INTRODUCTION

Albendazole and fenbendazole are two broad-spectrum benzimidazolic anthelmintics. They are both used in the treatment of a wide array of parasitic worm infections [1]. Benzimidazole anthelmintics hinder the development of nematodes by interfering in important structural as well as other functions. This is accomplished by inhibiting synthetization of microtubules, and in the case of some species even through an ovicidal effect.

Fenbendazole is currently used around the world for treating livestock, pets and other animals for helminthic infections and its safety has been well assessed over the more than three decades since its being used. Fenbendazole, although currently not used for anthelmintic treatment in humans, based on limited data has been shown to be safe for human in doses up to 500 mg or even 2000 mg, with no adverse effects being reported.

Fenbendazole is absorbed only in limited quantities in the intestine after oral administration and is rapidly metabolized by liver microsomes to oxfendazole through sulfoxidation. This metabolism step however is reversible and can lead to the formation of fenbendazole. Studies have also shown promising antitumor effects of fenbendazole in mice when combined with certain supplementary vitamins which in the future might lead to further research and a possible new application of fenbendazole in humans [2].

Albendazole has also been widely used to treat humans with helmintic infections, but also animals such as livestock and pets [3], and is also one of the drugs listed on the WHO's Essential Drugs-list [4]. Toxicity of albendazole is low after oral adminstration, resulting in low plasma levels of albendazole because of rapid metabolization by liver microsomes to its sulfoxilated metabolite, albendazole sulfoxide, which is further metabolized to albendazole sulfone [3].

It is thought that both enzymes CYP3A4 and CYP2C19, along with other cytochrome P450 isoforms are responsible for the formation of sulfoxide metabolites from albendazole and fenbendazole [5]. Thus, albendazole and fenbendazole may be susceptible to drug-drug interactions if combined with inhibitors of these enzymes, such as for example fluconazole. This might be essential for example, as pointed out by the authors of the study discovering possible antitumor effects of fenbendazole [2], if fenbendazole is to be used in the treatment of cancer, in which case studies investigating drug interactions of fenbendazole with inhibitor drugs of CYP3A4 and other cytochrome P450 isoforms, as well as further bioavailability and other preclinical and clinical studies will need to be carried out on both on laboratory animals as well as human subjects.

Currently there are methods described in literature for the quantification of fenbendazole and albendazole, as well as some of their metabolites from

different types of biological samples, most often plasma, collected from both human subjects as well as a number of different species of animals [6-13]. Most of the methods described use LC-MS/MS methodologies due to the advantage this technique offers with regards to improved selectivity and sensitivity [6-10]. There have also been methods developed and described in literature which use liquid chromatography with UV or fluorescence detection [11-13].

The study was conducted in order to propose a simple, versatile and reliable analytical method suitable for high-throughput bioavailability, biomonitoring, bioequivalence or other types of clinical studies using a simple, fast and inexpensive sample preparation method, short analytical runtime and with performance parameters validated according to current guidelines in bioanalysis.

RESULTS AND DISCUSSION

The proposed method was fully validated according to FDA (Food and Drug Administration, USA) [14] and EMA (European Medicines Agency) [15] bioanalytical method validation guidelines.

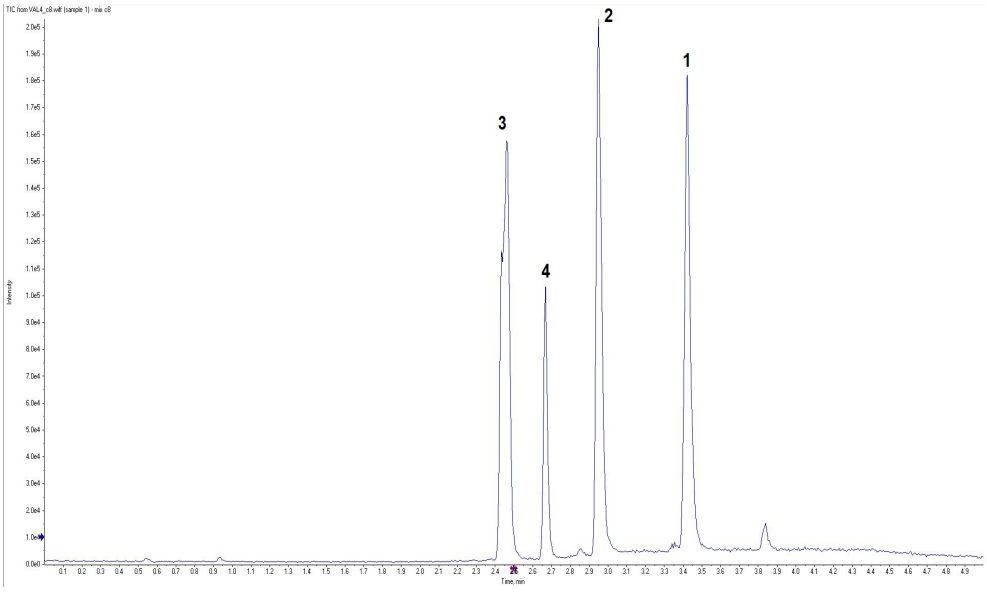

Figure 1. The Total Ion Chromatogram (TIC) of a standard solution containing fenbendazole (1), albendazole (2), albendazole sulfoxide (3) and fluconazole (4)

Under optimal mass spectrometer parameters and chromatographic conditions, the three analytes were detected using selected reaction monitoring (SRM): fenbendazole - ion m/z 268.05 from m/z 300.08; albendazole - ion m/z 234.07 from m/z 266.09; albendazole sulfoxide - ion m/z 240.04 from m/z 282.09; fluconazole - ion m/z 220.06 from m/z 307.60. Retention times were 3.4 minutes for fenbendazole, 2.9 minutes for albendazole, 2.5 minutes for albendazole sulfoxide and 2.7 minutes for the internal standard (fluconazole), all compounds being separated at individual retention times (Figure 1).

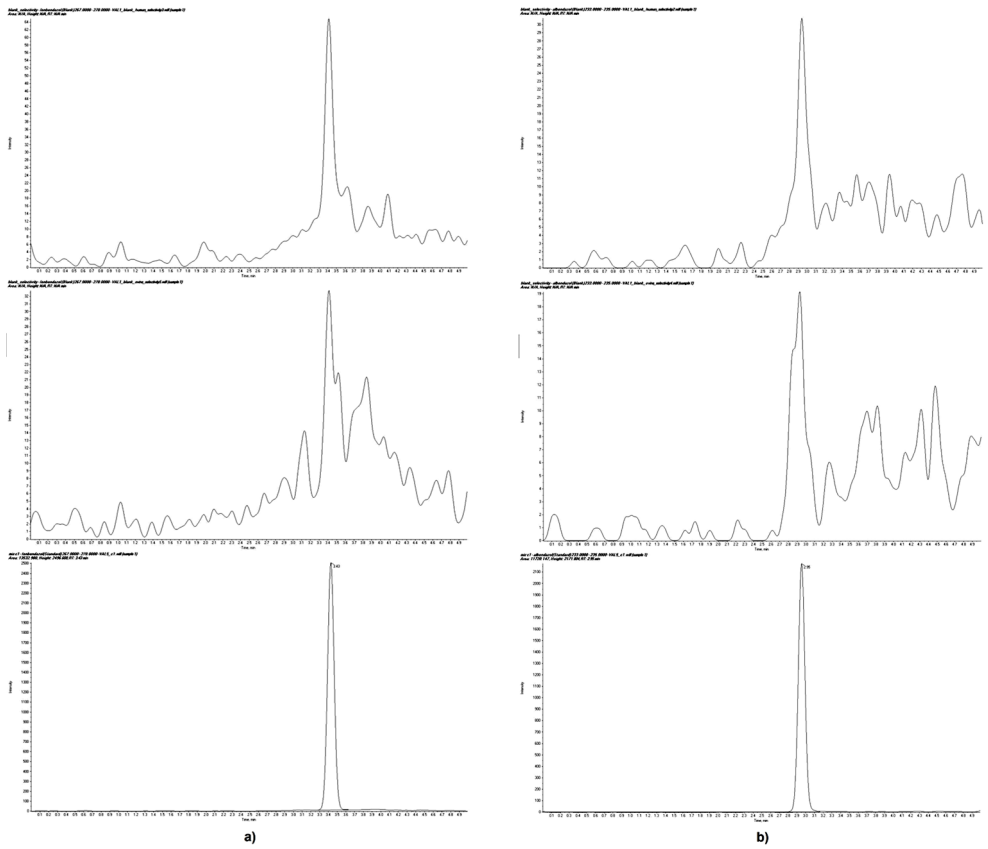

Figure 2. Extracted chromatograms of human blank plasma (top), ovine blank plasma (middle) and standard solution at the lower limit of quantification (bottom) for a) fenbendazole, b) albendazole

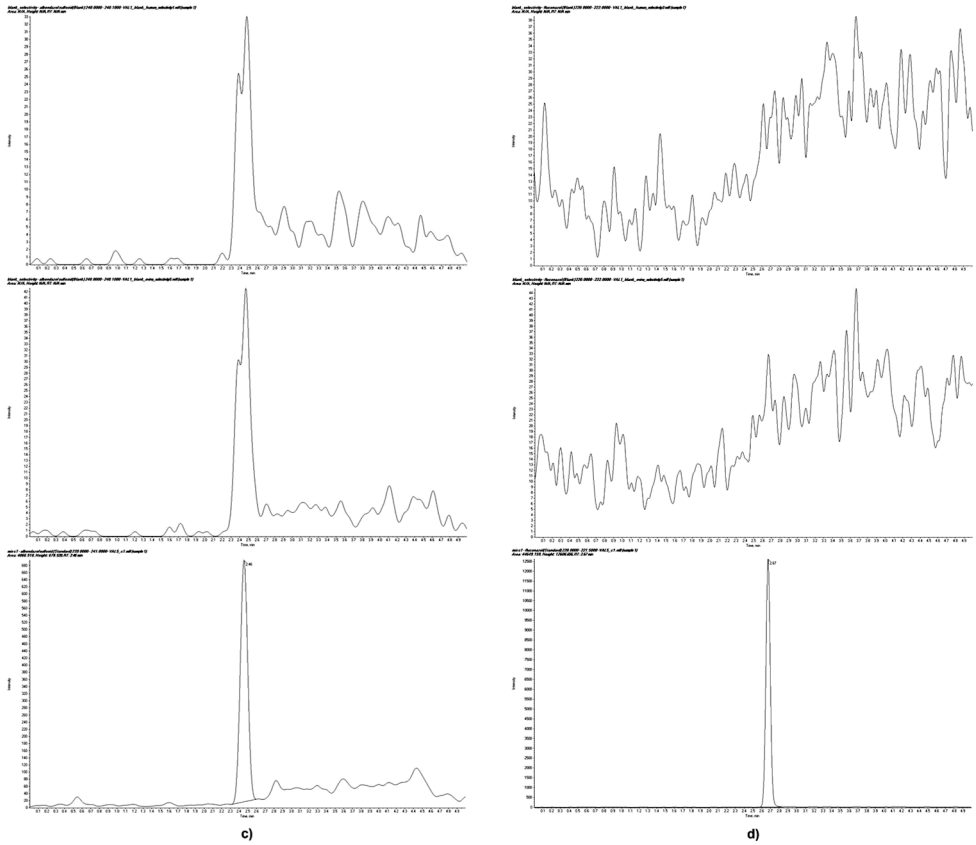

Figure 2. Extracted chromatograms of human blank plasma (top), ovine blank plasma (middle) and standard solution at the lower limit of quantification (bottom) for c) albendazole sulfoxide, d) fluconazole (internal standard)

Selectivity

The analytical method needs to distinguish the analytes and IS from endogenous compounds from the biological matrix (plasma) or other compounds which may be present in biological samples. For all six different blank samples tested, no interfering peaks with a peak area greater than 20% of analyte peak area at the lower limit of quantification (LLOQ) were detected (Figure 2). Results for selectivity testing are presented in Table 1.

Table 1. Selectivity for fenbendazole, albendazole and albendazole sulfoxide

Analyte	Mean Blank Area	LLOQ Area	Selectivity (%)
Fenbendazole	157.08	16826.62	99.07
Albendazole	122.80	15888.64	99.23
Albendazole sulfoxide	96.18	2800.81	96.57

Carry-over

The carry-over effect (contamination from one sample to the next) was studied by injecting a blank solution immediately after the most concentrated standard solution (250 ng/mL of each analyte) in each run of the validation. Carry-over was below 20% of LLOQ areas for analytes and below 5% of IS area. Results are presented in Table 2.

Table 2. Carry-over for fenbendazole, albendazole, albendazole sulfoxide and fluconazole (ISTD)

Analyte	Mean Blank Area	LLOQ Area	Carry-over (%)
Fenbendazole	1338.75	14149.38	9.68
Albendazole	0.0	12215.70	0.0
Albendazole sulfoxide	0.0	3402.30	0.0
Fluconazole (ISTD)	0.0	49783.52	0.0

Linearity and lower limit of quantification

Calibration curves proved to be linear over the proposed concentration range with a LLOQ of 5 ng/mL for each analyte. The accuracy of recalculated concentrations of calibration standards was within acceptance limits for all calibration curves and all analytes, with no single calibration curve being compiled of less than 7 calibration standards which have passed acceptance criteria. Mean calibration curves characteristics for fenbendazole, albendazole and albendazole sulfoxide are presented in Table 3. Five standard solutions at the LLOQ of 5 ng/mL of each analyte were analyzed in order to determine within and between run accuracy and precision (Tables 4-5) at this level of concentration.

Table 3. Characteristics of calibration curves, n = 5

Analyte	Conc. range, ng/mL	Slope±SD	Intercept±SD	Correlation coefficient range
Fenbendazole	5 - 250	0.0198 ± 0.0033	0.1905 ± 0.0375	0.9943-0.9992
Albendazole		0.0199 ± 0.0030	0.1529 ± 0.0417	0.9953-0.9973
Albendazole sulfoxide		0.0068 ± 0.0018	0.0331 ± 0.0118	0.9901-0.9943

Accuracy and precision

The results are presented in Tables 4-5. Mean accuracy and precision were within ±15% acceptance limit for each analyte, both within as well as between runs.

Table 4. Overall within-run accuracy and precision ranges for fenbendazole, albendazole and albendazole sulfoxide at LLOQ, QCA, QCB and QCC levels

Analyte	Avg. accuracy range (% bias)	Avg. precision range (% RSD)
Fenbendazole	-4.8 ÷ +8.2	5.5 ÷ 12.9
Albendazole	-3.4 ÷ +10.1	5.8 ÷ 8.7
Albendazole sulfoxide	-2.7 ÷ +11.0	4.3 ÷ 7.0

Table 5. Overall between-run accuracy and precision ranges for fenbendazole, albendazole and albendazole sulfoxide at LLOQ, QCA, QCB and QCC levels

Analyte	Avg. accuracy (% bias)	Avg. precision (% RSD)
Fenbendazole	-9.3 ÷ +8.1	2.1 ÷ 6.2
Albendazole	-8.5 ÷ +10.6	2.5 ÷ 9.4
Albendazole sulfoxide	-4.9 ÷ +12.7	3.6 ÷ 8.2

Stability

Extensive stability testing was carried out to determine the stability of analytes and internal standard in different conditions, using quality control plasma samples (lower and higher QC samples). Long term stability, short term stability, auto-sampler stability, freeze-thaw stability and stability of stock, working and IS solutions stability were studied. Results for average quality control sample accuracies in stability testing of each analyte are presented in Table 6.

Table 6. Stability of fenbendazole, albendazole and albendazole sulfoxide

Analyte	Stability test	Accuracy range (% bias)
Fenbendazole	Stock solution stability	-11.2 ÷ +13.2
	Freeze-thaw stability	-10.2 ÷ +13.0
	Short-term stability	-8.1 ÷ +10.7
	Post-preparative stability	-11.5 ÷ +10.7
	Long-term stability	-9.2 ÷ +8.0
Albendazole	Stock solution stability	-11.0 ÷ +12.4
	Freeze-thaw stability	-4.9 ÷ +8.9
	Short-term stability	-12.6 ÷ +9.3
	Post-preparative stability	-6.8 ÷ +8.7
	Long-term stability	-6.6 ÷ +10.3
Albendazole sulfoxide	Stock solution stability	-4.4 ÷ +13.2
	Freeze-thaw stability	+4.2 ÷ +11.4
	Short-term stability	+4.4 ÷ +12.6
	Post-preparative stability	-3.0 ÷ +12.7
	Long-term stability	-2.8 ÷ +9.8

Stock solutions of analytes and internal standard were stable for 48 hours at 5 ºC. Plasma samples were stable at -20 ºC for at least 30 days, while at room temperature they were stable for a minimum of 6 hours. Processed plasma samples were stable in the autosampler for 18 hours when kept thermostatted at 20°C. Stability of analytes during thawing and freezing of plasma samples was proven for at least two cycles (freezing at -20 ºC, thawing to room temperature, then freezing them back to -20 ºC).

Dilution integrity

The results are presented in Table 7. The 10 times dilution of a 600 ng/ml sample proved to be with acceptable accuracy and precision, both between-runs and within-run.

Table 7. Average accuracy, precision within and between runs for dilution integrity testing of fenbendazole, albendazole and albendazole sulfoxide – dilution factor of 10 from 600 ng/ml, n = 5

Analyte	Dilution integrity test	Avg. accuracy (% bias)	Avg. precision (% RSD)
Fenbendazole	Within runs	-2.7	3.6
	Between runs	1.4	7.5
Albendazole	Within runs	-0.1	3.3
	Between runs	-2.6	9.5
Albendazole sulfoxide	Within runs	1.9	8.2
	Between runs	-11.7	9.8

Matrix effect

As it can be seen in the results shown in Table 8, the internal standard (IS) normalized matrix effect (MF), calculated as the ratio of matrix factors of the analytes and the MF of the internal standard, and the relative standard deviation for IS normalized matrix factors proved that there is minimal effect of matrix (regardless if human or ovine plasma is used) on the final results.

Table 8. Matrix effect for fenbendazole, albendazole and albendazole sulfoxide

Analyte	IS Normalized MF	Coef. of variation (%)
Fenbendazole	0.969 - 1.051	3.22 - 3.49
Albendazole	1.005 - 1.049	1.94 - 2.20
Albendazole sulfoxide	0.954 - 1.027	2.92 - 6.57

Method comparison

While there are a number of bioanalytical methods described in literature for the quantification of fenbendazole and albendazole, and/or their metabolites respectively [6-13], none have been reported for quantifying fenbendazole, albendazole and albendazole sulfoxide from both human and ovine plasma. While albendazole is rapidly metabolized after absorption to albendazole sulfoxide which is the main active metabolite, in the case of fenbendazole the metabolization to oxfendazole is reversible [1], thus for biomonitoring, drug-interaction, bioequivalence and other types of clinical and preclinical studies the measurement of plasma levels of fenbendazole, albendazole and albendazole sulfoxide are relevant. Studies have shown that fenbendazole achieves a maximum plasmatic concentration of 200 ng/ml in sheep after oral administration of a typical dose of 5 mg/kg fenbendazole [16], while albendazole sulfoxide can reach maximum plasmatic concentrations of up to 1950 ng/ml after oral administration of a typical dose of 7.5 mg/kg albendazole [17]. In humans after oral administration of 400 mg of albendazole a rapid metabolization was shown to take place as albendazole concentration reach a peak concentration of around 100 ng/ml after a very short time [18] with albendazole sulfoxide being the main metabolite measurable in plasma and achieving plasmatic concentrations between 465 ng/ml and 909 ng/ml [19]. It is important to note that in the case of some kinds of studies, such as drug-drug interaction studies, metabolization of albendazole can be significantly decreased leading to higher plasmatic concentrations of albendazole and lowering the concentration of albendazole sulfoxide in the plasma. The lower limit

of quantification for each analyte was chosen in order meet the criteria described in guidelines for bioanalytical method validation (to be at least 5% of the maximum plasmatic concentration expected to be measured). In case of concentrations above the upper limit of quantification samples can be diluted with a dilution factor of 10 in order the obtain concentrations within the limits of the calibration curves.

Compared to classical HPLC methods with UV or fluorescence detection used by Bistoletti et al., Rummel et al. and Shaikh et al. [11-13], liquid chromatography coupled with tandem mass spectrometry offers superior selectivity as well as better sensitivity.

Chhonker et al. [6] developed and fully validated a highly selective method for quantifying albendazole and its metabolites from human plasma, however the sample preparation uses solid phase extraction which is more labor intensive and involves higher costs per sample compared to the protein precipitation used in the present work. The total runtime for each sample is also shorter for our method, considerably reducing not only analysis time in the case of multiple study samples but also the total analytical costs. Other methods described in literature, such as the ones described by Zu et al. and Zhang et al. [9-10], use liquid-liquid extraction for sample purification which is also time consuming and more labor intensive compared to protein precipitation.

The method developed by the research team lead by Bach [7] is able to quantify oxfendazole from human plasma reliably and selectively, and can be used in pharmacokinetic studies similarly to the method developed by our research team which quantifies fenbendazole. The method developed by Bach et al. [7] also uses a simple and inexpensive protein precipitation technique for sample purification, however the total runtime for each sample is longer when compared to our method, which in the case of clinical pharmacokinetic studies involving the analysis of large numbers of samples can add up and significantly increase total analysis time.

CONCLUSIONS

A simple, rapid, versatile, sensitive and selective method was successfully developed for the quantification of fenbendazole, albendazole and albendazole sulfoxide from both human and ovine plasma. The method requires small amounts of biological samples as well as easy and fast sample preparation.

The method was validated in accordance with current EMA (European Medical Agency) and FDA (Federal Drug Administration) guidelines, for use in bioavailability studies in humans and sheep and it thus easily applicable in biomonitoring, bioequivalence, drug interaction studies.

EXPERIMENTAL SECTION

Reagents

Fenbendazole, albendazole and albendazole sulfoxide reference substances were acquired from LGC Standards (Dr. Ehrenstorfer - Augsburg, Germany), fluconazole reference substance was acquired from the European Pharmacopoeia. HPLC grade acetonitrile and formic acid were acquired from VWR International (Radnor, USA). For the production of ultrapure water a Millipore Direct-Q 3 (Millipore - Milford, USA) system was used. Blank ovine blank plasma was provided by the University of Agriculture and Veterinary Medicine of Cluj-Napoca (Romania). Blank human plasma was provided by the local Transfusion Center in Targu-Mures (Romania). Both human and ovine blank plasma was collected in containers using K3EDTA as anticoagulant.

Apparatus and equipment

For chromatographic separation and detection an LC/MS system made up of an HPLC Perkin Elmer (Waltham, USA) FX-10 coupled with an AB Sciex (Framingham, USA) QTOF 4600 mass spectrometer was used. Other equipment used: Eppendorf (Hamburg, Germany) 5430R centrifuge; Partner Corporation (Bucharest, Romania) XA 523Y analytical scale; Velp Scientifica (Usmate Velate, Italy) vortex mixer; JP Selecta (Barcelona, Spain) Ultrasons H-D ultrasonic bath; Eppendorf Research Plus (Hamburg, Germany) pipettes.

LC-MS/MS parameters

Chromatographic separation of fenbendazole, albendazole, albendazole sulfoxide and fluconazole (internal standard - IS) was achieved using a Phenomenex Gemini NX-C18 HPLC column with dimensions 3.0 x 100 mm and 3 µm particles, using a mobile phase composed of acetonitrile and aqueous 0.2% formic acid solution at a constant flow rate of 0.6 mL/min. Mobile phase gradient composition was 90% aqueous 0.2% formic acid and 10% acetonitrile between 0-2.3 minutes, 60% aqueous 0.2% formic acid and 40% acetonitrile between 2.3-4.0 minutes and 90% aqueous 0.2% formic acid and 10% acetonitrile between 4.0-5.0 minutes.

Detection of analytes was carried out in selected reaction monitoring (SRM) mode by monitoring the following fragement ion m/z 268.05 from m/z 300.08 at a collision energy (CE) of 33V for fenbendazole; fragement ion m/z 234.07 from m/z 266.09 at CE 25V for albendazole and fragement ion m/z 240.04 from m/z 282.09 at CE 25V albendazole sulfoxide For the detection

of the internal standard (fluconazole) fragement ion m/z 220.06 from m/z 307.60 at CE 19V was monitored. The positive ionization of samples was performed using a heated electrospray ion source. The following ionization parameters were used for the ionization source: Spray voltage: 3500V, vaporizer temperature: 450 ^{o}C, Ion Gas Source 1: 35, Ion Gas Source 2: 20, Curtain Gas: 10, Declustering Potential: 100. The volume injected of each solution into the LC-MS system was 5 µL and the total sample run-time was 5 minutes per sample.

Standard solutions

Stock solution of fenbendazole, albendazole and albendazole sulfoxide in acetonitrile were prepared each having a concentration of 20 µg/mL. Using these solutions, a stock mix solution in formic acid 0.2% was prepared having a concentration of 1 µg/mL for each analyte. This stock mix solution was used for the preparation of standard working solutions and quality control (QC) working solutions. Internal standard (IS) solution with a concentration of 5 µg/mL fluconazole in acetonitrile was prepared. Working solutions, IS solution and blank plasma were used to prepare plasma standard solutions with concentrations of 5, 10, 25, 37.5, 50, 100, 150 and 250 ng/mL, 5 ng/mL being the lower limit of quantification – LLOQ for each analyte, and plasma QC samples with concentrations of 15 ng/mL (lower), 75 ng/mL (medium) and 175 ng/mL (upper) of each of the three analytes. In order to prepare these plasma standard and QC solutions 100 µL of the appropriate working mix solution (in formic acid 0.2%), 100 µL blank plasma and 50 µL IS solution (5 µg/mL fluconazole) were mixed in Eppendorf tubes, finally adding 600 µL acetonitrile. The mixture was vortexed for 2 minutes and centrifuged for 10 minutes at 12000 rpm. Supernatant was transferred to chromatographic vials to be injected into the LC-MS/MS system. The final concentration of the IS in plasma calibration standard solutions was 295 ng/mL fluconazole. Fluconazole was chosen as internal standard due to having the advantage of reduced cost compared to stable isotope labeled internal standards and validation of the method proved that it is adequate for use as the internal standard for the method proposed

Sample preparation and analyte extraction

In order to analyze plasma samples from bioavailability or biomonitoring studies the following method of analyte extraction and sample purification can be used: 100 µL formic acid 0.2%, 100 µL plasma sample and 50 µL IS solution (5 µg/mL fluconazole) are mixed in Eppendorf tubes, finally adding 600 µL acetonitrile. After 2 minutes of vortexing and centrifugation for 10 minutes at

12000 rpm, the supernatant is transferred to a chromatographic vial and injected into the LC-MS/MS system.

Method validation

In order to assess the method selectivity, plasma samples spiked with the three analytes, with a concentration at the lower limit of quantification, and IS were analyzed and the obtained chromatograms were compared with chromatograms of six different blank plasma samples, three human and three ovine plasma.

The method was tested for carry-over effect by injecting a blank sample after a high concentration plasma calibration standard sample (250 ng/mL) in each run of the validation process and monitoring if analyte peaks appear in the blank solutions.

The mathematical model used for calibration curves was the internal standard calibration method with a linear fit, using 1/y2 weighting factor.

Accuracy and precision were tested by analyzing five quality control samples (n=5), at four different levels of concentrations corresponding to LLOQ and QCs samples. Accuracy or bias% (the relative difference between obtained and theoretical concentration) and precision or relative standard deviation, RSD%, were determined for samples analyzed in the same analytical run and in different analytical runs.

The dilution process was studied with regards to accuracy and precision by preparing samples with a concentration of 600 ng/mL, above upper limit of quantification (ULOQ) of 250 ng/mL, which were then diluted, with a dilution factor of 10, with blank plasma to a concentration of 60 ng/mL, a value within the calibration curve. Accuracy and precision of diluted samples was calculated both between runs as well as within one analytical run in order to determine the integrity of the dilution.

Recovery of the analytes as well as the effect of the matrix on analyte measurements were investigated by processing and analyzing six low concentration and six high concentration quality control samples which were prepared in three of each human plasma and ovine plasma, and one lower and one high concentration quality control sample prepared in purified water. Ratios of peak areas obtained in the presence and the absence of matrix for the analytes and IS was determined to asses the recovery. The matrix factor (MF), calculated as the ratio between the peak areas in the presence of matrix and in the absence of matrix, for both the analytes and internal standard were calculated. Next, the relative standard deviation of the IS normalized matrix factors (ratio of MF of the analyte and MF of the internal standard) was calculated for all three analytes from both lower and high concentration quality samples.

To test the stability of the analytes under different conditions quality control samples processed for stability testing were compared to freshly prepared quality control samples. Average concentration for each analyte at each concentration level needed to be within 85% and 115% of nominal concentration in order to asses stability of the analytes.

Stability of stock solution of the analyte mixture and internal standard solution was tested by analyzing quality control samples prepared using stock solutions and IS solution prepared previously and kept at 5^{o}C for 48 hours before use. QCA and QCC samples, four of each solution, were prepared and analyzed in order to study the stability of the stock solutions.

Freeze-thaw stability was studied by analyzing quality control samples at two concentrations (QCA and QCC), by mixing 100 µL working solution with 100 µL blank plasma. These samples were prepared at the start of the validation process and were frozen and thawed twice (two cycles). During each cycle samples were frozen and kept in the freezer at -20^{o}C for approximately 20 hours then thawed and kept at room temperature for approximately 4 hours. After repeating this cycle twice, the samples were processed and analyzed.

Short-term stability at room temperature was studied analyzing quality control samples at two concentration levels (QCA and QCC), by mixing 100 µL working solution with 100 µL blank plasma. These samples were prepared and were kept at room temperature for 6 hours before being processed and analyzed.

Post-preparative stability in the autosampler was studied analyzing five quality control samples (five of each) at three concentration levels: QCA, QCB and QCC. These control samples were prepared and used for within-run accuracy and precision testing then left in the autosampler for 18 hours thermostatted at a constant temperature of 20^{o}C, after which they were reinjected and analyzed.

Long-term stability was studied by analyzing quality control samples at two concentrations (QCA and QCC), by mixing 100 µL working solution with 100 µL blank plasma. These samples were prepared and were, frozen and kept in the freezer (-20^{o}C) for 30 days, after which they were thawed, processed and analyzed.

ACKNOWLEDGMENTS

This study was financed through Doctoral Research Grant no. 1680/3/19.01.2018 provided by the “Iuliu Hatieganu” University of Medicine and Pharmacy Cluj-Napoca.

Special acknowledgement goes to the Center for Advanced Medical and Pharmaceutical Research of the “George Emil Palade” University of Medicine, Pharmacy, Sciences, and Technology Targu Mures for the support offered in carrying out the study.

REFERENCES

1. Committe for Medicinal Products for Veterinary Use. CVMP assessment report for Panacur AquaSol (EMEA/V/C/002008/X/0003). https://www.ema.europa.eu/en/documents/variation-report/panacur-aquasol-v-c-2008-x-03-epar-assessment-report-extension_en.pdf [retrieved November 2nd 2020]
2. P. Gao; C.V. Dang; J. Watson; *J Am Assoc Lab Anim Sci*., **2008**, *47(6)*, 37–4
3. Committe For Veterinary Medicinal Products. Summary Report for Netobimin (EMEA/MRL/556/99-FINAL). https://www.ema.europa.eu/en/documents/mrl-report/netobimin-summary-report-2-committee-veterinary-medicinal-products_en.pdf [retrieved November 2nd 2020]
4. World Health Organization model list of essential medicines: 21st list 2019. (WHO/MVP/EMP/IAU/2019.06). https://apps.who.int/iris/bitstream/handle/10665/325771/WHO-MVP-EMP-IAU-2019.06-eng.pdf?sequence=1&isAllowed=y [accessed November 2nd 2020]
5. Z. Wu; D. Lee; J. Joo; J.H. Shin; W. Kang; S. Oh; D.Y. Lee; S.J. Lee; S.S. Yea; H.S. Lee; T. Lee; K.H. Liu; *Antimicrob. Agents Chemother.*, **2013**, *57(11)*, 5448-5456
6. Y.S. Chhonker; C. Edi; D.J. Murry; *J Pharm Biomed Anal.*, **2018**, *151*, 84-90
7. T. Bach; S. Bae; R. D'Cunha; P. Winokur; G. An; *J Pharm Biomed Anal.*, **2019**, *171*, 111-117
8. J. Lakritz; D. Linden; D.E. Anderson; T.A. Specht; *Vet Med. (Auckl)*, **2015**, *6*, 71-81
9. X. Zhu; S. Wang; Q. Liu; Q. Xu; C. Zhang; S. Xu; X. Wang; D. Li; H. Hu; *J. AOAC Int,* **2011,** *94(3),* 839-846
10. X. Zhang; H. Xu; H. Zhang;Y. Guo; Z. Dai; X. Chen; *Anal Bioanal Chem,* **2011**, *401,* 727–734
11. M. Bistoletti; L. Moreno; L. Alvarez; C. Lanusse; *Food Chem.*, **2011**, *126*, 793-800
12. N. Rummel; I. Chung; B. Shaikh; *J Liq Chromatogr Relat Technol.*, **2011**, *34(18)*, 2211-2223
13. B. Shaikh; N. Rummel; R. Reimschuessel; *J Agric Food Chem.*, **2003**, *51*, 3254-3259
14. Guidance for Industry. Bioanalytical Method Validation. U.S. Department of Health and Human Services Food and Drug Administration Ce nte r for Drug Evaluation and Re s earch (CDER)Center for Veterinary Medicine (CVM). https://www.fda.gov/media/70858/download [accesed November 2nd 2020]
15. Guideline on bioanalytical method validation. European Medicines Agency. Committe for Medicinal Products for Human Use (CHMP). 275542/2014. https://www.ema.europa.eu/en/documents/scientific-guideline/guideline-bioanalytical-method-validation_en.pdf [accessed November 2nd 2020]

16. H.A. Benchaoui; Dose titration and efficacy studies with the combination fenbendazole-piperonyl butoxide in sheep, in *Factors Affecting the Pharmacokinetics, Metabolism and Efficacy of Anthelmintic Drugs;* ProQuest LLO, Ann Harbor, USA, **2018**, Chapter 4, page 87
17. H.A. Benchaoui; Effect of piperonyl butoxide on the pharmacokinetics of albendazole and fenbendazole in sheep and goats, in *Factors Affecting the Pharmacokinetics, Metabolism and Efficacy of Anthelmintic Drugs;* ProQuest LLO, Ann Harbor, USA, **2018**, Chapter 3, page 65
18. L. Ceballos; A. Krolewiecki; M. Juarez; L. Moreno; F. Schaer; L.I. Alvarez; R. Cimino; J. Walson; C.E. Lanusse; *PLoS Negl Trop Dis.,* **2018**, *12(1)*, e0005945
19. A. Mirfazaelian; S. Dadashzadeh; M.R. Rouini; *Eur J Clin Pharmacol.,* **2002**, *58*, 403-408.